Structure and Bonding 179
Series Editor: D.M.P. Mingos

Markus W. Ribbe *Editor*

Metallocofactors that Activate Small Molecules

With Focus on Bioinorganic Chemistry

Springer

179
Structure and Bonding

Aims and Scope

Structure and Bonding is a publication which uniquely bridges the journal and book format. Organized into topical volumes, the series publishes in depth and critical reviews on all topics concerning structure and bonding. With over 50 years of history, the series has developed from covering theoretical methods for simple molecules to more complex systems.

Topics addressed in the series now include the design and engineering of molecular solids such as molecular machines, surfaces, two dimensional materials, metal clusters and supramolecular species based either on complementary hydrogen bonding networks or metal coordination centers in metal-organic framework materials (MOFs). Also of interest is the study of reaction coordinates of organometallic transformations and catalytic processes, and the electronic properties of metal ions involved in important biochemical enzymatic reactions.

Volumes on physical and spectroscopic techniques used to provide insights into structural and bonding problems, as well as experimental studies associated with the development of bonding models, reactivity pathways and rates of chemical processes are also relevant for the series.

Structure and Bonding is able to contribute to the challenges of communicating the enormous amount of data now produced in contemporary research by producing volumes which summarize important developments in selected areas of current interest and provide the conceptual framework necessary to use and interpret mega-databases.

We welcome proposals for volumes in the series within the scope mentioned above. Structure and Bonding offers our authors and readers:

- OnlineFirst publication. Each chapter is published online as it is finished, ahead of the print volume
- Wide dissemination. The chapters and the volume will be available on our platform SpringerLink, one of the largest collections of scholarly content in the world. SpringerLink attracts more than 50 million users at 15.000 institutions worldwide.
- Easy manuscript preparation. Authors do not have to spend their valuable time on the layout of their contribution. Springer will take care of all the layout related issues and will provide support throughout the complete process.

More information about this series at http://www.springer.com/series/430

Markus W. Ribbe
Editor

Metallocofactors that Activate Small Molecules

With Focus on Bioinorganic Chemistry

With contributions by

J. J. H. Cotelesage · A. M. Crawford · H. Dobbek · G. N. George · C. J. Hiller · Y. Hu · M. L. Kirk · C. C. Lee · S. J. Nieter Burgmayer · Y. Ohki · R. C. Prince · L. A. Rettberg · T. Spatzal · M. T. Stiebritz · K. Tanifuji · B. B. Wenke

Springer

Editor
Markus W. Ribbe
Departments of Molecular Biology &
Biochemistry, and Chemistry
University of California
Irvine, CA, USA

ISSN 0081-5993 ISSN 1616-8550 (electronic)
Structure and Bonding
ISBN 978-3-030-25896-2 ISBN 978-3-030-25897-9 (eBook)
https://doi.org/10.1007/978-3-030-25897-9

This Springer imprint is published by the registered company Springer Nature Switzerland AG.
The registered company address is: Gewerbestrasse 11, 6330 Cham, Switzerland

Preface

Metallocofactors containing various metals, such as iron, molybdenum, vanadium, and nickel, are essential for all forms of life on Earth. Structurally diverse and fascinating, these metallocofactors are found in many bacteria, performing some of the most remarkable redox chemistry to enable the activation of small molecule substrates, including N_2, CO, H_2, and CO_2, for biomass accumulation and energy metabolism. There is substantial interest in understanding how these metallocofactors function at the atomic level, especially in the context of sustainably feeding and fueling our planet, since knowledge in this regard could facilitate future design of synthetic catalysts that mimic the functions of these metallocofactors in Nature. However, despite intense efforts in this research area, key questions remain with respect to the mechanism and biosynthesis of these complex metallocofactors. The complexity of this subject topic presents a continuous challenge and a strong incentive for biochemists, biophysicists, and chemists to seek answers to the mechanistically relevant questions of these metallocofactors. This volume will highlight the recent progress on the fundamental chemistry and mechanistic understanding of the metallocofactors of nitrogenase, carbon monoxide dehydrogenase, and Moco-containing enzymes, with an emphasis on the major development in these areas from the perspective of bioinorganic chemistry.

Irvine, CA, USA — Markus W. Ribbe

Contents

Struct Bond (2019) 179: 1–14
DOI: 10.1007/430_2018_28

Published online: 9 November 2018

Looking at Nitrogenase: Insights from Modern Structural Approaches

Belinda B. Wenke and Thomas Spatzal

Contents

Abstract Nitrogenase, the primary biological source of fixed nitrogen, has been studied by various biochemical and biophysical methods to determine the mechanism of nitrogen reduction to ammonia. Previously, structural studies have contributed to determining the arrangement and identity of the unique metallocofactors of the as-isolated nitrogenase enzyme. Due to the multi-protein, dynamic nature of catalysis in nitrogenase, structurally capturing intermediates is not trivial. Recently, we have developed methods for preparing crystallographic samples of nitrogenase from active assay mixtures. The "out-of-assay" approach has yielded structures of small molecules bound to the active site cofactor, revealing an unexpected rearrangement of the belt sulfur atoms. The activity-based methods provide a framework for accessing non-resting states of the cofactor and introduce new questions surrounding the controlled binding and release of substrates. In the following, we discuss recent structural advances in the field and the novel directions for future activity-based research.

Keywords CO · FeMo-cofactor · Freeze quench · Nitrogenase · Selenium · X-ray crystallography

B. B. Wenke and T. Spatzal (✉)
Division of Chemistry and Chemical Engineering, California Institute of Technology, Pasadena, CA, USA
e-mail: spatzal@caltech.edu

1 Introduction to Nitrogenase

The nitrogenase enzyme system is the representational biological model for nitrogen fixation and has served as a source of inspiration for inorganic catalysts [1–4]. Nitrogenase catalyzes the reduction of atmospheric dinitrogen into ammonia. The Mo-nitrogenase model system is a two-component protein complex, comprised of the MoFe and Fe proteins. The MoFe protein contains two unique metalloclusters: the FeMo-cofactor ([7Fe:9S:C:Mo]-*R*-homocitrate) and the P-cluster ([8Fe:7S]) [5]. The Fe protein contains a [4Fe:4S] cluster. During nitrogen reduction, reduced Fe protein [4Fe:4S] transfers electrons to the P-cluster and ultimately the FeMo-cofactor (FeMo-co). Reduction of dinitrogen requires multiple association and dissociation events between the Fe protein and the MoFe protein, requiring ATP binding and hydrolysis by the Fe protein [6, 7]. The nitrogenase enzyme system presents a unique challenge for studying catalysis: in order to bind substrates to the MoFe protein, the FeMo-co (and, in sequence, the P-cluster and Fe protein [4Fe:4S]) must be in the correct reduction state. In vitro, the accumulation of six electrons and protons to convert nitrogen to ammonia necessarily involves an intermediate with two or more electrons and protons that evolve hydrogen gas and return the cofactor to its as-isolated resting state. In addition, multiple metal sites confound the challenge of unambiguously identifying the site of substrate binding by almost all spectroscopic techniques. Furthermore, the active site (Fig. 1) itself has an intrinsic threefold symmetry, which significantly complicates investigations in general.

The active site FeMo-co is ligated to the protein by only two residues (α-His442 and α-Cys257) in protein purified from the most common model system, *Azotobacter vinelandii* (Fig. 1) [8], which limits the traditional biochemical approach of active

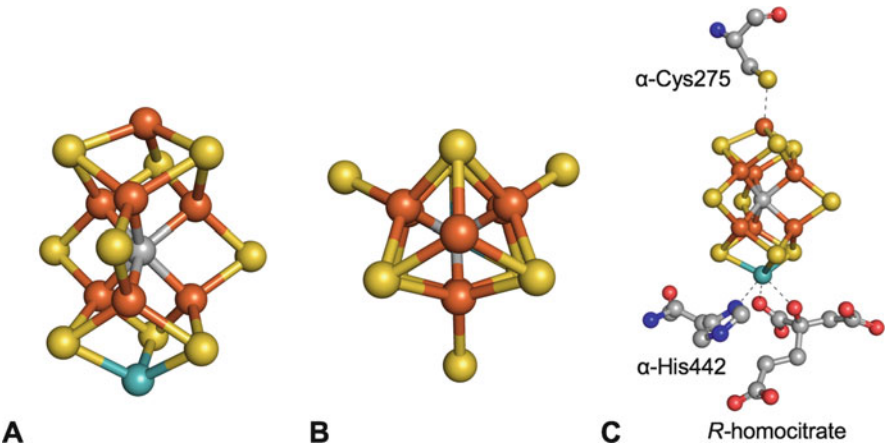

Fig. 1 (**a**) The FeMo-cofactor. The central carbon is shown in gray, the molybdenum in blue, irons in orange, and sulfur in yellow. (**b**) Top view of the FeMo-co down the Fe1-Mo axis, demonstrating the threefold symmetry of the belt sulfurs. (**c**) FeMo-co with ligands Cys275, His442, and *R*-homocitrate, as found in the molybdenum-iron nitrogenase from *Azotobacter vinelandii* [5]

site mutagenesis to almost exclusively second shell ligands. Direct studies of the cofactor and its reactivity have been conducted on the organic solvent-extracted cluster [9, 10], but the effects of the protein environment on catalysis are missing. In the intact protein, enzyme kinetics and substrate scope have been explored, but little is known about the details of substrate binding and reduction, and consequently the mechanism of catalysis remains enigmatic. The following chapter is therefore solely dedicated to the investigation of substrate interactions with the nitrogenase active site by means of recent structural approaches based on the active site in its native, unaltered protein environment in the *A. vinelandii* model system.

The technical challenges of isolating a uniform sample of a substrate-bound FeMo-co have previously frustrated structural studies. However, the recent development of assay-based (turnover-dependent) protein crystallography [11, 12] has yielded several new structures at resolutions sufficient to unambiguously describe binding modes of small molecules for the first time. This approach also cumulated in structures that have revealed striking structural changes in the FeMo-co that demonstrate that FeMo-co cannot be treated as a static molecule during catalysis. In the following, we describe an overview of the recently obtained insights into substrate binding to the active site of nitrogenase, the structural alterations within FeMo-co, and possible catalytic implications.

2 The Molybdenum Nitrogenase Model System

2.1 Substrate and Inhibitor Binding to the Active Site: A Structural Approach

Carbon monoxide as a ligand has been of particular interest in nitrogenase catalysis. CO is isoelectronic to and a reasonable approximation of dinitrogen. Like nitrogen, CO only binds to a reduced form of FeMo-co, relative to its resting state.

CO interacts with FeMo-co in a yet not fully characterized manner. It is a noncompetitive inhibitor for non-proton substrates but is also a substrate, resulting in the formation of products with C–C bonds such as ethylene, ethane, propylene, and propane [13–15]. In deuterium solvent, four-carbon products have also been detected [15]. Previous electron paramagnetic resonance (EPR) studies identified spectral changes in MoFe protein pressured with CO consistent with a singly-bound CO molecule ("lo-CO" at 0.08 atm) and multiply-bound CO ("high-CO" at 0.5 atm). Due to the above outlined complexity of FeMo-co, the spectral data could not unambiguously identify a binding site on FeMo-co [16].

An important development in understanding CO interactions with FeMo-co was the first crystal structure of a CO molecule bound to FeMo-co, which also depicts the first substrate-bound structure of the active site (Figs. 2 and 5a) [11]. The 1.5-Å structure obtained under turnover conditions was achieved by an "out-of-assay" based strategy, advancing the previously obtained structural information that only

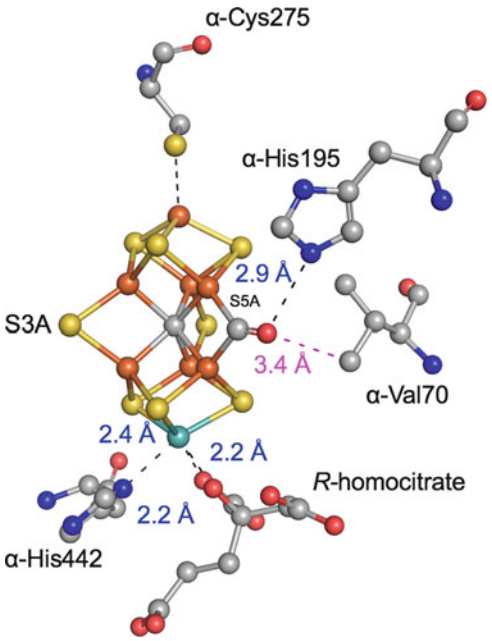

Fig. 2 Environment around the FeMo-cofactor with CO bound at the S2B site. Hydrogen bonds to the cofactor are shown in blue, and the distance to Val70-methyl is shown in magenta. OC-Fe2/6 bond lengths are 1.86 Å (compared to 2.2 Å to sulfur [5]), and the Fe2–Fe6 bond length is 2.5 Å. PDB 4TKV [11]

represented the system resting state. The CO-bound protein required continuous CO presence in active assay conditions (consisting of MoFe protein, Fe protein, ATP, substrate, reductant, and an enzymatic ATP regeneration system), to trap CO on the FeMo-co at the proper reduction state, which is achieved only by reduction via the Fe protein. Complete inhibition of the MoFe protein by CO binding was assayed by the cessation of acetylene reduction activity. The CO-inhibited MoFe protein was re-isolated by overpressure concentration and filtration under a CO atmosphere. Conditions for rapid crystallization (<5 h) were identified, and from the assay-based inhibition, the CO-bound MoFe protein was crystallized.

The 1.5-Å crystal structure revealed one CO molecule bound per FeMo-co, in a μ_2-briding mode between Fe2 and Fe6. The binding of CO was accompanied with an unprecedented displacement of belt sulfur S2B. The replacement of the belt sulfur induced compensatory adjustments in the overall FeMo-co structure: the distance between Fe2 and Fe6 shortened from 2.6 to 2.5 Å, and the central carbon-iron bonds lengthened from 1.86 to 2.2 Å. Overall, the cofactor is pinched relative to the resting state, with an overall deviation of 6° relative to the Fe1-C-Mo axis [11]. The CO ligand is in close proximity to the protein residues α-His195 (Nε2-OC) and α-Val70 (CH3-OC) (Fig. 2). These residues are known to have important mechanistic implications in nitrogen reduction, as obtained from mutagenesis studies: α-His195 to α-Gln195 abolishes nitrogen reduction activity [17], and α-Val70 replacement with α-Ala/Gly70 lead to long carbon-chain substrates [18]. CO binds exclusively at the Fe2–Fe6 face, breaking the threefold symmetry of the FeMo-co,

hence leading to a discrimination of the S2B site in comparison to the other two belt sulfur sites (S5A and S3A).

The mechanism of S2B displacement and CO binding is thought to proceed through protonation of S2B, possibly from donation from α-His195 to generate H_2S or HS^-. The FeMo-co must also be reduced by at least two electrons to be in a state electronically competent to bind CO. The displacement of S2B reveals an open Fe-binding site, subsequently allowing CO to bind. The removal of S2B may necessitate highly reduced forms of the FeMo-co to proceed [11].

The CO ligand binds close to the catalytically important residue α-Val70, which functions as size filter for the reduction of substrates [19], implying that a mechanistically important state has been captured. The Fe2–Fe6 edge of FeMo-co might therefore be the initial site for dinitrogen binding and reduction.

Subsequently it was demonstrated that the CO-inhibited active site FeMo-co can also be reactivated, showing full recovery of the S2B belt sulfur. The recovery of the resting state is further evidence for the catalytic importance of the CO-binding site. The unexpected structural rearrangements of FeMo-co reveal a structural plasticity in its more reduced forms that could not be predicted based on the previously known resting state. The lability of S2B (and eventually all the belt sulfurs) is a crucial feature of the active site that sheds light on the function of the belt sulfurs in occluding the iron sites for substrate and intermediate binding and reduction.

2.2 The Active Site FeMo-co: Incorporation of a Traceable Probe

The observed lability of the belt sulfur S2B in the CO-bound enzyme opened a new strategy for subsequent binding of alternative small molecules to the active site of nitrogenase. In addition to further exploring the role of the revealed Fe2–Fe6 binding site for the initial substrate binding event, the removal of S2B breaks the intrinsic threefold symmetry of the FeMo-co, simplifying the identification of subsequent intermediates through quantitative spectroscopic methods. The possibility of replacing a belt sulfur atom of the active site additionally provides the opportunity to insert traceable probes, which could enable valuable insights into cluster dynamics during catalysis.

As known for decades, nitrogenase can accept sulfur-containing substrates [20]. Conveniently, the physical properties of selenium, in addition to being a conservative substitute for sulfur, make it an excellent probe for a variety of spectroscopies and crystallographic studies. Selenium has already been incorporated into iron-sulfur clusters of varying nuclearity [21]. In the context of inorganic clusters, selenium can replace a sulfur atom in a known position and be used as a tracer to understand mechanisms of cluster fusion and interconversion [21–24]. Similarly, in the case of the FeMo-cofactor, a single-atom replacement (selenium in

place of sulfur at the S2B site) might create a starting point for a more detailed investigation of structural dynamics.

For binding studies, the small molecule selenocyanate ($SeCN^-$) was chosen due to the previously characterized inhibition and reactive properties of thiocyanate (SCN^-) [12, 20]. SCN^-, like CO, is a reversible inhibitor and a substrate, forming methane in the reaction. $SeCN^-$ has reactive properties similar to SCN^- (see Sect. 2.4). Adapting the strategy used to crystallize the CO-bound FeMo-co, MoFe protein was incubated in assay conditions and titrated with $SeCN^-$ until acetylene reduction activity reached a minimum [12]. Re-isolation of the MoFe protein yielded a 1.60-Å resolution crystal structure with a single selenium substitution at the S2B site (Figs. 3 and 5b).

The crystal structure re-isolated from the $SeCN^-$-inhibited nitrogenase activity assay [12] gave rise to a [7Fe:8S:Se:Mo:C]-*R*-homocitrate cluster (FeMoSe-co). The selenium substitution was identified with anomalous difference Fourier maps collected at the selenium K-edge at 12,662 eV. The selenium substitution caused no measurable differences in the cluster geometry and bond lengths. No density was identified for the cyanide group bound at the cofactor or in the surrounding protein matrix. Notably, the [7Fe:8S:Se:Mo:C]-*R*-homocitrate cluster could not be isolated from reaction mixtures of MoFe protein incubated with KSeCN alone nor MoFe protein incubated with Na_2Se. The selenium-substituted cluster could only be recovered under active turnover conditions and could not be soaked in without active incorporation.

The selective replacement of one Se atom in FeMo-cofactor (at Se2B) represented the first artificially generated structural mimic of the nitrogenase active site in vitro.

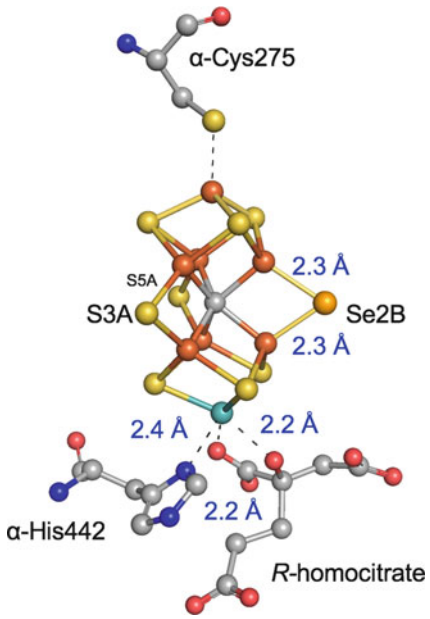

Fig. 3 Environment of the selenium-incorporated FeMo-cofactor. Bonds to the cofactor are indicated in blue. The selenium replacement at the S2B site is conservative, retaining 2.3 Å bond lengths to Fe2 and Fe6, compared to 2.2 Å in S2B [5]

FeMoSe-co lacks threefold symmetry and features an easily discriminated spectroscopic and crystallographic label while retaining catalytic activity.

2.3 A Modified Active Site: Mechanistic Implications

The MoFe protein with selenium incorporated at the S2B site (MoFe-Se2B) could be purified to homogeneity using size-exclusion chromatography, and the selenated protein is still able to reduce nitrogen and acetylene [12]. The kinetics of the reaction exhibited an extended lag phase compared to native MoFe protein from *A. vinelandii*. To further investigate the interaction of substrates with MoFe-Se2B, freeze-quench approaches were developed to trap the modified MoFe protein during catalysis. The freeze-quenching setup proved to be of crucial importance in generating samples arrested at mechanistically interesting time points during turnover and which were crystallizable [12].

In this approach, turnover conditions were initialized by introducing Se-substituted enzyme (MoFe-Se2B) to assay conditions in the presence of acetylene as a substrate. Samples were subsequently re-isolated at seven time points during turnover using a newly developed protocol to limit heterogeneity in the samples. The re-purification of the trapped states by crystallization yielded crystal structures for each of the seven states at resolutions ranging from 1.32 to 1.66 Å (Fig. 4). The freeze-quench strategy culminated in a series of crystal structures that enabled a previously unavailable glimpse into the FeMo-cofactor at work.

The series of crystal structures showed concomitant rearrangement and displacement of all three belt sulfurs of the active site as a function of acetylene reduction. Together, these structures highlight the lability of all three belt sulfurs, with the possibility of interchange at each site. The starting material in the reaction was the single sulfur-substituted MoFe-Se2B (with one selenium atom incorporated only at the Se2B position). Over the course of ongoing acetylene reduction, selenium atoms populate the two remaining belt sulfur positions S5A and S3A. At an endpoint of several thousand turnovers, selenium is entirely expelled from the cofactor, and sulfur is recovered, resulting in a resting state FeMo-cofactor (Fig. 4). The migration of Se within the FeMo-co sulfur belt reflects a significant and unexpected structural rearrangement in the FeMo-co during substrate reduction. In addition to the evidence that the S5A and S3A positions are labile, the selenium at S2B was ultimately regenerated with sulfur, suggesting that sulfide can be scavenged from the reaction mixture. From these data, the entry or exit pathway from the FeMo-co and the origin of the replacement sulfur are unclear.

In a parallel experiment using protons as a substrate, MoFe-Se2B demonstrated no Se migration from the Se2B to the S5A and S3A positions. When using CO as a substrate for MoFe-Se2B, CO displaces the majority of Se at the Se2B position (90% CO occupancy, 10% Se) (Fig. 5c), and the starting material S5A and S3A positions of the active site exhibit a mixture of selenium and sulfur (35% Se at 3A and 44% Se at 5A) at the conclusion of the experiment. The combinatorial experimental approach

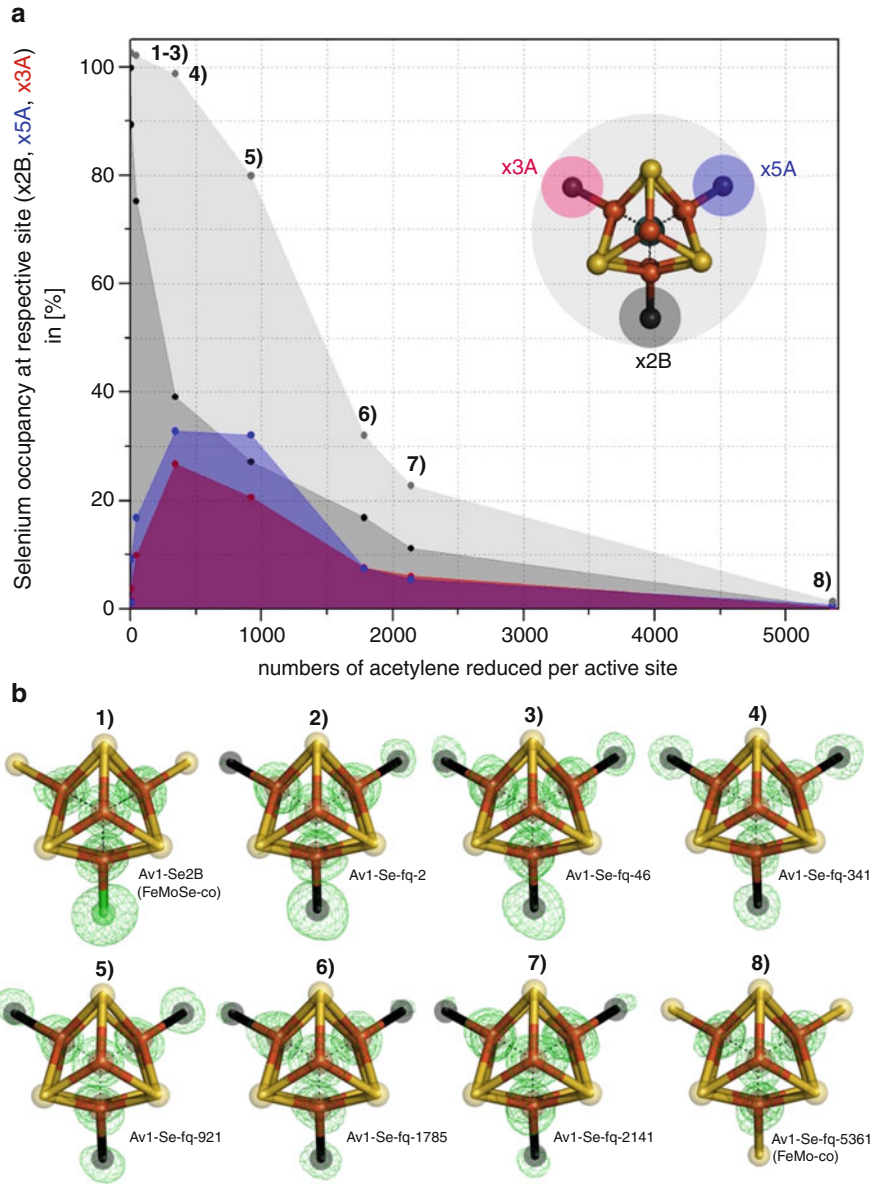

Fig. 4 Overview of selenium redistribution in MoFe-Se2B as a function of acetylene turnover number. Reproduced with permission from [12]. (**a**) Selenium occupancy in the three belt positions as a function of acetylene turnover. (**b**) Assay freeze-quench structures with anomalous density (contoured at 5 σ) used to quantify occupancy and migration

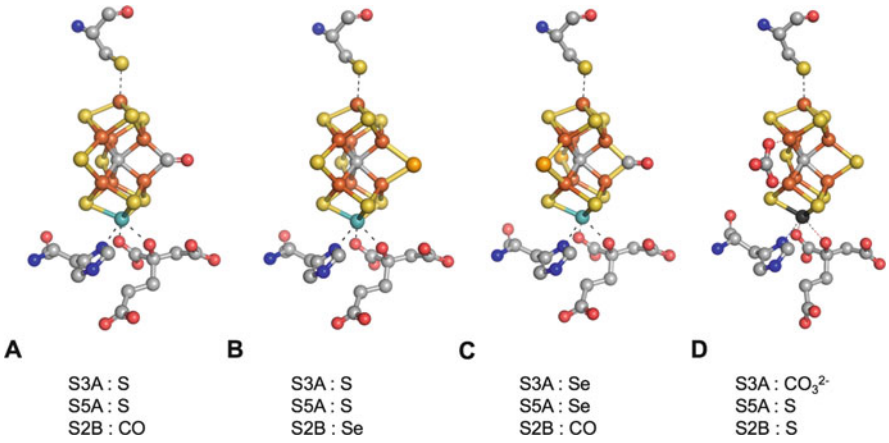

Fig. 5 (**a**) CO-bound MoFe protein, 4TKV. (**b**) Se-substituted MoFe protein, 5BVG. (**c**) CO-bound, Se-substituted MoFe protein, 5BVH. (**d**) Isolated VFe protein, 5N6Y

demonstrated that with a single CO-binding event, a complete rearrangement of the FeMo-co belt sulfurs is triggered. Comparatively, several thousand turnovers of acetylene are required to observe a similar effect. Currently, a preferred exit pathway for Se and/or S has not been identified. In contrast, all experimental data based on CO-binding and Se-incorporation unanimously identifies the Fe2–Fe6 edge of the FeMo-co as the substrate entry point for catalysis.

The observation of selenium redistribution suggests a number of possible exchange mechanisms to bind substrates to the irons of the FeMo-cofactor. Once such mechanism could be a rotary-type mechanism [25], in which the two halves of the FeMo-cofactor twist, exchanging the atoms at the belt positions. Other mechanisms may involve a sequential protonation and removal of individual belt sulfurs, revealing the Fe3–Fe7 and Fe4–Fe5 edges for substrate or intermediate binding. Thus far, no experiments have shown that sulfurs in non-belt positions can be replaced in a turnover-dependent fashion. The demonstrated exchange of belt sulfurs in a substrate-dependent manner may provide a framework to build a molecular mechanism for nitrogenase.

2.4 Kinetic Effects of a Surrogate Substrate: SeCN Versus SCN

The frontier of catalysis and binding in the *A. vinelandii* nitrogenase model system is exploring the transiently exposed, non-resting states of the FeMo-co. The well-known property of nitrogenase to interact with small molecules acting as both an inhibitor and substrate is of great interest and mechanistic relevance. In the case of comparing SCN^- to its recently discovered surrogate $SeCN^-$ [12], profound kinetic

differences in their interaction with the MoFe protein are observable. SCN^- can reversibly bind a proton to form thiocyanic acid (HSCN) or tautomerize to isothiocyanic acid (SCNH) with a pKa of 1.1 at 20°C [26]. Sulfur replacement with selenium further decreases the pKa to <1 [27]. Structurally within metal clusters, sulfur to selenium has been considered a conservative substitution, due to the small difference in ionic radius ($S^{2-} = 1.84$ Å versus $Se^{2-} = 1.91$ Å) and small effect on the cluster midpoint potential (<50 mV shift to positive potentials using selenium) [12]. Both SCN^- and $SeCN^-$ compounds were observed to inhibit the reduction of acetylene to ethylene in purified nitrogenase protein [12, 20]. Under standard assay conditions (pH 7.5), $SeCN^-$ is a more potent inhibitor compared to SCN^-, with an inhibition constant 30-fold lower ($K_i(SeCN^-) = 0.41 \pm 0.03$ mM compared to $K_i(SCN^-) = 12.7 \pm 1.2$ mM) [12]. The pronounced inhibition of $SeCN^-$ could be related to its enhanced nucleophilicity in comparison with sulfur, due to its polarizability [28], leading to incorporation into the FeMo-co.

Nitrogenase catalyzes the conversion of SCN^- (below its K_i) to CH_4, HCN, H_2S, and NH_4 [20]. Below the K_i of $SeCN^-$, CH_4, H_2, and NH_4 are detected as products. Compared to SCN^-, $SeCN^-$ has a lower V_{max} for CH_4 production as well as H_2 production. The lag phase observed in generating the MoFe-Se2B from $SeCN^-$ may reflect the accumulation of an intermediate relative to reactions with SCN^-, but further experiments are required to explore the mechanism.

Additionally, the capability of MoFe-Se2B to catalyze substrate reduction in a similar fashion to the all-sulfur FeMo-co, with kinetically different properties, enables a broad range of future experiments to systematically probe FeMo-co.

3 Alternative Nitrogenases: A Brief Look at the Vanadium Counterpart

Recently, the crystal structure of the vanadium nitrogenase (VFe protein) has been reported (Figs. 5d and 6) [29]. Vanadium nitrogenases form as an alternative to the molybdenum nitrogenase in molybdenum-limiting conditions. VFe protein is expressed by a distinct *vnf* gene cluster that allows for diazotrophic growth [30, 31]. In comparison to the MoFe protein, VFe protein is distinctly different in terms of its subunit composition, substrate range, and catalytic properties. The VFe protein requires significantly more equivalents of ATP to reduce N_2 to $2NH_4$ (40 MgATP versus 16 MgATP in MoFe protein), as well as forming three equivalents of H_2 compared to one equivalent of H_2 in MoFe protein [32].

The crystal structure revealed that besides the presence of an additional δ subunit (leading to an overall composition $\alpha_2\beta_2\delta_2$), the FeV-cofactor (VFe-co) is composed of [V:7Fe:8S:C], with a homocitrate and His423 ligand, as well as an apical Cys257 ligand analogous to the FeMo-cofactor. The structure also revealed that the x3A belt position, which is occupied by a sulfur in the FeMo-co, is occupied likely by a carbonate (CO_3^{2-}). The carbonate bridges the Fe4–Fe5 face and has bond lengths of

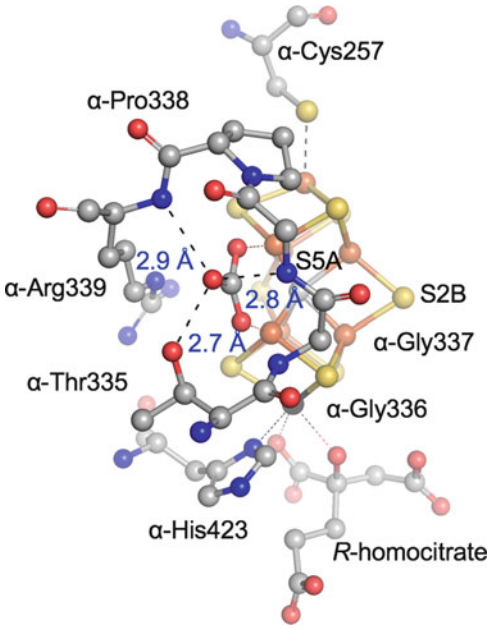

Fig. 6 Environment of the carbonate bound to the FeV-cofactor. In blue, interactions to backbone α-Arg339, backbone α-Gly337, and α-Thr335 Oγ are indicated. PDB 5N6Y [29]

~1.3 Å. The distance between Fe4 and Fe5 increases from 2.61 to 2.76 Å, shortening the distance between Fe5 and V. The carbonate is coordinated to the backbone amides of α-Gly337 and α-Arg339 and to the α-Thr335 hydroxyl. In comparison to the MoFe protein, the pocket is sterically hindered by α-Pro360 residue, but S3A is well-coordinated by the backbone amides of α-Gly356, α-Gly357, and α-Arg359 (Fig. 6) [29].

The observation of a small molecule, such as CO_3^{2-}, being coordinated in a belt position in FeV-co, provides a very notable structural difference compared to FeMo-co. The kinetic profile of FeV-co in the turnover of various substrates is distinctly different from that of FeMo-co, which suggests that modulating the belt sulfur structure in the nitrogenase active sites is an effective method of tuning the reactive properties. The exchangeability and replaceability of the belt sulfur structure in nitrogenase's active site are thus crucial for its reactivity and mark an important starting point for a new series of investigations aiming at the elucidation of its molecular mechanism.

4 Conclusions

Structural biology, specifically X-ray crystallography, has recently led to several new discoveries in the identification of substrate binding to one of nature's most elaborate metalloenzymes. A key step toward achieving this goal is a crystallographic sample preparation out of turnover conditions, which revealed unexpected

structural plasticity in the nitrogenase active site, the FeMo-cofactor. This new approach in the structural biology of nitrogenase is a gate opener toward a multitude of structural investigations aiming at "looking" at nitrogenase's active site at work.

The resulting series of protein structures have drawn specific attention to FeMo-co's belt sulfur positions, which might only serve as protecting groups shielding the iron edges of the active site from substrate binding and reduction. The discovered lability of FeMo-co's belt sulfur structure consisting of S2B, S3A, and S5A strongly suggests the direct involvement of all six iron sites of FeMo-co in substrate binding and reduction. The carbon atom in the center of the active site might therefore solely serve as a structural stabilizer during belt sulfur migration and abstraction during catalysis. The binding studies involving CO, a substrate/inhibitor isoelectronic to N_2, demonstrated that a single binding event is able to trigger a virtually complete rearrangement of the active site belt atom structure. Future studies, particularly based on modified active sites, will explore the detailed relationship between substrate binding and structural rearrangements, thus characterizing the discreet binding sites available on the cluster based on the provided substrate. Lastly, the feasibility of a time-resolved structural analysis via a freeze-quench approach demonstrated that deriving a molecular mechanism based on structural data might be possible.

Acknowledgments The authors thank Douglas C. Rees, James B. Howard and Kathryn A. Perez for their support and helpful discussions, as well as the scientists of Beamline 12-2, Stanford Synchrotron Radiation Lightsource (Department of Energy, DE-AC02-76SF00515). The authors are supported by the National Institute of Health grant GM45162 as well as NIH/NRSA training grant 5 T32 GM07616.

References

1. Yandulov DV, Schrock RR (2003) Catalytic reduction of dinitrogen to ammonia at a single molybdenum center. Science 301(5629):76–78
2. Peters JC, Mehn MP (2006) Bio-organometallic approaches to nitrogen fixation chemistry. Activation Small Mol Organomet Bioinorg Perspect:81. https://doi.org/10.1002/9783527609352.ch3
3. Arashiba K, Miyake Y, Nishibayashi Y (2011) A molybdenum complex bearing PNP-type pincer ligands leads to the catalytic reduction of dinitrogen into ammonia. Nat Chem 3 (2):120–125
4. Anderson JS, Rittle J, Peters JC (2013) Catalytic conversion of nitrogen to ammonia by an iron model complex. Nature 501(7465):84
5. Spatzal T, Aksoyoglu M, Zhang L, Andrade SLA, Schleicher E, Weber S, Rees DC, Einsle O (2011) Evidence for interstitial carbon in nitrogenase FeMo cofactor. Science 334(6058):940
6. Burgess BK, Lowe DJ (1996) Mechanism of molybdenum nitrogenase. Chem Rev 96 (7):2983–3012
7. Thorneley RNF, Lowe DJ (1985) Kinetics and mechanism of the nitrogenase enzyme system. Mol Enzym 7:221–284
8. Rees DC, Howard JB (2000) Nitrogenase: standing at the crossroads. Curr Opin Chem Biol 4 (5):559–566

9. Burgess BK (1990) The iron-molybdenum cofactor of nitrogenase. Chem Rev 90(8):1377–1406
10. Fay AW, Lee C-C, Wiig JA, Yilin H, Ribbe MW (2011) Protocols for cofactor isolation of nitrogenase. Nitrogen fixation. Humana Press, New York, pp 239–248
11. Spatzal T, Perez KA, Einsle O, Howard JB, Rees DC (2014) Ligand binding to the FeMo-cofactor: structures of CO-bound and reactivated nitrogenase. Science 345(6204):1620–1623
12. Spatzal T, Perez KA, Howard JB, Rees DC (2015) Catalysis-dependent selenium incorporation and migration in the nitrogenase active site iron-molybdenum cofactor. Elife 4:e11620
13. Yang ZY, Dean DR, Seefeldt LC (2011) Molybdenum nitrogenase catalyzes the reduction and coupling of CO to form hydrocarbons. J Biol Chem 286:19417–19421
14. Lee CC, Hu Y, Ribbe MW (2010) Vanadium nitrogenase reduces CO. Science 329:642
15. Hu Y, Lee CC, Ribbe MW (2011) Extending the carbon chain: hydrocarbon formation catalyzed by vanadium/molybdenum nitrogenases. Science 333:753–755
16. Cameron LM, Hales BJ (1998) Investigation of CO binding and release from Mo-nitrogenase during catalytic turnover. Biochemistry 37(26):9449–9456
17. Kim C-H, Newton WE, Dean DR (1995) Role of the MoFe protein alpha-subunit histidine-195 residue in FeMo-cofactor binding and nitrogenase catalysis. Biochemistry 34(9):2798–2808
18. Barney BM, Igarashi RY, Dos Santos PC, Dean DR, Seefeldt LC (2004) Substrate interaction at an iron-sulfur face of the FeMo-cofactor during nitrogenase catalysis. J Biol Chem 279 (51):53621–53624
19. Christiansen J, Cash VL, Seefeldt LC, Dean DR (2000) Isolation and characterization of an acetylene-resistant nitrogenase. J Biol Chem 275(15):11459–11464
20. Rasche ME, Seefeldt LC (1997) Reduction of thiocyanate, cyanate, and carbon disulfide by nitrogenase: kinetic characterization and EPR spectroscopic analysis. Biochemistry 36 (28):8574–8585
21. Zheng B, Chen X-D, Zheng S-L, Holm RH (2012) Selenium as a structural surrogate of sulfur: template-assisted assembly of five types of tungsten-iron-sulfur/selenium clusters and the structural fate of chalcogenide reactants. J Am Chem Soc 134(14):6479–6490
22. Reynolds JG, Holm RH (1980) Improved syntheses of the dimeric complexes [Fe2X2 (SC6H4Y) 4] 2-and [Fe2X2 ((SCH2) 2C6H4) 2] 2-(X= sulfur, selenium), analogs of the 2-Fe sites of oxidized ferredoxin proteins. Inorg Chem 19(11):3257–3260
23. Moulis JM, Meyer J (1982) Characterization of the selenium-substituted 2 [4Fe-4Se] ferredoxin from Clostridium pasteurianum. Biochemistry 21(19):4762–4771
24. Beinert H (2000) Iron-sulfur proteins: ancient structures, still full of surprises. J Biol Inorg Chem 5(1):2–15
25. Hernández JV, Kay ER, Leigh DA (2004) A reversible synthetic rotary molecular motor. Science 306(5701):1532–1537
26. Martell AE, Smith RM, Motelaitis RJ (2001) NIST Database 46. National Institute of Standards and Technology, Gaithersburg
27. Boughton JH, Keller RN (1966) Dissociation constants of hydropseudohalic acids. J Inorg Nucl Chem 28(12):2851–2859
28. Reich HJ, Hondal RJ (2016) Why nature chose selenium. ACS Chem Biol 11(4):821–841
29. Sippel D, Einsle O (2017) The structure of vanadium nitrogenase reveals an unusual bridging ligand. Nat Chem Biol 13(9):956
30. Joerger RD, Loveless TM, Pau RN, Mitchenall LA, Simon BH, Bishop PE (1990) Nucleotide sequences and mutational analysis of the structural genes for nitrogenase 2 of Azotobacter vinelandii. J Bacteriol 172(6):3400–3408
31. Hales BJ (1990) Alternative nitrogenase. Adv Inorg Biochem 8:165–198
32. Lee CC, Yilin H, Ribbe MW (2009) Unique features of the nitrogenase VFe protein from Azotobacter vinelandii. Proc Natl Acad Sci 106(23):9209–9214

Struct Bond (2019) 179: 15–32
DOI: 10.1007/430_2018_29

Published online: 9 November 2018

Current Understanding of the Biosynthesis of the Unique Nitrogenase Cofactor Core

Caleb J. Hiller, Lee A. Rettberg, Chi Chung Lee, Martin T. Stiebritz, and Yilin Hu

Contents

Abstract Nitrogenase catalyzes the remarkable chemical transformations of N_2 to NH_3, and C_1 substrates to hydrocarbons, under ambient conditions. The best-studied Mo-nitrogenase utilizes a complex metallocofactor ([$MoFe_7S_9C$(*R*-homocitrate)]) for substrate binding and reduction; however, the complexity of this cofactor has hindered a better understanding of its mechanistic details and chemical synthesis so far. Driven by the pressing questions related to the structure and function of the nitrogenase cofactor, research in the past decades has been focused on unraveling the biosynthetic mechanism of this metallocluster in order to cultivate knowledge of how the cofactor is functionalized in this process. In this review, we summarize the recent advances toward a better understanding of the biosynthesis of the nitrogenase cofactor, with a particular focus on the biosynthetic events related to the generation

C. J. Hiller
Department of Molecular Biology and Biochemistry, University of California, Irvine, Irvine, CA, USA

Department of Chemistry, University of California, Irvine, Irvine, CA, USA

L. A. Rettberg, C. C. Lee, M. T. Stiebritz, and Y. Hu (✉)
Department of Molecular Biology and Biochemistry, University of California, Irvine, Irvine, CA, USA
e-mail: yilinh@uci.edu

of its unique core structure. Information derived from these studies has unveiled a novel, radical SAM-dependent mechanism of carbide insertion that orchestrates the coupling and rearrangement of two 4Fe cluster modules into a unique 8Fe cofactor core, as well as a sulfite-based route that incorporates a '9th sulfur' at the catalytically important "belt" region of the cofactor. Continued efforts along this line of investigation will further unravel the biosynthetic mechanism of the nitrogenase cofactor while facilitating investigations into the elusive catalytic mechanism of nitrogenase.

Keywords '9th sulfur' · Interstitial carbide · M-cluster (cofactor) · Nitrogenase · Radical SAM

1 Introduction

Nitrogenase catalyzes one of the most challenging chemical transformations in nature: the reductive cleavage of dinitrogen (N_2) to form ammonia (NH_3), whereby the relatively inert N_2 is converted into a bioavailable form of nitrogen that is essential for life on this planet [1, 2]. In a reaction that is usually depicted as $N_2 + 8e^- + 8H^+ + 16\,MgATP \rightarrow 2NH_3 + H_2 + 16\,MgADP + 16P_i$ [3], nitrogenase is capable of carrying out the energetically demanding scission of the N ≡ N triple bond under ambient temperatures and pressures. In addition, nitrogenase can reduce carbon monoxide (CO) and carbon dioxide (CO_2) to hydrocarbons in reactions that recycle carbon wastes into useful fuel products under ambient conditions [4–11]. Thus, nitrogenase catalyzes reactions that mirror two important industrial processes: the Haber-Bosch (HB) process, which combines N_2 and hydrogen (H_2) into NH_3 [12], and the Fischer-Tropsch (FT) process, which combines CO and H_2 into carbon fuels [13]. The ability of nitrogenase to utilize protons (H^+) instead of the expensive syngas, H_2, to enable the ambient HB- and FT-like reactions makes this enzyme a potential template for future development of strategies for cost-efficient ammonia- and hydrocarbon-producing strategies.

Three homologous nitrogenases, which are distinguished mainly by the transition metal composition within the enzyme active sites, have evolved to enable the remarkable chemical transformations of small molecules: the molybdenum (Mo)-nitrogenase, which contains iron (Fe) and Mo; the vanadium (V)-nitrogenase, which contains Fe and V; and the Fe-only nitrogenase, which contains only Fe and no heterometal [7, 10]. Among them, the Mo-nitrogenase from *Azotobacter vinelandii* has been extensively studied and shows superior catalytic N_2 reduction activity as compared to its V- and Fe-only counterparts [1–3, 5]. This enzyme consists of two component proteins: one, designated the Fe protein (or NifH), is a homodimer containing a subunit-bridging [Fe_4S_4] cluster and an MgATP-binding site within each subunit; the other, designated the MoFe protein (or NifDK), is an $\alpha_2\beta_2$-heterotetramer containing a P-cluster ([Fe_8S_7]) at each α/β-subunit interface and an M-cluster (also known as cofactor or FeMoco; [$MoFe_7S_9C$(*R*-homocitrate)]) within

each α-subunit [14–17]. Upon substrate turnover, the two components form a functional complex [18, 19], which allows electrons to be transferred concomitant with ATP hydrolysis from the [Fe_4S_4] cluster of NifH, via the P-cluster, to the M-cluster of NifDK, where substrate reduction occurs (Fig. 1a, b). The unique assortment of metalloclusters along the electron transfer pathway, and, in particular, the substrate-reducing site (or M-cluster) that is located at the end of this pathway, underscores the unique catalytic abilities of nitrogenase.

Arguably the most complex metallocluster found in nature, the M-cluster, can be viewed as [$MoFe_3S_3$] and [Fe_4S_3] subclusters bridged by three μ_2-coordinated, "belt" sulfides in between. Other than having a complex, high-nuclearity metal-sulfur core structure, the M-cluster is also noted for the presence of an organic homocitrate entity at its Mo end and a μ_6-coordinated interstitial carbide in its central cavity (Fig. 1c). The homocitrate moiety, which is −4 upon deprotonation of its hydroxyl group, is thought to give the M-cluster an overall negative charge despite a proposed charge of +1 or +3 for the metal-sulfur core of this cofactor in the resting state [20–24]. The interstitial carbide, on the other hand, likely plays a role in stabilizing the structure of the M-cluster, particularly given that it cannot be exchanged upon substrate turnover [25, 26]. This argument is further supported by recent studies that imply the lability of belt sulfides during substrate turnover, which

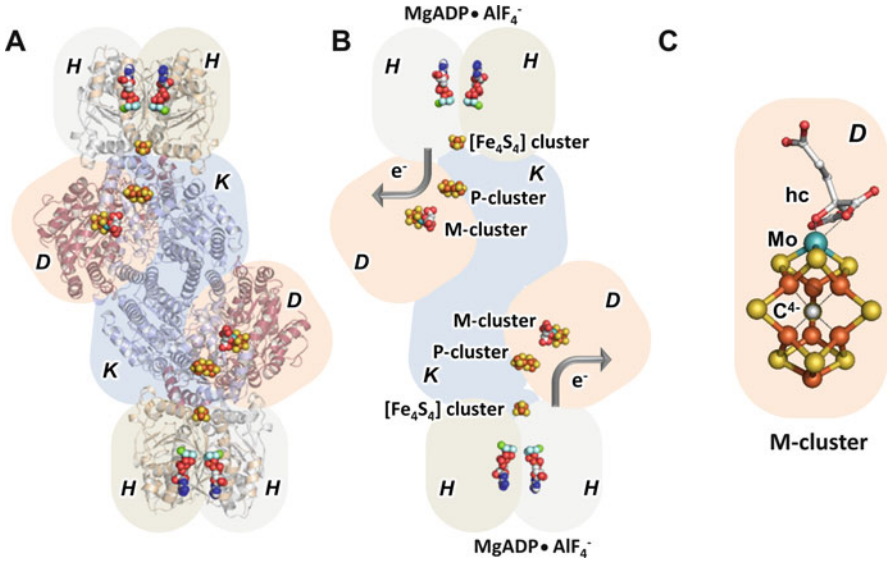

Fig. 1 Structures of the Mo-nitrogenase and its cofactor. (**a**) Ribbon and (**b**) schematic presentations of MgADP•AlF_4^--stabilized Mo-nitrogenase complex (PDB entry: 1N2C) between the Fe protein (NifH) and the MoFe protein (NifDK) and (**c**) crystal structure of the cofactor (M-cluster). The two subunits of NifH are colored in different shades of gray; the D (α)- and K (β)-subunits of NifDK are colored in shades of pale orange and pale blue. The clusters are shown as ball-and-stick models. Colors of atoms: Fe, orange; S, yellow; Mo, cyan; O, red; C, gray; N, blue; Mg, green; Al, azure; F, light blue

further point to a possible role of the interstitial carbide as an "anchor" that holds the cluster structure together upon loss of a belt sulfide [27, 28]. Although the question of whether this interstitial carbide directly participates in catalysis remains elusive, its possible function in modulating the reactivity of the M-cluster or interacting with the substrate cannot be ruled out at this point [29]. Interestingly, despite its structural complexity, the M-cluster is ligated by only two ligands, $Cys^{\alpha 275}$ (at its Fe end) and $His^{\alpha 442}$ (at its Mo end), in the α-subunit of NifDK. Such a coordination pattern could in turn explain why the M-cluster can be extracted intact into an organic solvent, such as *N*-methylformamide, and act as a catalyst on its own in reducing C_1 substrates (i.e., CO, CN^- and CO_2) to hydrocarbons when a strong reductant is used to drive the reaction [6, 30–32].

The fact that the M-cluster can function both as a protein-bound cofactor and as an isolated metallocatalyst makes it an attractive biomimetic target for future developments of nitrogenase-based applications. However, the complexity of the M-cluster has precluded successful chemical synthesis, as well as a comprehensive mechanistic understanding of this unique cofactor thus far. Understanding the biosynthetic mechanism of M-cluster is, therefore, of critical importance for enabling practical applications and mechanistic investigations of nitrogenase-based reactions. Previous studies have led to the proposal that a large number of gene products are required for the assembly of the cofactor of the *nif*-encoded Mo-nitrogenase [33–68]. In the past decade, biochemical, spectroscopic, and structural studies have narrowed this list down to a minimum set of *nif* gene products that play key roles in the biosynthesis of the nitrogenase cofactor [33, 69–78], which involves formation of an 8Fe core of the cofactor, maturation of the 8Fe core into a cofactor, and transfer of the cofactor to its targeted binding site (Fig. 2).

Of all the biosynthetic events that ultimately lead to the formation of a mature cofactor, the determining steps are those giving rise to the unique core structure of

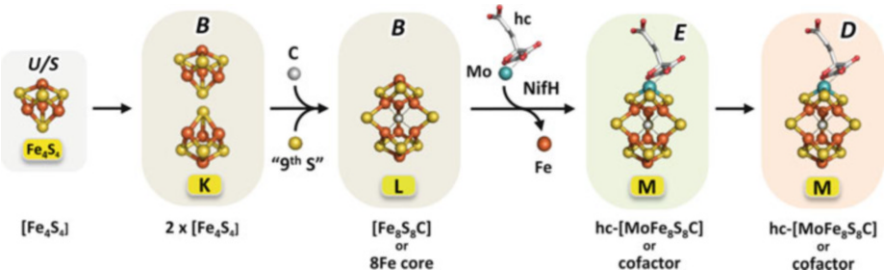

Fig. 2 Flow diagram of the M-cluster assembly pathway. Biosynthesis of the M-cluster is initiated by NifS and NifU, which generate $[Fe_4S_4]$ units that are delivered to NifB. Subsequently, two $[Fe_4S_4]$ clusters (K-cluster) are coupled into an $[Fe_8S_9C]$ cluster (L-cluster) on NifB concomitantly with the radical SAM-dependent C insertion and the addition of a '9th' S. The L-cluster is then transferred to NifEN, where it undergoes further processing into a fully assembled M-cluster (hc-$[MoFe_7S_9C]$; hc, homocitrate) upon NifH-mediated insertion of Mo and hc. Finally, the M-cluster is transferred from NifEN to the cofactor-binding site in NifDK. For the purpose of simplicity, only the protein subunits housing the clusters (B, E, D) are depicted. All clusters are shown as ball-and-stick models, with the atoms colored as those in Fig. 1

this cofactor, which are highlighted by sophisticated chemistry that transforms standard FeS building blocks into a chemically unprecedented metallocofactor. Recent studies have significantly advanced our understanding of the biosynthesis of the nitrogenase cofactor core structure. These studies will be discussed in detail in this chapter, followed by a brief summary and outlook onto the future directions of this research topic.

2 Generation of the Unique Core of Nitrogenase Cofactor

The most critical stage in the biosynthesis of the nitrogenase cofactor is the formation of the unique cofactor core structure. This process is initiated by NifS and NifU, which mobilize Fe and S for the production of small FeS clusters as the building blocks for cofactor assembly. NifS is believed to serve as a pyridoxal phosphate-dependent cysteine desulfurase in this process, which presumably generates a protein-bound cysteine persulfide that is subsequently transferred to its assembly partner, NifU, for the sequential formation of $[Fe_2S_2]$ and $[Fe_4S_4]$ clusters [34, 36–40, 79]. Once generated, the $[Fe_4S_4]$ clusters are delivered to NifB, a radical SAM enzyme, where a pair of $[Fe_4S_4]$ clusters are coupled and rearranged into an $[Fe_8S_9C]$ cofactor core via the unique radical SAM chemistry (Fig. 2).

2.1 Cluster Modules Involved in Core Formation

The essential role of NifB in cofactor biosynthesis was established by the previous observations of a lack of nitrogenase activity in the crude extracts of *nifB*-deletion strains [41–44], as well as an absence of cofactor from the NifDK protein isolated from a *nifB*-deletion strain of *A. vinelandii* [41, 80]. Sequence analysis of NifB revealed the presence of a canonical CxxxCxxC motif typically used by radical SAM enzymes for the ligation of a SAM-binding $[Fe_4S_4]$ cluster, along with a number of conserved Cys and His ligands that could coordinate the entire complement of Fe atoms of the cofactor [77]. Metal and EPR analyses of a NifEN-B fusion protein from *A. vinelandii*, where NifB was fused to its downstream assembly partner NifEN, supported the sequence-based predictions of the presence of different cluster species on NifB. In particular, NifB displayed a composite $S = 1/2$ EPR signal at $g = 2.02$, 1.95 and 1.90 (Fig. 3a), which could arise from approximately three 4Fe cluster species based on spin quantitation. Excitingly, this composite $S = 1/2$ signal disappeared upon addition of SAM concomitant with the appearance of a $g = 1.94$ signal (Fig. 3b) [81] that had been previously assigned to a $[Fe_8S_9C]$ cluster (designated the L-cluster) – a cluster closely resembling the M-cluster in the core structure but with Fe substituting for Mo/homocitrate at one end of the cluster [82–85]. Taken together, these observations have led to the proposal that NifB has two types of cluster species (Fig. 3c): one, designated the SAM-cluster, is a $[Fe_4S_4]$

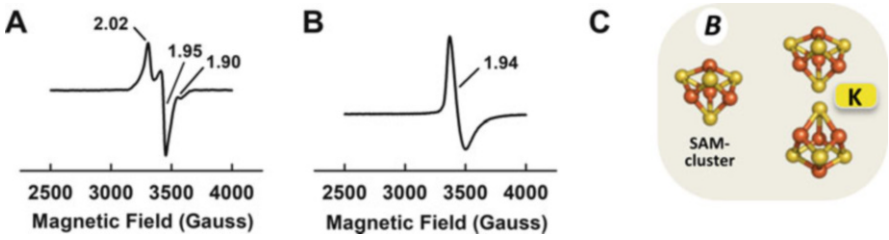

Fig. 3 EPR features and compositions of the cluster species on NifB. (**a**) The composite $S = 1/2$ signal originating from the SAM- and K-clusters on NifB in the dithionite-reduced state. (**b**) The L-cluster-specific $g = 1.94$ signal that appears upon incubation of NifB with SAM, which suggests the conversion of a K-cluster to an L-cluster. (**c**) The presence of two cluster species, namely, the SAM- and K-clusters, on NifB. The SAM-cluster is a $[Fe_4S_4]$ cluster, whereas the K-cluster comprises a pair of $[Fe_4S_4]$ clusters

cluster that is bound to the SAM-binding motif; the other, designated the K-cluster, is a pair of $[Fe_4S_4]$ clusters that can be used for the synthesis of an $[Fe_8S_9C]$ L-cluster [81]. The K- and SAM-clusters are likely located in close vicinity to each other, which could account for the concurrent response of the EPR signals arising from the SAM- and K-clusters to the addition of SAM.

Direct evidence for the 4Fe nature of the cluster species on NifB came from the mutagenic studies of NifB from *Methanosarcina acetivorans* (designated *Ma*NifB). MaNifB shares a good degree of sequence homology with its *A. vinelandii* counterpart (designated *Av*NifB), and it cross reacts well with NifEN, the downstream assembly protein, from *A. vinelandii*, resulting in ~100% in vitro cofactor maturation as compared to that achieved by *Av*NifB in the same assay [86]. However, contrary to *Av*NifB, *Ma*NifB can be co-expressed well along with the FeS-assembly machinery, IscSUA, in *Escherichia coli* [86], making genetic manipulations of this protein a lot easier than its *A. vinelandii* counterpart in its original host. Sequence analysis of *Ma*NifB suggests a possible assignment of three groups of highly conserved Cys residues as potential ligands for the SAM- and K-clusters (Fig. 4a): (1) Cys^{50}, Cys^{54}, and Cys^{57} (arranged as a CxxxCxxC motif), which could be assigned to the SAM-module; (2) Cys^{30}, Cys^{63}, and Cys^{129}, which could be assigned to one 4Fe module of the K-cluster (designated the K1-module); and (3) Cys^{264}, Cys^{274}, and Cys^{277}, which could be assigned to the other 4Fe module of the K-cluster (designated the K2-module). Three constructs were generated based on this assignment, each carrying a single SAM-, K1-, or K2-module upon mutation of the Cys ligands of the two modules to Ala [87]. When co-expressed in *E. coli* with the FeS-assembly machinery (IscSUA) and reconstituted with synthetic $[Fe_4S_4]$ clusters, each NifB variant displayed a $[Fe_4S_4]^{1+}$ cluster-characteristic, $S = 1/2$ EPR signal in the dithionite-reduced state, with the simulated spectrum showing distinct *g*-values from those of the others, as expected from clusters originating from different origins (Fig. 4b) [87]. One-dimensional electron spin echo envelope modulation (ESEEM) and two-dimensional hyperfine sub-level correlation (HYSCORE) pulse EPR studies further revealed coordination of the K1-module by a fourth, histidine ligand, which is lost upon the K- to L-cluster conversion in the

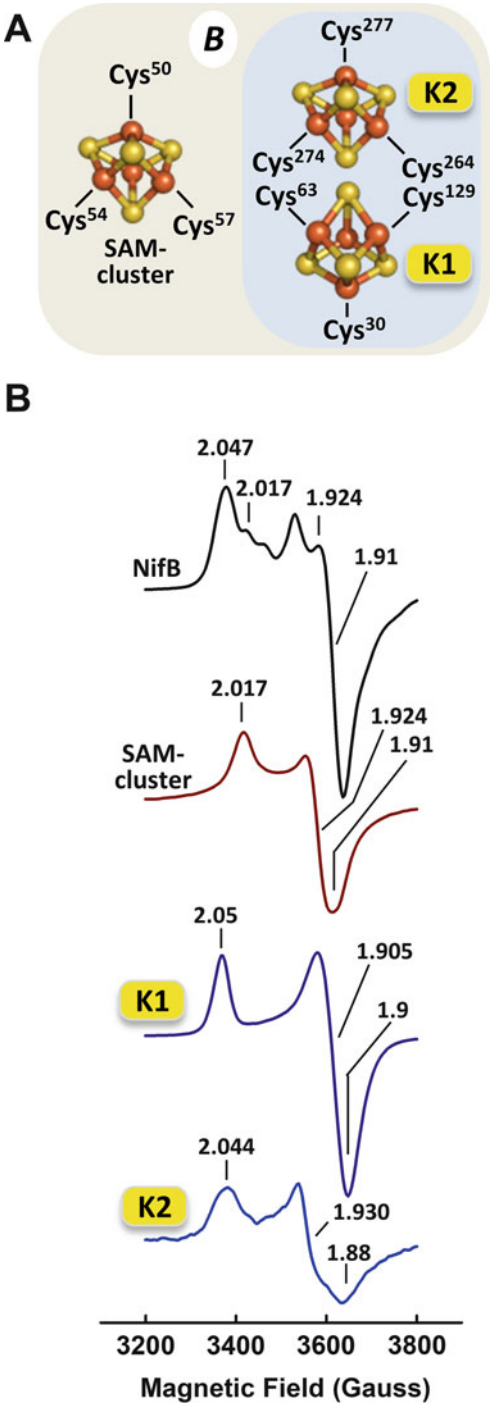

Fig. 4 Proposed protein ligands and EPR features of the cluster species on NifB. (**a**) Schematic presentations of the 3-Cys ligation patterns of SAM-, K1-, and K2-modules in *Methanosarcina acetivorans* NifB (*Ma*NifB). (**b**) EPR spectra of the $[Fe_4S_4]$ cluster-reconstituted wildtype *Ma*NifB (black) and *Ma*NifB variants carrying the SAM (brown), K1 (dark blue), and K2 (bright blue) modules, respectively

presence of SAM [87]. These observations are exciting, as they provide direct proof for the 4Fe identity of the K1- and K2-modules while suggesting a conformational rearrangement upon SAM-dependent coupling of the K1- and K2-modules into an 8Fe core of the cofactor.

2.2 *Radical SAM-Dependent Carbide Insertion*

Identification of the cleavage products of SAM upon incubation with NifB provided some initial insights into the radical SAM-dependent mechanism of cofactor core assembly [88, 89]. SAM was shown to be cleaved by NifB into two products: 5′-deoxyadenosine (5′-dA) and *S*-adenosyl-homocysteine (SAH) (Fig. 5a) [88]. Incubation of [methyl-d_3] SAM (instead of unlabeled SAM) with NifB, on the other hand, resulted in the formation of SAH and a mixture of deuterated 5′-dA (5′-dAD) and unlabeled 5′-dA (5′-dAH) (Fig. 5b) [88]. Drawing analogy to the radical SAM RNA methyltransferases RlmN and Cfr [90, 91], which show similar SAM cleavage patterns and deuterium substitution effects, NifB could very well catalyze two SAM-related reactions: one of them involves an S_N2-type methyl transfer from one equivalent of SAM to the protein, which results in the formation of SAH, whereas the other involves hydrogen abstraction of the methyl group by a 5′-deoxyadenosyl radical (5′-dA•) that is generated via homolytic cleavage of a second equivalent of SAM, which results in the formation of 5′-dAH. In support of this argument, radiolabeling experiments revealed an accumulation of ^{14}C label in NifB upon incubation of this protein with [methyl-^{14}C] SAM and further demonstrated that the ^{14}C label was not associated with the polypeptides of NifB but instead with the L-cluster extracted from this protein [88]. These observations provide compelling evidence that the methyl group of SAM is the origin of the interstitial carbide and that the methyl group is transferred directly from SAM onto the cluster instead of being routed via a protein-bound intermediate.

Acid-quenching experiments supplied further evidence for methyl transfer from SAM to a K-cluster-associated sulfur atom [92]. Incubation of NifB with unlabeled SAM or [methyl-d_3] SAM, followed by acid treatment, gave rise to methanethiol (CH_3SH) or methane-d_3-thiol (CD_3SH), consistent with transfer of the SAM-derived methyl group to an acid-labile sulfur atom of the NifB-associated cluster (Fig. 5c, d) [92]. When NifB-bound clusters were reconstituted with $FeCl_3/Na_2Se$ and subjected to incubation with SAM, methylselenol (CH_3SeH) was detected as the product of acid quenching, again pointing to the sulfur atom of the NifB-associated cluster as the place for methyl attachment (Fig. 5e) [92]. Interestingly, NifB variants carrying a single SAM-, K1-, or K2-module or both SAM- and K1-modules were unable to cleave SAM into SAH and 5′-dAH; in contrast, the NifB variant carrying both SAM- and K2-modules generated SAH and 5′-dAH upon incubation with SAM [87]. These observations suggest that the presence of both SAM- and K2-modules is the prerequisite for the two SAM-related reactions to occur: the K2-module provides a sulfur atom for the attachment of SAM-derived methyl group and the SAM-module

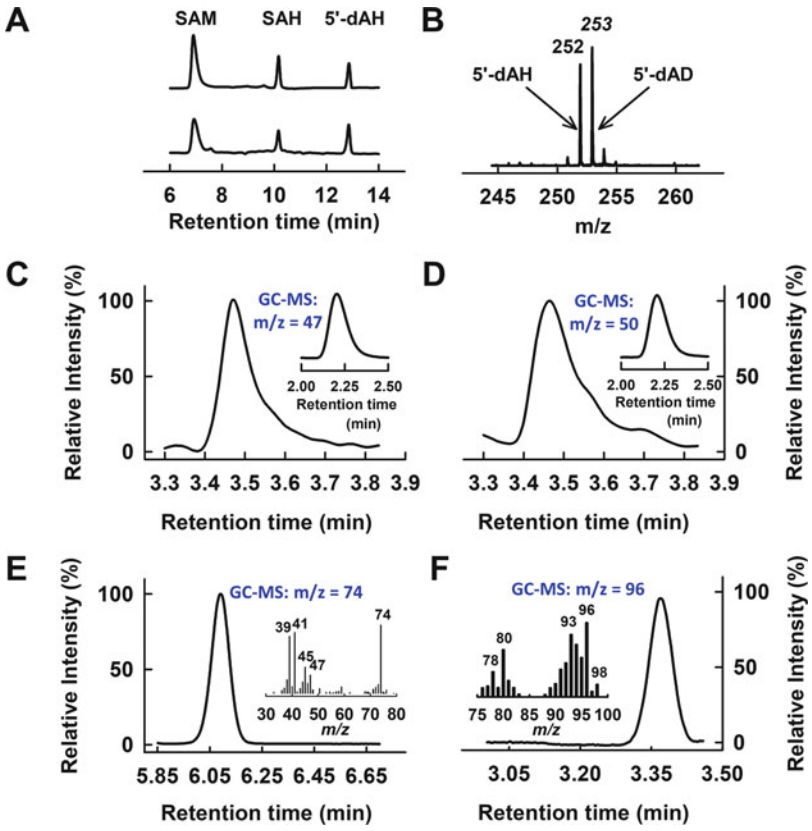

Fig. 5 HPLC and GC/GC-MS analyses of K- to L-cluster conversion on NifB. (**a**) HPLC elution profile of SAM cleavage products, SAH and 5′-dAH, upon incubation of SAM with NifB and dithionite (lower) in comparison with that of a mixture of SAM, SAH, and 5dAH standards (upper). (**b**) LC-MS analysis showing the formation of 5′-dAD upon incubation of NifB with [methyl-d_3] SAM as a product of hydrogen atom abstraction from the SAM-derived methyl group. (**c**, **d**) GC and GC-MS (inset) analyses of methanethiol (m/z = 47) or methane-d_3-thiol (m/z = 50) formed upon acid quench of an incubation mixture containing NifB and either (**c**) SAM or (**d**) [methyl-d_3] SAM. (**e**) GC and GC-MS (inset) analyses of methylselenol (m/z = 74) formed upon acid quench of an incubation mixture containing Fe/Se-reconstituted NifB and SAM. (**f**) GC and GC-MS (inset) analyses of allylthiol (m/z = 96) formed upon acid quench of an incubation mixture containing NifB and allyl SAM

supplies a SAM-derived 5′-dA• radical for hydrogen abstraction of the methyl group. Consistent with this suggestion, only the NifB variant carrying both SAM- and K2-modules gave rise to methanethiol upon incubation with SAM, followed by acid quenching, pointing to a K2-associated, acid-labile sulfur as the place of methyl attachment. As for the sequence of events between methyl transfer and hydrogen abstraction, a SAM analog containing an allyl group (-CH-CH=CH_2) in place of

a methyl group (-CH_3) was used, which would allow allyl transfer (in analogy to methyl transfer) but not 5′-dA•-based hydrogen abstraction (because of the chemical nature of the allyl group). Interestingly, incubation of NifB with allyl SAM generated SAH (but not 5′-dAH) as the sole product of the reaction, whereas acid quenching of this incubation mixture led to the formation of allylthiol ($CH_2 = CH\text{-}CH\text{-}SH$) [92]. Taken together, these results provide conclusive evidence that allyl transfer (representing the methyl transfer event) occurs independent of, and prior to, the hydrogen abstraction event (Fig. 5f) [92].

2.3 *Origin and Incorporation of the '9th Sulfur'*

Combined results from studies of the interactions between NifB and SAM have led to a better understanding of the radical SAM-dependent insertion of carbide during the cofactor core assembly process. One important event that has not been unaccounted for in these studies, however, is the origin of the '9th sulfur' and the step at which this atom is incorporated into the cofactor structure. Recently, these questions were tackled via the use of synthetic [Fe_4S_4] clusters for the reconstitution of NifB-associated clusters, thereby generating a K-cluster-replete form of the protein that was free of sulfur impurities and ready for examination of the source and fate of the '9th sulfur' [93]. When the three physiologically relevant sulfur forms – sulfide (S^{2-}), sulfite (SO_3^{2-}), and sulfate (SO_4^{2-}) – were each used as a potential '9th sulfur' source along with the carbide source (SAM) in the presence of a sulfur-free reductant [94], only SO_3^{2-} supported the K- to L-cluster conversion in the in vitro maturation assay [93]. Substitution of $^{35}SO_3^{2-}$ for unlabeled SO_3^{2-} in the same incubation mixture resulted in an accumulation of the ^{35}S radiolabel on NifB (Fig. 6a, left), which could be further traced to the L-cluster upon extraction from NifB (Fig. 6a, right). Most interestingly, when incubated with SAM, NifB showed the same SAM cleavage pattern (Fig. 6b) and EPR spectroscopic changes (Fig. 6c, d) with or without SO_3^{2-} treatment; however, the K- to L-cluster conversion only occurred upon incubation of NifB with both SAM and SO_3^{2-} based on activity analysis (Fig. 6e). The appearance of the 8Fe core-specific, $g = 1.94$ signal *after* incubation of NifB with SAM, but *before* treatment with SO_3^{2-} (Fig. 6d), implies that the SAM-dependent carbide insertion and the concomitant 8Fe core rearrangement occur prior to the insertion of the '9th S', thereby adding another assembly intermediate (designated the L*-cluster) before the final product (L-cluster) of this process. Tentatively assign as a [Fe_8S_8C] cluster, the L*-cluster closely resembles the L-cluster in architecture but does not have the '9th S' in the belt region of the cluster.

Identification of sulfite as a source of the '9th sulfur' is somewhat surprising, given that sulfite is one of the central hubs of sulfur metabolism in the cell [95–97]. Curiously, 11 out of 13 nitrogen-fixing microbes whose genomes were surveyed in a recent study [93], including *A. vinelandii* and *M. acetivorans*, possess genes encoding the 3′-phosphoadenosine 5′-phosphosulfate sulfotransferase (PAPS transferase), an enzyme that converts PAPS to sulfite as part of the assimilatory sulfate

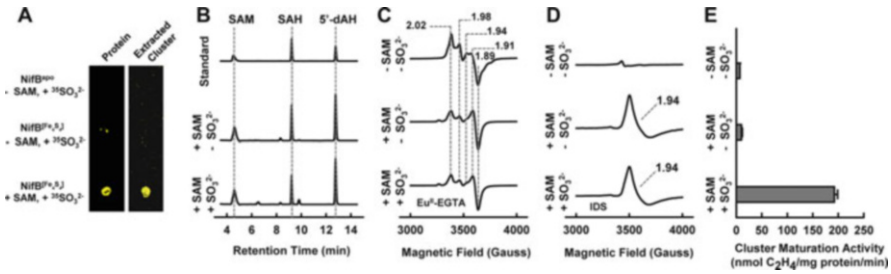

Fig. 6 Experiments tracing the source and insertion of '9th' S on NifB. (**a**) Radiolabel experiments of apo *Ma*NifB (*Ma*NifB^{apo}) re-isolated after incubation with $^{35}SO_3^{2-}$ (upper) and [Fe_4S_4]-cluster-reconstituted *Ma*NifB (*Ma*NifB$^{[Fe4S4]}$) re-isolated after incubation with $^{35}SO_3^{2-}$ (middle) or $^{35}SO_3^{2-}$ plus SAM (lower) (**a**, left). The radiolabels can be further traced to the clusters extracted from the respective proteins (**a**, right). (**b**) The HPLC elution profiles of SAM, SAH, and 5′-dAH standards (upper) and *Ma*NifB$^{[Fe4S4]}$ incubated with SAM (middle) or SAM plus SO_3^{2-} (lower). (**c**, **d**) EPR spectra of Eu^{II}-EGTA-reduced (**c**) or IDS-oxidized (**d**) *Ma*NifB$^{[Fe4S4]}$ treated with no additive (upper) and *Ma*NifB$^{[Fe4S4]}$ incubated with SAM (middle) or SAM plus SO_3^{2-} (lower). (**e**) The activities of *Ma*NifB$^{[Fe4S4]}$ treated with no additive (upper) and *Ma*NifB$^{[Fe4S4]}$ incubated with SAM (middle) or SAM plus SO_3^{2-} (lower)

reduction pathway [93]. This observation supplies evidence for the possible physiological relevance of sulfite or related compounds to the biosynthesis of nitrogenase. The sulfite-based insertion of the '9th sulfur' is also interesting from a chemical perspective. In parallel to the observation that only an oxidized form of sulfur, such as SO_3^{2-}, can be used as a source of the '9th S', it has been reported that the belt sulfur of the M-cluster only exchanges with the more oxidized Se in selenocyanate ($SeCN^-$) but not with the more reduced Se in selenide (Se^{2-}) upon turnover [28]. It is possible, therefore, that insertion of the '9th S' involves donation of electrons from the electron-rich cluster to the sulfur source. In this light, it is interesting to note that SO_4^{2-} cannot be used for incorporation as a '9th sulfur', either due to the inability of the sulfur atom in SO_4^{2-} to directly interact with the cluster-associated Fe atoms and/or due to the redox potential assumed by the cofactor that does not permit the redox change required for the conversion of SO_4^{2-} into a '9th S'. In any case, the 'vacant' site in the L*-cluster, which is likely occupied by a putative cysteine thiolate or H_2O ligand, is highly intriguing, particularly given the potential catalytic relevance of the belt region of the cofactor [27, 28].

2.4 Proposed Pathway for Cofactor Core Formation

A pathway of the K- to L-cluster conversion on NifB can be proposed based on these results (Fig. 7), which starts with methyl transfer from one SAM molecule to a bridging sulfide of the K2-module via an S_N2-type mechanism. This event is followed by formation of a 5′-dA• radical via homolytic cleavage of a second SAM molecule that is bound to the SAM-module and abstraction of a hydrogen atom from the

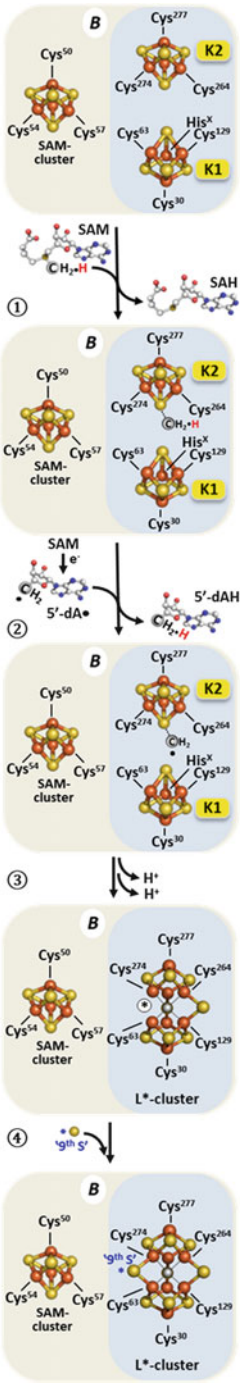

Fig. 7 Proposed model of L-cluster formation on NifB. The first step of this process involves S_N2-type transfer of the methyl group from one SAM equivalent to a sulfide of the K2 module of NifB (①). Subsequently, a second SAM molecule undergoes homolytic cleavage at the SAM-module to yield a 5′-dA• radical, which subsequently abstracts a hydrogen from the K2-bound methyl group, leading to the formation of a methylene ($–CH_2•$) radical (②). The $–CH_2•$ radical then initiates the coupling and rearrangement of the K2- and K1-modules into an L*-cluster ($[Fe_8S_8C]$) that resembles the L-cluster ($[Fe_8S_9C]$) but misses a belt sulfur (the '9th' sulfur) (③). The final conversion of an L*-cluster to an L-cluster involves incorporation of the '9th' sulfur concomitant with further deprotonation and/or dehydrogenation of the carbon intermediate until an interstitial C^{4-} ion is generated in the center of the L-cluster (④). Note the structural rearrangement of the cluster is accompanied by the loss of a conserved His ligand to the K1 module and, possibly, one or more Cys ligands to both the K1- and K2-modules (see ③, ④)

K2-associated methyl group. This series of events generate a K2-bound methylene ($-CH_2\bullet$) radical, which then initiates the coupling and rearrangement of the K2- and K1-modules into an L*-cluster ($[Fe_8S_8C]$) that has the core structure of the mature cofactor. Subsequently, the '9th sulfur' is inserted concomitantly with further dehydrogenation or deprotonation of the carbon intermediate until a μ_6-coordinated C^{4-} ion appears in the central cavity of the L-cluster ($[Fe_8S_9C]$).

3 Summary and Outlook

Recent studies have led to a working model for the cofactor core assembly, which highlights the novel, radical SAM-dependent carbide insertion mechanism, as well as the somewhat unexpected, sulfite-based incorporation of the '9th sulfur' at the belt region of the cofactor. It is interesting to note the pivotal role carbide insertion plays in the process of cofactor core formation, capitalizing on the radical chemistry for the processing of a methyl group into an interstitial carbide while in the same time directing the coupling and rearrangement of two 4Fe units into a unique 8Fe core. Likewise, the origin of the '9th sulfur' is intriguing in that it potentially establishes a tie between nitrogen fixation and sulfur metabolism in a broader biological context. Further investigation of the cofactor core formation will focus on elucidating the mechanistic details of the conversion of carbon intermediate into an interstitial carbide, as well as how this process is related to the structural rearrangement required for the formation of an 8Fe cluster. Additionally, given the potential catalytic relevance of the interstitial carbide and the '9th sulfur', efforts will be dedicated to generating labeled cofactor species at these positions, taking advantage of the tools established in the recent studies that have made the specific labeling of the cofactor possible. Combined research along these lines will hopefully unravel the unique chemistry underlining the generation of a nitrogenase cofactor core and provide useful insights into the catalytic mechanism of nitrogenase.

Acknowledgements This work was supported by NIH-NIGMS grant GM67626 (to Markus W. Ribbe and Yilin Hu).

References

1. Burgess BK, Lowe DJ (1996) Mechanism of molybdenum nitrogenase. Chem Rev 96:2983–3011
2. Howard JB, Rees DC (1996) Structural basis of biological nitrogen fixation. Chem Rev 96:2965–2982
3. Hoffman BM, Lukoyanov D, Yang ZY et al (2014) Mechanism of nitrogen fixation by nitrogenase: the next stage. Chem Rev 114:4041–4062
4. Lee CC, Hu Y, Ribbe MW (2010) Vanadium nitrogenase reduces CO. Science 329:642

5. Hu Y, Lee CC, Ribbe MW (2011) Extending the carbon chain: hydrocarbon formation catalyzed by vanadium/molybdenum nitrogenases. Science 333:753–755
6. Lee CC, Hu Y, Ribbe MW (2011) Tracing the hydrogen source of hydrocarbons formed by vanadium nitrogenase. Angew Chem Int Ed Engl 50:5545–5547
7. Rebelein JG, Hu Y, Ribbe MW (2014) Differential reduction of CO_2 by molybdenum and vanadium nitrogenases. Angew Chem Int Ed Engl 53:11543–11546
8. Lee CC, Hu Y, Ribbe MW (2015) Catalytic reduction of CN^-, CO, and CO_2 by nitrogenase cofactors in lanthanide-driven reactions. Angew Chem Int Ed Engl 54:1219–1222
9. Rebelein JG, Hu Y, Ribbe MW (2015) Widening the product profile of carbon dioxide reduction by vanadium nitrogenase. Chembiochem 16:1993–1996
10. Yang ZY, Dean DR, Seefeldt LC (2011) Molybdenum nitrogenase catalyzes the reduction and coupling of CO to form hydrocarbons. J Biol Chem 286:19417–19421
11. Yang ZY, Moure VR, Dean DR et al (2012) Carbon dioxide reduction to methane and coupling with acetylene to form propylene catalyzed by remodeled nitrogenase. Proc Natl Acad Sci U S A 109:19644–19648
12. Schlögl R (2003) Catalytic synthesis of ammonia-a "never-ending story". Angew Chem Int Ed Engl 42:2004–2008
13. Rofer-DePoorter CK (1981) A comprehensive mechanism for the Fischer-Tropsch synthesis. Chem Rev 81:447–474
14. Einsle O, Tezcan FA, Andrade SL et al (2002) Nitrogenase MoFe-protein at 1.16 Å resolution: a central ligand in the FeMo-cofactor. Science 297:1696–1700
15. Spatzal T, Aksoyoglu M, Zhang L et al (2011) Evidence for interstitial carbon in nitrogenase FeMo cofactor. Science 334:940
16. Kim J, Rees DC (1992) Crystallographic structure and functional implications of the nitrogenase molybdenum-iron protein from *Azotobacter vinelandii*. Nature 360:553–560
17. Lancaster KM, Roemelt M, Ettenhuber P et al (2011) X-ray emission spectroscopy evidences a central carbon in the nitrogenase iron-molybdenum cofactor. Science 334:974–977
18. Tezcan FA, Kaiser JT, Mustafi D et al (2005) Nitrogenase complexes: multiple docking sites for a nucleotide switch protein. Science 309:1377–1380
19. Schindelin H, Kisker C, Schlessman JL et al (1997) Structure of ADP x AlF_4^--stabilized nitrogenase complex and its implications for signal transduction. Nature 387:370–376
20. Fay AW, Lee CC, Wiig JA et al (2011) Protocols for cofactor isolation of nitrogenase. Methods Mol Biol 766:239–248
21. Burgess BK (1990) The iron-molybdenum cofactor of nitrogenase. Chem Rev 90:1377–1406
22. Shah VK, Brill WJ (1977) Isolation of an iron-molybdenum cofactor from nitrogenase. Proc Natl Acad Sci U S A 74:3249–3253
23. Lee HI, Hales BJ, Hoffman BM (1997) Metal-ion valencies of the FeMo cofactor in CO-inhibited and resting state nitrogenase by ^{57}Fe Q-band ENDOR. J Am Chem Soc 119:11395–11400
24. Yoo SJ, Angove HC, Papaefthymiou V et al (2000) Mössbauer study of the MoFe protein of nitrogenase from *Azotobacter vinelandii* using selective ^{57}Fe enrichment of the M-centers. J Am Chem Soc 122:4926–4936
25. Wiig JA, Lee CC, Hu Y et al (2013) Tracing the interstitial carbide of the nitrogenase cofactor during substrate turnover. J Am Chem Soc 135:4982–4983
26. Lee HI, Benton PM, Laryukhin M et al (2003) The interstitial atom of the nitrogenase FeMo-cofactor: ENDOR and ESEEM show it is not an exchangeable nitrogen. J Am Chem Soc 125:5604–5605
27. Spatzal T, Perez KA, Einsle O et al (2014) Ligand binding to the FeMo-cofactor: structures of CO-bound and reactivated nitrogenase. Science 345:1620–1623
28. Spatzal T, Perez KA, Howard JB et al (2015) Catalysis-dependent selenium incorporation and migration in the nitrogenase active site iron-molybdenum cofactor. elife 4:e11620
29. Moret ME, Peters JC (2011) N_2 functionalization at iron metallaboratranes. J Am Chem Soc 133:18118–18121

30. Lee CC, Hu Y, Ribbe MW (2012) ATP-independent formation of hydrocarbons catalyzed by isolated nitrogenase cofactors. Angew Chem Int Ed Engl 51:1947–1949
31. Lee CC, Hu Y, Ribbe MW (2015) Insights into hydrocarbon formation by nitrogenase cofactor homologs. MBio 6:e00307–e00315
32. Tanifuji K, Sickerman N, Lee CC et al (2016) Structure and reactivity of an asymmetric synthetic mimic of nitrogenase cofactor. Angew Chem Int Ed Engl 55:15633–15636
33. Dos Santos PC, Dean DR, Hu Y et al (2004) Formation and insertion of the nitrogenase iron-molybdenum cofactor. Chem Rev 104:1159–1173
34. Kennedy C, Dean D (1992) The *nifU*, *nifS* and *nifV* gene products are required for activity of all three nitrogenases of *Azotobacter vinelandii*. Mol Gen Genet 231:494–498
35. Zheng L, White RH, Cash VL et al (1994) Mechanism for the desulfurization of L-cysteine catalyzed by the *nifS* gene product. Biochemistry 33:4714–4720
36. Zheng L, White RH, Cash VL et al (1993) Cysteine desulfurase activity indicates a role for NifS in metallocluster biosynthesis. Proc Natl Acad Sci U S A 90:2754–2758
37. Dos Santos PC, Johnson DC, Ragle BE et al (2007) Controlled expression of *nif* and *isc* iron-sulfur protein maturation components reveals target specificity and limited functional replacement between the two systems. J Bacteriol 189:2854–2862
38. Smith AD, Jameson GNL, Dos Santos PC et al (2005) NifS-mediated assembly of [4Fe-4S] clusters in the N- and C-terminal domains of the NifU scaffold protein. Biochemistry 44:12955–12969
39. Yuvaniyama P, Agar JN, Cash VL et al (2000) NifS-directed assembly of a transient [2Fe-2S] cluster within the NifU protein. Proc Natl Acad Sci U S A 97:599–604
40. Zheng LM, Dean DR (1994) Catalytic formation of a nitrogenase iron-sulfur cluster. J Biol Chem 269:18723–18726
41. Christiansen J, Goodwin PJ, Lanzilotta WN et al (1998) Catalytic and biophysical properties of a nitrogenase apo-MoFe protein produced by a *nifB*-deletion mutant of *Azotobacter vinelandii*. Biochemistry 37:12611–12623
42. Paustian TD, Shah VK, Roberts GP (1990) Apodinitrogenase: purification, association with a 20-kilodalton protein, and activation by the iron-molybdenum cofactor in the absence of dinitrogenase reductase. Biochemistry 29:3515–3522
43. Hawkes TR, Smith BE (1983) Purification and characterization of the inactive MoFe protein (NifB-Kp1) of the nitrogenase from *nifB* mutants of *Klebsiella pneumoniae*. Biochem J 209:43–50
44. Hawkes TR, Smith BE (1984) The inactive MoFe protein (NifB-Kp1) of the nitrogenase from *nifB* mutants of *Klebsiella pneumoniae*. Its interaction with FeMo-cofactor and the properties of the active MoFe protein formed. Biochem J 223:783–792
45. Shah VK, Allen JR, Spangler NJ et al (1994) *In vitro* synthesis of the iron-molybdenum cofactor of nitrogenase. Purification and characterization of NifB cofactor, the product of NifB protein. J Biol Chem 269:1154–1158
46. Allen RM, Chatterjee R, Ludden PW et al (1995) Incorporation of iron and sulfur from NifB cofactor into the iron-molybdenum cofactor of dinitrogenase. J Biol Chem 270:26890–26896
47. George SJ, Igarashi RY, Xiao Y et al (2008) Extended X-ray absorption fine structure and nuclear resonance vibrational spectroscopy reveal that NifB-co, a FeMo-co precursor, comprises a 6Fe core with an interstitial light atom. J Am Chem Soc 130:5673–5680
48. Rubio LM, Ludden PW (2008) Biosynthesis of the iron-molybdenum cofactor of nitrogenase. Annu Rev Microbiol 62:93–111
49. Roll JT, Shah VK, Dean DR et al (1995) Characteristics of NifNE in *Azotobacter vinelandii* strains. Implications for the synthesis of the iron-molybdenum cofactor of dinitrogenase. J Biol Chem 270:4432–4437
50. Robinson AC, Burgess BK, Dean DR (1986) Activity, reconstitution, and accumulation of nitrogenase components in *Azotobacter vinelandii* mutant strains containing defined deletions within the nitrogenase structural gene cluster. J Bacteriol 166:180–186

51. Filler WA, Kemp RM, Ng JC et al (1986) The *nifH* gene product is required for the synthesis or stability of the iron-molybdenum cofactor of nitrogenase from *Klebsiella pneumoniae*. Eur J Biochem 160:371–377
52. Robinson AC, Dean DR, Burgess BK (1987) Iron-molybdenum cofactor biosynthesis in *Azotobacter vinelandii* requires the iron protein of nitrogenase. J Biol Chem 262:14327–14332
53. Hoover TR, Imperial J, Ludden PW et al (1988) Biosynthesis of the iron-molybdenum cofactor of nitrogenase. Biofactors 1:199–205
54. Robinson AC, Chun TW, Li JG et al (1989) Iron-molybdenum cofactor insertion into the apo-MoFe protein of nitrogenase involves the iron protein-MgATP complex. J Biol Chem 264:10088–10095
55. Tal S, Chun TW, Gavini N et al (1991) The Δ*nifB* (or Δ*nifE*) FeMo cofactor-deficient MoFe protein is different from the Δ*nifH* protein. J Biol Chem 266:10654–10657
56. Gavini N, Burgess BK (1992) FeMo cofactor synthesis by a *nifH* mutant with altered MgATP reactivity. J Biol Chem 267:21179–21186
57. Allen RM, Homer MJ, Chatterjee R et al (1993) Dinitrogenase reductase- and MgATP-dependent maturation of apodinitrogenase from *Azotobacter vinelandii*. J Biol Chem 268:23670–23674
58. Rangaraj P, Ludden PW (2002) Accumulation of ^{99}Mo-containing iron-molybdenum cofactor precursors of nitrogenase on NifNE, NifH, and NifX of *Azotobacter vinelandii*. J Biol Chem 277:40106–40111
59. Zheng LM, White RH, Dean DR (1997) Purification of the *Azotobacter vinelandii nifV*-encoded homocitrate synthase. J Bacteriol 179:5963–5966
60. Pau RN, Lawson DM (2002) Transport, homeostasis, regulation, and binding of molybdate and tungstate to proteins. Met Ions Biol Syst 39:31–74
61. Hernandez JA, Curatti L, Aznar CP et al (2008) Metal trafficking for nitrogen fixation: NifQ donates molybdenum to NifEN/NifH for the biosynthesis of the nitrogenase FeMo-cofactor. Proc Natl Acad Sci U S A 105:11679–11684
62. Imperial J, Ugalde RA, Shah VK et al (1984) Role of the *nifQ* gene product in the incorporation of molybdenum into nitrogenase in *Klebsiella pneumoniae*. J Bacteriol 158:187–194
63. Ugalde RA, Imperial J, Shah VK et al (1985) Biosynthesis of the iron-molybdenum cofactor and the molybdenum cofactor in *Klebsiella pneumoniae*: effect of sulfur source. J Bacteriol 164:1081–1087
64. Rangaraj P, Ruttimann-Johnson C, Shah VK et al (2001) Accumulation of ^{55}Fe-labeled precursors of the iron-molybdenum cofactor of nitrogenase on NifH and NifX of *Azotobacter vinelandii*. J Biol Chem 276:15968–15974
65. Homer MJ, Dean DR, Roberts GP (1995) Characterization of the gamma protein and its involvement in the metallocluster assembly and maturation of dinitrogenase from *Azotobacter vinelandii*. J Biol Chem 270:24745–24752
66. Hernandez JA, Igarashi RY, Soboh B et al (2007) NifX and NifEN exchange NifB cofactor and the VK-cluster, a newly isolated intermediate of the iron-molybdenum cofactor biosynthetic pathway. Mol Microbiol 63:177–192
67. Rubio LM, Rangaraj P, Homer MJ et al (2002) Cloning and mutational analysis of the gamma gene from *Azotobacter vinelandii* defines a new family of proteins capable of metallocluster binding and protein stabilization. J Biol Chem 277:14299–14305
68. Dean DR, Jacobson MR (1992) Biochemical genetics of nitrogenase. In: Stacey G, Burris RH, Evan HJ (eds) Biological nitrogen fixation. Chapman & Hall, New York, pp 763–834
69. Hu Y, Ribbe MW (2016) Biosynthesis of the metalloclusters of nitrogenases. Annu Rev Biochem 85:455–483
70. Hu Y, Ribbe MW (2016) Maturation of nitrogenase cofactor-the role of a class E radical SAM methyltransferase NifB. Curr Opin Chem Biol 31:188–194
71. Hu Y, Ribbe MW (2016) Nitrogenases – a tale of carbon atom(s). Angew Chem Int Ed Engl 55:8216–8226
72. Ribbe MW, Hu Y, Hodgson KO et al (2014) Biosynthesis of nitrogenase metalloclusters. Chem Rev 114:4063–4080

73. Hu Y, Ribbe MW (2013) Biosynthesis of the iron-molybdenum cofactor of nitrogenase. J Biol Chem 288:13173–13177
74. Hu Y, Ribbe MW (2013) Nitrogenase assembly. Biochim Biophys Acta 1827:1112–1122
75. Hu Y, Ribbe MW (2011) Biosynthesis of nitrogenase FeMoco. Coord Chem Rev 255:1218–1224
76. Hu Y, Ribbe MW (2011) Biosynthesis of the metalloclusters of molybdenum nitrogenase. Microbiol Mol Biol Rev 75:664–677
77. Schwarz G, Mendel RR, Ribbe MW (2009) Molybdenum cofactors, enzymes and pathways. Nature 460:839–847
78. Hu Y, Fay AW, Lee CC et al (2008) Assembly of nitrogenase MoFe protein. Biochemistry 47:3973–3981
79. Zheng L, White RH, Cash VL et al (1994) Mechanism for the desulfurization of L-cysteine catalyzed by the *nifS* gene product. Biochemistry 33:4714–4120
80. Schmid B, Ribbe MW, Einsle O et al (2002) Structure of a cofactor-deficient nitrogenase MoFe protein. Science 296:352–356
81. Wiig JA, Hu Y, Ribbe MW (2011) NifEN-B complex of *Azotobacter vinelandii* is fully functional in nitrogenase FeMo cofactor assembly. Proc Natl Acad Sci U S A 108:8623–8627
82. Kaiser JT, Hu Y, Wiig JA et al (2011) Structure of precursor-bound NifEN: a nitrogenase FeMo cofactor maturase/insertase. Science 331:91–94
83. Fay AW, Blank MA, Lee CC et al (2011) Spectroscopic characterization of the isolated iron-molybdenum cofactor (FeMoco) precursor from the protein NifEN. Angew Chem Int Ed Engl 50:7787–7790
84. Corbett MC, Hu Y, Fay AW et al (2006) Structural insights into a protein-bound iron-molybdenum cofactor precursor. Proc Natl Acad Sci U S A 103:1238–1243
85. Lancaster KM, Hu Y, Bergmann U et al (2013) X-ray spectroscopic observation of an interstitial carbide in NifEN-bound FeMoco precursor. J Am Chem Soc 136:610–612
86. Fay AW, Wiig JA, Lee CC et al (2015) Identification and characterization of functional homologs of nitrogenase cofactor biosynthesis protein NifB from methanogens. Proc Natl Acad Sci U S A 112:14829–14833
87. Rettberg LA, Wilcoxen J, Lee CC et al (2018) Probing the coordination and function of Fe4S4 modules in nitrogenase assembly protein NifB. Nat Commun 9:2824
88. Wiig JA, Hu Y, Lee CC et al (2012) Radical SAM-dependent carbon insertion into the nitrogenase M-cluster. Science 337:1672–1675
89. Boal AK, Rosenzweig AC (2012) Biochemistry. A radical route for nitrogenase carbide insertion. Science 337:1617–1618
90. Boal AK, Grove TL, McLaughlin MI et al (2011) Structural basis for methyl transfer by a radical SAM enzyme. Science 332:1089–1092
91. Grove TL, Benner JS, Radle MI et al (2011) A radically different mechanism for *S*-adenosylmethionine-dependent methyltransferases. Science 332:604–607
92. Wiig JA, Hu Y, Ribbe MW (2015) Refining the pathway of carbide insertion into the nitrogenase M-cluster. Nat Commun 6:8034
93. Tanifuji K, Lee CC, Sickerman NS et al (2018) Tracing the 'ninth sulfur' of the nitrogenase cofactor via a semi-synthetic approach. Nat Chem 10:568–572
94. Vincent KA, Tilley GJ, Quammie NC et al (2003) Instantaneous, stoichiometric generation of powerfully reducing states of protein active sites using Eu(II) and polyaminocarboxylate ligands. Chem Commun 20:2590–2591
95. Brychkova G, Grishkevich V, Fluhr R et al (2013) An essential role for tomato sulfite oxidase and enzymes of the sulfite network in maintaining leaf sulfite homeostasis. Plant Physiol 161:148–164
96. Carbonero F, Benefiel AC, Alizadeh-Ghamsari AH et al (2012) Microbial pathways in colonic sulfur metabolism and links with health and disease. Front Physiol 3:448
97. Kertesz MA (2000) Riding the sulfur cycle – metabolism of sulfonates and sulfate esters in gram-negative bacteria. FEMS Microbiol Rev 24:135–175

Struct Bond (2019) 179: 33–62
DOI: 10.1007/430_2018_26

Published online: 28 August 2018

Recent Advances in the Chemical Synthesis of Nitrogenase Model Clusters

Kazuki Tanifuji and Yasuhiro Ohki

Contents

Abstract The only enzyme that is able to fix nitrogen, nitrogenase, reduces inert and abundant dinitrogen (N_2) into bioavailable ammonia (NH_3) under ambient conditions. The most investigated variant, the MoFe nitrogenase, uses three metallo-cofactors: the $[Fe_4S_4]$ cluster in the electron-carrier component (Fe protein), as well as the $[Fe_8S_7]$ (P-cluster) and $[MoFe_7S_9C]$ (M-cluster) clusters in the catalytic component (MoFe protein). To better understand the physical properties of these cofactors, various methods have been developed for the chemical synthesis of model metal-sulfur clusters. In this review, we address the following topics with emphasis on recent developments: (a) the synthesis of all-ferrous $[Fe_4S_4]^0$ clusters, which are isoelectronic to the *super-reduced* state of the cluster in the Fe protein, (b) the reproduction of

K. Tanifuji (✉)
Department of Molecular Biology and Biochemistry, University of California, Irvine, Irvine, CA, USA
e-mail: tanifujk@uci.edu

Y. Ohki (✉)
Department of Chemistry, Graduate School of Science, Nagoya University, Nagoya, Japan
e-mail: ohki@chem.nagoya-u.ac.jp

the unique [Fe_8S_7] inorganic core of the P-cluster, and (c) the synthesis of metal-sulfur clusters relevant to the M-cluster and their variants that incorporate a light atom. Even though reproduction of the M-cluster remains elusive, some recent advances seem promising toward new classes of metal-sulfur clusters that satisfy the key structural features of the M-cluster.

Keywords [Fe_4S_4] cluster · M-cluster (FeMo cofactor) · Nitrogenase · P-cluster · Synthetic models

1 Introduction: Biological N_2 Fixation and Nitrogenase Systems

Nitrogen is an essential element in nucleic and amino acids, which are in turn indispensable to biological activities. Such organic nitrogen compounds are produced through numerous metabolic pathways, where ammonia (NH_3) is used as a raw material. Even though most organisms are unable to supply NH_3, a biological process is present for the reduction of inert and abundant dinitrogen (N_2).

Nitrogenase is the only known enzyme that catalyzes the reduction of N_2 into NH_3. Three variants, i.e., MoFe, VFe, and Fe-only nitrogenases, have been identified and named after their essential metal content [1]. These enzymes, encoded in *nif*, *vnf*, and *anf* gene clusters, respectively, are co-induced with the corresponding biosynthetic machinery under nitrogen-deficient environments. As a survival strategy of N_2-fixing bacteria under varying conditions, the variant to be expressed is regulated by the availability of the metals. Likely following the order of catalytic activity, the bacteria prioritize the production of the MoFe, VFe, or Fe-only variant [1]. All these variants are homologous and consist of two components, i.e., an electron-carrier oxidoreductase and a catalytic component.

The MoFe nitrogenase is the best-studied variant, whose catalytic component, known as the MoFe protein, is encoded by *nifD* and *nifK* genes. The resulting $\alpha_2\beta_2$ tetrameric protein receives electrons from the Fe protein, which is the homodimeric oxidoreductase component encoded by *nifH*. In the Fe protein, two binding sites for adenosine triphosphate (ATP) are present. The ATP-bound form associates with the MoFe protein to form a transient complex that leads to the electron transfer from the Fe protein to the MoFe protein. Hydrolysis of the protein-bound ATP into adenosine diphosphate (ADP) and monophosphate (Pi) has been suggested to trigger the dissociation of the Fe protein from the MoFe protein [2]. By repeating this ATP-dependent process, nitrogenase transfers electrons from the Fe protein to the MoFe protein, and eventually to N_2 together with protons, for the formation of NH_3. The reduction of one molecule of N_2 is presumably accompanied by the obligate production of one molecule of H_2 according to the following chemical equation: $N_2 + 8H^+ + 8e^- + 16ATP \rightarrow 2NH_3 + H_2 + 16ADP + 16Pi$ [3, 4].

To achieve its extraordinary activity, the MoFe nitrogenase uses three redox-active metallo-cofactors, which are metal-sulfur clusters consisting of multiple metal and sulfur atoms. The metallo-cofactor in the Fe protein is a typical [Fe_4S_4] cluster, while the other two in the MoFe protein are unique to nitrogenase and designated as the P-cluster and M-cluster, whose compositions have been determined as [Fe_8S_7] [5] and [(cit)$MoFe_7S_9C$] (cit = *R*-homocitrate) [6, 7], respectively (Fig. 1). Recent protein crystallographic analyses associated with biochemical studies have further elucidated some properties of these metallo-cofactors, such as the predominant involvement of the $1e^-$ redox process of the P-cluster under the turnover conditions [8] and the proposed displacement of one of the bridging sulfides of the M-cluster for the generation of the reactive form [9, 10]. Recently, the possible removal of a bridging sulfide has been revisited based on the protein crystallographic analyses of the VFe nitrogenase [11, 12], where a light atom (theoretically proposed as an OH moiety derived from H_2O) [13] replaces one of the bridging sulfides under reducing conditions. Even though enzymatic studies have uncovered some important clues as to how such nitrogenase metallo-cofactors might work, a number of uncertainties remain regarding their structure-function relationships that represent a major issue to be addressed from a chemical perspective. Thus, the chemical synthesis of model

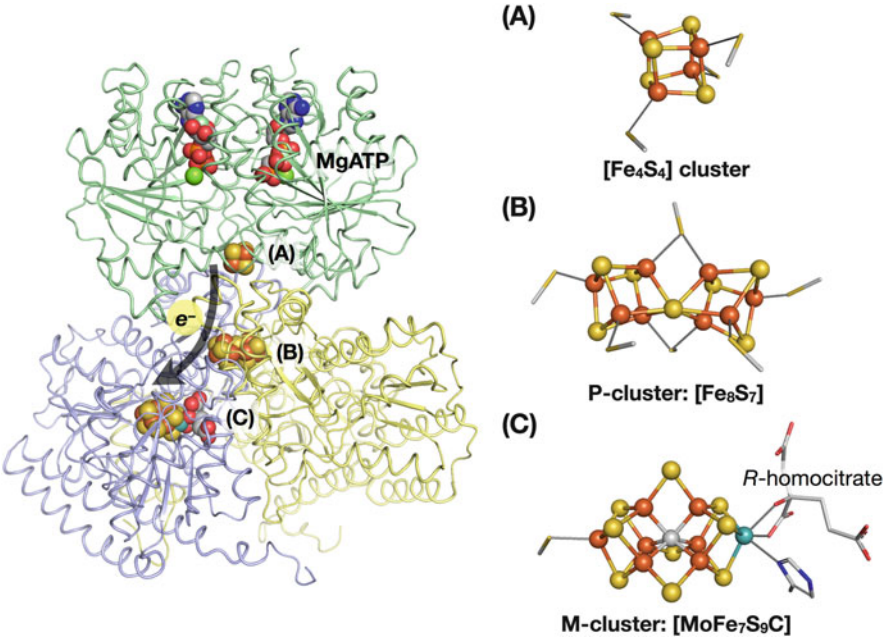

Fig. 1 Schematic illustration of the electron-transfer pathway in the MoFe nitrogenase, highlighting the metallo-cofactors and the protein-bound MgATP molecules. (**a**) [Fe_4S_4] cluster of the Fe protein; (**b**) P-cluster and (**c**) M-cluster of the MoFe protein. The Fe protein is colored in green, while the MoFe protein is colored in purple and yellow. Only half of the $\alpha_2\beta_2$-heterotetramer of the MoFe protein is shown for clarity. PDB ID: 4WZA (left) and 3U7Q (right). Color legend: C, gray; Fe, orange; N, blue; Mo, teal; O, red; S, yellow

compounds and the analysis of their detailed properties and reactivity could provide valuable insight into the metallo-cofactors. While some reviews have been published on model compounds of nitrogenase metallo-cofactors (for representative reviews of the model chemistry of nitrogenase, see [14, 15]), here we revisit this topic with emphasis on the most recent advances.

2 Model $[Fe_4S_4]$ Clusters of the Fe Protein

Cuboidal $[Fe_4S_4]$ clusters are arguably the most prominent class of biological iron-sulfur clusters, and their oxidation states typically range between $[Fe_4S_4]^{+}$ and $[Fe_4S_4]^{3+}$ (for representative reviews, see [16–19]). In contrast to ordinary $[Fe_4S_4]$ clusters, the cluster in the Fe protein can be reduced to the formal oxidation state $[Fe_4S_4]^{0}$ (for a review specifically focusing on Fe protein, see [20]), the so-called *super-reduced* state, in the presence of reducing agents [21, 22]. The physiological importance of this *super-reduced* state still remains unclear; however, it demonstrates the exceptional stability of the $[Fe_4S_4]$ cluster of the Fe protein under reducing conditions. Furthermore, recent studies have revealed that the Fe proteins from some prokaryotes and archaea are able to catalyze the reduction of carbon dioxide to furnish carbon monoxide and short-chain hydrocarbons [23, 24]. Thus, synthetic $[Fe_4S_4]$ clusters in the reduced states are of interest not only as the models for the cluster in the Fe protein but also as potential catalyst precursors for artificial carbon fixation and small-molecule activation.

2.1 Synthesis of Super-Reduced $[Fe_4S_4]$ Clusters

In a pioneering study from 1972, Holm et al. reported the first chemical synthesis of an $[Fe_4S_4]$ cluster bearing four thiolate ligands [25]. Since then, over 80 examples of thiolate-supported $[Fe_4S_4]$ clusters in $[Fe_4S_4]^{+/2+/3+}$ oxidation states have been synthesized, while only a limited number of $[Fe_4S_4]^{0}$ clusters are accessible. As the chemistry of $[Fe_4S_4]^{+/2+/3+}$ clusters has been summarized elsewhere (for representative reviews, see [26–29]), this section focuses on synthetic $[Fe_4S_4]^{0}$ clusters.

Even though the $[Fe_4S_4]$ cluster in the Fe protein is supported exclusively by cysteine residues [30], no thiolate-supported $[Fe_4S_4]^{0}$ cluster has been synthesized and isolated thus far. As short-lived species, $[Fe_4S_4(SR)_4]^{4-}$ have been generated under certain electrochemical measurement conditions [31–33], but their instability has so far prevented their isolation. This instability arises from the dissociation of thiolate(s) from $[Fe_4S_4(SR)_4]^{4-}$, as the σ-donation of thiolate anions is not suitable for the stabilization of relatively low-valent, electron-rich metal centers. In contrast, π-acceptor ligands stabilize electron-rich metals through back-bonding [34]. As phosphines (PR_3) are a representative class of π-acceptor ligands for transition metals, Holm and co-workers have employed phosphines for the attempted

stabilization of the *super-reduced* $[Fe_4S_4]^0$ cluster in the form $[Fe_4S_4(PR_3)_4]^0$ (R = cyclohexyl (Cy), isopropyl (^{i}Pr), *tert*-butyl (^{t}Bu)). However, the synthesis of $[Fe_4S_4(PR_3)_4]^0$ via the chemical reduction of $[Fe_4S_4(PR_3)_4]^+$ using sodium acenaphthalenide was not successful due to the subsequent dissociation of some of the phosphines from the postulated $[Fe_4S_4(PR_3)_4]^0$, resulting in the formation of an $[Fe_4S_4]$ dimer (R = Cy) or tetramers (R = ^{i}Pr, ^{t}Bu), in which the $[Fe_4S_4]$ units are connected via Fe-S edges [35–37]. In order to prevent the dissociation of supporting ligands from Fe, Holm and co-workers then employed cyanide as a more π-acidic ligand and successfully isolated the first *super-reduced* $[Fe_4S_4]^0$ cluster, $[Fe_4S_4(CN)_4]^{4-}$ (**1**), where the 4^- net charge results in high susceptibility toward oxidation [38]. Moreover, the strong binding properties of N-heterocyclic carbenes toward Fe [39] were able to stabilized another $[Fe_4S_4]^0$ cluster, $[Fe_4S_4(I^iPrMe_2)_4]$ (**2**, I^iPrMe_2 = 1,3-diisopropyl-4,5-dimethylimidazol-2-ylidene) (Fig. 2) [40]. These examples indicate that the use of stabilizing ligands that exhibit a combination of π-acidic and strong σ-bonding properties is crucial for the isolation of synthetic $[Fe_4S_4]^0$ clusters.

2.2 Physical Properties of the Super-Reduced Clusters

The Fe centers of $[Fe_4S_4]^0$ clusters **1** and **2** are supported by non-native π-acidic ligands. Nevertheless, their structures closely resemble the $[Fe_4S_4]^0$ cluster in the Fe

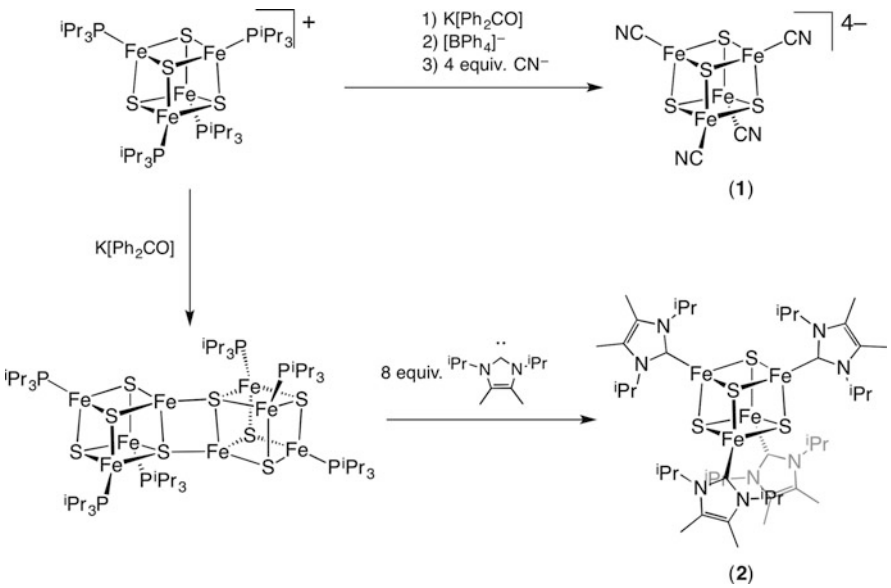

Fig. 2 Synthesis of $[Fe_4S_4]^0$ clusters $[Fe_4S_4(CN)_4]^{4-}$ (**1**) and $[Fe_4S_4(I^iPrMe_2)_4]$ (**2**; I^iPrMe_2 = 1,3-diisopropyl-4,5-dimethylimidazol-2-ylidene)

protein from *Azotobacter vinerandii* (*Av*). As summarized in Table 1, the average Fe-Fe/Fe-S bond distances of **1** and **2** are nearly identical to those of the *super-reduced Av* Fe protein, as determined by X-ray crystallography [42] and extended X-ray absorption fine structure (EXAFS) spectroscopy [43]. A structural comparison of $[Fe_4S_4]^0$ clusters and the $[Fe_4S_4]^+$ cluster $[Fe_4S_4(CN)_4]^{3-}$ [41], which is the one-electron oxidized form of **1**, allows evaluating the influence of the oxidation state on the $[Fe_4S_4]$ core structures. A notable difference in $[Fe_4S_4]^{0,+}$ clusters lies in the volumes of the S_4 tetrahedra, which are larger for $[Fe_4S_4]^0$ clusters (6.14–6.21 Å^3) than for the $[Fe_4S_4]^+$ cluster $[Fe_4S_4(CN)_4]^{3-}$ (5.64 Å^3). Similarly, the volume of the S_4 tetrahedron in the thiolate-supported $[Fe_4S_4]^{2+}$ and $[Fe_4S_4]^+$ clusters, $[Fe_4S_4(SR)_4]^{2-/3-}$, is smaller than 6 Å^3 [27], indicating that the volume of the S_4 tetrahedron may serve as a diagnostic parameter to identify the *super-reduced* $[Fe_4S_4]^0$ state. Some theoretical studies have been conducted in order to understand the physical properties of the $[Fe_4S_4]^0$ clusters [44, 45], but the postulated relationship between the oxidation state of $[Fe_4S_4]$ clusters and the volume of the S_4 tetrahedron remains unclear.

Similarities between the $[Fe_4S_4]^0$ clusters of **1** and **2** and the *super-reduced Av* Fe protein can also be found in their Mössbauer spectra. The spectra of **1** and **2** display two doublets with $\delta = 0.65/0.65$ mm/s and $\Delta E_Q = 1.45/2.00$ mm/s (1:1 ratio; **1**) as well as $\delta = 0.54/0.62$ mm/s and $\Delta E_Q = 2.92/1.54$ mm/s (1:3 ratio; **2**) at 77 K [38, 40]. The spectrum for the *super-reduced Av* Fe protein exhibits two doublets at $\delta = 0.68/0.68$ mm/s with $\Delta E_Q = 3.08/\sim 1.5$ mm/s (1:3 ratio). Electron paramagnetic resonance (EPR) and more detailed Mössbauer spectroscopic investigations on **2** revealed an $S = 4$ ground state for this cluster [45], and the same assignment should be applicable to the *super-reduced* Fe protein, as the g tensor of **2** ($g = 16.08$) observed by parallel-mode EPR is very similar to that of the *Av* Fe protein ($g = 16.4$) [22].

Table 1 Comparison of the bond distances (Å) and Fe_4/S_4 tetrahedron volumes (Å^3) for the *super-reduced* $[Fe_4S_4]^0$ cluster of the Fe protein and synthetic $[Fe_4S_4]^{0,+}$ clusters

	$[Fe_4S_4(CN)_4]^{3-}$ [41]	$[Fe_4S_4(CN)_4]^{4-}$ [38] (**1**)	$[Fe_4S_4(^iPr_2NHCMe_2)_4]$ [40] (**2**)	Fe protein	
				XRD [42]	EXAFS [43]
Oxidation state	$[Fe_4S_4]^+$	$[Fe_4S_4]^0$			
Av. Fe-Fe	2.70(2)	2.67(2)	2.68(6)	2.65	2.60
Av. Fe-S	2.29(1)	2.33(2)	2.33(2)	2.33	2.26
Volume (Fe_4)	2.34	2.25	2.26	2.17	–
Volume (S_4)	5.64	6.21	6.14	6.21	–

3 P-Cluster Models

The [Fe_8S_7] composition common to the MoFe and VFe nitrogenases is referred to as the P-cluster, which has been suggested to mediate electron-transfer processes through its redox activity. In the reduced form, denoted as the P^N state, the [Fe_8S_7] core has been described as a fused form of two cuboidal [Fe_4S_4] clusters that share one of the sulfides. This inorganic core is supported by two bridging and four terminal thiolate moieties from cysteine residues. The two-electron oxidized form of P^N is denoted as the P^{OX} state (or the P^{2+} state), which has the same core composition but a more *open* configuration due to the cleavage of two Fe-S bonds with the central sulfide and coordination of a serine residue and a backbone amide moiety (Fig. 3) [5]. The one-electron oxidized P^{1+} state has been detected as a transient species using spectroscopic methods [46, 47], while its structure has recently been determined by X-ray crystallography upon electrochemical generation of such a P^{1+} state [48]. In comparison with the P^N-cluster, the [Fe_8S_7] core in the P^{1+} state lacks an Fe-S bond with respect to the central sulfide and instead forms an Fe-O bond with a serine residue. Thus, the P^{1+} state displays an intermediary structure between the P^N and P^{OX} states. The redox-dependent dynamic structural rearrangements across the P^N, P^{1+}, and P^{OX} states should be important to regulate the electron flow from the [Fe_4S_4] cluster of the Fe protein to the P-cluster and then to the M-cluster, while the redox couple of the P^N/P^{1+} states has been proposed to be predominant under the turnover conditions of nitrogen fixation [8].

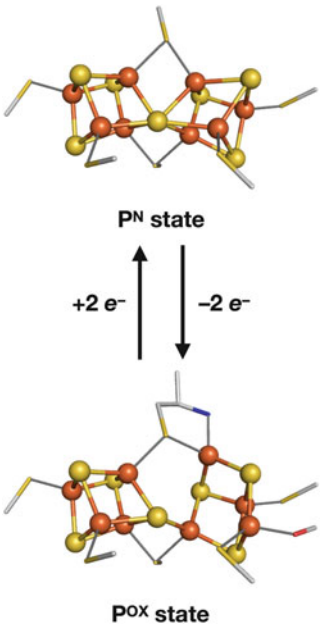

Fig. 3 Redox-dependent structural rearrangement of the P-cluster in the MoFe protein. PDB ID: 3U7Q. Color legend: C, gray; Fe, orange; N, blue; O, red; S, yellow

Early structural models of the P-cluster were based on dimers of $[Fe_4S_4]$ cubes, such as the sulfido-bridged $[Fe_4S_4]$-(μ_2-S)-$[Fe_4S_4]$ and edge-bridged $[Fe_4S_4]$-$[Fe_4S_4]$ clusters [14, 15, 26–29], because the structure of the P-cluster had initially been proposed as two $[Fe_4S_4]$ clusters bridged by cysteine residues [49] until the precise structure was reported in 1997 [5]. Although these $[Fe_4S_4]$ dimers are no longer considered to represent P-cluster models, the former $[Fe_4S_4]$-(μ_2-S)-$[Fe_4S_4]$ cluster was coincidentally discovered to be the cofactor of a double-cubane cluster protein from *Carboxydothermus hydrogenoformans* ($DCCP_{Ch}$) [50]. The $[Fe_4S_4]$-(μ_2-S)-$[Fe_4S_4]$ cluster of $DCCP_{Ch}$ catalyzes the reduction of acetylene, which indicates its potential for the reduction of small molecules.

Previous attempts to extract the P-cluster from the protein by addition of excess thiol (HSR, R = *p*-[dichloro(fluoro)methyl]phenyl) resulted in the degradation of the $[Fe_8S_7]$ core, furnishing $[Fe_4S_4]$ clusters in high yield (>90%) [51]. This result indicates the importance of the specific arrangement of six cysteines for the stabilization of the $[Fe_8S_7]$ core of the P-cluster, which renders the chemical synthesis of the $[Fe_8S_7]$ cluster challenging. It should also be noted that the μ_6-S atom at the center of the $[Fe_8S_7]$ core is not only unique to the P-cluster among the biological iron-sulfur clusters but also rare in synthetic metal-sulfur clusters. Thus, synthetic strategies for the P-cluster models have been directed toward how to generate such an unusual μ_6-S center. Here we address three strategies that have been devised to meet this requirement.

3.1 *Rearrangement of Edge-Bridged Mo(V)-Fe-S Double-Cubane Clusters*

While the P-cluster core contains only Fe and S atoms, the first structurally identified molecule with μ_6-S atoms was a heterometallic Mo-Fe-S cluster. An edge-bridged $[MoFe_3S_4]$ double-cubane precursor, $[(Cl_4\text{-cat})MoFe_3S_4(PEt_3)_3]_2$ (**3**, Cl_4-cat = tetrachlorocatecholate) [52], was treated with 2 equiv. of $[NEt_4][SH]$, leading to the rearrangement of the cluster core to give a complicated mixture. From this mixture, crystals of the giant $[Mo_2Fe_6S_9]$-$[Mo_2Fe_8S_{12}]$-$[Mo_2Fe_6S_9]$ cluster, which consists of two P-cluster-like $[Mo_2Fe_6S_9]$ units and a bridging $[Mo_2Fe_8S_{12}]$ units, were obtained [53]. From a similar reaction of **3** with $[NEt_4][SH]$ and $KC_{14}H_{10}$ (potassium anthracenide), a dimer of P-cluster-like $[Mo_2Fe_6S_9]$ clusters bridged by potassium atoms and sulfides was obtained. This synthetic method was further modified to employ $[MFe_3S_4]$-$[MFe_3S_4]$ (M = Mo (**4a**), V (**4b**)) clusters bearing tris(pyrazolyl)hydroborate (Tp) ligands on the heterometals (M), and their structural rearrangement in the presence of $[NEt_4][SH]$ proceeds in a more controlled manner to provide the P-cluster models $[(Tp)_2Mo_2Fe_6S_9(SH)_2]^{3-}$ (**5a**) and $[(Tp)_2V_2Fe_6S_9(SH)_2]^{4-}$ (**5b**) (Fig. 4) [54, 55]. In this case, the protection of M by the tridentate Tp ligand may extend the lifetime of intermediary species

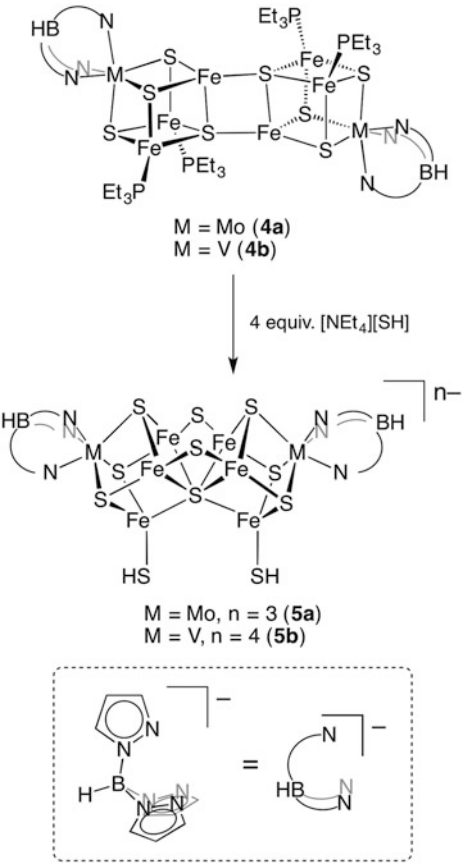

Fig. 4 Core rearrangement of the edge-bridged double-cubane clusters into $[(Tp)_2Mo_2Fe_6S_9(SH)_2]^{3-}$ (**5a**) and $[(Tp)_2V_2Fe_6S_9(SH)_2]^{4-}$ (**5b**)

generated from the precursor, facilitating the formation of **5a** and **5b**. A possible intermediate is a sulfur-voided $[MFe_3S_3]$-$[MFe_3S_4]$ cluster that contains an incomplete cubane-type $[MFe_3S_3]$ fragment (cf. Sect. 4.1.2), in which the sulfur-voided corner can accommodate a sulfur atom of the neighboring $[MFe_3S_4]$ cube to furnish a central μ_6-S atom.

The structural rearrangement of the $[MFe_3S_3]$-$[MFe_3S_4]$ double-cubane into P^N-type $[M_2Fe_6S_9]$ is triggered by hydrosulfide (HS^-), hydroselenide (HSe^-), methoxide (MeO^-), or ethane thiolate (EtS^-). Attempts to introduce further structural modifications on the $[M_2Fe_6S_9]$ clusters have had limited success so far. For example, terminally bound HS^- ligands or μ_2-bridging sulfides have been replaced with cyanides [56] and MeO^- [57], respectively, while substitution of μ_2-sulfides with thiolates has not been achieved. Recovery of the double-cubane structure from the P^N-type cluster has been demonstrated by the reaction of $[(Tp)_2Mo_2Fe_6S_8(OMe)_3]^{3-}$ with Me_3SiX (X = Cl, Br), where MeO^- is replaced by X^-. Such core convertibility

indicates a comparable thermodynamic stability for the $[MoFe_3S_3]$-$[MoFe_3S_4]$ and $[Mo_2Fe_6S_9]$ cores.

A number of M-Fe-S (M = Mo or V) clusters in this section feature a $[M_2Fe_6S_9]$ core, which is a fused form of two cubes with a central μ_6-S atom, two inter-cubane μ_2-sulfides, and peripheral M atoms, that exhibits a similar arrangement to that of the metal and sulfur atoms in the P^N-cluster. Their structural similarity is further supported by the superposition of the $[M_2Fe_6S_9]$ cores of **5a** (M = Mo) and **5b** (M = V) with the $[Fe_8S_7(\mu_2\text{-S-Cys})_2]$ core of the P^N-cluster and the obtained weighted root mean square deviations (RMSDs) of 0.38 Å (**5a** vs. P^N) and 0.33 Å (**5b** vs. P^N) [54]. In the Mössbauer spectra of clusters **5a** and **5b** at 4.2 K, a broad doublet is observed for **5a** at $\delta = 0.55$ mm/s with $\Delta E_Q = 0.62$ mm/s, while two overlapping doublets are found for **5b** at $\delta = 0.52/0.59$ mm/s with $\Delta E_Q = 1.23/0.65$ mm/s (major/minor = 3:1). These δ values indicate a relatively reduced Fe (II) state, in agreement with an all-ferrous state of the P^N-cluster [58]. The relatively low Fe(II) state in $[M_2Fe_6S_9]$ clusters indicates the retention of the oxidation state of Fe in edge-bridged double-cubane precursors prepared by chemical reduction of single cubanes. For instance, cluster **3** was prepared by reduction of the chloride-bound $[MoFe_3S_4]$ cube in the presence of PEt_3 [52]. Similarly, the $[MoFe_3S_3]$-$[MoFe_3S_4]$ precursor for **5a** was prepared from $[(Tp)MoFe_3S_4Cl_3]^-$ through substitution of the iron-bound chlorides with PEt_3 and subsequent reduction with $[NBu_4][BH_4]$.

3.2 Self-Assembly in a Nonpolar Media

A successful approach to reproduce the $[Fe_8S_7]$ core of the P-cluster is the self-assembly reaction shown in Fig. 5, where an iron(II) amide complex $Fe\{N(SiMe_3)_2\}_2$ is treated with HSTip (Tip = 2,4,6-tri(isopropyl)phenyl), tetramethylthiourea $[SC(NMe_2)_2]$, and elemental sulfur (S_8) in toluene. This reaction selectively furnishes the crystalline $[Fe_8S_7]$ cluster $[Fe_4S_3\{N(SiMe_3)_2\}(SC(NMe_2)_2)]_2(\mu_6\text{-S})\{\mu_2\text{-N}(SiMe_3)_2\}_2$ (**6**) in up to 82% yield [59, 60]. For this assembly reaction, some elementary steps can be postulated: (1) the $-N(SiMe_3)_2$ group on iron should serve as a Brønsted base to abstract a proton from HSTip, which leads to a ligand exchange between $-N(SiMe_3)_2$ and –STip; (2) a subsequent treatment with S_8 results in the oxidation of the Fe centers via the formation of Fe-S bonds; (3) the oxidation reaction in (2) should be followed by a reduction process to retain the average oxidation state of Fe between Fe(II) and Fe(III) through the reductive elimination of disulfide TipS-STip; (4) upon dissociation of some –STip ligands as TipS-STip, vacant coordination sites are generated on the Fe centers, which facilitate the aggregation of small iron-sulfur intermediates into high-nuclearity species. Steps (2)–(4) are repeated until (a) the depletion of S_8 and (b) the product becomes thermodynamically and/or kinetically stable enough for isolation. It is interesting to note that once isolated, **6** is stable for a few hours in solution at 50°C, suggesting that the core structure of the P-cluster is one of the thermodynamically stable forms of such iron-sulfur clusters.

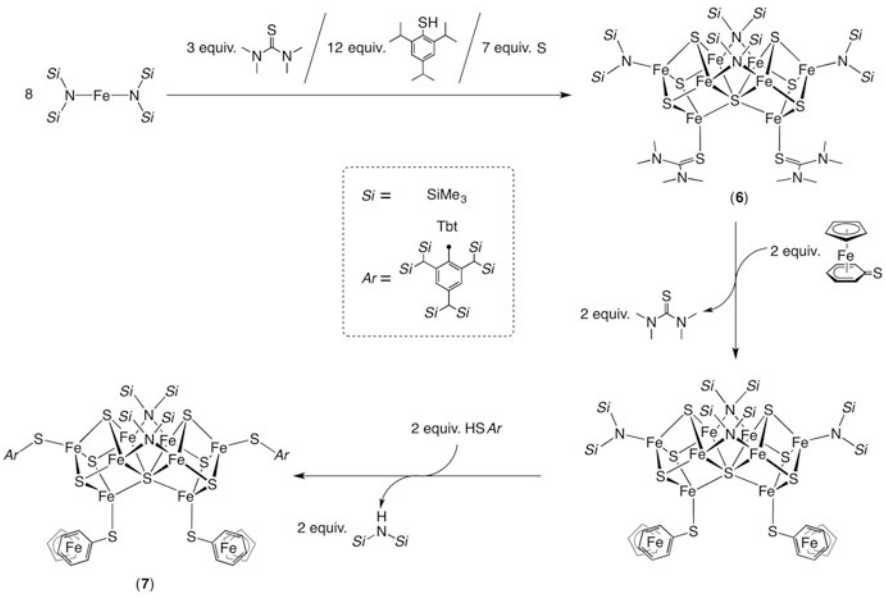

Fig. 5 Synthesis of the $[Fe_8S_7]$ clusters $[Fe_4S_3\{N(SiMe_3)_2\}(SC(NMe_2)_2)]_2(\mu_6\text{-}S)\{\mu_2\text{-}N(SiMe_3)_2\}_2$ (**6**) and $[(SAr)\{CpFe(C_6H_5S)\}Fe_4S_3]_2(\mu_6\text{-}S)\{\mu\text{-}N(SiMe_3)_2\}_2$ (**7**; *Ar* = 2,4,6-tris[bis(trimethylsilyl) methyl]phenyl), which reproduce the core of the P-cluster

The $[Fe_8S_7]$ core of cluster **6** reproduces well that of the P^N-cluster (Fig. 6), and in fact, a structural comparison between **6** and the P^N-cluster from the Protein Data Bank (ID: 3U7Q) [6] provided a low RMSD value (0.34 Å) [61]. The Mössbauer spectrum of **6** exhibits two doublets in an approximate ratio of 3:1 at $\delta = 0.61/0.37$ mm/s with $\Delta E_Q = 0.54/1.28$ mm/s (major/minor), which indicates a formal $Fe(II)_6Fe(III)_2$ oxidation state. This oxidation state corresponds to the P^{OX} state, which is the two-electron oxidized form of the all-ferrous P^N state [62], while cluster **6** adopts a P^N-type structure. The discrepancy between the oxidation states of **6** and the P^N-cluster may be partly attributed to tentative hydrogen bonding between the P^N-cluster and adventitious water and/or the peptide backbone. The dependence of the redox potentials of $[Fe_4S_4]$ clusters on the number of hydrogen bonds between the clusters and the water/peptide backbone has been discussed elsewhere [29, 63, 64]. In contrast to the P^N-cluster embedded in the protein, cluster **6** is in a completely hydrophobic environment, facilitating a higher oxidation state. An additional factor speculated for the relatively high oxidation state of **6** is the strong electron-donating property of the $-N(SiMe_3)_2$ ligands.

The $[Fe_8S_7]$ core of **6** is supported by amide and thiourea ligands, which have less relevance to the native P-cluster. Thus, replacement of these ligands with cysteine analogues was attempted to provide improved models. The $-N(SiMe_3)_2$ and thiourea ligands in **6** could be replaced by –SR via reactions with HSR and –SR, respectively; however, such ligand exchange reactions require careful optimization of the

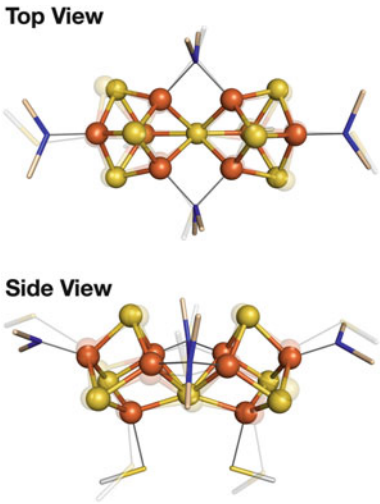

Fig. 6 Structural comparison of **6** and the P^N-cluster (transparent) via an overlay. The P^N-cluster is obtained from a crystal structure of MoFe nitrogenase (PDB ID: 3U7Q). Color legend: C, gray; Fe, orange; N, blue; S, yellow; Si, wheat

conditions due to the facile degradation of the $[Fe_8S_7]$ core. Thus, the reaction of **6** with 2 equiv. of $CpFe(C_6H_5S)$ (Cp = cyclopentadienyl) [65] and HS*Ar* (*Ar* = 2,4,6-tris[bis(trimethylsilyl)methyl]phenyl) at −40°C in fluorobenzene enabled the substitution of the terminal amide and thiourea ligands with thiolates to afford the $[Fe_8S_7]$ cluster $[(SAr)\{CpFe(C_6H_5S)\}Fe_4S_3]_2(\mu_6\text{-}S)\{\mu\text{-}N(SiMe_3)_2\}_2$ (**7**), which bears four terminal thiolate ligands (Fig. 5) [60]. In agreement with the facile degradation of the native P-cluster in the presence of excess thiol [51], the $[Fe_8S_7]$ core of **6** readily decomposes into $[Fe_4S_4]$ clusters in the presence of proton sources and nucleophiles, possibly because cleavage of the μ_2-bridging ligand in the middle of the cluster triggers such irreversible degradation. This assumption may also explain why the replacement of the $\mu_2\text{-}N(SiMe_3)_2$ ligands in **6** has not been successful so far.

3.3 Reductive Desulfurization of a High-Valent $[Fe_4S_4]$ Cluster

Another "nonpolar" approach for the formation of the P^N-type $[Fe_8S_7]$ cluster is the reductive desulfurization of a highly oxidized $[Fe_4S_4]$ cluster [66]. $[Fe_4S_3\{N(SiMe_3)_2\}(SPR_3)]_2(\mu_6\text{-}S)\{\mu_2\text{-}N(SiMe_3)_2\}_2$ (R = Me (**8a**), Et (**8b**)), i.e., analogues of **6** that bear phosphine sulfides SPR_3 (R = Me, Et) instead of tetramethylthiourea, have been obtained from the reaction of an all-ferric $[Fe_4S_4]^{4+}$ cluster $[Fe_4S_4\{N(SiMe_3)_2\}_4]$ [67] with phosphines (Fig. 7a). In this reaction, the phosphine abstracts

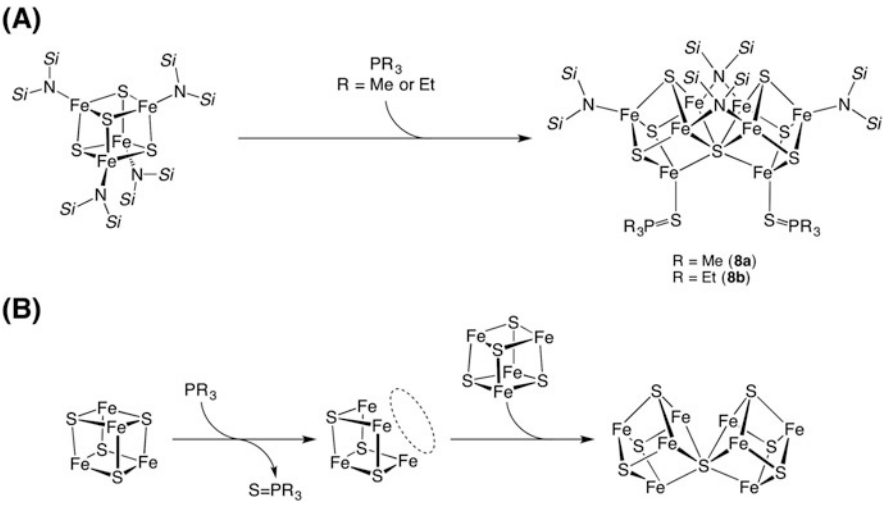

Fig. 7 (**a**) Synthesis of $[Fe_4S_3\{N(SiMe_3)_2\}(SPR_3)]_2(\mu_6\text{-}S)\{\mu_2\text{-}N(SiMe_3)_2\}_2$ (R = Me (**8a**), Et (**8b**)) from an all-ferric $[Fe_4S_4]$ cluster. (**b**) Proposed reaction pathway toward the $[Fe_8S_7]$ core via the formation of an $[Fe_4S_3]$ intermediate

one of the sulfur atoms of the $[Fe_4S_4]$ cube to produce SPR_3 and a transient sulfur-voided $[Fe_4S_3]$ cluster. The vacant Fe sites of this tentative $[Fe_4S_3]$ intermediate have been proposed to capture a sulfur atom of the $[Fe_4S_4]$ cube to furnish the central μ_6-S atom of the resulting $[Fe_8S_7]$ core (Fig. 7b).

The reaction pathway proposed for the formation of **8a** and **8b** has relevance to the biosynthesis of the P-cluster. The maturation of the P-cluster has been postulated as the coupling of two $[Fe_4S_4]$ clusters under reducing conditions (for recent reviews, see [68, 69]). Gene knockouts and subsequent isolation of the MoFe protein from the resulting strain revealed that there is a precursor state of the P-cluster (P*-cluster) with an $S = 1/2$ EPR feature in the dithionite-reduced form, which is characteristic for $[Fe_4S_4]^+$ clusters [70]. The assignment of the P*-cluster as a pair of $[Fe_4S_4]$ cubes was further supported by an Fe K-edge EXAFS analysis [71]. The P*-cluster can be converted into the P-cluster in the presence of the Fe protein with ATP and a chaperone-like supporting protein (NifZ), as evident from the appearance of the characteristic EPR signal of the P-cluster at $g = 11.8$ in the parallel-mode spectrum [71, 72]. Thus, the P*-cluster, a pair of $[Fe_4S_4]$ clusters, is likely converted into the $[Fe_8S_7]$ core of the P-cluster via removal of a sulfur atom and generation of an $[Fe_4S_3]$-type intermediate [73].

4 M-Cluster Models

The catalytic site of MoFe nitrogenase, denoted as the M-cluster, is arguably the most complex and enigmatic metallo-cofactor in nature. The M-cluster core in the resting state consists of one Mo, seven Fe, nine S, and one C atoms. This [$MoFe_7S_9C$] core can be viewed as a fused form of [$MoFe_3S_3C$] and [Fe_4S_3C] cubes that share the central C atom and that is supported by three μ_2-S atoms in the middle [6, 7]. As one of the μ_2-S atoms can be exchanged with an inhibitor carbon monoxide molecule or a Se atom [9, 10], the displacement of such "belt" S atoms represents a plausible explanation for the generation of the catalytically active M-cluster.

In an early stage of the biosynthetic pathway of the M-cluster, the coupling of two [Fe_4S_4] clusters occurs via incorporation of a carbon atom derived from *S*-adenosylmethionine to give an [Fe_8S_9C] species, denoted as the L-cluster (Fig. 8) [74]. Subsequent replacement of one of the peripheral Fe atoms of the [Fe_8S_9C] core with Mo and incorporation of a homocitrate moiety, followed by inter-protein transfer of the cluster, eventually furnishes the M-cluster [68, 69, 75, 76]. Given that most of the details of the biosynthesis of the M-cluster have been uncovered, imitation of the biosynthetic processes seems to be a promising approach for the chemical synthesis of M-cluster models. However, two major obstacles are easily identified when attempting to mimic the biosynthetic pathway based on the current synthetic methods of metal-sulfur clusters: (a) the incorporation of a carbon atom derived from the CH_3 moiety of *S*-adenosylmethionine and (b) the selective and asymmetric substitution of an Fe atom with Mo. Methods to carry out these difficult reactions remain challenging.

One of the intriguing properties of the M-cluster is its stability, even in the absence of a protein scaffold. Unlike the P-cluster, which is supported by six cysteine residues, the M-cluster is bound to the MoFe protein only by one cysteine and one histidine residues, and the Mo site carries a bidentate *R*-homocitrate ligand

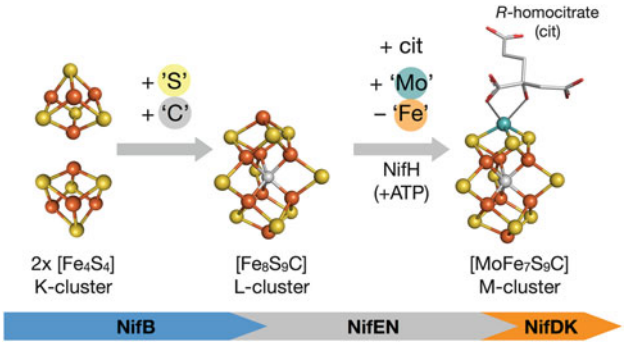

Fig. 8 Overview of the M-cluster biosynthesis. The precursors, a pair of [Fe_4S_4] clusters (K-cluster) in the NifB protein, are transformed into the [Fe_8S_9C] cluster (L-cluster) and then into the M-cluster that is accompanied by inter-protein transfer of the clusters to NifEN and then to NifDK. Color legend: C, gray; Fe, orange; N, blue; Mo, teal; O, red; S, yellow

as a nonprotein ligand. Probably owing to the loose binding from only two protein residues, the M-cluster can be extracted from the protein into organic solvents such as *N*-methylformamide, *N*,*N*-dimethylformamide, or acetonitrile without significant degradation, where the catalytic activity is recovered after reintroduction into the original protein-binding site [77, 78]. The robustness of the M-cluster as a discrete molecule in solution has stimulated the interest of synthetic chemists toward its reproduction. While the significant amount of work related to M-cluster models is summarized elsewhere ([14, 15]; for representative reviews on the functional models of nitrogenase, see [79–81]), we will herein focus on some recent advances in synthetic models and potential approaches toward the reproduction of the M-cluster core.

4.1 [MS_3] (M = Mo, W) Complexes as Building Blocks

Prior to the structural identification of the M-cluster, the available information was limited to, e.g., the proposed $MoFe_8S_6$ composition of the extracted cofactor [77]. Soon after, Holm and co-workers reported the synthesis of a double-cubane cluster with thiolate/sulfide inter-cubane bridges, $[MoFe_3S_4(SEt)_3](\mu_2\text{-}S)_2(\mu_2\text{-}SEt)$, through the assembly reaction of $[MoS_4]^{2-}$, $FeCl_3$, and EtS^- [82]. The $[MoFe_3S_4]$ cluster was intensively studied thereafter, together with other heterometallic cubanes such as the $[VFe_3S_4]$ and $[WFe_3S_4]$ clusters. One of the most significant results from these studies is arguably the synthesis of the P^N-type model clusters, which is described in Sect. 3.1 [14]. Although the chemistry of these cubanes in the field of heterometallic cofactor models has been well developed, we herein approach the utility of metal trisulfide $[MS_3]$ (M = Mo, W) complexes, which serve as building blocks for heterometallic clusters.

4.1.1 [M_6S_9]-Type Clusters Derived from [MS_3] Precursors

After the synthesis of organometallic trisulfide complexes of the type $[Cp^*MS_3]$ (M = Mo, W; Cp* = pentamethylcyclopentadienyl) [83], the reactivity of the sulfide moiety was examined through the synthesis of various heterometallic clusters with noble metals such as Cu, Ag, and Au [84]. The successful isolation of discrete heterometallic clusters demonstrated the synthetic potential of $[MS_3]$ complexes as building blocks for biomimetic Mo-Fe-S and W-Fe-S clusters. In this context, $[(Tp^*)WS_3]^-$ (**9**, Tp* = tris(3,5-dimethylpyrazolyl)hydroborate) [85] was the first trisulfide complex in the field of nitrogenase cofactor models. While the initial study [86] reported analogues of relevant Tp-M systems (Tp = tris(pyrazolyl)hydroborate; M = Mo, V) (cf. Sect. 3.1 as well as [54–57, 87]), later this approach proved the utility of the $[WS_3]$ precursor in the synthesis of high-nuclearity clusters.

The reaction of **9** with $FeCl_2$ (2 equiv.) and HS^- (2 equiv.) generated $[(Tp^*)_2W_2Fe_4S_9]^-$ (**10**), which can be further reduced to $[(Tp^*)_2W_2Fe_4S_9]^{2-}$ (**11**)

by treatment with $[BH_4]^-$ (Fig. 9) [88]. More importantly, a slightly modified reaction using Se^{2-} instead of HS^- led to the formation of $[(Tp^*)_2W_2Fe_4S_6Se_3]^{2-}$ (**12**), which confirmed the retention of the $[(Tp^*)WS_3]$ platform even after the assembly reaction with Fe and Se sources (Fig. 9). Retention of three sulfides on M (Mo or W) is a common feature in cluster synthesis employing $[MS_3]$ precursors. Analogous reactions of $[(^tBu_3tach)MS_3]$ (M = Mo (**13**), W (**14**); $^tBu_3tach$ = 1,3,5-tri-(*ter*-butyl)-1,3,5-triazacyclohexane) with $FeCl_2$, RS^-, and Se^{2-} provided heterochalcogenide-incorporated $[MFe_3S_3Se]$ cubes (**15**–**18**), in which three sulfides are bound to M and thus the selenide is located at the position opposite to M (Fig. 10) [89].

The zero-field ^{57}Fe Mössbauer spectra of **10** and **11** show signals at $\delta = 0.37$ ($\Delta E_Q = 1.21$) and $\delta = 0.42$ ($\Delta E_Q = 0.98$), respectively, suggesting $W(IV)_2Fe(III)_3Fe(II)$ (**10**) and $W(IV)_2Fe(III)_2Fe(II)_2$ (**11**) states. Cyclic voltammetry (CV) measurements on **11** and **12** revealed that the incorporation of Se stabilizes the *reduced* states of the $[W_2Fe_4S_6Q_3]$ (Q = S, Se) core, which is reflected in the positive shift of the [2–/3–] redox couple ($E_{1/2} = -1.91$ V (**12**) and -1.97 V (**11**) in DMF vs. saturated calomel electrode (SCE)) as well as in the appearance of an irreversible [3–/4–] couple for **12**. It should be noted that **10**–**12** are not the only $[M_6S_9]$-type clusters, i.e., other precedents of this class exist, e.g., $[Fe_6S_9(SR)_2]^{4-}$ [90–93], $[Fe_6Se_9(SR)_2]^{4-}$ [94], and $[(edt)_2Mo_2Fe_4S_9]^{3-/4-}$ (edt = ethane-1,2-dithiolate) [95], while that their synthesis involves typical assembly reactions employing Fe (and Mo) precursors, thiolates, and sulfide (selenide) sources.

Even though the trisulfide $[MS_3]$ (M = Mo, W) complexes are useful precursors for M-Fe-S(Se) clusters, reproduction of the asymmetric arrangement of metals in the M-cluster, in particular the location of Fe and Mo atoms at the opposite ends, has remained a significant challenge. We have recently revisited $[Cp^*MoS_3]^-$ (**19**) as a precursor of the Mo-Fe-S cluster and found a way to replicate the asymmetric arrangement of metals in the M-cluster. Surprisingly, a simple assembly reaction of **19** with $FeCl_2$ (5 equiv.) and HS^- (20 equiv.) resulted in the formation of $[Cp^*MoFe_5S_9(SH)]^{3-}$ (**20**) in 54% yield (Fig. 11a) [96]. Similarly to other clusters,

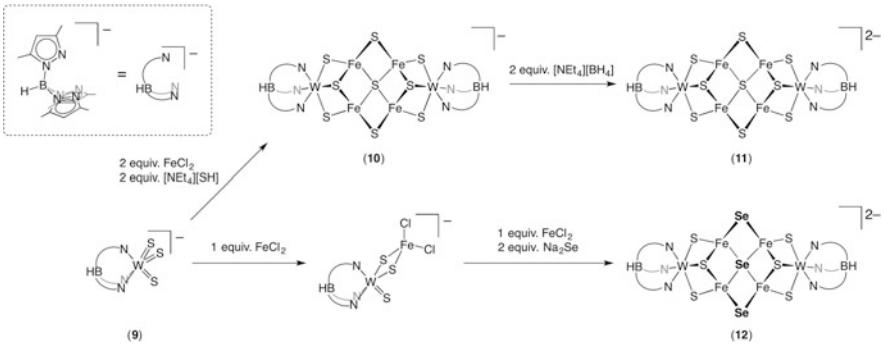

Fig. 9 Synthesis of $[(Tp^*)_2W_2Fe_4S_9]^{n-}$ ($n = 1$ (**10**) or 2 (**11**); Tp* = tris(3,5-dimethylpyrazolyl) hydroborate) and Se-containing $[(Tp^*)_2W_2Fe_4S_6Se_3]^{2-}$ (**12**) from a template $[WS_3]$ complex

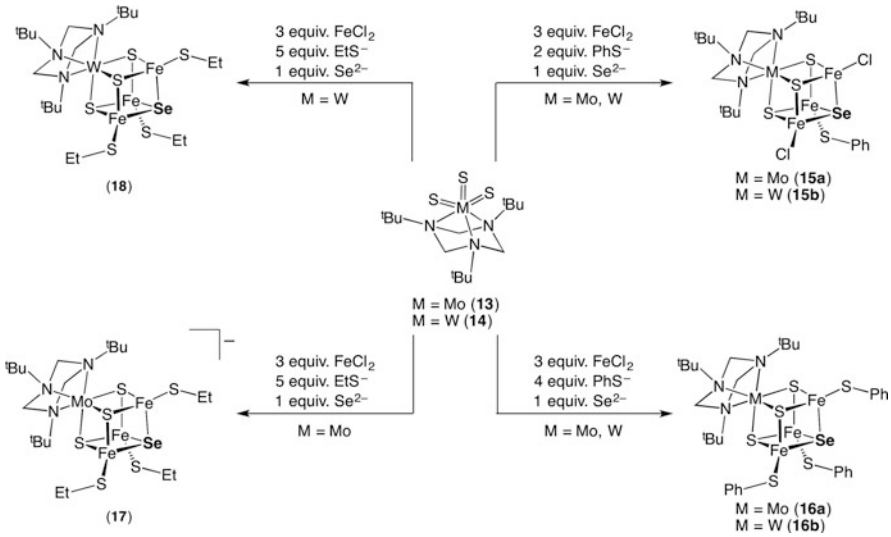

Fig. 10 Heterochalcogenide incorporation into cubane clusters by using [(^{t}Bu$_3$tach)MS$_3$] (M = Mo (**13**), W (**14**); ^{t}Bu$_3$tach = 1,3,5-tri-(*tertiary*-Butyl)-1,3,5-triazacyclohexane) as a structural template

20 also exhibits reversible redox properties at $E_{1/2} = -0.91$ V ([2–]/[3–] couple) and −2.06 V ([3–]/[4–] couple) vs. Ag/AgNO$_3$ in acetonitrile. It is interesting to note that **20** and $[Fe_6S_9(SEt)_2]^{4-}$ catalyze the reduction of C_1 substrates such as CN^-, CO, and CO_2 into short-chain hydrocarbons in the presence of reducing agents and proton sources [97].

A single-crystal X-ray diffraction analysis confirmed the asymmetric [MoFe$_5$S$_9$] core of **20**. As shown in Fig. 11b, the peripheral positions of the [M$_6$S$_9$]-type inorganic core are occupied by Mo and Fe atoms. In comparison with the M-cluster [6], **20** lacks one of the Fe-(μ_2-S)-Fe moieties and possesses a central μ_4-S atom instead of the μ_6-C atom of the M-cluster. As a result, cluster **20** adopts a more *open* conformation than the M-cluster, which is indicated by the longer Mo···Fe distance between the opposite ends of **20** (7.473(1) Å) compared to the corresponding distance in the M-cluster (7.00 Å) (Fig. 11b) and the smaller dihedral angles between two Fe-(μ_3-S)-Fe planes opposing the μ_4-S atom in **20** (58.87(5)°) relative to the corresponding angle in the M-cluster with respect to the μ_6-C atom (83.1–86.6°) (Fig. 11c).

4.1.2 Conversion of [MS$_3$] Complexes into Cuboidal Clusters as Potential Precursors for M-Cluster Models

Until the turn of the millennium, the central μ_6-atom of the M-cluster had not been identified, and its core structure had been considered as a pair of sulfur-deficient

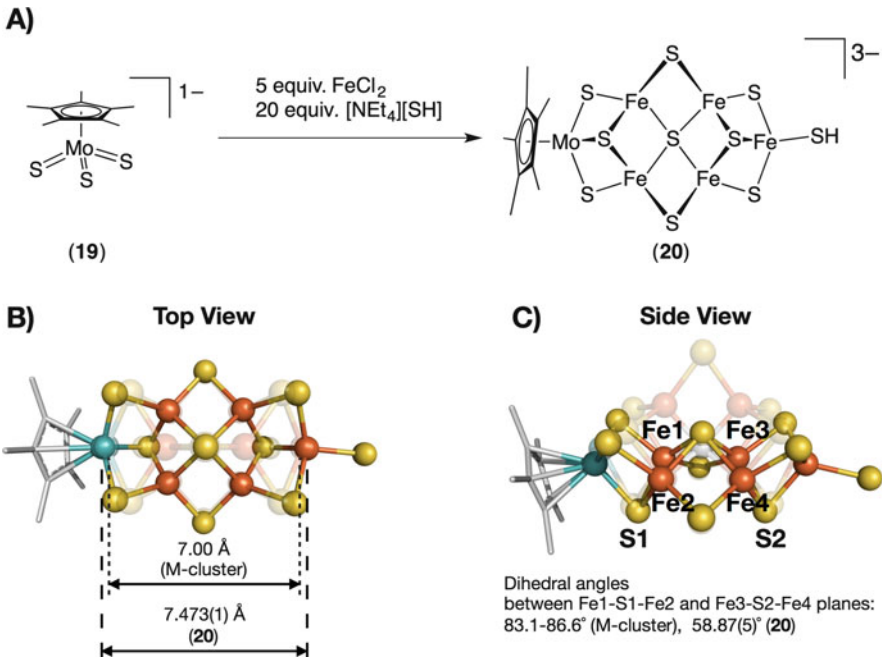

Fig. 11 (**a**) Synthesis of $[Cp^*MoFe_5S_9(SH)]^{3-}$ (**20**). Overlay of **20** and the M-cluster (transparent): (**b**) top view and (**c**) side view. PDB ID: 3U7Q

$[M_4S_3]$-type incomplete cubanes linked by three μ_2-S atoms. Thus, sulfur-voided $[M_4S_3]$-type clusters drew attention as suitable precursors for M-cluster models, and these are summarized elsewhere [15, 26]. Even after the precise structure of the M-cluster had been determined, the $[M_4S_3]$-type clusters or their equivalents remained potential and attractive precursors, given that a carbon atom can be accommodated at the sulfur-voided corner of the $[M_4S_3]$ core to possibly link two $[M_4S_3]$ fragments with a central μ_6-C atom. Even though the incorporation of a carbide ligand in a metal-sulfur cluster remains unprecedented, this section provides some examples of cubic and trinuclear clusters with a bridging light atom (N or O). The methods described herein may serve as a guide to devise further strategies to furnish metal-sulfur clusters that contain a μ_6-C atom.

Recently, cubic clusters of the type $[WFe_3S_3Q]$ (Q = Cl, Br), in which Q is expected to be exchangeable, have been synthesized. For example, $[(Tp^*)WFe_3S_3(\mu_3\text{-}Q)Q_3]^{2-}$ (Q = Cl (**21**), Br(**22**)) have been obtained from the reaction of the trisulfide complex $[(Tp^*)WS_3]^-$ (**9**) with FeQ_2 (3 equiv.) in the presence of sodium benzophenone ketyl as the reducing agent (Fig. 12) [98]. As in the cases of other clusters prepared from such trisulfide complexes, the three sulfur atoms in the

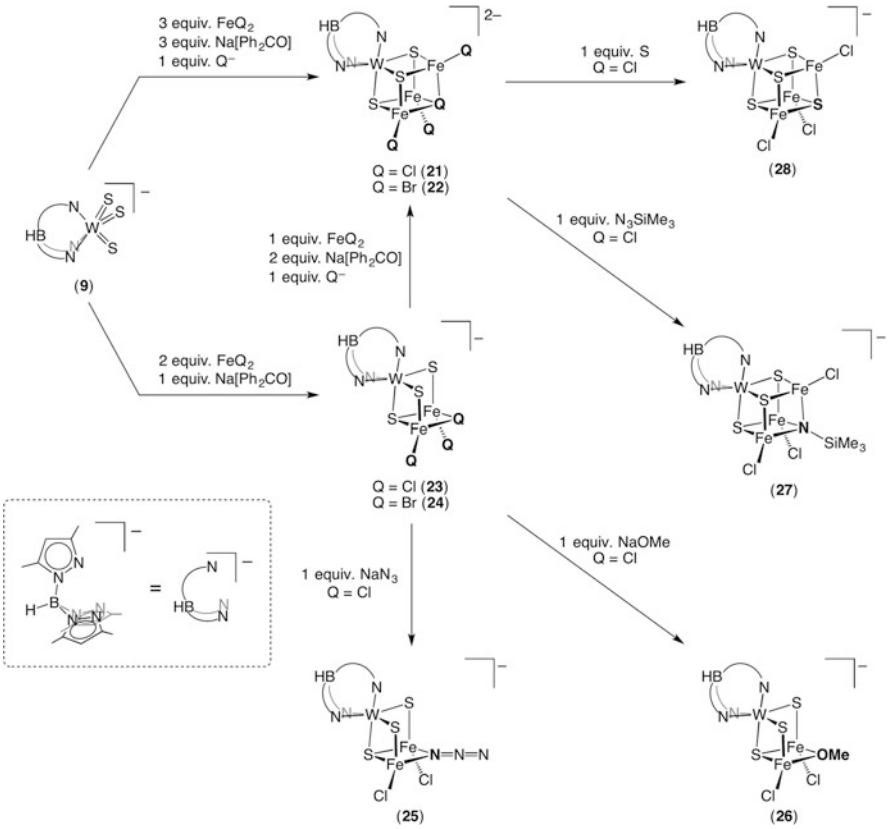

Fig. 12 Synthesis of halide-containing clusters $[(Tp^*)WFe_3S_3(\mu_3\text{-}Q)Q_3]^{2-}$ (Q = Cl (**21**), Br(**22**)) and $[(Tp^*)WFe_2S_3(\mu_2\text{-}Q)Q_2]^{-}$ (Q = Cl (**23**), Br (**24**)) from a template $[WS_3]$ complex and their ligand substitution reactions

$[WFe_3S_3Q]$ core remain attached to the W atom, and thus halide Q in clusters **21** and **22** occupies the corner opposite to W. An analogous reaction in the presence of FeQ_2 (2 equiv.) led to the formation of trinuclear clusters $[(Tp^*)WFe_2S_3(\mu_2\text{-}Q)Q_2]^{-}$ (Q = Cl (**23**), Br (**24**); Fig. 12). It has been proposed that in these cases, the presence of a reducing agent is important for the successful incorporation of halides in the cubic $[WFe_3S_3(\mu_3\text{-}Q)]^{2+}$ or the trinuclear $[WFe_2S_3(\mu_2\text{-}Q)]^{2+}$ cores. Other notable examples of cubic metal-sulfur clusters with $\mu_3\text{-}RN^{2-}$ ligands are $[Fe_4(N^tBu)_nS_{4-n}Cl_4]^{z-}$ ($n = 0$–3, $z = 0$–2) [99–101], which were synthesized via stepwise assembly reactions using intermediary dinuclear iron-imide or iron-imide-sulfide complexes.

The structure of trinuclear $[WFe_2S_3]$ cluster **23**, which was determined by a single-crystal X-ray diffraction analysis, revealed that the mean Fe-(μ_3-Cl) distance (2.495 (3) Å) is longer than the Fe-$Cl_{terminal}$ distance (2.284(4) Å), suggesting a possible substitution of Cl. In fact, the core μ_2-Cl of **23** was replaced through salt metathesis

reactions to furnish [WFe_2S_3] clusters with μ_2-N_3 (**25**) and μ_2-OMe (**26**) ligands. On the other hand, an analogous approach for the substitution of μ_3-Cl in the cubic [WFe_3S_3Cl] cluster **21** remained unsuccessful, which indicates that the μ_3-Cl ligand is less labile relative to the μ_2-Cl ligand in **23**. Successful examples for the replacement of μ_3-Cl in **21** include reactions with oxidative reactants such as $Me_3SiN_3^-$ and S_8, from which cubic clusters [(Tp*)$WFe_3S_3(\mu_3$-X)$Cl_3]^-$ (X = Me_3SiN^{2-} (**27**), S^{2-} (**28**)) were obtained.

4.2 *Nonpolar Approach and the Incorporation of Light Atoms*

Following the successful synthesis of [Fe_8S_7] clusters modeling the P^N-cluster (*c.f.* Sect. 3.2), the *nonpolar* approach was further extended to the synthesis of relevant iron-sulfur clusters, which are structurally analogous to the M-cluster [102, 103]. The precursors, i.e., an iron-thiolate complex [Fe(STip)(μ-SDmp)]$_2$ (Tip = 2,4,6-tri(isopropyl)phenyl, Dmp = 2,6-di(mesityl)phenyl) and an iron-thiolate-mesityl complex (DME)Fe(SDmp)(mesityl) (DME = 1,2-dimethoxyethane), react with elemental sulfur in toluene at ambient temperature to afford [Fe_8S_7] clusters [(DmpS)$Fe_4S_3]_2(\mu$-SDmp)$_2(\mu$-SR)(μ_6-S) (R = Tip (**29a**), mesityl (**29b**)), which feature a central μ_6-S atom (Fig. 13). In these assembly reactions, the use of bulky thiolate ligands appears to be important to dissolve the precursors in toluene and to stabilize the products at an appropriate size with eight Fe atoms. By encapsulating the Fe-S cores, bulky substituents may provide kinetic stabilization that prevents further assembly beyond the target size, while sufficient thermodynamic stability is a general prerequisite for the synthesis of metal-sulfur clusters.

The molecular structures of **29a** and **29b** revealed that their common inorganic core is a fused form of two [Fe_4S_4] cubes that share the central μ_6-S atom, which is additionally supported by two μ_2-SDmp and one μ_2-SR (R = Tip or mesityl) ligands. The six inner Fe atoms around the μ_6-S atom are arranged in a slightly distorted trigonal prism. The sulfur-centered trigonal prismatic structure of **29a–b** resembles that of the M-cluster. Due to the large size of the μ_6-S atom of **29a–b** relative to the μ_6-C atom of the M-cluster, the edge Fe-Fe distances of the trigonal prisms of **29a** (2.9103(10)–3.7050(10) Å) and **29b** (2.9212(7)–3.6506 (6) Å) are significantly longer than the corresponding distances of the M-cluster (2.58–2.62 Å). Given their homometallic nature, **29a–b** can also be considered as structural models of the L-cluster (Fig. 8), which is a recently identified [Fe_8S_9C] precursor of the M-cluster [68, 69, 104, 105]. Antiferromagnetic interactions across the eight Fe atoms are a common feature of the L-cluster and **29a–b**. In the EPR spectrum, the oxidized form of the L-cluster exhibits an isotropic $S = 1/2$ signal at $g = 1.92$ [105, 106], while clusters **29a–b** in the $[Fe_8S_7]^{5+}$ state display rhombic $S = 1/2$ signals at $g = 2.19$, 2.07, and 1.96 (**29a**) and $g = 2.21$, 2.07, and

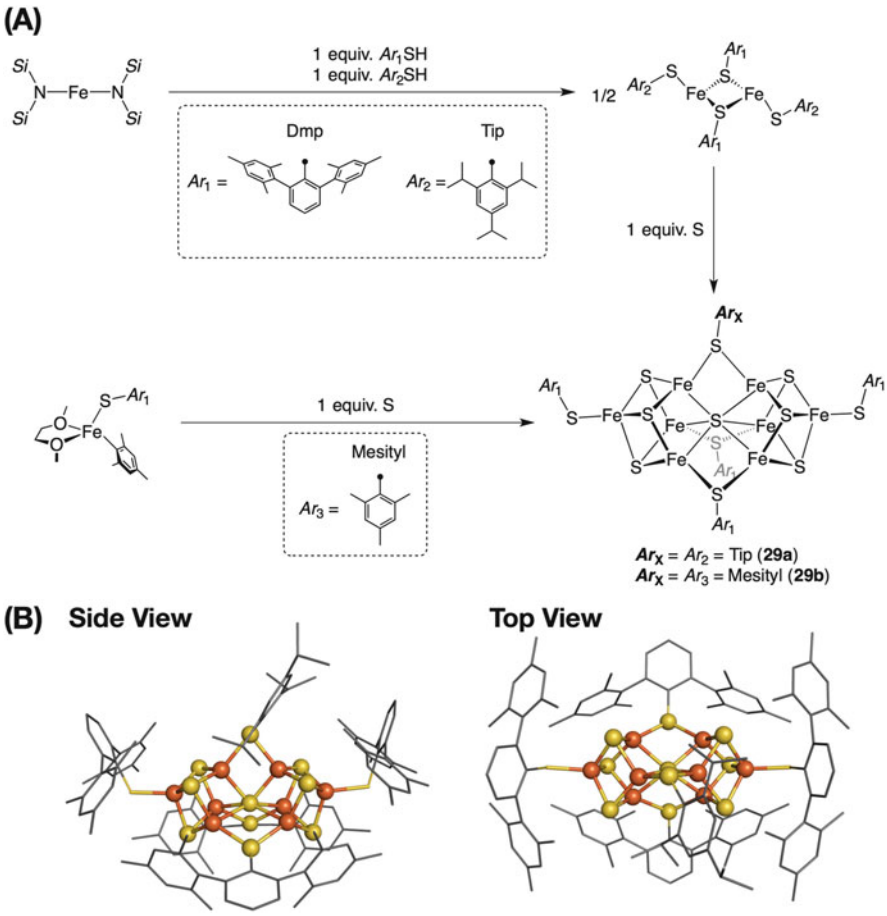

Fig. 13 (**a**) Synthesis of $[(DmpS)Fe_4S_3]_2(\mu\text{-SDmp})_2(\mu\text{-SR})(\mu_6\text{-S})$ (R = Tip (**29a**), mesityl (**29b**)). (**b**) Crystal structure of **29a** (side and top view). Color legend: C, gray; Fe, orange; S, yellow

1.95 (**29b**). These EPR signals are different from the $S = 3/2$ feature that appears at $g = 4.31$, 3.67, and 2.01 for the M-cluster in the resting state.

An oxygen atom can be encapsulated within an Fe-S cluster by the reaction of $[Fe(OCPh_3)(\mu_2\text{-SDmp})]_2$ with H_2O and S_8 (Fig. 14) [107]. The major product from this reaction, an $[Fe_8S_6O]$ cluster (**30**), often co-crystallizes with the $[Fe_8S_7]$ by-product (**31**). Therefore, their occupancy ratio within single crystals varies from 100/0 to 75/25 (**30/31**). In the crystal structure of **30**, the central O atom displays a μ_4-binding mode, which stands in sharp contrast to the μ_6-mode of the central atoms of **29a–b** (μ_6-S) and the M-cluster (μ_6-C). As a result, two inner Fe atoms of **30** deviate from the oxygen atom and interact with the mesityl groups of the μ_2-SDmp ligands (2.505 (2) Å for the shortest Fe-C distance) surrounding the inner Fe atoms. Given the absence of some Fe-$O_{central}$ bonds and the presence of compensating Fe-mesityl

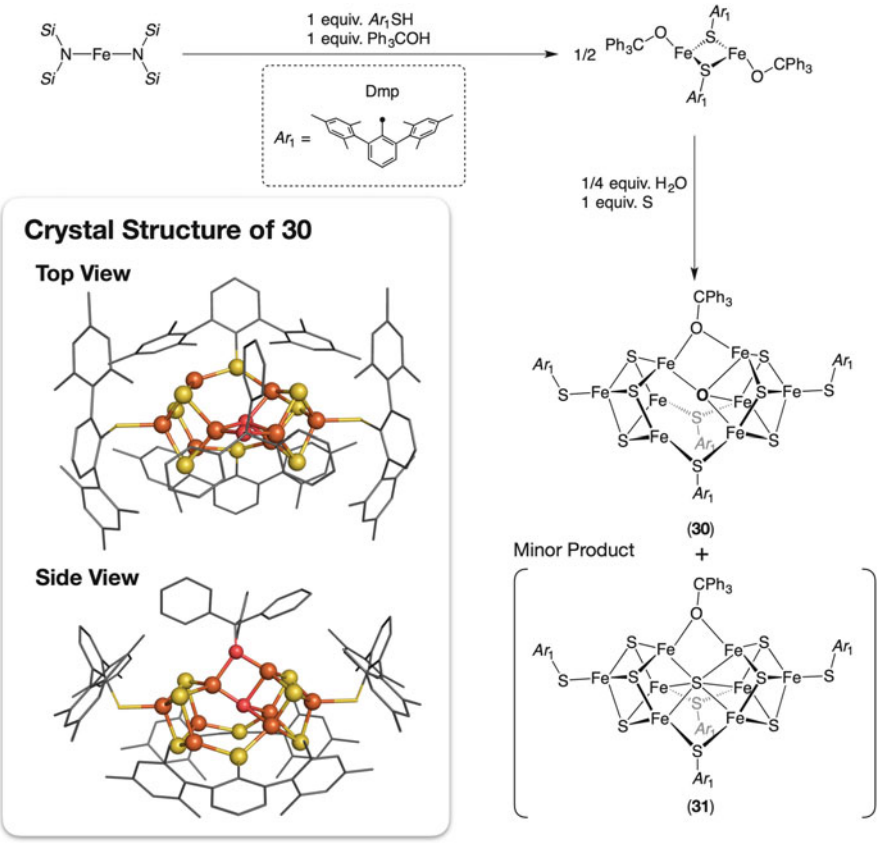

Fig. 14 Synthesis and crystal structure of $[(DmpS)Fe_4S_3O][(DmpS)Fe_4S_3](\mu\text{-}SDmp)_2(\mu\text{-}OCPh_3)$ (**30**)

interactions, it seems possible to assume an analogous mode of substrate binding to the inner Fe atoms of the M-cluster. This speculation is consistent with a proposal for the M-cluster, where the N_2-binding site is generated through the reversible cleavage or weakening of an Fe-(μ_6-C) bond [108, 109].

5 Concluding Remarks and Future Directions for Nitrogenase Model Studies

In this review, we have summarized recent advances in synthetic metal-sulfur clusters that serve as models for the nitrogenase metallo-cofactors as well as some selected notable achievements of older studies. Representative recent developments include (a) the synthesis of all-ferrous $[Fe_4S_4]^0$ clusters as models for the

super-reduced $[Fe_4S_4]$ cluster of the Fe protein; (b) the synthesis of $[Mo_2Fe_6S_9]$, $[V_2Fe_6S_9]$, and $[Fe_8S_7]$ clusters, which model or reproduce the P-cluster; and (c) the synthesis of Mo-Fe-S, W-Fe-S, Fe-S, and Fe-S-O clusters, which are structurally relevant to the M-cluster. The chemical synthesis of such model clusters and their structural modifications remain attractive research topics, especially with respect to a better understanding of the properties of metallo-cofactors, given that spectroscopic studies on nitrogenases are often hampered by the presence of nontarget clusters. Since the (potential) models for the M-cluster remain insufficient as they lack key structural features, one of the most important issues to be addressed in future studies is the synthesis of more reliable M-cluster models, e.g., carbon-centered Mo-Fe-S clusters with eight metal atoms.

Another remaining major issue in nitrogenase studies is the relationship between the structure of the M-cluster and its N_2-reducing function. Recent protein crystallographic studies on MoFe and VFe nitrogenases have disclosed some important details in this respect [9–12], implying the displacement of one of the belt μ_2-S atoms may be necessary for the generation of the reactive species. Thus, synthetic metal-sulfur clusters that feature such belt μ_2-S and central μ_6-C atoms are required. Furthermore, the N_2 chemistry of metal-sulfur clusters is in a very early stage, and synthetic developments are needed to uncover the requirements for the reduction of N_2 on metal-sulfur clusters. In this regard, it should be noted that a cubic Mo-Ti-S cluster is able to activate N_2 at the Ti site under reducing conditions. The N_2 moiety bridging two $[MoS_4Ti]$ cubes was converted into sub-stoichiometric amounts of NH_3 and N_2H_4, demonstrating the molecular basis for the reduction of N_2 on metal-sulfur clusters [110].

The application of synthetic metal-sulfur clusters in biochemical studies can offer a relatively new avenue of research. For instance, we have achieved the incorporation of $[Fe_6S_9(SEt)_2]^{4-}$ into the M-cluster-binding site of the *apo*-MoFe protein and demonstrated the catalytic reduction of acetylene and CN^- with this protein [111]. Furthermore, we have recently employed a synthetic $[Fe_4S_4]$ cluster to elucidate the source of an additional sulfur atom required for the biosynthesis of the M-cluster [112]. Since analogous strategies should be applicable to various iron-sulfur proteins, the combination of synthetic chemistry and biochemistry represents one of the future directions for metal-sulfur chemistry.

Acknowledgment Y. O. thanks the Japanese Ministry of Education, Culture, Sports, Science and Technology (16H04116 and 18H04246) and the Takeda Science Foundation for funding.

References

1. Eady RR (1996) Structure−function relationships of alternative nitrogenases. Chem Rev 96:3013–3030. https://doi.org/10.1021/cr950057h
2. Danyal K, Dean DR, Hoffman BM, Seefeldt LC (2011) Electron transfer within nitrogenase: evidence for a deficit-spending mechanism. Biochemistry 50:9255–9263. https://doi.org/10.1021/bi201003a

3. Burgess BK, Lowe DJ (1996) Mechanism of molybdenum nitrogenase. Chem Rev 96:2983–3012. https://doi.org/10.1021/cr950055x
4. Hoffman BM, Lukoyanov D, Yang Z et al (2014) Mechanism of nitrogen fixation by nitrogenase: the next stage. Chem Rev 114:4041–4062. https://doi.org/10.1021/cr400641x
5. Peters JW, Stowell MHB, Soltis SM, Finnegan MG, Johnson MK, Rees DC (1997) Redox-dependent structural changes in the nitrogenase P-cluster. Biochemistry 36:1181–1187. https://doi.org/10.1021/bi9626665
6. Spatzal T, Aksoyoglu M, Zhang L et al (2011) Evidence for interstitial carbon in nitrogenase FeMo cofactor. Science 334:940–940. https://doi.org/10.1126/science.1214025
7. Lancaster KM, Roemelt M, Ettenhuber P, Hu Y, Ribbe MW, Neese F, Bergmann U, DeBeer S (2011) X-ray emission spectroscopy evidences a central carbon in the nitrogenase iron-molybdenum cofactor. Science 334:974–977. https://doi.org/10.5061/dryad.6m0f6870
8. Seefeldt LC, Hoffman BM, Dean DR (2009) Mechanism of Mo-dependent nitrogenase. Annu Rev Biochem 78:701–722. https://doi.org/10.1007/978-1-61779-194-9_2
9. Spatzal T, Perez KA, Einsle O, Howard JB, Rees DC (2014) Ligand binding to the FeMo-cofactor: structures of CO-bound and reactivated nitrogenase. Science 345:1620–1623. https://doi.org/10.1126/science.1256679
10. Spatzal T, Perez KA, Howard JB, Rees DC (2015) Catalysis-dependent selenium incorporation and migration in the nitrogenase active site iron-molybdenum cofactor. elife 4:e11620. https://doi.org/10.7554/eLife.11620
11. Sippel D, Einsle O (2017) The structure of vanadium nitrogenase reveals an unusual bridging ligand. Nat Chem Biol 13:956–960. https://doi.org/10.1038/nchembio.2428
12. Sippel D, Rohde M, Netzer J, Trncik C, Gies J, Grunau K, Djurdjevic I, Decamps L, Andrade SLA, Einsle O (2018) A bound reaction intermediate sheds light on the mechanism of nitrogenase. Science 359:1484–1489. https://doi.org/10.1126/science.aar2765
13. Benediktsson B, Thorhallsson AT, Bjornsson R (2018) QM/MM calculations reveal a bridging hydroxo group in a vanadium nitrogenase crystal structure. Chem Commun 54:7310–7313. https://doi.org/10.1039/C8CC03793K
14. Lee SC, Holm RH (2004) The clusters of nitrogenase: synthetic methodology in the construction of weak-field clusters. Chem Rev 104:1135–1157. https://doi.org/10.1021/cr0206216
15. Ohki Y, Tatsumi K (2013) New synthetic routes to metal-sulfur clusters relevant to the nitrogenase metallo-clusters. Z Anorg Allg Chem 639:1340–1349. https://doi.org/10.1002/zaac.201300081
16. Holm RH, Kennepohl P, Solomon EI (1996) Structural and functional aspects of metal sites in biology. Chem Rev 96:2239–2314. https://doi.org/10.1021/cr9500390
17. Beinert H, Holm RH, Münck E (1997) Iron-sulfur clusters: nature's modular, multipurpose structures. Science 277:653–659. https://doi.org/10.1126/science.277.5326.653
18. Beinert H (2000) Iron-sulfur proteins: ancient structures, still full of surprises. J Biol Inorg Chem 5:2–15. https://doi.org/10.1007/s007750050002
19. Johnson DC, Dean DR, Smith AD, Johnson MK (2005) Structure, function, and formation of biological iron-sulfur clusters. Annu Rev Biochem 74:247–281. https://doi.org/10.1146/annurev.biochem.74.082803.133518
20. Jasniewski AJ, Sickerman NS, Hu Y, Ribbe MW (2018) The Fe protein: an unsung hero of nitrogenase. Inorganics 6:25. https://doi.org/10.3390/inorganics6010025
21. Watt GD, Reddy KRN (1994) Formation of an all ferrous Fe_4S_4 cluster in the iron protein component of *Azotobacter vinelandii* nitrogenase. J Inorg Biochem 53:281–294. https://doi.org/10.1016/0162-0134(94)85115-8
22. Angove HC, Yoo SJ, Burgess BK, Münck E (1997) Mössbauer and EPR evidence for an all-ferrous Fe_4S_4 cluster with $S = 4$ in the Fe protein of nitrogenase. J Am Chem Soc 119:8730–8731. https://doi.org/10.1021/ja9712837
23. Rebelein JG, Stiebritz MT, Lee CC, Hu Y (2016) Activation and reduction of carbon dioxide by nitrogenase iron proteins. Nat Chem Biol 13:147–149. https://doi.org/10.1038/nchembio.2245

24. Stiebritz MT, Hiller CJ, Sickerman NS, Lee CC, Tanifuji K, Ohki Y, Hu Y (2018) Ambient conversion of CO2 to hydrocarbons by biogenic and synthetic [Fe_4S_4] clusters. Nat Catal 1:444–451. https://doi.org/10.1038/s41929-018-0079-4
25. Herskovitz T, Averill BA, Holm RH, Ibers JA, Phillips WD, Weiher JF (1972) Structure and properties of a synthetic analogue of bacterial iron-sulfur proteins. Proc Natl Acad Sci U S A 69:2437–2441. https://doi.org/10.1073/pnas.69.9.2437
26. Rao PV, Holm RH (2004) Synthetic analogues of the active sites of iron − sulfur proteins. Chem Rev 104:527–560. https://doi.org/10.1021/cr020615
27. Tan LL, Holm RH, Lee SC (2013) Structural analysis of cubane-type iron clusters. Polyhedron 58:206–217. https://doi.org/10.1016/j.poly.2013.02.031
28. Holm RH, Lo W (2016) Structural conversions of synthetic and protein-bound iron − sulfur clusters. Chem Rev 116:13685–13713. https://doi.org/10.1021/acs.chemrev.6b00276
29. Ohta S, Ohki Y (2017) Impact of ligands and media on the structure and properties of biological and biomimetic iron-sulfur clusters. Coord Chem Rev 338:207–225. https://doi.org/10.1016/j.ccr.2017.02.018
30. Georgiadis MM, Komiya H, Chakrabarti P et al (1992) Crystallographic structure of the nitrogenase iron protein from *Azotobacter vinelandii*. Science 257:1653–1659. https://doi.org/10.1126/science.1529353
31. DePamphilis BV, Averill BA, Herskovitz T, Que L Jr, Holm RH (1974) Synthetic analogs of the active sites of iron-sulfur proteins. VI. Spectral and redox characteristics of the tetranuclear clusters $[Fe_4S_4(SR)_4]^{2-}$. J Am Chem Soc 96:4159–4167. https://doi.org/10.1021/ja00820a018
32. Cambray J, Lane RW, Wedd AG, Johnson RW, Holm RH (1977) Chemical and electrochemical interrelationships of the 1-Fe, 2-Fe, and 4-Fe analogues of the active sites of iron-sulfur proteins. Inorg Chem 16:2565–2571. https://doi.org/10.1021/ic50176a030
33. Zhou C, Raebiger JW, Segal BM, Holm RH (2000) The influence of net charge on the redox potentials of Fe_4S_4 cubane-type clusters in aprotic solvents. Inorg Chim Acta 300–302:892–902. https://doi.org/10.1016/S0020-1693(99)00593-9
34. Crabtree RH (2014) The organometallic chemistry of the transition metals, 6th edn. Wiley, Hoboken
35. Goh C, Segal BM, Huang J et al (1996) Polycubane clusters: synthesis of $[Fe_4S_4(PR_3)_4]^{1+,0}$ (R = Bu^t, Cy, Pr^i) and $[Fe_4S_4]^0$ core aggregation upon loss of phosphine. J Am Chem Soc 118:11844–11853. https://doi.org/10.1021/ja9620200
36. Zhou H-C, Holm RH (2003) Synthesis and reactions of cubane-type iron-sulfur-phosphine clusters, including soluble clusters of nuclearities 8 and 16. Inorg Chem 42:11–21. https://doi.org/10.1021/ic020464t
37. Deng L, Majumdar A, Lo W, Holm RH (2010) Stabilization of 3:1 site-differentiated cubane-type clusters in the $[Fe_4S_4]^{1+}$ core oxidation state by tertiary phosphine ligation: synthesis, core structural diversity, and $S = 1/2$ ground states. Inorg Chem 49:11118–11126. https://doi.org/10.1021/ic101702b
38. Scott TA, Berlinguette CP, Holm RH, Zhou H-C (2005) Initial synthesis and structure of an all-ferrous analogue of the fully reduced $[Fe_4S_4]^0$ cluster of the nitrogenase iron protein. Proc Natl Acad Sci U S A 102:9741–9744. https://doi.org/10.1073/pnas.0504258102
39. Ingleson MJ, Layfield RA (2012) N-heterocyclic carbene chemistry of iron: fundamentals and applications. Chem Commun 48:3579–3589. https://doi.org/10.1039/c2cc18021a
40. Deng L, Holm RH (2008) Stabilization of fully reduced iron-sulfur clusters by carbene ligation: the $[Fe_nS_n]^0$ oxidation levels (n = 4, 8). J Am Chem Soc 130:9878–9886. https://doi.org/10.1021/ja802111w
41. Scott TA, Zhou H-C (2004) The first all-cyanide Fe4S4 cluster: $[Fe_4S_4(CN)_4]^{3-}$. Angew Chem Int Ed 43:5628–5631. https://doi.org/10.1002/anie.200460879
42. Strop P, Takahara PM, Chiu HJ, Angove HC, Burgess BK, Rees DC (2001) Crystal structure of the all-ferrous [4Fe-4S]^0 form of the nitrogenase iron protein from *Azotobacter vinelandii*. Biochemistry 40:651–656. https://doi.org/10.1021/bi0016467

43. Musgrave KB, Angove HC, Burgess BK, Hedman B, Hodgson KO (1998) All-ferrous titanium (III) citrate reduced Fe protein of nitrogenase: an XAS study of electronic and metrical structure. J Am Chem Soc 120:5325–5326
44. Torres RA, Lovell T, Noodleman L, Case DA (2003) Density functional and reduction potential calculations of Fe_4S_4 clusters. J Am Chem Soc 125:1923–1936. https://doi.org/10.1021/ja0211104
45. Chakrabarti M, Deng L, Holm RH, Münck E, Bominaar EL (2009) Mössbauer, Electron paramagnetic resonance, and theoretical study of a carbene-based all-ferrous Fe_4S_4 cluster: electronic origin and structural identification of the unique spectroscopic site. Inorg Chem 48:2735–2747
46. Tittsworth RC, Hales BJ (1993) Detection of EPR signals assigned to the 1-equiv-oxidized P-clusters of the nitrogenase MoFe-protein from *Azotobacter vinelandii*. J Am Chem Soc 115:9763–9767. https://doi.org/10.1021/ja00074a050
47. Chan JM, Christiansen J, Dean DR, Seefeldt LC (1999) Spectroscopic evidence for changes in the redox state of the nitrogenase P-cluster during turnover. Biochemistry 38:5779–5785. https://doi.org/10.1021/bi982866b
48. Keable SM, Zadvornyy OA, Johnson LE, Ginovska B, Rasmussen AJ, Danyal K, Eilers BJ, Prussia GA, LeVan AX, Raugei S, Seefeldt LC, Peters JW (2018) Structural characterization of the P^{1+} intermediate state of the P-cluster of nitrogenase. J Biol Chem 293:9629–96354. https://doi.org/10.1074/jbc.RA118.002435
49. Kim J, Rees DC (1992) Structural models for the metal centers in the nitrogenase molybdenum-iron protein. Science 257:1677–1682
50. Jeoung J-H, Dobbek H (2018) ATP-dependent substrate reduction at an $[Fe_8S_9]$ double-cubane cluster. Proc Natl Acad Sci U S A 115:2994–2999. https://doi.org/10.1073/pnas.1720489115
51. Kurtz DM Jr, McMillan RS, Burgess BK, Mortenson LE, Holm RH (1979) Identification of iron-sulfur centers in the iron-molybdenum proteins of nitrogenase. Proc Natl Acad Sci U S A 76:4986–4989. https://doi.org/10.1073/pnas.76.10.4986
52. Demadis KD, Campana CF, Coucouvanis D (1995) Synthesis and structural characterization of the new $Mo_2Fe_6S_8(PR_3)_6(Cl_4\text{-cat})_2$ clusters. Double cubanes containing two edge-linked $[MoFe_3S_4]^{2+}$ reduced cores. J Am Chem Soc 117:7832–7833
53. Osterloh F, Sanakis Y, Staples RJ, Münck E, Holm RH (1999) A molybdenum–iron–sulfur cluster containing structural elements relevant to the P-cluster of nitrogenase. Angew Chem Int Ed 38:2066–2070
54. Zhang Y, Zuo JL, Zhou H-C, Holm RH (2002) Rearrangement of symmetrical dicubane clusters into topological analogues of the P-cluster of nitrogenase: nature's choice? J Am Chem Soc 124:14292–14293. https://doi.org/10.1021/ja0279702
55. Zhang Y, Holm RH (2003) Synthesis of a molecular $Mo_2Fe_6S_9$ cluster with the topology of the P N cluster of nitrogenase by rearrangement of an edge-bridged Mo 2 Fe_6S_8 double cubane. J Am Chem Soc 125:3910–3920. https://doi.org/10.1021/ja0214633
56. Pesavento RP, Berlinguette CP, Holm RH (2007) Stabilization of reduced molybdenum-iron-sulfur single- and double-cubane clusters by cyanide ligation. Inorg Chem 46:510–516. https://doi.org/10.1021/ic061704y
57. Zhang Y, Holm RH (2004) Structural conversions of molybdenum-iron-sulfur edge-bridged double cubanes and P^N-type clusters topologically related to the nitrogenase P-cluster. Inorg Chem 43:674–682. https://doi.org/10.1021/ic030259t
58. McLean PA, Papaefthymiouv V, Orme-Johnson WH, Münck E (1987) Isotopic hybrids of nitrogenase. J Biol Chem 262:12900–12903
59. Ohki Y, Sunada Y, Honda M, Katada M (2003) Synthesis of the P-cluster core of nitrogenases. J Am Chem Soc 125:4052–4053
60. Ohki Y, Imada M, Murata A et al (2009) Synthesis, structures, and electronic properties of [8Fe-7S] cluster complexes modeling the nitrogenase P-cluster. J Am Chem Soc 131:13168–13178

61. The RMSD value was calculated using the PyMOL software package (ver. 2.0.6). PyMol is an open-source software, released under https://pymol.org/2/
62. Pierik AJ, Wassink H, Haaker H, Hagen WR (1993) Redox properties and EPR spectroscopy of the P-clusters of *Azotobacter vinelandii* molybdenum-iron protein. Eur J Biochem 212:51–61. https://doi.org/10.1111/j.1432-1033.1993.tb17632.x
63. Dey A, Jenney FE, Adams MWW et al (2007) Solvent tuning of electrochemical potentials in the active sites of HiPIP versus ferredoxin. Science 318:1464–1468. https://doi.org/10.1126/science.1147753
64. Cowan JA, Lui SM (1998) Structure-function correlations in high-potential IRON proteins. Adv Inorg Chem 45:313–350. https://doi.org/10.1016/S0898-8838(08)60028-8
65. Helling JF, Hendrickson WA (1979) Synthesis and deprotonation of η^6-Arene-η^5-cyclopentadienyliron(II) compexes bearing NH_2, OH or SH substituents. J Organomet Chem 168:87–95. https://doi.org/10.1016/S0022-328X(00)91996-X
66. Ohki Y, Tanifuji K, Yamada N, Cramer RE, Tatsumi K (2012) Formation of a nitrogenase P-cluster [Fe_8S_7] core via reductive fusion of two all-ferric [Fe_4S_4] clusters. Chem Asian J 7:2222–2224. https://doi.org/10.1002/asia.201200568
67. Ohki Y, Sunada Y, Tatsumi K (2005) Synthesis of [2Fe–2S] and [4Fe–4S] clusters having terminal amide ligands from an iron(II) amide complex. Chem Lett 34:172–173. https://doi.org/10.1246/cl.2005.172
68. Hu Y, Ribbe MW (2013) Nitrogenase assembly. Biochim Biophys Acta Bioenerg 1827:1112–1122. https://doi.org/10.1016/j.bbabio.2012.12.001
69. Ribbe MW, Hu Y, Hodgson KO, Hedman B (2014) Biosynthesis of nitrogenase metalloclusters. Chem Rev 114:4063–4080. https://doi.org/10.1021/cr400463x
70. Ribbe MW, Hu Y, Guo M et al (2002) The Femoco-deficient MoFe protein produced by a *nifH* deletion strain of *Azotobacter vinelandii* shows unusual P-cluster features. J Biol Chem 277:23469–23476. https://doi.org/10.1074/jbc.M202061200
71. Lee CC, Blank MA, Fay AW et al (2009) Stepwise formation of P-cluster in nitrogenase MoFe protein. Proc Natl Acad Sci U S A 106:18474–18478. https://doi.org/10.1073/pnas.0909149106
72. Hu Y, Fay AW, Lee CC, Ribbe MW (2007) P-cluster maturation on nitrogenase MoFe protein. Proc Natl Acad Sci U S A 104:10424–10429. https://doi.org/10.1073/pnas.0704297104
73. Rupnik K, Lee CC, Hu Y et al (2018) A VTVH MCD and EPR spectroscopic study of the maturation of the "second" nitrogenase P-cluster. Inorg Chem 57:4719–4725. https://doi.org/10.1021/acs.inorgchem.8b00428
74. Wiig JA, Hu Y, Lee CC, Ribbe MW (2012) Radical SAM-dependent carbon insertion into the nitrogenase M-cluster. Science 337:1672–1675. https://doi.org/10.1126/science.1224603
75. Hu Y, Ribbe MW (2016) Biosynthesis of the metalloclusters of nitrogenases. Annu Rev Biochem 85:455–483. https://doi.org/10.1146/annurev-biochem-060614-034108
76. Sickerman NS, Ribbe MW, Hu Y (2017) Nitrogenase cofactor assembly: an elemental inventory. Acc Chem Res 50:2834–2841. https://doi.org/10.1021/acs.accounts.7b00417
77. Shah VK, Brill WJ (1977) Isolation of an iron-molybdenum cofactor from nitrogenase. Proc Natl Acad Sci U S A 74:3249–3253. https://doi.org/10.1073/pnas.74.8.3249
78. Burgess BK (1990) The iron-molybdenum cofactor of nitrogenase. Chem Rev 90:1377–1406. https://doi.org/10.1021/cr00106a002
79. McWilliams SF, Holland PL (2015) Dinitrogen binding and cleavage by multinuclear iron complexes. Acc Chem Res 48:2059–2065. https://doi.org/10.1021/acs.accounts.5b00213
80. Nishibayashi Y (2015) Recent progress in transition-metal-catalyzed reduction of molecular dinitrogen under ambient reaction conditions. Inorg Chem 54:9234–9247. https://doi.org/10.1021/acs.inorgchem.5b00881
81. Burford RJ, Fryzuk MD (2017) Examining the relationship between coordination mode and reactivity of dinitrogen. Nat Rev Chem 1:0026. https://doi.org/10.1038/s41570-017-0026
82. Wolff TE, Berg JM, Warrick C, Hodgson KO, Holm RH, Frankel RB (1978) The molybdenum-iron-sulfur complex $[Mo_2Fe_6S_9(SC_2H_5)_8]^{3-}$. A synthetic approach to the

molybdenum site in nitrogenase. J Am Chem Soc 100:4630–4632. https://doi.org/10.1021/ja00482a070
83. Kawaguchi H, Yamada K, Lang J, Tatsumi K (1997) A new entry into molybdenum/tungsten sulfur chemistry: synthesis and reactions of mononuclear sulfido complexes of pentamethylcyclopentadienyl–molybdenum(VI) and -tungsten(VI). J Am Chem Soc 119:10346–10358. https://doi.org/10.1021/ja971725e
84. Lang J, Ji S, Xu Q et al (2003) Structural aspects of copper(I) and silver(I) sulfide clusters of pentamethylcyclopentadienyl trisulfido tungsten(VI) and molybdenum(VI). Coord Chem Rev 241:47–60. https://doi.org/10.1016/S0010-8545(02)00309-0
85. Seino H, Arai Y, Iwata N et al (2001) Preparation of mononuclear tungsten Tris(sulfido) and molybdenum sulfido-tetrasulfido complexes with hydridotris(pyrazolyl)borate coligand and conversion of the former into sulfido-bridged bimetallic complex having Pt(μ-S)$_2$WS core. Inorg Chem 40:1677–1682. https://doi.org/10.1021/ic0008823
86. Hong D, Zhang Y, Holm RH (2005) Heterometal cubane-type WFe_3S_4 and related clusters trigonally symmetrized with hydrotris(3,5-dimethylpyrazolyl)borate. Inorg Chim Acta 358:2303–2311. https://doi.org/10.1016/j.ica.2004.11.051
87. Fomitchev DV, McLauchlan CC, Holm RH (2002) Heterometal cubane-type MFe_3S_4 clusters (M = Mo, V) trigonally symmetrized with hydrotris(pyrazolyl)borate(1–) and Tris(pyrazolyl) methanesulfonate(1–) capping ligands. Inorg Chem 41:958–966. https://doi.org/10.1021/ic011106d
88. Zheng B, Chen XD, Zheng SL, Holm RH (2012) Selenium as a structural surrogate of sulfur: template-assisted assembly of five types of tungsten-iron-sulfur/selenium clusters and the structural fate of chalcogenide reactants. J Am Chem Soc 134:6479–6490. https://doi.org/10.1021/ja3010539
89. Majumdar A, Holm RH (2011) Specific incorporation of chalcogenide bridge atoms in molybdenum/tungsten-iron-sulfur single cubane clusters. Inorg Chem 50:11242–11251. https://doi.org/10.1021/ic2018117
90. Christou G, Holm RH, Sabat M, Ibers JA (1981) A hexanuclear iron-sulfide-thiolate cluster: assembly and properties of $[Fe_6S_9(S\text{-}t\text{-}C_4H_9)_2]^{4-}$ containing three types of bridging sulfur atoms. J Am Chem Soc 103:6269–6271. https://doi.org/10.1021/ja00410a071
91. Christou G, Sabat M, Ibers JA, Holm RH (1982) A new structural type in iron-sulfide-thiolate chemistry: preparation, properties, and structure of the hexanuclear cluster $[Fe_6S_9(S\text{-}t\text{-}C_4H_9)_2]^{4-}$. Inorg Chem 21:3518–3526. https://doi.org/10.1021/ic00139a048
92. Henkel G, Strasdeit H, Krebs B (1982) $[Fe_6S_9(SCH_2C_6H_5)_2]^{4-}$: a hexanuclear iron–sulfur cluster anion containing the square–pyramidal [(μ_4–S)Fe_4] unit. Angew Chem Int Ed 21:201–202. https://doi.org/10.1002/anie.198202011
93. Strasdeit H, Krebs B, Henkel G (1984) Synthetic route to $[Fe_6S_9(SR)_2]^{4-}$ clusters (R = alkyl). Their spectroscopic and magnetic properties and the solid-state structures of $[Fe_6S_9(SCH_2Ph)_2]^{4-}$ and $[(Fe_6S_9(SMe)_2)_2Na_2]^{6-}$. Inorg Chem 9:1816–1825. https://doi.org/10.1021/ic00181a008
94. Strasdeit H, Krebs B, Henkel G (1987) Synthesis and characterization, and the X-ray structure of $(PhCH_2NEt_3)_4[Fe_6S_9(SMe)_2]$. Z Naturforsch 42b:565–572
95. Zhou H, Su W, Achim C, Rao PV, Holm RH (2002) High-nuclearity sulfide-rich molybdenum-iron-sulfur clusters: reevaluation and extension. Inorg Chem 41:3191–3201. https://doi.org/10.1021/ic0201250
96. Tanifuji K, Sickerman N, Lee CC, Nagasawa T, Miyazaki K, Ohki Y, Tatsumi K, Hu Y, Ribbe MW (2016) Structure and reactivity of an asymmetric synthetic mimic of nitrogenase cofactor. Angew Chem Int Ed 55:15633–15636. https://doi.org/10.1002/anie.201608806
97. Sickerman NS, Tanifuji K, Lee CC, Ohki Y, Tatsumi K, Ribbe MW, Hu Y (2017) Reduction of C_1 substrates to hydrocarbons by the homometallic precursor and synthetic mimic of the nitrogenase cofactor. J Am Chem Soc 139:603–606. https://doi.org/10.1021/jacs.6b11633
98. Xu G, Wang Z, Ling R, Zhou J, Chen X-S, Holm RH (2018) Ligand metathesis as rational strategy for the synthesis of cubane-type heteroleptic iron-sulfur clusters relevant to the FeMo cofactor. Proc Natl Acad Sci U S A 115:5089–5092. https://doi.org/10.1073/pnas.1801025115

99. Verma AK, Nazif TN, Achim C, Lee SC (2000) A stable terminal imide on iron. J Am Chem Soc 122:11013–11014. https://doi.org/10.1021/ja001147t
100. Chen X-D, Duncan JS, Verma AK, Lee SC (2010) Selective syntheses of iron-imide-sulfide cubanes, including a partial representation of the Fe-S-X environment in the FeMo cofactor. J Am Chem Soc 132:15884–15886. https://doi.org/10.1021/ja106478k
101. Chen XD, Zhang W, Duncan JS, Lee SC (2012) Iron–amide–sulfide and iron–imide–sulfide clusters: heteroligated core environments relevant to the nitrogenase FeMo cofactor. Inorg Chem 51:12891–12904. https://doi.org/10.1021/ic301868m
102. Ohki Y, Ikagawa Y, Tatsumi K (2007) Synthesis of new [8Fe-7S] clusters: a topological link between the core structures of P-cluster, FeMo-co, and FeFe-co of nitrogenases. J Am Chem Soc 129:10457–10465. https://doi.org/10.1021/ja072256b
103. Hashimoto T, Ohki Y, Tatsumi K (2010) Synthesis of coordinatively unsaturated mesityliron thiolate complexes and their reactions with elemental sulfur. Inorg Chem 49:6102–6109. https://doi.org/10.1021/ic100692v
104. Kaiser JT, Hu Y, Wiig JA et al (2011) Structure of precursor-bound NifEN: a nitrogenase FeMo cofactor maturase/insertase. Science 331:91–94. https://doi.org/10.1126/science.1196954
105. Fay AW, Blank MA, Lee CC et al (2011) Spectroscopic characterization of the isolated iron-molybdenum cofactor (FeMoco) precursor from the protein NifEN. Angew Chem Int Ed 50:7787–7790. https://doi.org/10.1002/anie.201102724
106. Hu Y, Fay AW, Ribbe MW (2005) Identification of a nitrogenase FeMo cofactor precursor on NifEN complex. Proc Natl Acad Sci U S A 102:3236–3241. https://doi.org/10.1073/pnas.0409201102
107. Ohta S, Ohki Y, Hashimoto T et al (2012) A nitrogenase cluster model $[Fe_8S_6O]$ with an oxygen unsymmetrically bridging two proto-Fe_4S_3 cubes: relevancy to the substrate binding mode of the FeMo cofactor. Inorg Chem 51:11217–11219. https://doi.org/10.1021/ic301348f
108. Rittle J, Peters JC (2013) Fe-N_2/CO complexes that model a possible role for the interstitial C atom of FeMo-cofactor (FeMoco). Proc Natl Acad Sci U S A 110:15898–15903. https://doi.org/10.1073/pnas.1310153110
109. Creutz SE, Peters JC (2014) Catalytic reduction of N_2 to NH_3 by an Fe–N_2 complex featuring a C-atom anchor. J Am Chem Soc 136:1105–1115. https://doi.org/10.1021/ja4114962
110. Ohki Y, Uchida K, Tada M, Cramer RE, Ogura T, Ohta T (2018) N_2 activation on a molybdenum-titanium-sulfur cluster. Nat Commun 9:3200. https://doi.org/10.1038/s41467-018-05630-6
111. Tanifuji K, Lee CC, Ohki Y, Tatsumi K, Hu Y, Ribbe MW (2015) Combining a nitrogenase scaffold and a synthetic compound into an artificial enzyme. Angew Chem Int Ed 54:14022–14025. https://doi.org/10.1002/anie.201507646
112. Tanifuji K, Lee CC, Sickerman NS, Tatsumi K, Ohki Y, Hu Y, Ribbe MW (2018) Tracing the 'ninth sulfur' of the nitrogenase cofactor via a semi-synthetic approach. Nat Chem 10:568–572. https://doi.org/10.1038/s41557-018-0029-4

Struct Bond (2019) 179: 63–100
DOI: 10.1007/430_2018_30

Published online: 6 February 2019

The Catalytic Mechanisms of the Molybdenum and Tungsten Enzymes

Andrew M. Crawford, Julien J. H. Cotelesage, Roger C. Prince, and Graham N. George

Contents

Abstract Molybdenum and tungsten are, respectively, the only second and third transition metal ions with well-defined functions in living organisms and with a single exception are found in association with a novel pyranopterin dithiolene cofactor called molybdopterin. This review focusses on the catalytic mechanisms

A. M. Crawford, J. J. H. Cotelesage, and G. N. George (✉)
Molecular and Environmental Sciences Group, Department of Geological Sciences, University of Saskatchewan, Saskatoon, SK, Canada
e-mail: g.george@usask.ca

R. C. Prince
Stonybrook Apiary, Pittstown, NJ, USA

of the molybdenum and tungsten enzymes, with an emphasis on the molybdenum and tungsten sites. Most, but not all, of the enzymes catalyze oxygen atom transferase redox chemistry, with the metal cycling between M(VI) and M(IV) formal oxidation states during the catalytic cycle. We discuss the range of reactions and what is known of mechanism for both oxo-transferase and non-oxo-transferase molybdenum and tungsten enzymes.

Keywords Molybdenum enzyme · Oxygen atom transferase · Tungsten enzyme

1 Introduction

This review will discuss the catalytic mechanisms of the molybdopterin-based molybdenum and tungsten enzymes. Molybdenum and tungsten are unique as the only second and third transition elements whose compounds play catalytic roles in biological systems [1]. We note in passing that cadmium plays roles in specific carbonic anhydrases from marine algae [2] but because Cd^{2+} is $4d^{10}$, like $3d^{10}$ Zn^{2+}, it is not formally a transition metal ion and we therefore exclude it. Tungsten is also distinguished by being the heaviest element with a known biological role. Apart from nitrogenase, which is distinct from all other Mo-containing enzymes [3, 4], all Mo and W enzymes contain either one or two pyranopterin dithiolene cofactors, known as molybdopterin, which chelates the metal through the dithiolene group. In order to distinguish the enzymes from nitrogenase, the enzymes have often been referred to as the mononuclear Mo or W enzymes [5]. The structure of the molybdenum cofactor, molybdopterin bound to molybdate, is shown in Fig. 1 in the fully reduced tetrahydro form. The molybdopterin cofactor can be found in ring-closed tricyclic or ring-open bicyclic tautomers (Fig. 2), and for *E.coli* dissimilatory nitrate reductase, two different crystal structures have been reported, one clearly showing a tricyclic molybdopterin [6] and the other a bicyclic ring-open form [7], and the

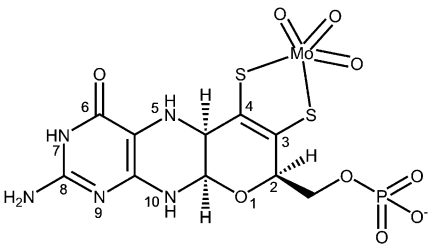

Fig. 1 Schematic structure of the molybdenum cofactor, molybdopterin. One of the structures postulated for the cofactor prior to insertion into the target enzyme is shown, with the pterin ring in the tetrahydro redox state. In the protein the phosphate can be free as shown (molybdopterin or MPT) or attached to guanosine (molybdopterin guanine dinucleotide or MGD) or cytosine (molybdopterin cytidine dinucleotide or MCD)

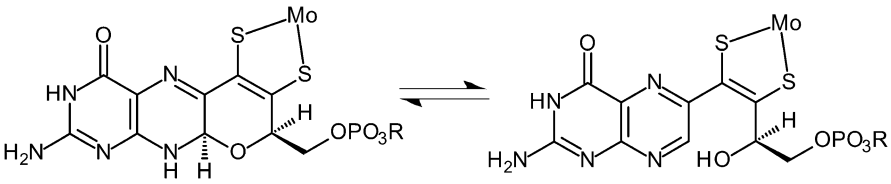

Fig. 2 Structure of ring-closed tricycle and ring-open bicycle molybdopterin, shown for the dihydro molybdopterin oxidation state

ring-open form has also been observed for ethylbenzene dehydrogenase [8]. Recent model compound studies have observed both ring-open and ring-closed forms [9]. Simple density functional theory calculations reveal that in the absence of protein, for the dihydro oxidation state, the ring-open form of molybdopterin is expected to be thermodynamically preferred, whereas for the tetrahydro form, the ring-closed form is more stable [10].

The field of molybdenum and tungsten enzymes has developed very rapidly; in the early 1970s, a total of six molybdenum enzymes were known [11], and while one tungsten enzyme had been reported [12]; it was not until 1992 that the tungsten enzymes were recognized as closely related to the mononuclear molybdenum enzymes [13]. Since this early work, a very large number of both molybdenum and tungsten enzymes have been discovered and characterized, and much is now known about their evolution, their biochemistry, and their catalytic mechanisms.

With some notable exceptions (Sect. 6), the mononuclear Mo and W enzymes catalyze two-electron redox reactions in which the metal cycles between formally M^{4+} and M^{6+} oxidation states with an oxygen atom from water being transferred either from or to substrate via the metal atom, according to the following stoichiometry:

$$E - Mo^{6+} + R + H_2O \leftrightarrow E - Mo^{4+} + R - O + 2H^+ \quad (1)$$

Thus, the vast majority of the enzymes either form or break bonds between oxygen and carbon, with, respectively, the source or destination of the oxygen being water. Many of the enzymes possess multiple redox-active groups that appear to form an electron transfer chain within the protein, linking the oxidative and reductive half-reactions. An example is shown in Fig. 3, that of xanthine oxidase. The Mo site converts the substrate; in this case xanthine is oxidized to uric acid via reduction of the Mo site by two electrons, from Mo(VI) to Mo(IV). Reducing electrons then equilibrate through intramolecular electron transfer to the different acceptor sites within the protein [14] (Figs. 3 and 4). The redox behavior of such multi-redox site enzymes can be complex, for example, each xanthine oxidase monomer can accept up to 6 electrons, 2 at Mo, 1 at each of the 2 FeS clusters, and 2 at the flavin site, giving a total of 36 possible redox states ranging from fully oxidized to six-electron-reduced enzyme [14]. In xanthine oxidase the electrons from the oxidation of xanthine are finally accepted through two one-electron

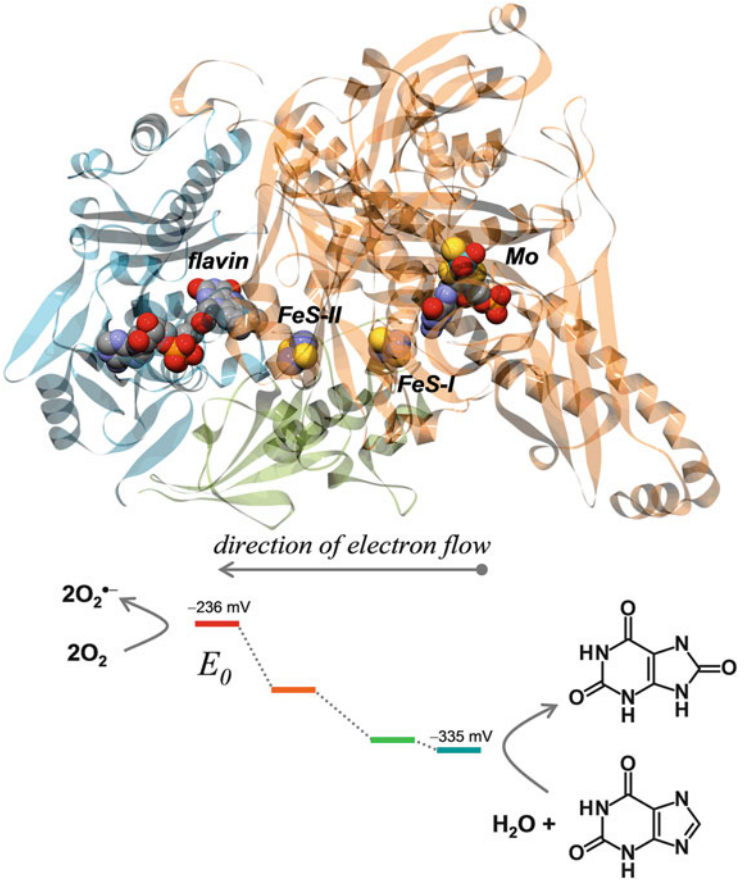

Fig. 3 Structure and large-scale catalytic mechanism of xanthine oxidase. At top is shown the crystal structure (pdb code 1F1Q) with the redox-active components depicted with CPK models. Below is shown both the oxidative half-reaction in which xanthine is converted to uric acid and the reductive half-reaction in which oxygen is converted to superoxide

reductions of dioxygen to form the superoxide radical anion, $O_2 \cdot^-$. In enzymes that have two molybdopterin dithiolenes coordinated to molybdenum or tungsten, in most cases, one of the molybdopterins is positioned approximately between the molybdenum/tungsten site and an adjacent iron-sulfur cluster, and this is referred to as the *proximal* or sometimes the P molybdopterin, while the other is called the *distal* or the Q molybdopterin (Fig. 4). As has been previously discussed, the redox state of the pterin probably cannot be distinguished by crystallography, at least at poorer crystallographic resolutions [1], although the ring-open and ring-closed forms appear unambiguous [1, 6–8]. The pterin in the oxidized dihydro redox state, which has a more planar structure than the other redox states, has been suggested

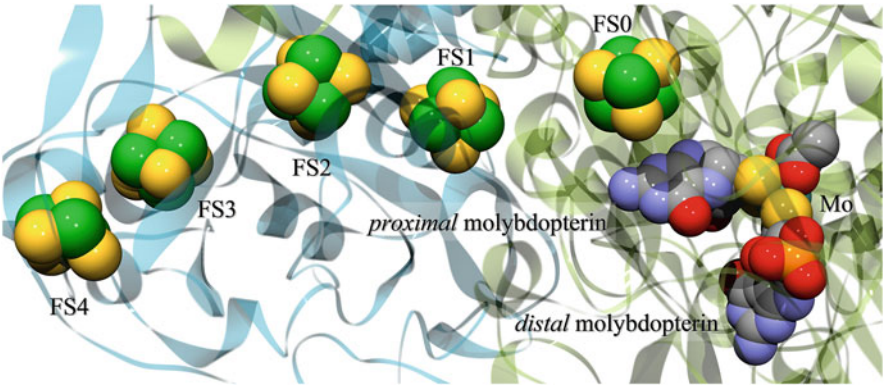

Fig. 4 Distal and proximal molybdopterin in *Escherichia coli* nitrate reductase. The proximal molybdopterin lies between the Mo and the first iron-sulfur cluster, FS0. Iron atoms are shown in green, sulfur in yellow, oxygen in red, carbon in gray, and nitrogen in blue. The string of five irons sulfur clusters is thought to act as an electron conduit to the Mo site

to direct electron transfer from the Mo site to the next acceptor in the protein, rather like an electrical wire [15].

This review will focus primarily on the mechanisms that are thought to operate at the molybdenum and tungsten sites themselves, such as the reductive half-reaction of xanthine oxidase (Fig. 3). We will discuss some aspects of electron transfer but will neglect the parts of the catalytic processes that do not directly involve the molybdenum or tungsten.

The Mo/W enzymes are a very widespread group, playing important roles in all kingdoms of life [1], and are likely very ancient [1, 16]. The enzymes fulfill diverse roles, ranging from microbial respiration (e.g., the dissimilatory nitrate reductases), through the uptake of nitrogen in green plants (e.g., the assimilatory nitrate reductases), to important roles in human health (e.g., sulfite oxidases) and drug metabolism (e.g., aldehyde oxidase). At the time of writing, only five examples of Mo/W enzymes are known to occur in eukaryotes, and all are molybdenum enzymes: sulfite oxidase, nitrate reductase, xanthine oxidase/dehydrogenase (counted as a single enzyme), aldehyde oxidase, and the recently discovered mitochondrial amidoxime reducing component (mARC). In contrast the prokaryotes present a vast array of both Mo and W enzymes, including homologues of the eukaryotic enzymes mentioned above, and a great many others besides. The enzymes are divided into three broad families according to their oxidized Mo(VI) active site structures and are named for the best-studied members of each family [16]: the sulfite oxidase family, the xanthine oxidase family, and the dimethyl sulfoxide (DMSO) reductase family. Within each family there is considerable diversity, both in terms of the active site structure and in the details of the catalytic mechanisms. Our knowledge of the active sites and mechanisms of the enzymes derives from ground-breaking crystallographic work, plus numerous spectroscopic studies of the metal sites of the proteins [17].

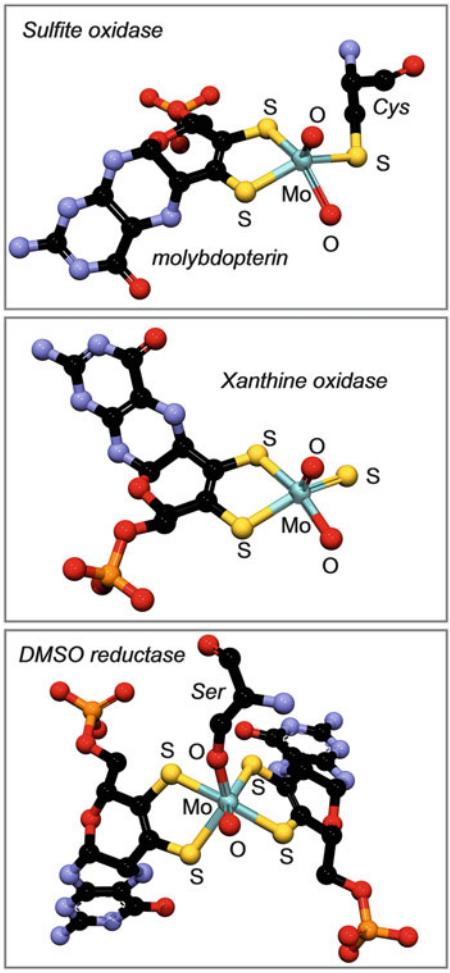

Fig. 5 Structures of the active sites in the oxidized Mo(VI) form of the prototypical members of the three families of enzymes. The structures shown are from crystallographic results (pdb codes 1SOX, 1F1Q and 1EU1, for sulfite oxidase, xanthine oxidase, and DMSO reductase, respectively), modified based on XAS data [17] to account for photoreduction, when present. For 1EU1 only the conformer model corresponding to the active enzyme is shown

The oxidized Mo(VI) active site structures of the prototypical members of each family are shown in Fig. 5:

- The sulfite oxidase family includes, in addition to the sulfite oxidases themselves [18, 19], the nitrate reductases of fungi and green plants [20], a number of prokaryotic sulfite dehydrogenases [21, 22], and the mitochondrial amidoxime reducing component (mARC) [23]. Members of the family have a single molybdopterin dithiolene and possess a cysteine thiolate coordination of molybdenum, with a *cis*-dioxo Mo(VI) making up the total five-coordinate metal site (Fig. 5).
- The xanthine oxidase family [24, 25] includes the aldehyde oxidases [26] plus a number of exotic members, in particular carbon monoxide dehydrogenases which contains a novel Mo/Cu binuclear active site [27, 28] and nicotinate

dehydrogenases which contain Mo = Se coordination in the oxidized enzyme [29, 30]. Like sulfite oxidase, members of the xanthine oxidase family are five-coordinate in the oxidized form. The metal lacks a coordinating amino acid and has a structure that is either *cis*-dioxo-thio $Mo(=O)_2 = S$ at high pH or mono-oxo-thio Mo(OH)(=O) = S at low pH [24] (Fig. 5).

- The DMSO reductase family is by far the most diverse and abundant family, containing a wide range of molybdenum enzymes, and all of the tungsten enzymes thus far discovered. All DMSO reductase family members contain two molybdopterins associated with the metal, with many but not all family members possessing a terminal oxo ligand to the metal and a coordinating amino acid. The DMSO family is thus further split into three main active site structural categories based on the coordinating amino acid. Type 1 possesses metal coordinated to either a cysteine or selenocysteine, Type 2 to an aspartate, and Type 3 to a serine. Figure 5 shows the active site of *Rhodobacter sphaeroides* DMSO reductase [31, 32] which is a Type 3 member. Many DMSO reductase family members might more properly be assigned to families of their own, because examples exist where no amino acid is bound to Mo or W [33], or the oxidized active site is apparently a *des*-oxo species.

The tungsten enzymes are alternatively allocated to a fourth family, the AOR family, named for *Pyrococcus furiosus* aldehyde oxidoreductase [13, 33]. This enzyme is still, however, incompletely characterized [17], and as there is greater structural variation in the accepted members of the DMSO reductase family, we choose to include the tungsten enzymes in that group. The tungsten enzymes are still relatively under-studied, so our review will focus on the molybdenum enzymes and where relevant point out possible parallels and examples from the tungsten enzymes.

2 Oxygen Atom Transferase Chemistry

Oxygen atom transferase activity is by far the most common activity among the molybdenum and tungsten enzymes. The exceptions are the molybdenum- and tungsten-containing formate dehydrogenases (Sect. 6.1), the molybdenum-containing pyrogallol transhydroxylases (Sect. 6.3), and the tungsten-containing acetylene hydratases (Sect. 6.2) and benzoyl co-A dehydrogenases (Sect. 6.4). These enzymes are discrete from the mainstream, are novel in their own right, and will be discussed in Sect. 6.

2.1 Spectator Oxo Effects

The enzymes that possess a *cis*-dioxo oxidized Mo(VI) active site may take advantage of what has been called the “spectator oxo effect” [34] to help drive

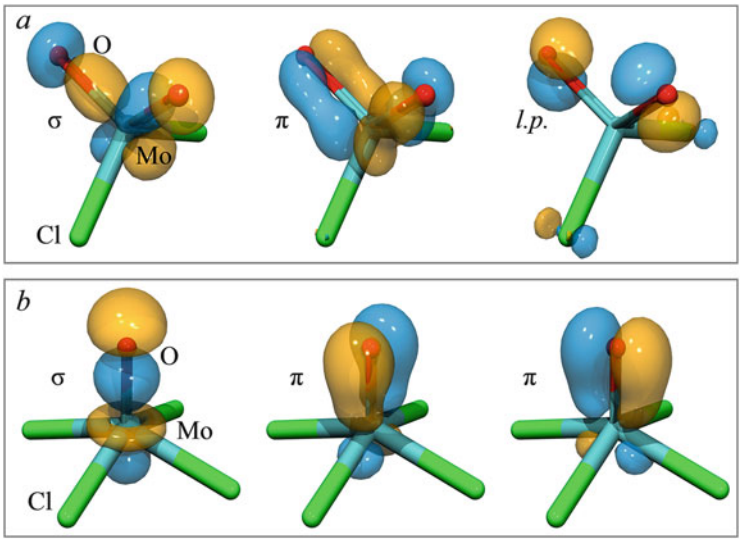

Fig. 6 Molecular orbitals for two simple examples, following [34]. (**a**) shows molecular orbitals for the hypothetical Mo(VI) system $[MoO_2Cl_2]$ showing σ and π, and the oxygen lone pair (*l.p.*), (**b**) shows molecular orbitals for the Mo(IV) species $[MoOCl_4]^{2-}$, a σ bond and two d-p π bonds, constituting the Mo ≡ O triple bond

the catalytic reaction. Here, the spectator oxo is an additional terminal oxygen atom bound to molybdenum that is not directly involved in oxygen atom transfer activity and remains after catalytic oxygen atom transfer. In *cis*-dioxo Mo (VI) species, both of the oxygens form Mo = O double bonds, with each comprised of a σ bond and a π-bond, and a non-bonding lone pair remaining on the oxygen (Fig. 6). In the monooxo Mo(IV) species, the oxygen forms a Mo ≡ O triple bond involving two electrons in 4d orbitals from the metal and four from the oxygen to give a σ bond and two π-bonds (Fig. 6). Such triple bonds cannot form in *cis*-dioxo Mo(VI) species because the use of two π-orbitals to make a triple bond would deprive the other oxygen of a d-orbital for its d-p π bond (Fig. 6). The bond strength of this Mo ≡ O triple bond with the spectator oxo is thought to act as a thermodynamic driver for oxygen atom transferase chemistry [34]. Numerous examples of *cis*-dioxo Mo(VI) and W(VI) enzymes are known, and specific examples of these will be discussed below.

2.2 *Non-spectator Oxygen Atom Transferase*

Spectator oxo effects are undoubtedly part of the overall picture but only make sense as thermodynamic drivers for oxygen transfer from metal to substrate and not the reverse. It is noteworthy that both molybdenum and tungsten show remarkable

flexibility in their coordination chemistry. Thus, searching the Cambridge structure database [35] gives a total of 374 sulfur-coordinated Mo(VI) compounds, of which 95 are des-oxo Mo(VI) species, 61 are monooxo species, 215 are *cis*-dioxo, and 3 are *cis*-trioxo Mo(VI) species. Tungsten shows similar flexibility in its coordination chemistry, with a total of 225 entries with sulfur-coordinated W(VI), comprised of 141 des-oxo, 54 monooxo, 27 *cis*-dioxo, and 3 *cis*-trioxo. At the time of writing, trioxo active sites are only known for mutant enzymes [36–38], but there are many examples of all the other categories of oxygen coordination. For now, we note that enzymes engaging in oxo atom transferase activity are expected to possess at least one terminal oxygen in the high-valent state, and the exceptions appear to be those enzymes that do not engage in such chemistry.

3 The Roles of Molybdopterin

Since the first structural information on molybdopterin began to emerge in 1982 [39], there have been suggestions of possible roles for molybdopterin beyond anchoring the active site within the protein [40]. In this section we will discuss current thinking on the roles that molybdopterin might play in the catalytic mechanism of the enzymes.

3.1 Molybdopterin in Electron Transfer

The first evidence that molybdopterin might function as an electron conduit for intramolecular electron transfer came from the initial crystal structures of molybdenum and tungsten enzymes [33, 41]; in particular this was suggested for the aldehyde oxidoreductase from *Desulfovibrio gigas*, a member of the xanthine oxidase family [41]. The notion that enzymes with two molybdopterins might show differential functions for the two cofactors, one acting as an electron conduit and the other to fine-tune the active site properties, was first suggested by Johnson and co-workers [42]. This work was subsequently expanded upon by Rothery et al. [15], with the suggestion that the molybdopterin acting as an electron conduit might be in the dihydro oxidation state and the other in the tetrahydro oxidation state. These workers have argued that the crystallographic results can be used to readily distinguish the different molybdopterin oxidation states. This was based on an alignment of DFT geometry-optimized structures at the relatively rigid aminopyrimidinone end of the cofactor, which showed large relative displacements of the other end (the pyranodithiolene) for the different oxidation states [15]. However, if the structures are aligned based on the entire molybdopterin structure, and not just one end, then the differences do not seem as marked. As we have previously noted [1], the resolution of many of the protein crystal structures may be insufficient to distinguish

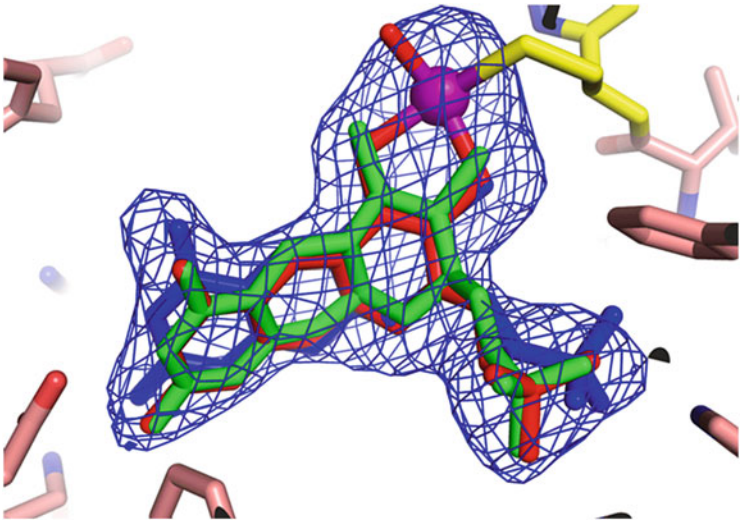

Fig. 7 Pterin redox state vs. fit to electron density. A difference map contoured at 3σ calculated using the modified coordinates (molybdopterin removed) and structure factors of *Pichia angusta* (now called *Ogataea angusta*) nitrate reductase (pdb code 2bih). The three redox isoforms of molybdopterin (shown in red, green, and blue) can all plausibly fit the electron density

the structural differences of the different molybdopterin redox states (Fig. 7), and at present there is reason for cautious skepticism about these deductions.

Kirk and co-workers have discussed the case of dithiolene coordination in enzymes with a single Mo ≡ O [43]; this group will serve to define the axial direction and orient the Mo $4d_{xy}$ redox-active orbital for maximal interaction with in-plane dithiolene sulfur p-orbitals (Fig. 8), yielding effective regeneration of the reduced enzyme following oxygen atom transfer. This role of a terminal oxo in facilitating electron transfer via the molybdopterin dithiolene has been referred to as the oxo-gate hypothesis [43].

We now turn to the effects of protein upon the molybdopterin and the effect that this might have on the metal site and, in turn, upon mechanisms of catalysis.

3.2 The Pterin Twist Hypothesis

As discussed above and in previous work [1, 17, 44], the bulky molybdopterin enfolded in the protein is expected to restrict the motions of the ligands around the metal site, and neglect of such effects is a weakness of some early computational chemistry [44, 45]. Figure 9 shows the *bis*-molybdopterin (molybdopterin guanine dinucleotide, MGD) enfolded within the polypeptide of DMSO reductase, clearly illustrating that the forces exerted by the protein must impact the coordination environment around molybdenum. Recent work on arsenite oxidase illustrates this

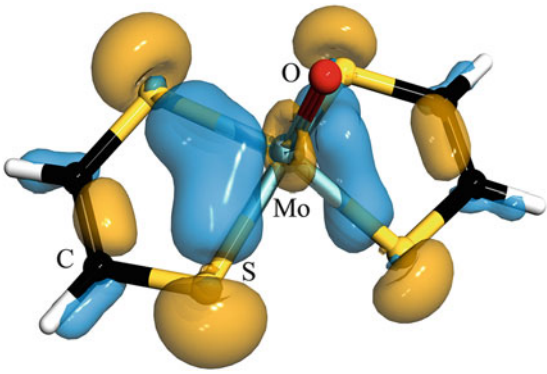

Fig. 8 Calculated molecular orbitals for an asymmetrically bound hypothetical Mo (V) dithiolene complex, as discussed by Kirk and co-workers [43], depicting the pseudo-σ interaction between Mo $4d_{xy}$ and in-plane S 3p orbitals that may facilitate electron transfer

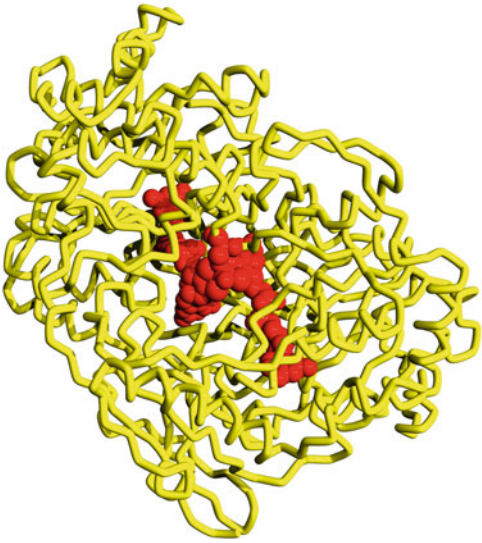

Fig. 9 Structure of DMSO reductase [pdb code 1EU1] showing the *bis*-molybdopterin MGD coordinated Mo site in red CPK (only the active conformer model is shown), with the polypeptide chain shown in yellow. The cofactor can be seen to be effectively enfolded by the protein, which is expected to restrict coordination geometry of the ligands at the metal site

point nicely, with a hypothesis called the pterin twist hypothesis [46]. The basic idea is that the polypeptide acts to distort the active site to a conformation that approaches the transition state. We will discuss this enzyme more fully below, but, in brief, the observed structure of the oxidized Mo(VI) active site appears to be distorted by the protein exerting a twist on the dithiolene by up to 55 kJ mol^{-1} above the low-energy conformation of an isolated active site [46] (Fig. 10). The proposed distortion can be expressed as a function of a single variable (a twist angle φ; Fig. 10) and is a variant of the Rây-Dutt twist of classical coordination chemistry which is used to understand racemization of six-coordinate *tris*-chelate complexes [47, 48]. To date, none of the crystal structures determined for molybdenum enzymes which conduct oxo-transferase chemistry show simple octahedral-type geometry, suggesting that all show some tuning of the active site by the protein and molybdopterin. We note that for systems that have ring-open molybdopterin, these mechanisms will be

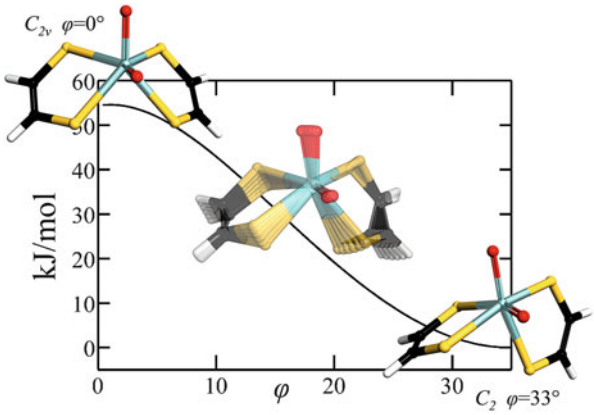

Fig. 10 Computed effects of a pterin twist, φ, between extremes defined by point group symmetry; C_{2v} for $\varphi = 0°$ and C_2 for $\varphi = 33°$. The geometry in the enzyme [46] is deduced to be close to $\varphi = 0°$ which elevates the energy above the minimum by ~55 kJ mol^{-1}. The centrally placed superimposed structures show the transformation from $\varphi = 0°$ to $\varphi = 33°$

inactive, because without the furan ring the pterin moiety can rotate relative to the dithiolene about the C_4–C_{4a} bond (see ring numbering Figs. 1 and 2).

4 Reliability of Structural Information

Before we turn to considering the enzymes themselves, we will briefly consider some problems with the structural methods that we rely on for our insights into mechanism. Essentially the sources of all quantitative structural information can be divided into spectroscopy and crystallography. For spectroscopy a detailed review has been recently reported [17]. Methods such as electron paramagnetic resonance (EPR) and its derivatives and vibrational spectroscopies such as resonance Raman and Fourier transform infrared spectroscopy can provide insights into metal ion coordination, and a major problem with all of these relates to confidence that the bulk of the sample is being investigated. For example, with EPR, only the paramagnetic Mo(V) form is being probed, and EPR gives no direct information at all upon the oxidized Mo(VI) or the fully reduced Mo(IV) forms. X-ray absorption spectroscopy provides access to all oxidation states, but analysis and in particular over-interpretation of data can mislead researchers, as we have discussed previously [17]. For crystallography, multiple occupancies of active sites within a near-identical polypeptide fold have misled researchers [17] (see Sect. 5.3), and the identity of some atoms has posed challenges in other studies, for example, with copper being mistaken for selenium [49], with consequent incorrect conclusions about the mechanism [14]. A major problem with almost all of the crystal structures of molybdenum and tungsten enzymes is photoreduction [50–52]. This occurs when X-ray-induced photochemical scission of water, or other components of the sample, produces energetic free radical species, such as hydrated electrons and hydroxyl radicals. The former are strong reductants and the latter are potent oxidants, and while most photochemical products recombine to form starting materials and heat, a proportion

can react with other components of the sample. The photoreduction of redox-active metals is substantially exacerbated by crystallographic cryoprotectants such as polyethylene glycols or glycerol [52]. This is because these species are very effective hydroxyl radical scavengers, leaving an excess of highly reducing hydrated electrons that can act upon the redox-active metal sites [52]. The same compounds that are added as cryoprotectants in crystallography are also commonly used as glassing agents for X-ray absorption spectroscopy to prevent artifacts due to crystalline ice diffraction [53]. While X-ray absorption spectroscopy is also susceptible to photoreduction, the sensitivity of the near-edge region to electronic structure means that this is usually detected [51, 52]. Moreover, the high energy of the X-ray beam at the Mo K-edge means that X-ray diffraction from any ice occurs at sufficiently low Bragg angles that ice diffraction artifacts are not registered by the detector; hence there is no need to add glassing agents, and the tendency for photoreduction is therefore much reduced [52]. While photoreduction of active sites was not recognized as such in some of the early crystallographic work on the Mo and W enzymes, crystallographers are increasingly aware of these issues, and a photoreduced active site is unlikely to be viewed as oxidized in any modern work.

5 The Enzymes

5.1 The Sulfite Oxidase Family

5.1.1 The Sulfite Oxidases

These enzymes catalyze the oxidation of sulfite to sulfate:

$$SO_3^{2-} + H_2O \rightarrow SO_4^{2-} + 2H^+ + 2e^- \quad (2)$$

As discussed above, these enzymes possess *cis*-dioxo Mo(VI) sites. Like most molybdenum and tungsten enzymes, nearly all structures of sulfite oxidases and sulfite dehydrogenases show clear signs that the enzyme has been photoreduced in the X-ray beam. The only exceptions are enzymes with site-directed mutations [36] that render the molybdenum site very difficult to reduce [37, 38]. Our understanding of the active sites and the catalytic mechanism has been derived from a combination of crystallographic and spectroscopic methods [17, 54]. The active site of sulfite oxidases from animals and plants, and the bacterial sulfite dehydrogenases have been studied by a variety of methods, including X-ray absorption spectroscopy, X-ray crystallography, and, with the $4d^1$ Mo(V) form, electron paramagnetic resonance and its derivative methods such as electron nuclear double resonance and electron spin echo envelope modulation [17].

Sulfite oxidases are found in both plants and animals. In mammals the enzyme is essential for health as it is part of the pathway for cysteine catabolism, and individuals possessing mutant sulfite oxidase with partial activity show buildup of abnormal

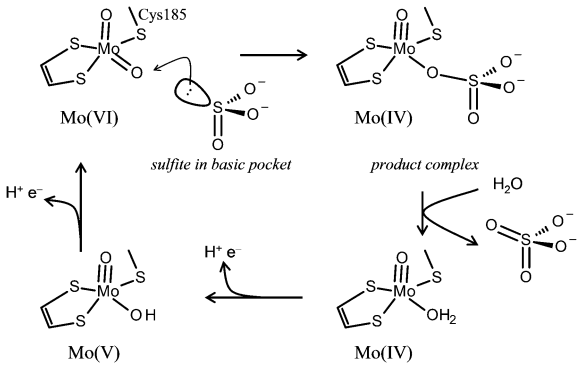

Fig. 11 Simplified sulfite oxidase oxidative half-reaction catalytic mechanism. The initial Mo (VI) enzyme is reduced to the Mo(IV) by substrate, with water subsequently liberating product. Mo (V) EPR signals corresponding to the product complex have been observed with the competitive inhibitors phosphate and arsenate (see Ref. [17])

sulfur metabolites, very severe neurological impairment, and usually death in utero or in infancy [55–57]. Residing in the mitochondrial inner-membrane space, the enzyme is dimeric with a subunit mass of about 52,000 with each monomer possessing molybdenum associated with one molybdopterin and a cytochrome b_5 iron-heme. Plant sulfite oxidases show considerable similarity at the molybdenum site, but lack the heme, and thus are the simplest of the eukaryotic molybdenum enzymes. The crystal structures of sulfite oxidases reveal a number of highly relevant details of the active site structure. The first sulfite oxidase crystal structure reported was that of the chicken enzyme [18], which was crystallized in the presence of sulfate. The structure showed two basic arginine-rich anion-binding pockets near the molybdenum site, at approximately 5 Å and 10 Å from Mo, both with sulfate bound, which serve to channel and locate substrate within the active site [18]. The electron density observed crystallographically at the 5 Å pocket was most consistent with mixed sulfite/sulfate occupancy in the pocket [18], with the three sulfite oxygen atoms oriented away from Mo so that the sulfur lone pair would point in the direction of the equatorial Mo = O oxygen, orienting the substrate correctly for catalytic oxygen atom transfer. The attack of the sulfite lone pair on this equatorial oxo ligand has been suggested to result in population of a Mo–O d_{xy}-pπ antibonding orbital, which in turn has been hypothesized to labilize the equatorial oxygen atom for transfer to substrate [58]. It has also been suggested that other aspects of the active site might fine-tune properties, specifically that the O_{oxo}–Mo–S–C(Cys) torsion angle is important in controlling overlap between a cysteine sulfur p-orbital and one of the two Mo = O π^* orbitals, with consequent activation of the oxo for transfer to substrate [59]. Figure 11 summarizes current views of the sulfite oxidase catalytic mechanism at the molybdenum site.

5.1.2 The Nitrate Reductases

The assimilatory plant and fungal nitrate reductases are very closely related to the sulfite oxidases and quite discrete from the dissimilatory nitrate reductases of prokaryotes.

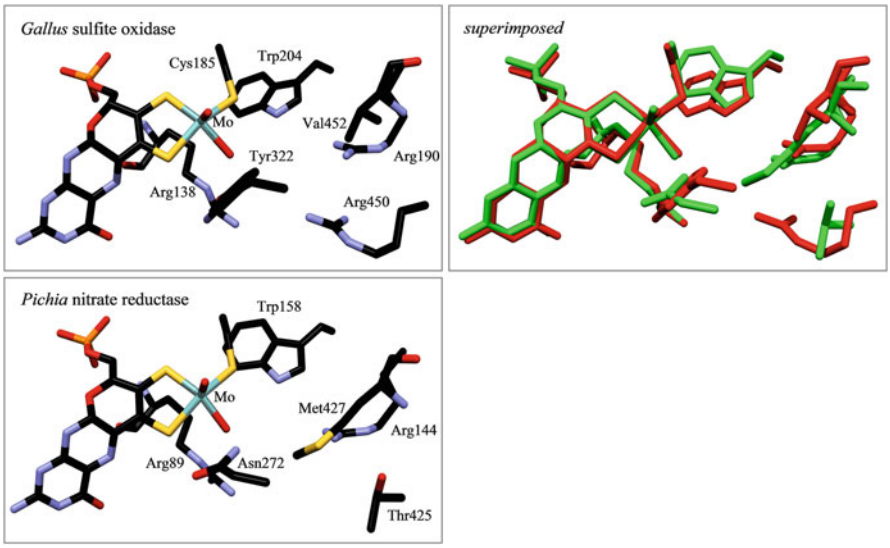

Fig. 12 Comparison of active sites of chicken sulfite oxidase (pdb code 1SOX) and yeast nitrate reductase (pdb code 2BII), together with a superposition showing sulfite oxidase (red) vs. nitrate reductase (green)

They catalyze the conversion of nitrate to nitrite, which is a key part of the nitrogen cycle:

$$NO_3^- + 2H^+ + 2e^- \rightarrow NO_2^- + H_2O \quad (3)$$

This reaction is known as the reductive half-reaction of nitrate reductase. Like the animal sulfite oxidases, plant and fungal nitrate reductases possess molybdenum and cytochrome b_5 and share structural features [60], with very similar oxidized Mo (VI) and reduced Mo(IV) active site structures [17, 61]. In addition the enzymes contain a flavin adenine dinucleotide (FAD) cofactor that serves to provide electrons to the cytochrome b_5 and molybdenum sites. The source of reduction of FAD is either NADH or NADPH; NADH-specific forms exist in higher plants, whereas NADPH-specific enzymes are found in some fungi. Bi-specific forms that can accept electrons from either NADPH or NADH are found in various plant and fungal species [62]. The structure of the nitrate reductase from the methylotrophic yeast *Pichia angusta* (now called *Ogataea angusta*) has been reported [60] and shows a basic substrate pocket ~5 Å from molybdenum homologous to that found in sulfite oxidase, but, with one fewer arginine, consistent with the lower charge on both substrate and product [60]: $[NO_3]^-$ vs. $[SO_3]^{2-}$. Yeast nitrate reductase and chicken sulfite oxidase (both alas with photoreduced Mo sites) are compared in Fig. 12. The nitrate reductase possesses two rather than three arginine residues in the substrate binding pocket of the active site, plus a highly conserved methionine (Met427) that is needed for activity. Other differences include an asparagine residue in place of a

tyrosine (Fig. 12). In an elegant demonstration of the close relationship between the two enzymes, a triple site-directed sulfite oxidase mutant (Tyr322 → Asn, Arg450 → Met, Val452 → Met) has been constructed to successfully convert sulfite oxidase into a nitrate reductase [63], with all three substitutions required to maximize activity [63]. As shown in Fig. 12, the structures of the molybdenum sites themselves are very similar indeed, with no substantive difference between the aforementioned O_{oxo}–Mo–S–C(Cys) torsion angle [59]. Given that one enzyme is an oxidase and the other a reductase, it seems unlikely that the postulated tuning using the cysteine torsion angle is important in the catalysis of either.

5.1.3 Mitochondrial Amidoxime Reducing Component

Quite recently a previously unknown eukaryotic molybdenum enzyme was reported [64], which is now thought to be part of the sulfite oxidase family [65]. This enzyme was named mARC (mitochondrial amidoxime reducing component) for its ability to reduce N-hydroxylated species, such as some amidoxime prodrugs into their active amino form drugs. At the time of writing, mARC is only the fifth eukaryotic molybdenum enzyme known and perhaps the simplest as it possesses only a molybdenum site. Both plant and animal mARC enzymes have been reported, and all known mammalian genomes contain two different mARC genes: *MARC1* and *MARC2* with the two enzymes known as mARC-1 and mARC-2, respectively. In general mARCs have broad substrate specificity, and the biochemical roles they play are still emerging [65, 66]. In addition to the amidoxime reductase activity already mentioned, the mARC enzymes are able to reduce a range of N-hydroxylated compounds, such as 6-N-hydroxylaminopurine to adenine, as well as nitrite to the cardiovascular-signaling molecule nitric oxide (NO). While the study of these enzymes is still in its infancy, and the active sites remain poorly characterized with only preliminary XAS and magnetic resonance reported to date [67, 68], there is no doubt that more work will follow [69, 70] to give important details about these intriguing enzymes.

We now turn to a quite different aspect of the sulfite oxidase mechanism. Although our primary focus in this review are the mechanisms specific to the molybdenum or tungsten active sites, the electron transfer between molybdenum and heme in sulfite oxidase proved something of a conundrum. Since it involves Mo active site components, we will discuss it briefly here. The first sulfite oxidase crystal structure [18] showed a long-range Mo···Fe distance of 32 Å, which is surprisingly large given the reported rapid rates of electron transfer between these two sites [71]. Moreover, the molybdopterin was observed to point away from the cytochrome b_5 heme, the least favorable orientation if this heterocycle was involved in electron transfer [18]. It was later suggested that the cytochrome domain, connected to the molybdenum by a flexible peptide, was mobile in solution and would reorient, docking with the Mo domain for effective electron transfer [71], with the observed conformation in the crystal structure being due to crystal packing forces. Subsequent molecular mechanics indicated that such domain motion was possible, although this study, which had

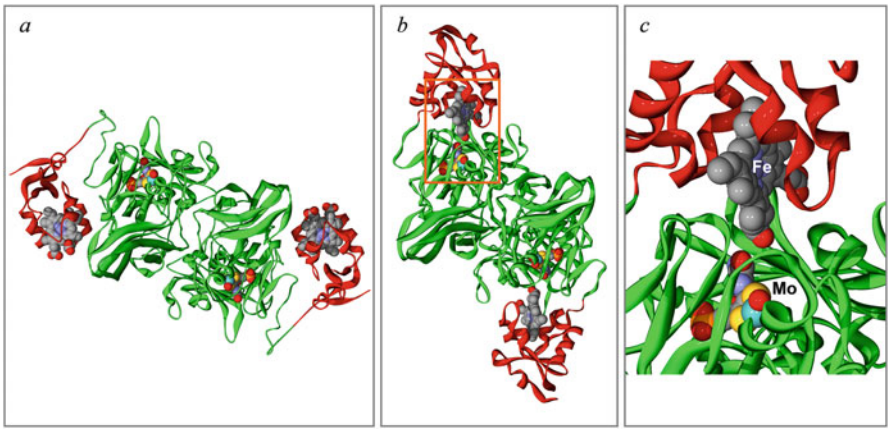

Fig. 13 Sulfite oxidase domain motion (**a**) shows the crystallographically observed homodimer with cytochrome domains (red) and Mo domains (green) oriented unfavorably for electron transfer between Mo and Fe. The postulated "docked" relocation of the cytochrome domains is shown in (**b**) with the detail of the hypothetical situation of Mo and Fe sites in (**c**) (corresponding to the orange box in **b**)

no imposed constraints or restraints, failed to show the specific docking that had been postulated [72]. Figure 13 shows schematic diagrams of the different domain arrangements. Subsequent *steered* molecular mechanics calculations did suggest a docked structure suitable for electron transfer [73], but a later electron-electron double resonance study of solution samples containing both Mo(V) and Fe(III) again indicated a Mo···Fe separation of 32 Å [74], strikingly the identical distance that had been determined by crystallography [18]. Added to this were results indicating that some of the amino acid residues of the Mo site were important for efficient electron transfer between iron and molybdenum [75]. Of particular note is the effect of the clinical mutation Arg160 → Gln, corresponding to Arg138 → Gln in chicken sulfite oxidase (Fig. 12). This mutation gave a three order of magnitude increase in the K_m for sulfite [18] and substantially poorer intramolecular rates of electron transfer [76]. Recently structural information on the bacterial sulfite dehydrogenase from *Sinorhizobium meliloti* has been reported [77]. This enzyme has discrete proteins that act together containing the molybdenum site and the cytochrome electron acceptor, called SorT and SorU, respectively. The crystal structures of the SorT and SorU proteins have been solved, both alone and in complex [77], and with the analogue of the clinical mutation Arg78 → Gln plus a number of other site-directed mutants [78]. The structure of wild-type SorT in complex with SorU showed that Arg78 of SorT hydrogen bonds to the propionate of the SorU heme and the Arg78 mutants all showed substantially impaired ability to transfer electrons to SorU. This work compellingly showed that SorU docks close to the Mo site of SorT in a position analogous to that proposed for sulfite oxidase (Fig. 13b) and that the aforementioned active site arginine Arg78 (Arg138 chicken) plays a pivotal role in both active site

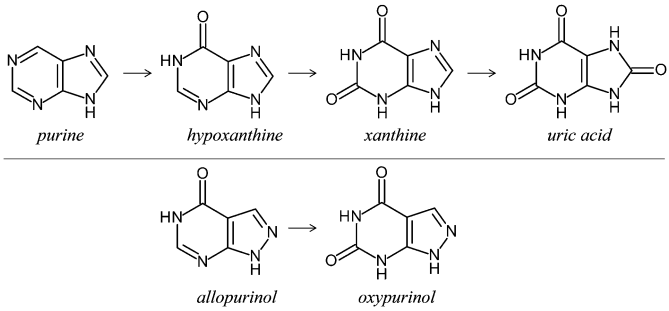

Fig. 14 Upper panel: Purine oxidation reactions catalyzed by xanthine oxidase/dehydrogenase. In the figure the more stable keto tautomers are shown, although oxidations by the enzyme are thought to be initially to the enol form (C–OH). Lower panel: the xanthine oxidase/dehydrogenase inhibitors allopurinol and oxypurinol; as with the upper panel, the more stable tautomers are shown

structure and in facilitating electron transfer to the heme. The reason why this conformation has not yet been actually observed in sulfite oxidase is as yet unclear, and the answer to this must await further studies.

5.2 The Xanthine Oxidase Family

5.2.1 Xanthine Oxidase and Aldehyde Oxidase

Xanthine oxidase and dehydrogenase are two different forms of the same enzyme, encoded by the same gene, the prototypical member of the xanthine oxidase family. From the molybdenum perspective, the oxidase and the dehydrogenase are essentially identical and can be interconverted either by proteolysis or by formation of a disulfide at the flavin site [79]. Xanthine oxidase is linked to gout, a painful condition in which crystals of monosodium urate monohydrate form in joint capsules [80, 81], in particular that at the base of the big toe. Gout can be prevented by administering the xanthine oxidase/dehydrogenase inhibitor allopurinol, which is oxidized in vivo by the enzyme to the active form that is known as alloxanthine or oxypurinol (Fig. 14) and which associates covalently with Mo in the inhibitory complex, forming a Mo–N bond [82, 83]. Human xanthine oxidase/dehydrogenase deficiency is known as xanthinuria, and, to the embarrassment of xanthine oxidase researchers, some individuals suffering from this can be in excellent health and completely asymptomatic, while others develop various problems associated with buildup of xanthine or hypoxanthine [84, 85].

The xanthine oxidase family also includes a range of other eukaryotic enzymes, as well as a substantial number of prokaryotic enzymes. Treating the oxidized active enzymes with cyanide converts the active site to an inactive “desulfo” form, with liberation of thiocyanate and reduction to Mo(IV). The cyanide-labile sulfur is now

known to be a Mo = S group in the oxidized enzyme, and its presence together with molybdopterin and oxygen coordination of the molybdenum defines the xanthine oxidase family. When oxidized, the inactive desulfo form of the enzyme contains a Mo = O group in place of the Mo = S. Xanthine oxidase has already been shown in Fig. 3 as an example of a multi-redox center molybdenum enzyme; the enzyme is a homodimer, with each subunit containing one Mo, two different [Fe_2S_2] clusters, and a flavin [86–88]. The physiological role of xanthine oxidase is thought to be purine oxidation, successively converting purine to hypoxanthine to xanthine to uric acid (Fig. 14). The enzyme has very broad substrate specificity and is capable of oxidation of a wide range of aldehydes [88]. It is also very closely related to the aldehyde oxidases [26], which also have broad substrate specificity, catalyzing oxidation of aldehydes to carboxylic acids (Eq. 4). These enzymes are of pharmaceutical importance through their role in clearing a number of aldehyde drugs and nitrogen heterocycles such as nicotine [89].

$$R - CHO + H_2O \rightarrow R - CO_2H + 2H^+ + 2e^- \quad (4)$$

Protein crystallography and spectroscopy have provided detailed structural information and potential insights about the catalytic mechanism. Early views on mechanism were advanced by Bray and co-workers, who used EPR spectroscopy in conjunction with substitution with stable isotopes. Labeling with ^2H showed that the proton from the substrate carbon undergoing oxygen atom transfer to form product is transferred to the molybdenum as a Mo(V)–SH (see [17] and refs. therein) and that the oxygen transferred to substrate originates from oxygen coordinated to Mo (see [17] and refs. therein). Early proposed mechanisms were formulated in terms of a molybdenum-bound hydride acceptor and molybdenum-bound oxygen acting as a nucleophile. A number of xanthine oxidase family members have Mo = Se in place of Mo = S; these include purine hydroxylase and xanthine dehydrogenases which have been purified and characterized from *Clostridium purinolyticum* [90] and nicotinate dehydrogenase from *Eubacterium barkeri*, which has been structurally characterized [91]. Moreover, early work indicated that desulfo turkey xanthine dehydrogenase could, at least in part, be reactivated by treatment with selenide, suggesting that the Mo = Se form of this enzyme could show activity [92]. As Mo = Se must play a similar role to Mo = S, and because Mo = Se is an outstanding nucleophile and a poor electrophile, these observations support a nucleophilic role for Mo = S/Se in the catalytic mechanism [93]. Some aspects of the catalytic mechanism are summarized in Fig. 15; the Mo = S abstracts a proton from the carbon undergoing oxo transfer, followed by formation of the Mo–O–C bond with concomitant reduction of the metal to Mo(IV). Importantly, pH-dependent changes of the active site structure correspond with one molybdenum-oxygen bond shortening from 1.97 Å at pH 6 to 1.75 Å at pH 10, consistent with the active oxygen deprotonating from Mo–OH at low pH to Mo = O at high pH [24].

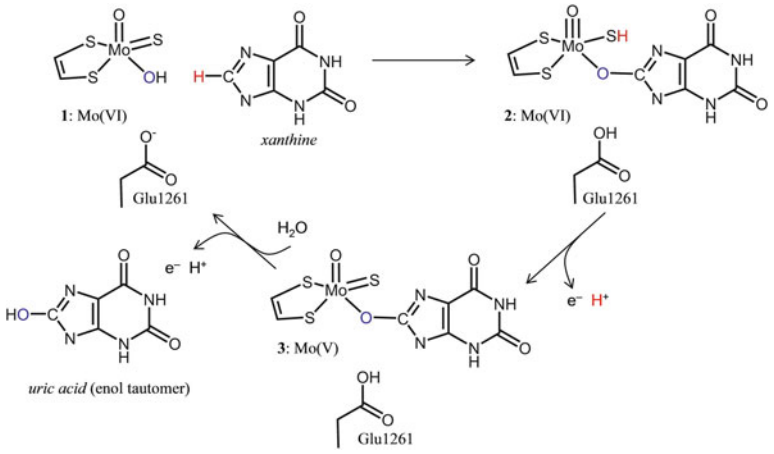

Fig. 15 Proposed catalytic mechanism for xanthine oxidase, involving the highly conserved active site residue Glu 1,261. Colors indicate the fate of atoms in the reaction as probed by stable isotopes starting with **1**; see [17] for a comprehensive review of the literature. The Mo(V) species **3** is the much-studied Very Rapid intermediate in which product is covalently bound to Mo [17]

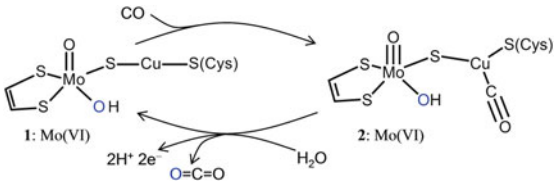

Fig. 16 Proposed catalytic mechanism for carbon monoxide dehydrogenase involving binding of CO to Cu(I) in the active site; for a comprehensive review, see [17]

5.2.2 Carbon Monoxide Dehydrogenase

The most unusual members of the xanthine oxidase family are undoubtedly the bacterial molybdenum-containing carbon monoxide dehydrogenases, owing to the presence of a Cu/Mo binuclear site in these systems. In essence, these enzymes possess a xanthine oxidase active site modified with an additional two-coordinate cuprous ion bound to a cysteine residue and to what in other more conventional enzymes would be Mo = S to form a Cu/Mo binuclear active site, as shown in Fig. 16, a structure deduced from a combination of crystallography [94] and XAS [95]. The enzymes catalyze oxidation of carbon monoxide to carbon dioxide, Eq. (5):

$$CO + H_2O \rightarrow CO_2 + 2e^- + 2H^+ \quad (5)$$

The substrate CO is thought to bind to Cu, positioning it adjacent to Mo in an ideal location for oxygen atom transfer from Mo to form CO_2, as shown in Fig. 16. The enzyme produces a novel Mo(V) EPR signal, with coupling from both $I = 3/2$ ^{63,65}Cu and $I = 5/2$ ^{95,97}Mo [94, 96, 97] with evidence of $I = 3/2$ ^{13}C hyperfine when ^{13}CO is used to develop the signal. This most novel member of the xanthine oxidase family thus provides a striking example of the flexibility of molybdenum enzyme active sites. How this system evolved, with ancient molybdenum alongside relatively recent copper, is at present unresolved.

5.3 The DMSO Reductase Family

The DMSO reductase family constitutes by far the most varied and numerous of the three families of enzymes. With two molybdopterin associated with the metal, this family is found in both archaea and bacteria, but not in eukaryotes. It includes all known tungsten enzymes, a wide range of molybdenum enzymes in various metabolic and respiratory roles, and the few known molybdenum/tungsten enzymes that are not oxo-transferases. The best studied are the *Rhodobacter* DMSO reductases. The *R. capsulatus* and *R. sphaeroides* enzymes have both been extensively studied, and as there appear to be only trivial differences between them, we will not distinguish them here. The DMSO reductases catalyze the following reaction:

$$(CH_3)_2S = O + 2H^+ + 2e^- \rightarrow (CH_3)_2S + H_2O \quad (6)$$

The group of very similar enzymes includes trimethylamine N-oxide reductase [98] dimethyl sulfide dehydrogenase [99], which catalyzes the reverse reaction of Eq. (6), and the biotin sulfoxide reductases [100]. Together these enzymes comprise the Type 3 DMSO reductase family members.

5.3.1 Rhodobacter DMSO Reductase

The active site structures of this enzyme were a source of early controversy, and because the reader may come across some of this early work, we will discuss this topic very briefly here. The first characterization of the active site was by XAS [101], and notably, given what was to later unfold, this work discussed the possibility of multiple structures at the active site [101]. Subsequent crystallography [102] gave very surprising conclusions, with unlikely molybdenum coordination environments, and was distinctly at odds with the XAS [101]. More crystallography followed by two different research groups [103–105], plus another XAS study which seemed to confirm one of the crystal structures [106]. Meanwhile, additional studies by resonance Raman spectroscopy disagreed with the crystallography and instead favored the conclusions of the original XAS study [42]. Subsequent to all of this work, the

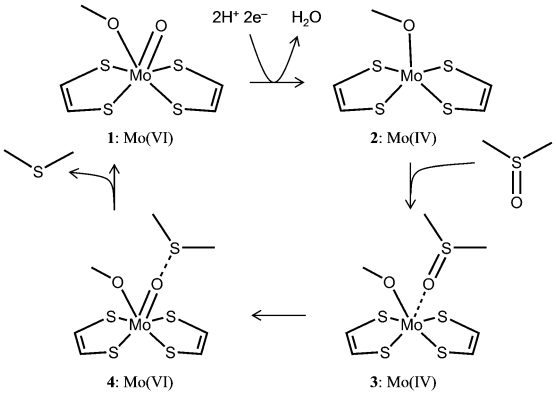

Fig. 17 Proposed catalytic mechanism for DMSO reductase; for a comprehensive review of spectroscopic evidence, see [17]. The DMSO binds to reduced enzyme **2** to produce a DMSO bound form **3** that has been studied both by crystallography and spectroscopy. The oxygen is transferred to Mo to form **4**, and release of dimethyl sulfide regenerates oxidized enzyme **1**

XAS was revisited with substantially the same result as the initial study [107]. This later study also pointed out that the structures that were suggested from analysis of the X-ray crystallography were chemically implausible, with some showing supposedly non-bonded atoms with overlapping van der Waals radii, and reinforced the earlier suggestion [101] that multiple forms of the active site might exist [107]. Finally, the crystallography was reexamined at higher resolution [108] and interpreted in terms of two different active site structures enfolded within near-identical proteins. Still later work explored the culprits; in part the choice of buffer (HEPES) and exposure to oxygen had modified the enzyme active site [109], a process which could be reversed by reduction and catalytic turnover [107].

The true structure of the oxidized active enzyme is now agreed to have two molybdopterin dithiolenes bound to give a total of four sulfur donors to Mo, with a serine oxygen coordinated and a single Mo = O, as shown in Fig. 5 and schematically in Fig. 17. The spectator oxo effect (Sect. 2.1) is unimportant in DMSO reductase and its siblings, because they possess only a single Mo = O ligand in the oxidized Mo(VI) form. As discussed above, the terminal oxo group may facilitate electron transfer [43] via one of the two molybdopterins, which have been suggested to function differently in catalysis [15, 42].

Various product- and product analogue-bound forms of DMSO reductase have been characterized spectroscopically [107, 110]. Most notably dimethyl sulfide binds to the oxidized enzyme to make a catalytically relevant DMSO complex (Fig. 17), and dimethyl selenide forms a similar complex [110]; moreover, trimethylarsine reacts with oxidized Mo(VI) enzyme to make a trimethylarsine-N-oxide bound to a reduced Mo(IV) site with stoichiometric Mo and As, which can be characterized by XAS from both the Mo and the As perspective [110] as coordinated through a Mo–O = As bond, suggesting a structure for a substrate complex. A schematic diagram of the catalytic process most probably employed in DMSO

reductase is shown in Fig. 17. The enzyme has been extensively studied by electron paramagnetic resonance spectroscopy [17], and the Mo(V) form has been examined by XAS and found to be five-coordinate, with four sulfurs from two molybdopterins plus one Mo–OH ligand but lacking the serine oxygen ligand to Mo [45]. How this coordination fits into the proposed catalytic cycle is at present unclear, but it illustrates that the active sites of these enzymes can by dynamic and change their coordination chemistry under different conditions.

5.3.2 Prokaryotic Nitrate Reductases

A widespread and well-studied group of Mo enzymes are the prokaryotic nitrate reductases [111, 112]. These can be divided into three distinct categories: the periplasmic nitrate reductase (Nap), the respiratory nitrate reductases (Nar), and the assimilatory nitrate reductase (Nas). All are DMSO reductase family members, although the Nas enzymes are not as completely studied. Structures for Nap indicate that these are Type 1 with a cysteine donor to Mo [113] plus another ligand which may be a sulfido [114], while the Nar enzymes are Type 2 DMSO reductase family members, with aspartate coordination to the metal [6, 7]. Both active site structures and possible mechanisms have recently been reviewed for the Nap enzymes [112, 114] which suggest that the cysteine may dissociate to allow nitrate to bind, in a postulated mechanism related to that suggested for formate dehydrogenase, which we will discuss below (Sect. 6.1). The Nar nitrate reductases have also been extensively studied using both crystallography [6, 7] and a variety of spectroscopic methods [17, 115]. The active site of Nar has two molybdopterin dithiolene ligands with an aspartate (Asp222) providing oxygen coordination to Mo. The enzyme shows a curious reductive activation [116] that we can speculate may be related to the ring-open/ring-closed forms of molybdopterin discussed above [6, 7] (Fig. 2). Possibly, the reductive activation is due to conversion of inactive and ring-open dihydro form, to an active and ring-closed tetrahydro form [116], and these are the forms that have been observed crystallographically [6, 7]. Insofar as the catalytic mechanism is concerned, nitrate is thought to bind to the Mo(IV) enzyme in a manner analogous to the nitrate complex that has been observed by EPR for the Mo(V) oxidation state [117], and a simplified mechanism is shown in Fig. 18.

Another relative of this family is the selenate reductase from *Thauera selenatis* [118], which has a monooxo Mo(VI) site and a des-oxo Mo(IV) site with close to four Mo–S ligands in both. The enzyme also possesses a mysterious selenium-containing group bound to a metal ion, most probably Fe [118].

5.3.3 Ethylbenzene Dehydrogenase

This enzyme catalyzes the anaerobic hydroxylation of ethylbenzene to (*S*)-1-phenylethanol in a highly stereospecific reaction [119], which is the first step in the anaerobic degradation of ethylbenzene [120]. The enzyme can hydroxylate a

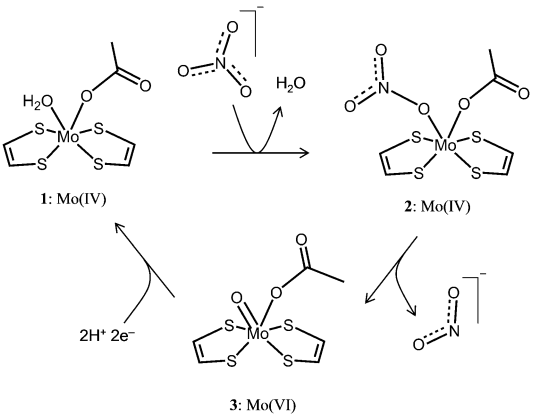

Fig. 18 Postulated catalytic cycle of Nar nitrate reductase

series of other compounds with methylene carbons adjacent to a benzene or other heterocyclic ring [121], and in most cases the reaction is strongly enantioselective [121]. The crystal structure of the enzyme shows a type 2 DMSO reductase family member [119], with the molybdenum coordinated by two molybdopterin dithiolenes and an aspartate side chain and one terminal oxygen group [119]. Similarly to one of the two Nar structures [7], one of the two molybdopterins has a bicycle ring-open structure, while the other is a tricyle furan (Fig. 2). Current views of the catalytic mechanism [122] involve abstraction of one hydrogen from the methylene by the Mo = O group of the oxidized Mo(VI) enzyme to form a free radical intermediate with a Mo(V) site with hydrogen from an adjacent histidine residue stabilizing the hydroxyl ligand. This is followed by a second one-electron transfer with the radical becoming a carbocation Mo(IV) species which then associates with Mo to form a bridging OH. Displacement of this by water then releases product and subsequent reoxidation through intramolecular electron transfer to regenerate the oxidized active site (Fig. 19). When 1,2-diethylbenzene is used as a substrate, the product is nearly racemic, arguing for the proposed reaction mechanism [123].

5.3.4 Arsenite Oxidase and Arsenate Reductase

These enzymes catalyze the oxidation of toxic arsenite to less toxic arsenate (arsenite oxidase) or the reverse (arsenate reductase), as shown in Eq. (7)

$$\mathrm{As(OH)_3 + H_2O \leftrightarrow \left[AsO(OH)_3\right]^- + 2H^+ + 2e^-} \tag{7}$$

Arsenite oxidase has been characterized from two different organisms by both crystallography [124, 125] and XAS [46, 126], with consistent results for each technique. As is often the case, and as we have discussed above, the crystal structures are clearly of photoreduced enzymes and show differences from the structure suggested from XAS [46, 126]. In the oxidized enzyme the active site possesses a

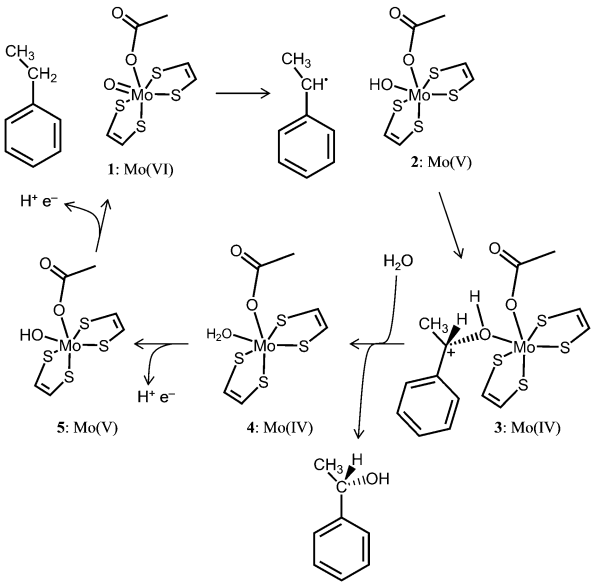

Fig. 19 Postulated reaction cycle of ethylbenzene dehydrogenase. We note that alternative mechanisms have been suggested for this enzyme for hydroxylation of 4-ethylphenol involving a nearby aspartate and a quinone methide intermediate [120]

cis-dioxo Mo(VI) with four nearly equivalent sulfur donors from the two molybdopterin dithiolenes, consistent with a square-based prismatic type geometry. The proposed catalytic mechanism is shown in Fig. 20 [46]. The pterin twist mechanism, discussed above, was postulated to distort the active site away from the low-energy octahedral-type geometry toward the transition state [46], energetically lowering the barrier between the initial substrate complex (Fig. 20, **1**) by adopting a geometry more typical of reduced Mo(IV) (Fig. 20). The reaction is assisted by the spectator oxo effect [46], which is also discussed above. The fully reduced product (Fig. 20) resembles the structures observed by X-ray crystallography. The enzyme is also remarkable in having fully crossed-over Mo(VI)/Mo(V) and Mo(V)/Mo (IV) redox potentials, so that the Mo(V) oxidation state cannot be observed [127] and the enzyme works only in the Mo(VI) and Mo(IV) formal oxidation states (Fig. 20).

The reduction of arsenate to arsenite is not as biochemically challenging as the reverse reaction from a thermodynamic perspective [46]. The arsenate reductases that concern us here are molybdenum-containing enzymes, but we note in passing that bacteria and yeasts possess unrelated non-Mo-containing arsenate reductases [128]. Although these are themselves unrelated, both prokaryotic and eukaryotic enzymes employ glutaredoxin with reduced glutathione as the source of electrons [128]. There is also a human enzyme about which little is known, which may be related to these enzymes as exogenous thiols are needed for activity [129]. These systems are not directly related evolutionarily or biochemically to the molybdenum-containing enzyme that is our focus, and we will not discuss them further.

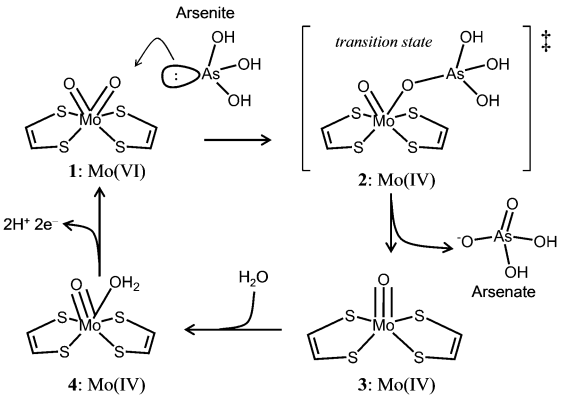

Fig. 20 Proposed catalytic mechanism for arsenite oxidase. The oxidized enzyme **1**, distorted by the protein through a pterin twist, reacts with arsenite via a transition state **2** from which is liberated arsenate

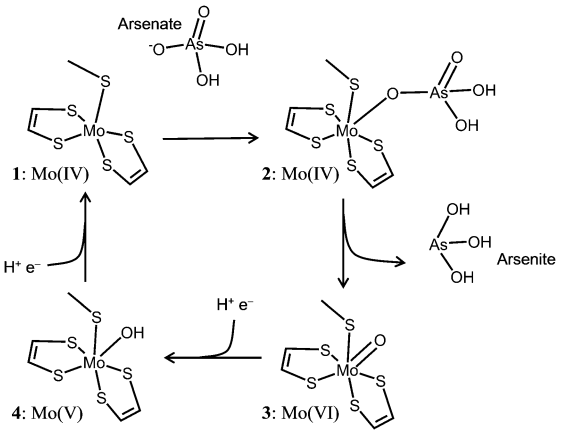

Fig. 21 Proposed catalytic mechanism for arsenate reductase

The Mo-containing arsenate reductase from *Shewanella* sp. ANA-3 has been studied crystallographically [1130], and, as is often observed, the initially oxidized enzyme appears to have been photoreduced during data collection [130]. The XAS of this enzyme has not yet been reported, but the detailed crystal structures suggest a catalytic mechanism that is quite distinct from that of arsenite oxidase [130] and an active site that belongs to the Type 1 DMSO reductase family, with cysteine coordination of Mo. The proposed mechanism is shown in Fig. 21, and in many ways resembles that of DMSO reductase, and is as expected for an oxo-transferase acting in a reductive capacity. The active site structure of the enzyme is unusual in having near-octahedral-type coordination around molybdenum.

6 Non-oxo-transferase Molybdenum and Tungsten Enzymes

As we have discussed above, the vast majority of the molybdenum and tungsten enzymes are oxo-transferases, but there are a few noteworthy exceptions as we now discuss.

6.1 Formate Dehydrogenase and Formylmethanofuran Dehydrogenase

Both tungsten and molybdenum formate dehydrogenases are known; the first tungsten enzyme to be described was the formate dehydrogenase from the thermophile *Clostridium thermoaceticum* [12]. Formate dehydrogenases are noteworthy in that they are one category of molybdenum/tungsten enzymes that do not employ oxygen atom transferase chemistry nor do they use water as a source of oxygen. They catalyze the conversion of formate to carbon dioxide or carbonate, as shown in Eq. (8).

$$HC(O)O^- \rightarrow CO_2 + H^+ + 2\,e^- \tag{8}$$

Both molybdenum and tungsten formate dehydrogenases contain two molybdopterins bound to the metal, and are found with selenocysteine associated with the metal [131], although cysteine coordinated analogues are also known [131]. *E. coli* has two different formate dehydrogenases (FDH), and much work has been done on the catalytic component of one of these, called FDH_H. We will focus on discussion of this enzyme here, although the other *E. coli* enzyme appears to be similar. There has been debate about the structure of the active site of FDH_H, and the original crystallography [132] has been reinterpreted [133, 134]. Our discussion here is based upon recent work on the mechanism [135] while noting that there is still contention [136], taking into account the definitive identification by XAS of a selenium sulfide covalent bond [137, 138]. The mechanism is guided by elegant experiments using stable isotopes; when ^{13}C-labeled formate in ^{18}O-enriched water is used, the enzyme produced $^{13}CO_2$ containing no ^{18}O [139], conclusively establishing that the enzyme does not catalyze incorporation of oxygen from water into product. Moreover, deuterated formate $^{2}HCO_2^-$ was used to show that the proton of formate is associated with the molybdenum after catalytic turnover [139]. A summary of a possible mechanism for formate dehydrogenase is shown in Fig. 22.

Effectively the reverse reaction to that catalyzed by formate dehydrogenase is catalyzed by formylmethanofuran dehydrogenase [151, 152], which fixes CO_2 (Fig. 23) and is the first step in the process of methane generation by some Archaea. The most prominent mechanism of biological CO_2 fixation is photosynthesis, but many others exist [140] of which archaeal methanogenesis is thought to be among

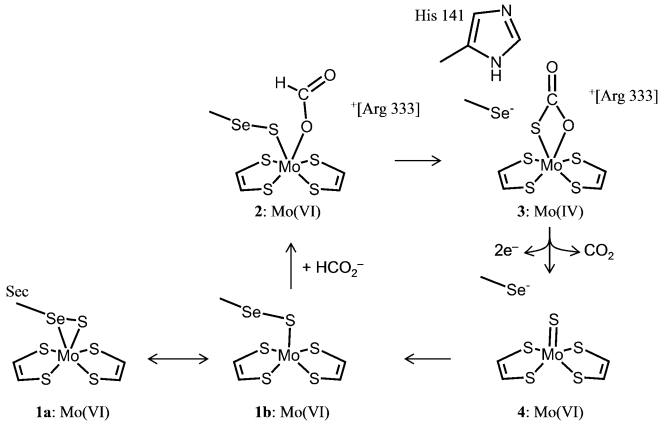

Fig. 22 Proposed catalytic mechanism for formate dehydrogenase, modified from [135] with the species 1a being that observed by XAS [137]

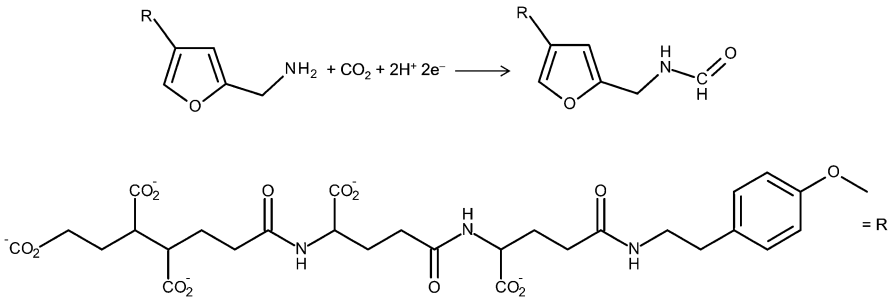

Fig. 23 Reaction catalyzed by formylmethanofuran dehydrogenase

the most ancient. While this mechanism was much more prevalent in the pre-photosynthetic world, it is still widespread in the environment, being responsible for such phenomena as marsh gas, deep-sea methane clathrates [141], and gastrointestinal flatulence in mammals [142]. As we have discussed above, both molybdenum and tungsten enzymes are known, and both have two molybdopterins and sulfide and cysteine sulfur donors forming an active site that is analogous to that of the cysteine-containing formate dehydrogenases and the selenocysteine enzymes discussed above. It seems likely that its catalytic mechanism is related to that of formate dehydrogenase [151, 152]. Aside from the chemistry that occurs at the tungsten site, the overall structure of the enzyme deserves comment.

The enzyme exists as two linked dodecamers (12), forming an overall tetracosamer (24) of some 800 kDa, containing a total of 46 iron-sulfur clusters. The surprising complexity of the enzyme seems to almost invite superlatives. The tungsten sites (4 per tetracosamer) are buried deep within the protein, and to reach them the substrate CO_2 must diffuse along a 40 Å hydrophobic internal channel

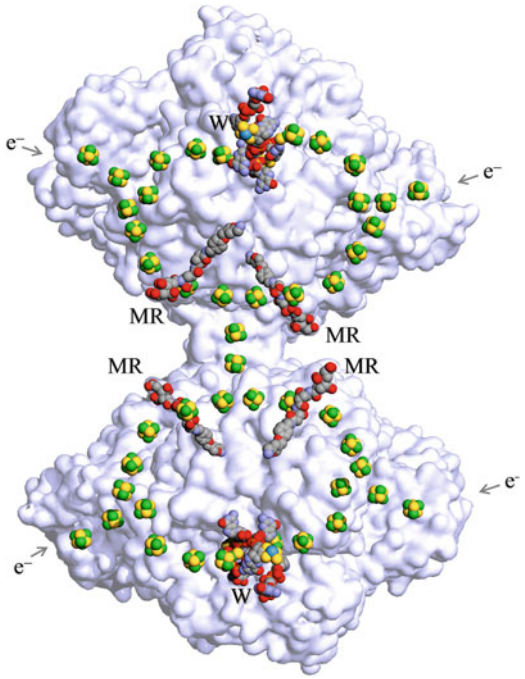

Fig. 24 Crystal structure of the tetracosamer ~800 kDa formylmethanofuran dehydrogenase (pdb: 5t61), containing 46 [4Fe-4S] clusters (green/yellow) and four tungsten sites, two in each dodecamer. The overall hourglass shape of the two dodecamer subunit arrangements is clear, with two of the [4Fe-4S] clusters (one from each dodecamer) acting as a bridge between them. The locations of the tungsten sites in the top and bottom of the figure are shown (W), as are the bound methanofuran (MR). The four external [4Fe-4S] clusters (marked e^-) are the postulated entry points of reductive electrons

before it is reduced to formate or formic acid. The product must then traverse another predominantly hydrophilic internal channel, this time some 43 Å-long, to a binuclear zinc site where it reacts with methanofuran to form formylmethanofuran [151]. The remarkable arrangement of iron-sulfur clusters in this novel enzyme is shown in Fig. 24, and while these clearly serve as an electrical connection, coupling the four tungsten sites over some 206 Å, why such complex arrangements are needed and the exact function of the [4Fe-4S] cluster arrays is as yet unclear [151].

6.2 Acetylene Hydratase

Acetylene hydratase is a second exception to the rule that molybdenum and tungsten enzymes are oxo-transferases. This enzyme is also unusual among molybdopterin-based enzyme in a second regard, in that the metal in the active site of the enzyme plays no apparent redox role, an anomaly shared only with the enzyme pyrogallol transhydroxylase, which we will discuss below (Sect. 6.3). The enzyme catalyzes the net hydration reaction converting acetylene to acetaldehyde, as shown in Eq. (9)

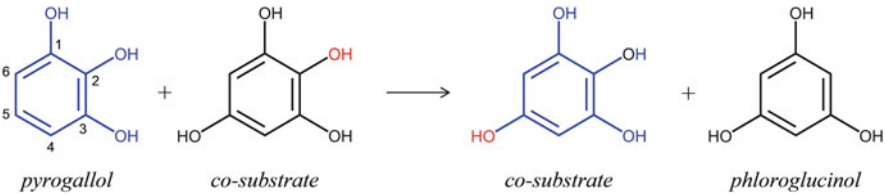

Fig. 25 Reaction catalyzed by pyrogallol transhydroxylase

$$HC \equiv CH + H_2O \rightarrow CH_3C(O)H \tag{9}$$

This reaction is exothermic by more than 110 kJ mol^{-1} and is of historical industrial interest, as the hydration of acetylene was the major source of acetaldehyde [143], and the analogous reaction with propyne ($CH_3C \equiv CH$) was used to produce acetone. In those early industrial processes, Hg(II) compounds served as catalysts to activate the acetylene, with attack of water yielding an enol (vinyl alcohol from acetylene) which then underwent tautomerization to form the keto product (acetaldehyde). The tungsten of acetylene hydratase [144] seems to play a role that is in some ways analogous to the Hg(II) of industrial chemistry, binding acetylene via the C ≡ C triple bond with attack of water on one carbon to make vinyl alcohol via a multi-stage process involving a nearby aspartate residue [145].

6.3 Pyrogallol Transhydroxylase

The pyrogallol transhydroxylase from the anaerobe *Pelobacter acidigallici* is another molybdenum enzyme for which water is not the source of oxygen, and like acetylene hydratase it does not catalyze a redox reaction [146]. The enzyme catalyzes the conversion of pyrogallol (1,2,3-trihydroxybenzene) to phloroglucinol (1,3,5-trihydroxybenzene), effectively moving –OH from the two- to the five-ring position. The enzyme uses a co-substrate 1,2,3,5-tetrahydroxybenzene, which in fact is the primary source of the product phloroglucinol (Fig. 25). The enzyme binds pyrogallol to Mo via the C_3–OH, and protons are abstracted from the 2 and 3 positions by nearby aspartate and histidine residues, respectively, stabilizing the diketo tautomer (1 hydroxy-2,3-benzoquinone). The co-substrate is located in the active site with its C_2–OH adjacent to the pyrogallol C_5 position, and its proton is picked up by a nearby tyrosine, forming an ether linkage between the substrate and co-substrate to make the intermediate 2,6-dihydroxy-4-(2,4,6-trihydroxyphenoxy)cyclohexa-2,5-dien-1-one. The catalytic cycle is completed by breaking the C_2–O bond, forming phloroglucinol from the co-substrate and co-substrate from the substrate. The enzyme is clearly related to others in the DMSO reductase family [146] and even possesses iron-sulfur clusters that apparently serve no redox purpose. The sole purpose of the molybdenum appears to be to bind the substrate C_3–OH, and the

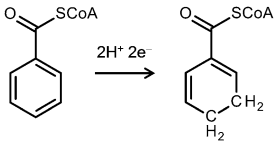

Fig. 26 Reaction catalyzed by benzoyl-CoA reductase

sole purpose of the two molybdopterins seems to be to appropriately locate the Mo in the active site.

6.4 Benzoyl-CoA Reductase

Our final example of a non-oxo-transferase is the tungsten-containing enzyme benzoyl-CoA reductase, which has been suggested to operate at the lowest redox potential of any biological reaction known to date [147]. It catalyzes the biological analogue (Fig. 26) of the Birch reduction, in which alkali metals (e.g., Na, Li) in solution in liquid ammonia are used to reduce aromatic rings [148]. Benzoyl Co-A dehydrogenase has tungsten coordinated by five sulfurs from two molybdopterin dithiolenes and a single cysteine residue. A sixth ligand is observed crystallographically but its identity is uncertain [147], although the crystal structure suggests that it is linear and diatomic, and enzyme activity increases upon addition of cyanide. The XAS is consistent with the sixth ligand as –CN, but FT-IR shows no evidence of such ligands. Tungsten does not appear to be in direct contact with the substrate, but rather it seems that the uncertain sixth ligand bridges to the aromatic ring of benzoyl-Co-A [147]. Cluka et al. [149] have employed computational chemistry to support water as the sixth ligand, but at the time of writing the identity of this pivotal ligand, and hence the exact nature of the catalytic mechanism of this intriguing enzyme, still seems uncertain.

7 Molybdenum Versus Tungsten

Holm, Solomon, and coworkers [150] have compared the chemistry of molybdenum and tungsten and its relation to the catalytic function of the molybdenum and tungsten enzymes. There are a few examples where organisms have both molybdenum and tungsten versions of similar enzymes, such as the formylmethanofuran dehydrogenases [151, 152]. There are also examples of native Mo enzymes where molybdenum has been successfully substituted by tungsten, including sulfite oxidase, where the tungsten enzyme essentially lacked any catalytic activity and was not reduced by sulfite [153] and DMSO reductase which showed substantially increased activity relative to the native molybdenum enzyme [154, 155].

We now turn to the question of why nature chose molybdenum and tungsten and why some organisms show preference for one over the other [1]. We have already

mentioned that the enzymes are thought to be very ancient [1, 156]. Molybdenum and tungsten share somewhat non-metallic chemistry in that both form oxyanions $[MO_4]^{2-}$ that are stable at lower redox potentials. Oxygen atom transferase chemistry would have been more problematic in the anoxic primordial earth than in our current oxic world [157], and the capability of these metals to carry out such chemistry at low redox potentials may have been essential for early life. The hyperthermophilic archaea are thought to have diverged from the rest of life earlier than many other organisms [158]. These organisms contain only tungsten enzymes, and thus it has been suggested that the tungsten enzymes were the precursors of the molybdenum enzymes [159]. Moreover, tungsten may have been more available than molybdenum in the primordial environment; modern seawater has much higher levels of molybdate than tungstate (100 nM and 60 pM, respectively) [160], and in the primordial oceans, this is likely to have been reversed because the anoxic sulfidic waters would precipitate insoluble MoS_2 while tungsten compounds would remain soluble [161].

As discussed by Holm, Solomon, and co-workers [150], relativistic effects are much more important for tungsten than for molybdenum, with relativistic contraction of the core orbitals enhancing bond strengths and destabilizing metal centered d-orbitals, thereby lowering redox potentials. Tungsten complexes are also more sensitive to oxygen [150], and the choice of molybdenum rather than tungsten may therefore depend more upon cellular redox conditions than other factors. Overall, tungsten is chemically better suited for catalysis of lower-potential redox reactions under anaerobic conditions, and at higher operating temperatures [150], which is what is observed in nature.

8 Concluding Remarks

Interest in the molybdenum and tungsten enzymes will continue to be stimulated by fields as diverse as drug metabolism [162] and potential biofuels [163]. Progress in the future will continue to be driven by structural and spectroscopic studies and will be facilitated by site-directed mutagenesis and discovering diversity with the revolution in metagenomic sequencing. Despite the rich diversity in metal coordination environment and enzyme function, there are some rules that can be observed. Low-molecular weight Mo(VI) and W(VI) compounds in the Cambridge Structural Database [35] predominantly show octahedral-type coordination environments. But the enzymes are different; nearly all of the enzyme active sites that conduct oxo-transferase chemistry show non-octahedral-type coordination of the metal. Significantly, for three out of four of the enzymes currently known that do not conduct oxo-transferase chemistry, namely, acetylene hydratase, pyrogallol transhydroxylase, and benzoyl-CoA reductase, the active sites do have octahedral-type coordination geometry. This suggests that the oxo-transferases provide examples of entatic states in which the active site is distorted by the protein to approach a transition state [46]. As we have discussed, conclusions related to catalytic mechanism combine a number of factors. The information from crystallography is of

pivotal importance, but the possibility of photoreduction and the limitations of resolution are important, as is the information from spectroscopy of various forms. In all cases not only the metal site but also the protein and molybdopterin must be considered. Despite the tremendous progress that has been made since the early days, and as we have discussed, there remain important unanswered questions related to the catalytic mechanisms. There is still confusion about the roles of various groups, and those that are excellent nucleophiles are probably acting as such. Among the most intriguing of these is the role of selenium in some of the enzymes, which is sometimes present as a metal-bound terminal selenide and sometimes as selenocysteine. Selenium is the essential element with by far the lowest crustal abundance [164], and it is incorporated into biological molecules at tremendous metabolic cost [165]. Hence, for enzymes such as the selenium-containing formate dehydrogenases (Sect. 6.1), it seems most unlikely that evolution would have incorporated selenium without a very good reason that is closely related to its chemistry. As we have previously discussed [166], selenium is probably the best nucleophile available to living organisms, and it therefore seems unlikely that its roles in catalysis would not involve nucleophilic attack. A number of proposed mechanisms have postulated ligand dissociation from molybdenum or tungsten (e.g., cysteine sulfur in the Nap nitrate reductases; Sect. 5.3), and while dissociation of one molybdopterin dithiolene has been observed in inactive forms of DMSO reductase family members [167], no catalytic role for such dissociation has, to our knowledge, yet been proposed in any system. Many other open questions also remain, such as the role played by ring-open and ring-closed forms of molybdopterin (Sect. 3) and the nature of the all-important mystery ligand in benzoyl-CoA reductase (Sect. 6.4). A different level of interest relates to the exact reasons behind the incredible complexity of formylmethanofuran dehydrogenase (Sect. 6.1). Finally, the roles played by molybdenum and tungsten in the origins of life on earth and in early organisms have been a topic of recent discussion [1, 156]. In particular the active sites of molybdenum and tungsten enzymes are members of only a handful of biological reagents capable of genuine $n = 2$ redox chemistry [127, 168], and such reactions may have played pivotal roles in life's origins [169].

Acknowledgments Research in the authors' laboratory is funded by the Natural Sciences and Engineering Research Council of Canada, the Saskatchewan Health Research Foundation (SHRF), the University of Saskatchewan, the Canada Foundation for Innovation, Chevron Energy Research Co., and a Canada Research Chair award (to G.N.G). R.C.P. acknowledges support from the Diane Gunson benevolence fund.

References

1. Pushie MJ, Cotelesage JJH, George GN (2014) Metallomics 6:15–24
2. Lane T, Saito MA, George GN, Pickering IJ, Prince RC, Morel FFM (2005) Nature 435:42
3. Hiller CJ, Rettberg LA, Lee CC, Stiebritz MT, Hu Y (2019) Current understanding of the biosynthesis of the unique nitrogenase cofactor core. Struct Bond. https://link.springer.com/chapter/10.1007/430_2018_29

4. Wenke BB, Spatzal T (2019) Looking at nitrogenase: insights from modern structural approaches. Struct Bond. https://link.springer.com/chapter/10.1007/430_2018_28
5. Hille R, Halt J, Basu P (2014) Chem Rev 114:3963–4038
6. Jormakka M, Richardson D, Byrne B, Iwata S (2004) Structure 12:95–104
7. Bertero MG, Rothery RA, Palak M, Hou C, Lim D, Blasco F, Weiner JH, Strynadka NCJ (2003) Nat Struct Biol 10:681–687
8. Kloer DP, Hagel C, Heider J, Schulz GE (2006) Structure 14:1377–1388
9. Gisewhite DR, Yang J, Williams BR, Esmail A, Stein BW, Kirk ML, Burgmayer SJN (2018) J Am Chem Soc 140:12808–12818
10. Cotelesage JJH, Crawford AM, Prince RC, George GN (unpublished)
11. Bray RC, Swann JC (1972) Struct Bond 11:107–144
12. Ljundahl LG, Andreesen JR (1975) FEBS Lett 54:279–282
13. George GN, Prince RC, Mukund S, Adams MWW (1992) J Am Chem Soc 114:3521–3523
14. Olson JS, Ballou DP, Palmer G, Massey V (1974) J Biol Chem 249:4363–4382
15. Rothery RA, Stein B, Solomonson M, Kirk ML, Weiner JH (2012) Proc Natl Acad Sci U S A 109:14773–14778
16. Stetter KO (2006) Philos Trans R Soc B 361:1837–1843
17. Pushie MJ, George GN (2011) Coord Chem Rev 255(9–10):1055–1084
18. Kisker C, Schindelin H, Pacheco A, Wehbi WA, Garrett RM, Rajagopalan KV, Enemark JH, Rees DC (1997) Cell 91:973–983
19. Schrader N, Fischer K, Theis K, Mendel RR, Schwarz G, Kisker C (2003) Structure 11:1251–1263
20. Fischer K, Barbier G, Hecht H-J, Mendel RR, Campbell WH, Schwarz G (2005) Plant Cell 17:1167–1179
21. Kappler U, Bailey S (2005) J Biol Chem 280:24999–25007
22. McGrath AP, Laming EL, Casas Garcia GP, Kvansakul M, Guss JM, Trewhella J, Calmes B, Bernhardt PV, Hanson GR, Kappler U, Maher MJ (2015) Elife 4:e09066–e09066
23. Plitzko B, Havemeyer A, Kunze T, Clement B (2015) J Biol Chem 290:10126–10135
24. Enroth C, Eger BT, Okamoto K, Nishino T, Nishino T, Pai EF (2000) Proc Natl Acad Sci U S A 97:10723–10728
25. Doonan CJ, Stockert A, Hille R, George GN (2005) J Am Chem Soc 127:4518–4522
26. Coelho C, Foti A, Hartmann T, Santos-Silva T, Leimkuhler S, Romao MJ (2015) Nat Chem Biol 11:779–783
27. Dobbek H, Gremer L, Kiefersauer R, Huber R, Meyer O (2002) Proc Natl Acad Sci U S A 99:15971–15976
28. Gnida M, Ferner R, Gremer L, Meyer O, Meyer-Klaucke W (2003) Biochemistry 42:222–230
29. Gladyshev VN, Khangulov SV, Stadtman TC (1994) Proc Natl Acad Sci U S A 91:232–236
30. Wagener N, Pierik AJ, Ibdah A, Hille R, Dobbek H (2009) Proc Natl Acad Sci U S A 106:1055–11060
31. George GN, Hilton J, Temple C, Prince RC, Rajagopalan RC (1999) J Am Chem Soc 121:1256–1266
32. Li HK, Temple C, Rajagopalan KV, Schindelin H (2000) J Am Chem Soc 122:7673–7680
33. Chan MK, Mukund S, Kletzin A, Adams MWW, Rees DC (1995) Science 267:1463–1469
34. Rappé AK, Goddard WA (1982) J Am Chem Soc 104:448–456
35. Groom CR, Bruno IJ, Lightfoot MP, Ward SC (2016) Acta Cryst B72:171–179
36. Qiu JA, Wilson HL, Pushie MJ, Kisker C, George GN, Rajagopalan KV (2010) Biochemistry 49:3989–4000
37. George GN, Garrett RM, Prince RC, Rajagopalan KV (1996) J Am Chem Soc 118:8588–8592
38. George GN, Garrett RM, Prince RC, Rajagopalan KV (2004) Inorg Chem 43:8456–8460
39. Johnson JL, Rajagopalan KV (1982) Proc Natl Acad Sci U S A 79:6856–6860
40. Rajagopalan KV (1991) In: Meister A (ed) Advances in enzymology and related areas of molecular biology. Wiley, New York, pp 215–290

41. Romão MJ, Archer M, Moura I, Moura JJG, LeGall J, Engh R, Schneider M, Hof P, Huber R (1995) Science 270:1170–1176
42. Garton SD, Hilton J, Hiroyuki O, Crouse BR, Rajagopalan KV, Johnson MK (1997) J Am Chem Soc 119:12906–12916
43. McNaughton RL, Helton ME, Rubie ND, Kirk ML (2000) Inorg Chem 39:4386–4387
44. Cotelesage JJH, Pushie MJ, Grochulski P, Pickering IJ, George GN (2012) J Inorg Biochem 115:127–137
45. Pushie MJ, Cotelesage JJH, Lyashenko G, Hille R, George GN (2013) Inorg Chem 52:2830–2837
46. Warelow TP, Pushie MJ, Cotelesage JJH, Santini JM, George GN (2017) Sci Rep 7:1757/1–1757/7
47. Rây P, Dutt NK (1943) J Indian Chem Soc 20:81–92
48. Rzepa HS, Cass ME (2007) Inorg Chem 46:8024–8031
49. Dobbek H, Gremer L, Meyer O, Huber R (1999) Proc Natl Acad Sci U S A 96:8884–8889
50. George GN, Pickering IJ, Kisker C (1999) Inorg Chem 38:2539–2540
51. George GN, Pickering IJ, Pushie MJ, Nienaber K, Hackett MJ, Ascone I, Hedman B, Hodgson KO, Aitken JB, Levina A, Glover C, Lay PA (2012) J Synchrotron Radiat 19:875–886
52. Nienaber KH, Pushie MJ, Cotelesage JJH, Pickering IJ, George GN (2018) J Phys Chem Lett 9:540–544
53. George GN (2016) X-ray absorption spectroscopy of molybdenum and tungsten enzymes. In: Kirk ML, Hille R, Schulzke C (eds) Molybdenum and tungsten enzymes: spectroscopic and theoretical investigations. Royal Society of Chemistry, Series on Meta, pp 121–167, ISBN 978-1-78262-878-1
54. Harris HH, George GN, Rajagopalan KV (2006) Inorg Chem 45:493–495
55. Shih VE, Abroms IF, Johnson JL, Carney M, Mandell R, Robb RM, Cloherty JP, Rajagopalan KV (1977) N Engl J Med 297:1022–1028
56. Johnson JL, Coyne KE, Garrett RM, Zabot M-T, Dorche C, Kisker C, Rajagopalan KV (2002) Hum Mutat 20:74
57. Karakas E, Wilson HL, Graf TN, Xiang S, Jaramillo-Busquets S, Rajagopalan KV, Kisker C (2005) J Biol Chem 280:33506–33515
58. Peariso K, McNaughton RL, Kirk ML (2002) J Am Chem Soc 124:9006–9007
59. Izumi Y, Glaser T, Rose K, McMaster J, Basu P, Enemark JH, Hedman B, Hodgson KO, Solomon EI (1999) J Am Chem Soc 121:10035–10046
60. Fischer K, Barbier G, Hecht H-J, Mendel RR, Campbell WH, Schwarz G (2005) Plant Cell 17:1167–1179
61. George GN, Mertens JA, Campbell WA (1999) J Am Chem Soc 121:9730–9731
62. Cambell WH, Kinghorn KR (1990) Trends Biochem Sci 15:315–319
63. Qiu JA, Wilson HL, Rajagopalan KV (2012) Biochemistry 51:1134–1147
64. Havemeyer A, Bittner F, Wollers S, Mendel R, Kunze T, Clement B (2006) J Biol Chem 281:34796–34802
65. Schneider J, Girreser U, Havemeyer A, Bittner F, Clement B (2018) Chem Res Toxicol 31:447–453
66. Llamas A, Chamizo-Ampudia A, Tejada-Jimenez M, Galvan A, Fernandez E (2017) Biofactors 43:486–494
67. Rajapakshe A, Astashkin AV, Klein EL, Reichmann D, Mendel RR, Bittner F, Enemark JH (2011) Biochemistry 50:8813–8822
68. Giles LJ, Ruppelt C, Yang J, Mendel RR, Bittner F, Kirk ML (2014) Inorg Chem 53:9460–9462
69. Yang J, Giles LJ, Ruppelt C, Mendel RR, Bittner F, Kirk ML (2015) J Am Chem Soc 137:5276–5279
70. Kubitza C, Ginsel C, Bittner F, Havemeyer A, Clement B, Scheidiga AJ (2018) Acta Cryst F74:337–344
71. Pacheco A, Hazzard JT, Tollin G, Enemark JH (1999) J Biol Inorg Chem 4:390–401

72. Pushie MJ, George GN (2010) J Phys Chem B 114:3266–3275
73. Utesch T, Mroginski MA (2010) J Phys Chem Lett 1:2159–2164
74. Atashkin AV, Rajapakshe A, Cornelison MJ, Johnson-Winters K, Enemark JH (2012) J Phys Chem B 116:1942–1950
75. Feng C, Wilson HL, Hurley JK, Hazzard JT, Tollin G, Rajagopalan KV, Enemark JH (2003) Biochemistry 42:12235–12242
76. Emesh S, Rapson TD, Rajapakshe SA, Kappler U, Bernhardt PV, Tollin G, Enemark JH (2009) Biochemistry 48:2156–2163
77. McGrath AP, Laming EL, Casus Garcia GPM, Guss JM, Trewella J, Calmes B, Bernhardt PV, Hanson GR, Kappler U, Maher MJ (2015) eLife 4:e09066/1–26
78. Hsiao J-C, McGrath AP, Kielmann L, Kalimuthu P, Darain F, Bernhardt PV, Harmer J, Lee M, Meyers K, Maher MJ, Kappler U (2018) BBA-Bioenergetics 1859:19–27
79. Enroth C, Eger BT, Okamoto K, Nishino T, Nishino T, Pai EF (2000) Proc Natl Acad Sci U S A 97:10723–10728
80. Burt HM, Dutt YC (1989) J Cryst Growth 94:15–22
81. Pascual E, Addadi L, Andrés M, Sivera F (2015) Nat Rev Rheumatol 11:725–730
82. Williams JW, Bray RC (1981) Biochem J 195:753–760
83. Hawkes TR, George GN, Bray RC (1984) Biochem J 218:961–968
84. Dent CE, Philpot GR (1954) Lancet 266:182–185
85. Ichida K, Amaya Y, Nishino T, Hosoya T, Sakai O (1997) J Clin Invest 99:2391–2397
86. Bray RC (1975) In: Boyer PD (ed) The enzymes. Academic Press, New York, pp 299–419
87. Enroth C, Eger BT, Okamoto K, Nishino T, Nishino T, Pai EF (2000) Proc Natl Acad Sci U S A 97:10723–10728
88. Hille R (1996) Chem Rev 96:2757–2816
89. Kitamura S, Sugihara K, Ohta S (2006) Drug Metab Pharmacokinet 21:83–98
90. Self WT, Stadtman TC (2000) Proc Natl Acad Sci U S A 97:7208–7213
91. Wagener N, Pierik AJ, Ibdah A, Hille R, Dobbek H (2009) Proc Natl Acad Sci U S A 106:1055–11060
92. Cleere WF, Coughlan MP (1974) Biochem J 143:331–340
93. Kim JH, Ryan MG, Knaut H, Hille R (1996) J Biol Chem 271:6771–6780
94. Dobbek H, Gremer L, Kiefersauer R, Huber R, Meyer O (2002) Proc Natl Acad Sci U S A 99:15971–15976
95. Gnida M, Ferner R, Gremer L, Meyer O, Meyer-Klaucke W (2003) Biochemistry 42:222–230
96. Zhang B, Hemann CF, Hille R (2010) J Biol Chem 285:12571–12578
97. Gourlay C, Nielsen DJ, White JM, Knottenbelt SZ, Kirk ML, Young CG (2006) J Am Chem Soc 128:2164–2165
98. Zhang L, Johnson Nelson K, Rajagopalan KV, George GN (2008) Inorg Chem 47:1074–1078
99. Creevey NL, McEwan AG, Hanson GR, Bernhardt PV (2008) Biochemistry 47:3770–3776
100. Temple CA, George GN, Hilton J, George MJ, Prince RC, Barber MJ, Rajagopalan KV (2000) Biochemistry 39:4046–4052
101. George GN, Hilton J, Rajagopalan KV (1996) J Am Chem Soc 118:1113–1117
102. Schindelin H, Kisker C, Hilton J, Rajagppalan KV, Rees DC (1996) Science 272:1615–1621
103. Schneider F, Löwe J, Huber R, Schindelin H, Kisker C, Knäblein J (1996) J Mol Biol 263:53–69
104. McAlpine AS, McEwan AG, Shaw AL, Bailey S (1997) J Biol Inorg Chem 2:690–701
105. McAlpine AS, McEwan AG, Bailey SJ (1998) J Mol Biol 275:613–623
106. Baugh PE, Garner CD, Charnock JM, Collison D, Davies ES, McAlpine AS, Bailey S, Lane I, Hanson GR, McEwan AG (1997) J Biol Inorg Chem 2:634–643
107. George GN, Hilton J, Temple C, Prince RC, Rajagopalan KV (1999) J Am Chem Soc 121:1256–1266
108. Li HK, Temple C, Rajagopalan KV, Schindelin H (2000) J Am Chem Soc 122:7673–7680
109. Bray RC, Adams B, Smith AT, Bennett B, Bailey S (2000) Biochemistry 39:11258–11269

110. George GN, Nelson KJ, Harris HH, Doonan CJ, Rajagopalan KV (2007) Inorg Chem 46:3097–3104
111. Sparacino-Watkinsa C, Stolz JF, Basua P (2014) Chem Soc Rev 43:676–706
112. Coelho C, Romão MJ (2015) Protein Sci 24:1901–1911
113. Dias JM, Than ME, Humm A, Huber R, Bourenkov GP, Bartunik HD, Bursakov S, Calvete J, Calderia J, Carneiro C, Moura JJG, Moura I, Romão MJ (1999) Structure 7:65–79
114. Cerqueira NM, Pakhira B, Sarkar S (2015) J Biol Inorg Chem 30:323–335
115. Rendon J, Biaso F, Ceccaldi P, Toci R, Seduk F, Magalon A, Guigliarelli B, Grimaldi S (2017) Inorg Chem 56:4422–4434
116. Ceccaldi P, Rendon J, Léger C, Toci R, Guigliarelli B, Magalon A, Grimaldi S, Fourmond V (2015) Biochim Biophys Acta 1847:1055–1063
117. George GN, Bray RC, Morpeth FF, Boxer DH (1985) Biochem J 227:925–931
118. Maher MJ, Santini J, Pickering IJ, Prince RC, Macy JM, George GN (2004) Inorg Chem 43:402–404
119. Kloer DP, Hagel C, Heider J, Schulz GE (2006) Structure 14:1377–1388
120. Heider J, Szaleniec M, Sünwoldt K, Boll M (2016) J Mol Microbiol Biotechnol 26:45–62
121. Szaleniec M, Hagel C, Menke M, Nowak P, Witko M, Heider J (2007) Biochemistry 46:7637–7646
122. Szaleniec M, Borowski T, Schühle K, Nowak P, Witko M, Heider J (2010) J Am Chem Soc 132:6014–6024
123. Szaleniec M, Dudzik A, Kozik B, Borowski T, Heider J, Witko M (2014) J Inorg Biochem 139:9–20
124. Ellis PJ, Conrads T, Hille R, Kuhn P (2001) Structure 9:125–132
125. Warelow TP, Oke M, Schoepp-Cothenet B, Dahl JU, Bruselat N, Sivalingam GN, Leimkühler S, Thalassinos K, Kappler U, Naismith JH, Santini JM (2013) PLoS One 8:e72535
126. Conrads T, Hemann C, George GN, Pickering IJ, Prince RC, Hille R (2002) J Am Chem Soc 124:11276–11277
127. Hoke KR, Cobb N, Armstrong FA, Hille R (2004) Biochemistry 43:1667–1674
128. Mukhopadhyay R, Rosen BP (2002) Environ Health Perspect 110:745–748
129. Radabaugh TR, Aposhian HV (2000) Chem Res Toxicol 13:26–30
130. Glasser NR, Oyala PH, Osborne TH, Santini JM, Newman DK (2018) Proc Natl Acad Sci U S A 115:E8614–E8623
131. Grimaldi S, Schoepp-Cothenet B, Ceccaldi P, Guigliarelli B, Magalon A (2013) Biochim Biophys Acta Bioenerg 1827:1048–1085
132. Boyington JC, Gladyshev VN, Khangulov SV, Stadtman TC, Sun PD (1997) Science 275:1305–1308
133. Raaijmakers H, Macieira S, Dias JM, Teixeira S, Bursakov S, Huber R, Moura JJ, Moura I, Romão MJ (2002) Structure 10:1261–1273
134. Raaijmakers H, Romão MJ (2006) J Biol Inorg Chem 11:849–854
135. Mota CS, Rivas MG, Brondino CD, Moura I, Moura JJ, Gonzalez PJ, Cerqueira NM (2011) J Biol Inorg Chem 16:1255–1268
136. Robinson WE, Bassegoda A, Reisner E, Hirst J (2017) J Am Chem Soc 139:9927–9936
137. George GN, Colangelo CM, Dong J, Scott RA, Khangulov SV, Gladyshev VN, Stadtman TC (1998) J Am Chem Soc 120:1267–1273
138. George GN, Costa C, Moura JJG, Moura I (1999) J Am Chem Soc 121:2625–2626
139. Khangulov SV, Gladyshev VN, Dismukes CG, Stadtman TC (1998) Biochemistry 37:3518–3528
140. Berg IA, Kockelkorn D, Ramos-Vera WH, Say RF, Zarzycki J, Hügler M, Alber BE, Fuchs G (2010) Nat Rev Microbiol 8:447–459
141. Pancost RD, Sinninghe Damsté JS, de Lint S, van der Maarel MJEC, Gottschal JC (2000) Appl Environ Microbiol 66:1126–1132
142. Schwörer B, Thauer RK (1991) Arch Microbiol 155:459–465
143. Ponomarev DA, Shevchenko SM (2007) J Chem Educ 84:1725–1726

144. Seiffert GB, Ullmann GM, Messerschmidt A, Schink B, Kroneck PMH, Einsle O (2007) Proc Natl Acad Sci U S A 104:3073–3077
145. Liao R-Z, Yu J-G, Himo F (2010) Proc Natl Acad Sci U S A 107:22523–22527
146. Messerschmidt A, Niessen H, Abt D, Einsle O, Schink B, Kroneck PMH (2004) Proc Natl Acad Sci U S A 101:11571–11576
147. Weinert T, Huwiler SG, Kung JW, Weidenweber S, Hellwig P, Stärk HJ, Biskup T, Weber S, Cotelesage JJ, George GN, Ermler U, Boll M (2015) Nat Chem Biol:586–591
148. Boll M, Fuchs G (1995) Eur J Biochem:921–933
149. Culka M, Huwiler SG, Boll M, Ullmann GM (2017) J Am Chem Soc 139:14488–14500
150. Holm RH, Solomon EI, Majumdar A, Tenderholt A (2011) Coord Chem Rev 255:993–1015
151. Wagner T, Ermler U, Shima S (2016) Science 354:114–117
152. Niks D, Hille R (2018) Protein Sci. https://doi.org/10.1002/pro.3498
153. Johnson JL, Rajagopalan KV (1976) J Biol Chem 251:5505–5511
154. Stewart LJ, Bailey S, Bennett B, Charnock JM, Garner CD, McAlpine AS (2000) J Mol Biol 299:593–600
155. Garner CD, Stewart LJ (2002) Met Ions Biol Syst 39:699–726
156. Schoepp-Cothenet B, van Lis R, Philippot P, Magalon A, Russell MJ, Nitschke W (2012) Sci Rep 2:263/1–263/5
157. Williams RJP, Fraústo da Silva JJR (2002) Biochem Biophys Res Commun 292:293–299
158. Stetter KO (2006) Philos Trans R Soc B 361:1837–1843
159. Kletzin A, Adams MWW (1996) FEMS Microbiol Rev 18:5–63
160. Bruland KW, Lohan MC (2006) In: Elderfield H (ed) The oceans and marine geochemistry. Elsevier, North Holland, pp 23–47
161. Licht S (1988) J Electrochem Soc 135:2971–2975
162. Romão MJ, Coelho C, Santos-Silva T, Foti A, Terao M, Garattini E, Leimkühler S (2017) Curr Opin Chem Biol 37:39–47
163. Bassegoda A, Madden C, Wakerley DW, Reisner E, Hirst J (2014) J Am Chem Soc 136:15473–15476
164. Wedepohl KH (1995) Geochim Cosmochim Acta 59:1217–1232
165. Reich HJ, Hondal RJ (2016) ACS Chem Biol 11:821–841
166. Dolgova NV, Nehzati S, Choudhury S, Regnier N, Crawford AM, Ponomarenko O, George GN, Pickering IJ (2018) Biochim Biophys Acta 1862:2383–2392
167. Zhang L, Johnson Nelson K, Rajagopalan KV, George GN (2008) Inorg Chem 47:1074–1078
168. Nitschke W, Russell MJ (2009) J Mol Evol 69:484–496
169. Nitschke W, Russell MJ (2011) Bioessays 34:106–109

Struct Bond (2019) 179: 101–152
DOI: 10.1007/430_2019_31

Published online: 1 June 2019

The Role of the Pyranopterin Dithiolene Component of Moco in Molybdoenzyme Catalysis

Sharon J. Nieter Burgmayer and Martin L. Kirk

Contents

Abstract An overview of the pyranopterin dithiolene (MPT) component of the molybdenum cofactor (Moco) and how MPT may contribute to enzymatic catalysis is presented. The chapter begins with a brief review of MPT and Moco biosynthesis and continues to explore the nature of what is arguably the most electronically complex ligand in biology. To explore this complexity, we have dissected MPT

S. J. Nieter Burgmayer (✉)
Department of Chemistry, Bryn Mawr College, Bryn Mawr, PA, USA
e-mail: sburgmay@brynmawr.edu

M. L. Kirk (✉)
Department of Chemistry and Chemical Biology, The University of New Mexico, Albuquerque, NM, USA
e-mail: mkirk@unm.edu

into its relevant molecular components. These include the redox-active ene-1,2-dithiolate (dithiolene) and pterin moieties, which are bridged by a pyran that may be found in ring-opened or ring-closed configurations. The various redox possibilities of MPT bound to Mo are presented, along with the electronic structure of the redox components. MPTs are found to display a remarkable conformational variance in pyranopterin Mo enzymes. This is discussed in terms of a relationship to enzyme function and the potential for the observed non-planer distortions to reflect different MPT oxidation and tautomeric states. The chapter ends with a series of case studies featuring model compounds that highlight how biomimetic small molecule studies have contributed to furthering our understanding of the roles this remarkable ligand plays in the catalytic cycles of the enzymes.

Keywords Dithiolene · Moco · Molybdenum cofactor · Molybdenum enzymes · Molybdopterin · Pyranopterin

1 Introduction and Scope

Pyranopterin molybdenum (Mo) enzymes are essential to human health and contribute to a variety of key life processes in most organisms on earth. In humans the health significance of these enzymes is exemplified by their important roles in purine and amino acid catabolism [1], detoxification of xenobiotics [1], drug metabolism [1], prodrug activation and conversion [2–4], Moco sulfuration [5, 6], NO biosynthesis, [7, 8] nitrate/nitrite reduction leading to accumulation of NO in cardiac tissue [9], the production of reactive oxygen species (ROS) leading to oxidative stress and postischemic reperfusion injury [10, 11], and, critically, infant mortality deriving from Moco deficiency [12]. The pyranopterin Mo enzymes are unique since they require a biosynthesized pyranopterin dithiolene (molybdopterin; MPT or PDT) in order to function properly. There are three primary pyranopterin Mo enzyme families (Fig. 1), and these include the xanthine oxidase (XO), the sulfite oxidase (SO), and dimethyl sulfoxide reductase (DMSOR) families [9]. Pyranopterin Mo enzymes

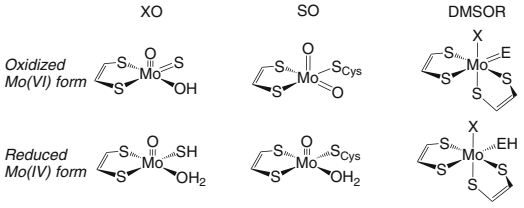

Fig. 1 Bond line drawings for consensus oxidized and reduced forms of the three canonical pyranopterin molybdenum enzyme families. For DMSOR family enzymes, E may be O, S, or Se, and X may be OH_2, OH, O_{Ser}, O_{Asp}, S_{Cys}, Se_{Sec}, or absent entirely

that catalyze the formal insertion of an oxygen atom into a substrate C-H bond (e.g., hydroxylation) belong to the XO family and include xanthine oxidoreductase (XOR) and aldehyde oxidase (AO) [13–18]. Most other pyranopterin Mo enzymes perform oxygen atom transfer reactions [19, 20], whereby an oxygen atom is transferred between the substrate and the Mo center. These enzymes include the sulfite oxidase family and DMSOR family enzymes. SO family enzymes include the mitochondrial amidoxime reductase component (mARC), nitrate reductases, and sulfite oxidizing enzymes. The DMSOR family enzymes are markedly broader in structure and reactivity than those found in the XO and SO enzyme families and include, for example, the DMSO reductases, formate dehydrogenases, and nitrate reductases, among others. With the exception of nitrite reduction to NO [21, 22], these enzymes primarily catalyze two-electron redox reactions [17, 23–25]. However, remarkably little is known regarding the role of the pyranopterin dithiolene in catalysis [26]. This lack of knowledge has severely impeded our ability to understand how MPT functions in the catalytic cycles of pyranopterin Mo enzymes. Although many excellent reviews have recently been published that detail various facets of pyranopterin molybdenum (Mo) enzyme structure, spectroscopy [14, 27, 28], reactivity, and cofactor biosynthesis [9, 13, 16, 28–35], there has not been a detailed review of the small molecule analog chemistry that has contributed greatly to our understanding of the electronic and geometric structure of the Mo-MPT interaction with an emphasis on MPT.

In this review, we start with an overview of Moco and Moco biosynthesis and proceed to discuss the geometric and electronic structure implications of the three primary components of MPT: the dithiolene, the pterin, and the pyran ring, the latter of which connects the redox active dithiolene and pterin entities. We highlight how the MPT ligand bound to Mo in the proteins adopts a near continuum of non-planer distortions that can be correlated with enzyme function [26]. These studies are suggestive of the pterin component of MPT existing in different oxidation states or tautomeric states. However, as to whether MPT actually exists in different oxidation states in functional enzymes remains an ongoing question that has yet to be solved. The final component of the review highlights how model chemistry has contributed to a greater understanding of the MPT component of Moco. The scope of this review combines an overview of the current knowledge regarding MPT and a collection of recent synthetic model studies to develop a more comprehensive understanding of MPT geometric and electronic structure, including how MPT contributes to catalysis.

2 Moco and Moco Biosynthesis

All Mo-containing enzymes, with the sole exception of nitrogenase, possess the molybdenum cofactor (Moco). Moco is comprised of a Mo ion bound to molybdopterin (MPT) via a dithiolene chelate that is fused to a pyranopterin moiety and bound to ancillary ligands. The basic structure of Moco was first elucidated by

Rajagopalan in 1982 from degradation studies of the cofactor [36]. A properly synthesized molybdenum cofactor (Moco) is essential for the function of a wide variety of molybdoenzymes, the vast majority of which catalyze two-electron transfer reactions that are coupled to (a) the formal transfer of an oxygen atom between the substrate and the molybdenum center of the catalytic active site (oxygen atom transfer) or (b) the formal insertion of an oxygen atom into a substrate C-H bond (hydroxylation). Although non-redox and one-electron transformations are known for Moco enzymes, oxygen atom transfer and hydroxylation reactions dominate. Critically, the oxygen atom transferred during the catalytic cycle either derives from or is ultimately converted to water. Thus, for the molybdenum hydroxylases (e.g., xanthine oxidoreductase and aldehyde oxidase), the O atom that is transferred derives from H_2O and not dioxygen. Furthermore, reducing equivalents are generated rather than consumed in the catalytic cycle of the molybdenum hydroxylases, [25] further distinguishing them from heme [37, 38], non-heme [37], and copper [39, 40] hydroxylating enzymes.

Most organisms are dependent on enzymes that possess Moco, and thus Moco biosynthesis and Moco insertion into apoenzymes represent critical life processes. Moco biosynthesis involves six gene products, is evolutionarily old [41], and is highly conserved [30], being present in LUCA the *l*ast *u*niversal *c*ommon *a*ncestor of all cells [42]. As a result, pyranopterin Mo enzymes are widely found in bacteria, archaea, and eukarya. The importance of Moco in humans is exemplified by the fact that mutations in the biosynthetic pathway lead to a variety of maladies and disease states [29]. For example, Moco deficiency (MoCD) [29] is a severe neonatal metabolic disorder that results in neurodegeneration and infant death due to a loss in sulfite oxidase (SO) activity [29].

Our understanding of pyranopterin molybdenum enzymes is important, since these enzymes are essential to human health and life processes and catalyze a wide variety of important chemical transformations in the metabolic pathways of carbon, nitrogen, and sulfur compounds. The unique Mo-bound pyranopterin dithiolene (Mo-MPT = Moco) cofactor is biosynthesized by a highly conserved multistep pathway [43]. In humans, MOCS and GEPHYRIN proteins are involved in Moco biosynthesis, with bacteria and plants possessing analogous proteins for the construction of Moco [30].

Moco biosynthesis can be described as a four-step process as detailed in Fig. 2 [5, 6, 29, 30, 43, 44]. Here, the first step begins with the conversion of guanine triphosphate (GTP) to cyclic pyranopterin monophosphate (cPMP), and this cyclization reaction is catalyzed in humans by the MOCS1A and MOCS1B proteins. In the second step, the MOCS2A, MOCS2B, and MOCS3 proteins convert cPMP to MPT, resulting in the formation of the dithiolene chelate via sulfur insertion into cPMP. The formation of adenylated MPT (MPT-AMP) is catalyzed by GEPHYRIN-G prior to MPT-AMP binding to GEPHYRIN-E. Here, the multistep Moco biosynthetic pathway culminates in the biochemical activation of molybdate. This final biosynthetic step involves Mo insertion (from molybdate, MoO_4^{2-}) into MPT, which is catalyzed in humans, plants, and bacteria by insertase proteins. This biosynthetic pathway is important, since a properly constructed Moco is essential

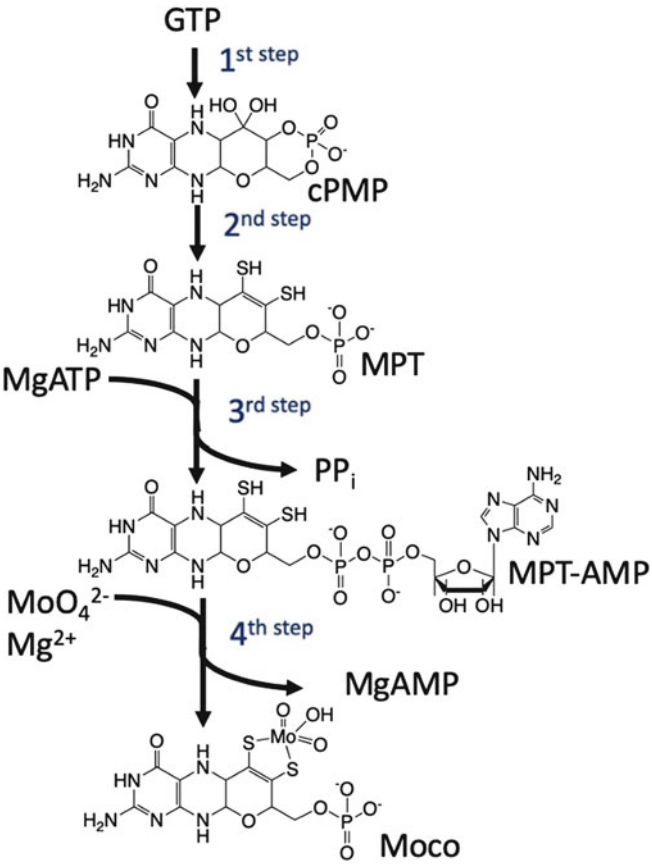

Fig. 2 Proposed mechanism for Moco formation (Adapted from [46])

for human life processes with Moco deficiency resulting in severe neurological disorders and infant mortality [12, 29].

Considerable progress has been made regarding our understanding of the biosynthetic mechanism for the synthesis of MPT from cPMP and its conversion to MPT-AMP, the basic organic component of Moco, in the third step of the sequence. Originally, it was thought that AMP derived from MPT-AMP hydrolysis was necessary for the formation of adenosine-5′-phosphomolybdate [45], a proposed activated molybdate species for the catalyzed molybdate insertion reaction. However, this no longer appears to be a viable mechanism based on recent structural work [46, 47]. It has more recently been suggested that the AMP from MPT-AMP may serve as an anchor to properly position the MPT dithiolene for eventual binding to enzyme-bound molybdate [46, 47]. Thus, the final molybdenum insertion steps remain the least understood component in the biosynthetic formation of Moco.

Finally, Moco as depicted in Fig. 2 may be further modified for use in xanthine oxidase and DMSO reductase family enzymes. Molybdenum sulfurase proteins catalyze the insertion of a terminal sulfido (thio) ligand into the Mo first coordination sphere for a highly specialized role [48, 49] as a formal hydride acceptor in xanthine oxidase family enzymes (e.g., xanthine oxidoreductase, aldehyde oxidase). Additional modifications are also found in enzymes from archaea and bacteria, where a nucleotide is attached to the MPT phosphate to form a dinucleotide version of the cofactor (Fig. 3). Bacterial enzymes of the DMSO reductase family possess a bis-MGD cofactor, and this is obtained by the addition of GMP to the MPT terminal phosphates of a Mo bis-MPT cofactor (Fig. 3). Moco is therefore comprised of the molybdenum ion and either one unmodified, one modified, or two modified MPT ligands where modification is due to dinucleotide incorporation [50].

In the enzymes, the molybdenum ion is also coordinated by additional ligands that may include amino acid donors (Fig. 1). In the xanthine oxidase and sulfite oxidase enzyme families, MPT is found to be chelated to the Mo ion in a stereospecific manner [51]. These two stereospecific configurations are termed "up," for XO family enzymes and "down" for SO family enzymes, where "up" and "down" are in reference to the position of the terminal oxo (oxido) ligand. Pictorial descriptions of these two configurations are given in Fig. 4.

Although a variety of roles have been proposed for MPT in the catalytic cycles of pyranopterin molybdenum enzymes [26, 27, 52–54], the exact role of this intricate ligand remains an area of intense study. Primary roles postulated for MPT include functioning as an anchor to firmly bind Moco to the protein, a modulator of the catalytic active site reduction potential [14, 55–59], a contributor of the redox equivalents necessary for performing two electron reductive transformations of substrates coupled to oxygen atom transfer [60], and an electron transfer conduit

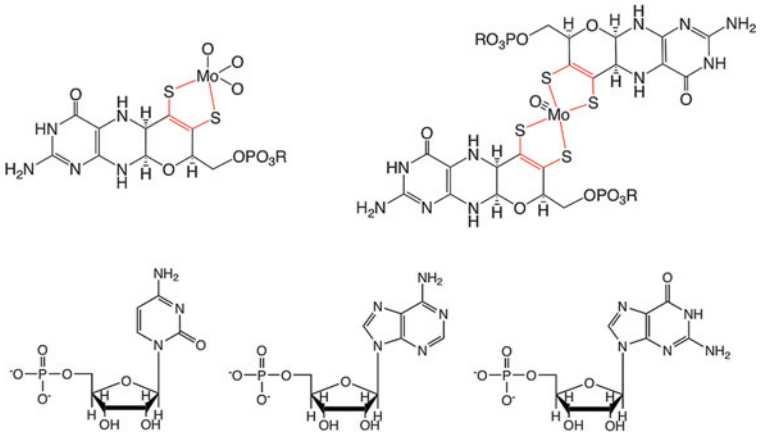

Fig. 3 *Top*: two versions of the molybdenum cofactor (Moco) with the dithiolene chelate shown in red. *Bottom:* the R group may be H or one of the depicted nucleotides

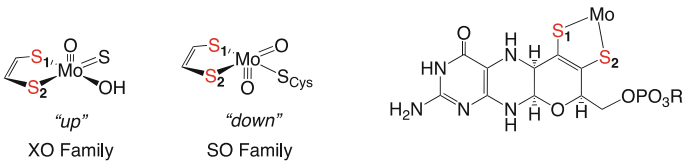

Fig. 4 Stereospecific configurations of MPT relative to the apical oxo ligand in oxidized members of the XO ("up") and SO ("down") enzyme families

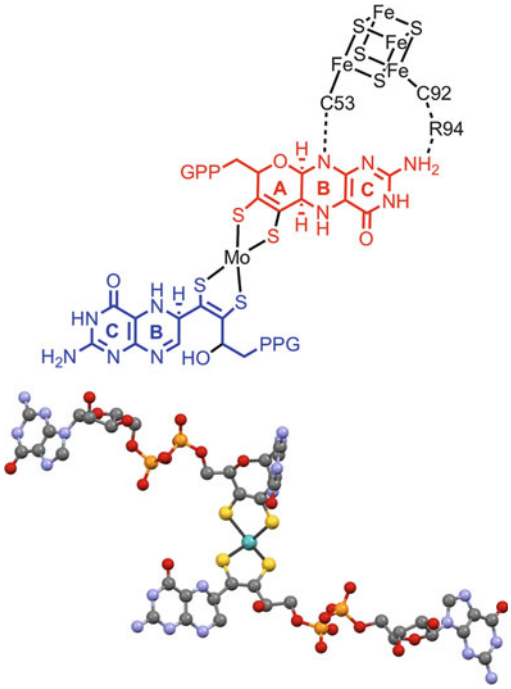

Fig. 5 (*Left*) The two pterin dithiolene ligands of the periplasmic nitrate reductase NarGHI from *E. coli* PDB 1Q16. The pyranopterin dithiolene is comprised of pyrimidine (C), pyrazine (B), and pyran (A) rings of the proximal MPT (red) adjacent to the [4Fe-4S] cluster FS0, and the distal MPT (blue) is bicyclic. Dashed lines represent hydrogen bonding interactions between Moco and FS0. A bidentate carboxylate interaction from Asp222 completes the Mo coordination sphere. PPG denotes a guanosine dinucleotide group (*right*). Detailed view of Moco from NarGHI illustrating the markedly different conformations of the proximal vs distal pterin regions. (Obtained with permission from (JACS, 2018, 140, 12808–12818). Copyright (2018) American Chemical Society)

that properly couples the molybdenum ion with other intraprotein electron transfer centers (e.g., 4Fe4S, 2Fe2S, FAD, heme) or electron transfer sites exogenous to the enzyme [15, 61]. The importance of synergistic interactions between the pterin ring system and the dithiolene in catalysis is supported by a number of recent enzyme crystal structures which show that the pyran ring of the ligand can exist in either a ring-closed pyrano form or a non-cyclized open form (Figs. 4 and 5) [62–64].

Interestingly, MPT is not covalently attached to the protein but is bound to the protein via an extensive network of hydrogen bonds that vary among different enzymes. Structural investigations of XO family enzymes using X-ray crystallography have provided evidence that Moco is tightly bound to the protein through 14 highly conserved hydrogen bonding interactions [65–68]. Moco is not covalently bound to the protein in XO family enzymes since there are no amino acid donors that serve as ligands to Mo. The nature of these hydrogen bonding interactions may serve as a means to modify electron and atom transfer reactivity in the catalytic cycles of the enzymes by changing the electronic structure of the pterin component of MPT, *vide supra*. This protein-MPT hydrogen bonding may allow MPT to convert protein vibrational energy into specific electronic structure changes at the Mo ion. This could occur through changes in the five-membered chelate ring fold angle [26, 69, 70], to control the Mo-dithiolene charge redistribution (electronic buffer effect [69]) either statically or dynamically during the course of catalysis [70].

Evidence supporting an electron transfer role derives from kinetic measurements of electron transfer between Mo, 2Fe2S I, 2Fe2S II, and FAD sites in xanthine oxidase [25, 61, 71, 72], resonance Raman spectroscopy [73], and the X-ray structure of bovine XDH, where the Mo – 2Fe2S I, 2Fe2S I – 2Fe2S II, and 2Fe2S II – FAD distances were determined to be 14.7 Å, 11.4 Å, and 7.6 Å, respectively [66]. All of these distances are well within the range for a superexchange electron transfer mechanism to be operative [74, 75].

The complex biosynthesis of Moco, its subsequent modifications for activity in a variety of pyranopterin molybdenum enzymes, and the postulated roles for the MPT component of Moco in catalysis speak to the remarkable utility of the basic cofactor structure in facilitating both the oxidative and reductive half reactions in the catalytic cycles of the enzymes. In the next section, we will deconstruct the individual components of MPT in an effort to understand how structural distortions, protonation states, oxidation state changes, and changes in Mo-$S_{dithiolene}$ covalency can further modulate the electronic structure of Moco to affect catalytic transformations in organisms from all three domains of life. Although this review will focus on the pyranopterin component (MPT) of Moco, we are cognizant of the synergy between the Mo ion and MPT and how Mo-S covalency further modulates the role of MPT in the catalytic cycles of the enzymes.

3 Chemical Dissection of the Pyranopterin Dithiolene (MPT)

A stated earlier, MPT is comprised of a dithiolene chelate and a heterocyclic pterin ring system, which are bridged by a pyran ring (Figs. 1, 2, 3, and 4) that may be found in the ring-opened form in some enzymes [62–64]. Thus, from a biosynthetic [41, 51], structural [26], and functional [14, 27] viewpoint, MPT is a very elaborate ligand that possesses the potential for additional redox possibilities at the dithiolene

and pterin components of the ligand [53, 55, 57, 76] and is arguably one of the most complex and electronically flexible ligands found in biology [14]. The dominant two-electron redox chemistry found in the catalytic cycles of nearly all pyranopterin-containing molybdenum enzymes can be accounted for by redox cycling through the Mo(IV), Mo(V), and Mo(VI) oxidation states of the metal center [25]. However, we stress that the actual redox state of the MPT is not currently known in the enzymes.

3.1 The Dithiolene

Recent studies of metallodithiolene chemistry highlight the remarkable redox flexibility of this chelating ligand in addition to the highly covalent nature of the metal-sulfur bonding scheme. The dithiolene ligand is known to be two-electron redox active and is therefore described as a non-innocent ligand [77–83] when bound to transition metal ions. Thus, the oxidation state of the dithiolene can vary between dianionic dithiolate, the radical monoanion [84], and neutral dithione/dithiete ligand forms (Fig. 6) [85]. The relevant valence molecular orbitals for the dianionic dithiolene are given in Fig. 7. Although Fig. 7 shows the highest energy occupied dithiolene orbitals, it omits the π-bonding ethenyl C=C orbital at deeper binding energy and the higher-energy C=C π*-antibonding orbital, the latter of which is always found to be unoccupied. The high-energy occupied dithiolene orbitals of Fig. 7 possess large MO coefficients on the sulfur atoms in agreement with

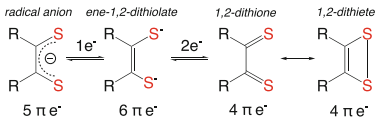

Fig. 6 Valence bond description of various dithiolene redox states

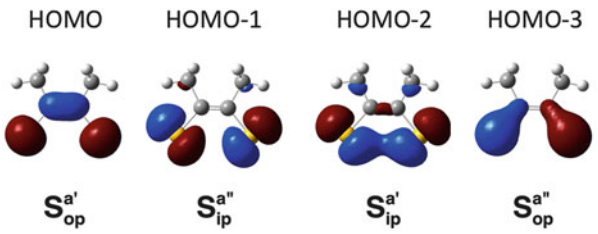

Fig. 7 Occupied molecular orbitals for the simple dithiolene $[S_2C_2Me_2]^{2-}$. C_{2v} symmetry labels are included as superscripts, and subscripts denote the orientation of the S p orbitals relative to the S-C=C-S plane (ip = in-plane; op = out-of-plane). Orbital energies: HOMO (0.0 cm^{-1}); HOMO-1 (−4,355 cm^{-1}); HOMO-2 (−7,662 cm^{-1}); HOMO-3 (−11,130 cm^{-1}). (Adapted with permission from (JACS, 2011, 133, 9762–9774). Copyright (2011) American Chemical Society)

experimental results from both photoelectron spectroscopy [69, 93–95] and optical spectroscopic studies [14, 19, 58, 76, 86–92].

The reduced dianionic dithiolene is considered a six-π-electron system with both S_{op} orbitals being occupied in addition to the C=C π-bonding orbital [89]. One-electron oxidation removes an electron from the S_{op} HOMO to yield the five-π-electron radical mono-anion form of the ligand. The two-electron oxidized, four-π-electron, neutral form of the ligand possesses two limiting resonance structures known as the dithione and the dithiete [89, 96, 97] ligand forms. If the two electrons are removed from the dianion HOMO, the dithione ligand form results. The dithione is highly electron withdrawing and can serve as a potent π-acceptor ligand under appropriate circumstances [76, 86, 98–101]. Formally, removal of two electrons from the HOMO-1 dithiolene orbital yields the dithiete ligand form, which possesses disulfide bonding character. Summarizing, the dithiolene's capacity for adopting different redox states and resonance forms drives the non-innocent metal-ligand redox behavior that has often been encountered in metallodithiolenes [84, 85, 102], and a valence-bond description of this interplay leads to extreme two-electron valence tautomeric forms of the biological Mo-dithiolene unit that range from Mo(VI)-dithiolene to Mo(IV)-dithione. Thus, oxidation-state assignments for the Mo and dithiolene should be made with caution. Although dithione, dithiete, or radical forms of the dithiolene ligand have yet to be confirmed in any pyranopterin Mo enzyme, the highly covalent nature of the Mo-dithiolene bond does not preclude this possibility. When the dithiolene ligand is coupled with the two-electron redox activity of Mo and the potential four-electron redox active capability of the pterin, this results in Moco being one of the most intricate electronically labile units in biology, allowing for the catalytic transformation of an extremely wide range of substrates using the same basic Moco catalyst.

An additional aspect of how the dithiolene can interact with the Mo ion is encountered when the Mo-dithiolene chelate ring folds, allowing for new Mo-dithiolene bonding interactions to arise. The four highest occupied dithiolene molecular orbitals of Fig. 7 can be further subdivided into a set of in-plane and out-of-plane orbitals relative to the S-C=C-S dithiolene plane, and they will mix with Mo 4d orbitals of the appropriate symmetry to form bonding and antibonding Mo-dithiolene molecular orbitals. For mono-oxo molybdenum dithiolene systems, the metal-based redox orbital is the Mo(xy) orbital (Fig. 8), which is oriented perpendicular to the strong field oxo ligand. Depending on the axis frame choice, this redox orbital may also be labeled as Mo(x^2-y^2). As an example of the

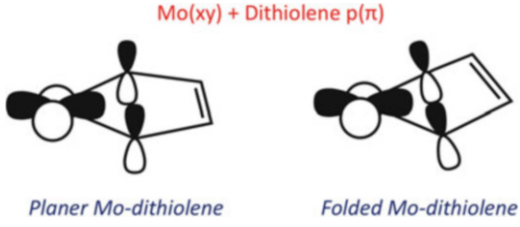

Fig. 8 Chelate ring sulfur folding effect on out-of-plane Mo(xy)-Sp(π) bonding

complexity associated with the highly covalent Mo-dithiolene bonding scheme, envelope fold distortions within the Mo-dithiolene chelate ring can mix in-plane and out-of-plane dithiolene orbitals in addition to modulating the degree of Mo-dithiolene covalency [70]. Extreme variations in this folding effect have recently been shown to accompany electron occupancy in the metal d(xy) orbital, which have been described in terms of vibronic coupling associated with the pseudo Jahn-Teller (pJT) effect, *vide infra* [86, 103]. These fold angle distortions occur along very low-frequency ($\lessapprox$100 cm^{-1}) modes [103], allowing for dynamic distortions in the proteins to dramatically control the degree of Mo-dithiolene coupling, modulate the enzyme redox potential, and couple the active site into superexchange pathways for electron transfer regeneration of the catalytically competent active site [90]. In pyranopterin molybdenum enzymes, fold angle distortions may be modulated through dynamic distortions involving the dithiolene component of MPT. As a result, the dithiolene may serve as a type of transducer, converting vibrational energy associated with protein conformational distortions to changes in the dithiolene fold angle during the course of catalysis [70]. These dynamic changes in fold angle could function to redistribute charge at the active site along both the atom- and electron-transfer reaction coordinates.

Thus, the dithiolene component of MPT is extremely important since it covalently connects the MPT pyranopterin to the Mo ion, providing a means to shuttle electrons in or out of the Mo center during the electron transfer half reaction of the catalytic cycle. This Mo-MPT interaction is modulated through electronic and geometric structural contributions to Mo-$S_{dithiolene}$ covalency. Dithiolene contributions to the role of MPT in electron transfer have been directly probed in bovine xanthine oxidase (XO) and *R. capsulatus* xanthine dehydrogenase (XDH) using a combination of resonance Raman spectroscopy and vibrational frequency computations [73]. The experimental approach took advantage of the known ability of these enzymes to oxidize lumazine to violopterin [104–106], producing a reduced Mo(IV) enzyme-product complex that possesses an intense charge transfer band, [107] which has been assigned as a Mo(IV) → violopterin metal-to-ligand charge transfer transition (Fig. 9) [73, 108].

Raman spectra collected on resonance with this MLCT band using the enzyme-catalyzed oxidation of 2,4-dithiolumazine and 4-thiolumazine to 2,4-dithioviolapterin (2,4-TV) and 4-thioviolapterin (4-TV), respectively, show at least nine low-frequency vibrational modes between 200 and 600 cm^{-1} [73]. The Raman spectra display in-plane bending modes that derive from the bound 2,4-TV and 4-TV product complexes in addition to important low-frequency vibrations that are assigned as arising from the asymmetric S-Mo-S dithiolene stretch vibration (Mo^{IV}-4-TV = 351 cm^{-1}; Mo^{IV}-2,4-TV = 351 cm^{-1}), the symmetric S-Mo-S dithiolene core vibration (Mo^{IV}-4-TV = 326 cm^{-1}; Mo^{IV}-2,4-TV = 326 cm^{-1}), an asymmetric ring distortion vibration with Mo-SH and pyranopterin contributions (Mo^{IV}-4-TV = 290 cm^{-1}; Mo^{IV}-2,4-TV = 286 cm^{-1}), and a complex vibrational mode that derives from a combination of dithiolene folding, Mo≡O rocking, and delocalized pyranopterin motions (Mo^{IV}-4-TV = 234 cm^{-1}; Mo^{IV}-2,4-TV = 236 cm^{-1}) (Fig. 10). Note this MLCT transition transfers electron density

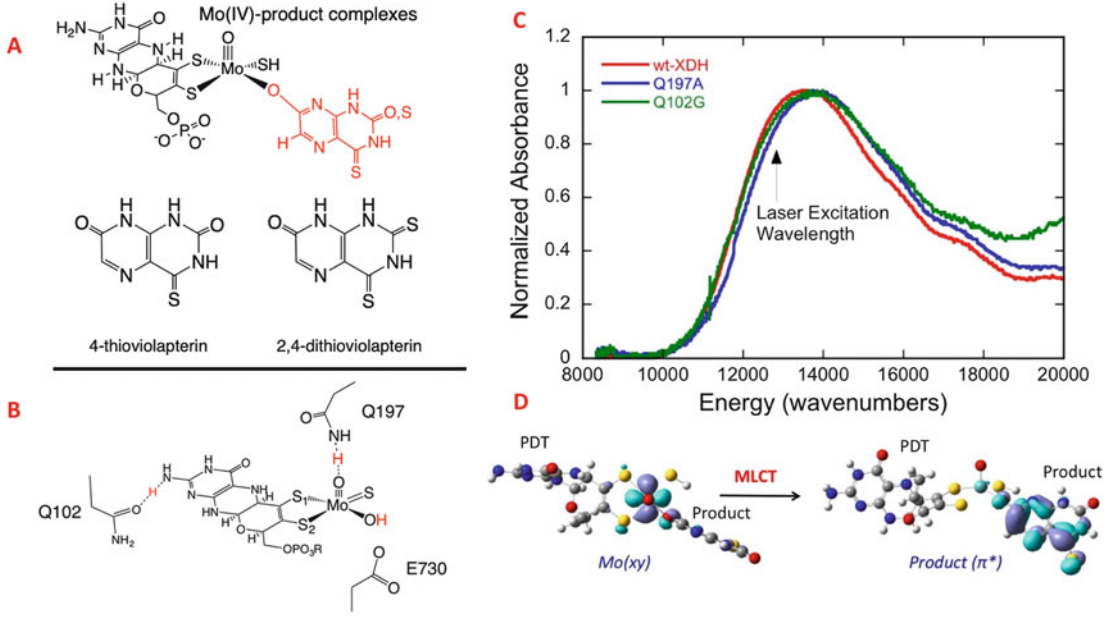

Fig. 9 (**a**) XO and XDH Mo(IV)-product complexes with 4-TV and 2,4-TV. (**b**) Schematic diagram of the *R. capsulatus* XDH active site. Both Q102 and Q197 have been suggested to form hydrogen bonds to the amino terminus of MPT and the terminal oxo ligand coordinated to Mo. (**c**) Electronic absorption spectra showing NIR MLCT transition for wt-XDH and its Q197A and Q102G variants reduced by 4-TL. (**d**) CASSCF calculation describing the nature of the Mo (xy) → product (π*) MLCT transition. (Adapted with permission from Inorganic Chemistry, 2017, 56, 6830–6837. Copyright (2017) American Chemical Society)

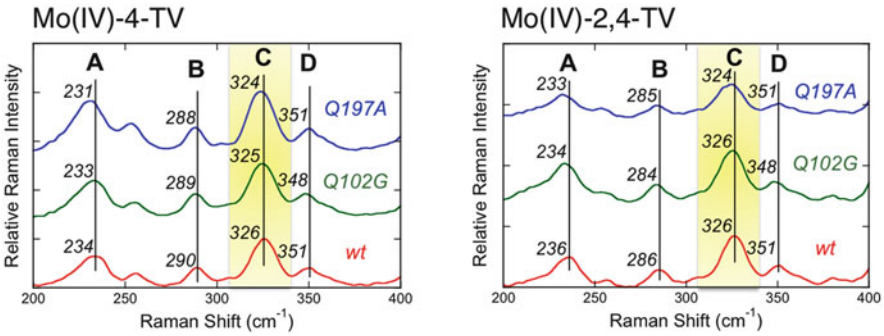

Fig. 10 Low-frequency rR spectra for wt, Q102G, and Q197A XDH. Mo(IV)–4-TV (*left*) and Mo(IV)–2,4-TV (*right*). Raman spectra collected on resonance with the Mo(IV)–P MLCT band using 780 nm laser excitation (Adapted with permission from Inorganic Chemistry, 2017, 56, 6830–6837. Copyright (2017) American Chemical Society)

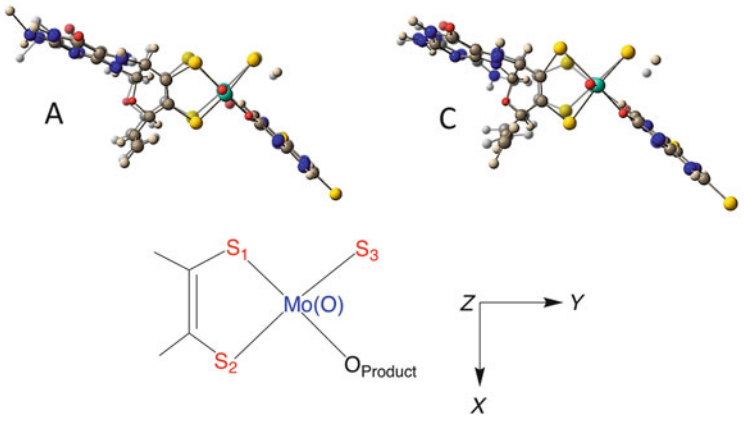

Fig. 11 Normal-mode depictions for vibrational bands A and C in FigIII.A.4 in the RcXHD Mo(IV)–2,4-TV enzyme-product intermediate. The vibrational modes are shown as a superposition of the maximum and minimum normal-mode displacements during the vibration. The molecular orientations are directed looking down the Mo≡O bond (Adapted with permission from Inorganic Chemistry, 2017, 56, 6830–6837. Copyright (2017) American Chemical Society)

from the reduced metal to the 2,4-TV or 4-TV product ligand. As a result of the large charge redistribution in this MLCT transition, photoexcitation into this band results in instantaneous hole generation on the Mo caused by transferring a Mo(xy) redox orbital electron to the product molecule. The analysis of the XO/XDH resonance Raman data indicates that the effects of this hole generation on Mo are felt all the way to the amino terminus of the MPT ligand (Fig. 9). Thus, it appears that Mo(IV) → Mo (V) oxidation is coupled to low-frequency Moco vibrations that involve the dithiolene and pterin components of MPT (Figs. 10 and 11), supporting the hypothesis that MPT is involved in enzymatic electron transfer, likely as an active conduit for shuttling electrons out of Mo and to the proximal 2Fe2S I cluster.

A similar large number of low-frequency vibrational modes have previously been observed in the resonance Raman spectra of plastocyanin and azurin blue copper proteins with photoexcitation into their $S_{Cys} \rightarrow Cu$ ligand-to-metal charge-transfer bands [109]. In these blue copper electron transfer proteins, the large number of resonantly enhanced vibrations results from a high degree of kinematic coupling between the $Cu-S_{Cys}$ stretching coordinate and the side chain of the cysteine ligand. This interpretation was used in blue copper proteins to define an electron transfer pathway that directly involves the coordinated cysteine. In XO/XDH, and likely any other pyranopterin Mo enzymes that used MPT as an electron transfer conduit, the observation of a large number of resonantly enhanced low-frequency vibrational modes may be taken as evidence that the dithiolene chelate directly couples the Mo ion into superexchange pathways for electron transfer that directly involve the pyranopterin component of MPT.

Little data exist that allow for a direct comparison of low-frequency rR vibrations in XO/XDH with other pyranopterin molybdenum enzymes [110–113]. However, for reduced Mo(IV) forms of DMSO reductase, the corresponding S-Mo-S core vibrations are observed at 352 cm^{-1} and 383 cm^{-1}, and these are observed to shift to 350 cm^{-1} and 370 cm^{-1} in the oxidized enzyme. Similar Mo-dithiolene core vibrations have also been observed at 393 cm^{-1} and 362 cm^{-1}, in the model compound Tp*Mo(bdt) (bdt = benzene-1,2-dithiolate) [70, 90]. In other Tp*Mo (dithiolate) complexes, frequency differences within the five-membered Mo-dithiolene core structure and the degree of mode mixing between symmetric stretching and bending coordinates are likely due to electronic structure differences between the different ligands, changes in the Mo-dithiolene S---S fold angles (Fig. 8), or differences in the degree of Mo(d) – S(p) orbital overlap. We note that bdt is not a "true" dithiolene as found in reduced forms of MPT due to the delocalized π character in the benzene ring. While the frequency differences between DMSO reductase and XO/XDH are not completely understood at this time, the origin of these differences may lie in the fact that DMSO reductase possesses two coordinated MPT ligands, while XO/XDH possess only one, and the nature of Mo-MPT bonding may differ between these enzymes as a result of their different functions.

3.2 The Pterin

The pterin structure within the MPT ligand, while unusual, is not an unprecedented ring system in biochemistry. The pterin core is familiar as the characteristic heterocycle of folate biochemistry where folates are critical cofactors for C1 transfer in amino acid synthesis. Another well-studied pterin cofactor is biopterin which plays redox roles in several enzymes used in neurotransmitter biosynthesis and is also required in nitric oxide synthase that produces NO for biochemical signaling. Pterins are members of the larger pteridine heterocycle family that share the fused pyrimidine-pyrazine bicyclic ring system, but pterins are distinct from other pteridines in having amino and carbonyl substituents at the 2- and 4-positions,

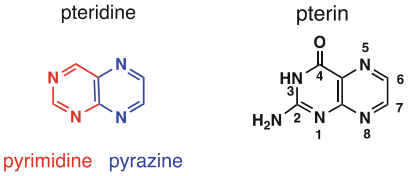

Fig. 12 The pteridine heterocyclic system and the pterin derivative

respectively (Fig. 12). An earlier review of the pterin component in Moco includes the many roles of pterin chemistry in biology, a discussion of synthetic methods for pterins, in addition to descriptions of relevant model syntheses [55].

By the time the pterin was discovered as a part of some unknown ligand in Moco [114], the roles of the pterin cofactors biopterin and the folates were already established as involving redox reactions. It is surprising therefore that redox roles for the pterin in MPT are not usually incorporated into the catalytic function of Mo enzymes. Three reasons are typically presented for why no pterin redox role is necessary. All the electrons involved in the overall substrate reaction have been accounted for. For example, redox titrations of XO have determined the total numbers of electrons involved are 2e− at Mo, 2 e− at FeS clusters, and 2e− at FAD [25, 115]. The structure of the MPT indicated from protein crystallography appears identical among all enzymes with only three exceptions [62, 63, 116] indicating no variation in MPT oxidation state. It should be noted that this premise ignores subtle conformational variation among all the pterins observed across the many Mo enzymes [26]. There has been no evidence from the protein studies that pterin redox occurs during turnover. This last claim is now challenged by recent reports where prereduction of isolated Mo enzymes necessary to initiate substrate turnover has been interpreted as occurring at the pterin in MPT [117, 118], and this hypothesis will be further discussed later in the Perspective section. Evidence for some pterin redox reactivity of Moco was obtained by Rajagopalan in redox titrations of sulfite oxidase [119, 120]. From these studies it was proposed that a different, as yet unknown, form of a dihydropterin was present in MPT.

Electrochemical redox chemistry for a simple monosubstituted pterin like biopterin operates according to the generalized scheme in Fig. 13 [121–125]. The pterin system can be reduced by a total of four electrons with four protons at the pyrazine ring. The semi-reduced dihydropterin state is accessible through several tautomers. The existence of these tautomers leads to a complicated overall scheme that relates the three main redox states: fully oxidized, semi-reduced or dihydro, and fully reduced or tetrahydro. One way to make sense of the scheme is to note that 2 e−/2 H+ oxidation of tetrahydropterin compared to the 2 e−/2 H+ reduction of oxidized pterin go through two *different* tautomers of semi-reduced dihydropterin (Fig. 13). Both of the redox partners of pterin and tetrahydropterin are unstable tautomeric forms of dihydropterin which rearrange to the more stable 7,8-dihydropterin. In summary, the distinctive aspects of pterin redox reactions are as follows: (a) a single structure is observed for the limiting forms of oxidized and reduced pterins, but many tautomers are possible for semi-reduced forms, and (b) most redox reactions are accompanied by rearrangements or tautomerizations. For example, in Fig. 13

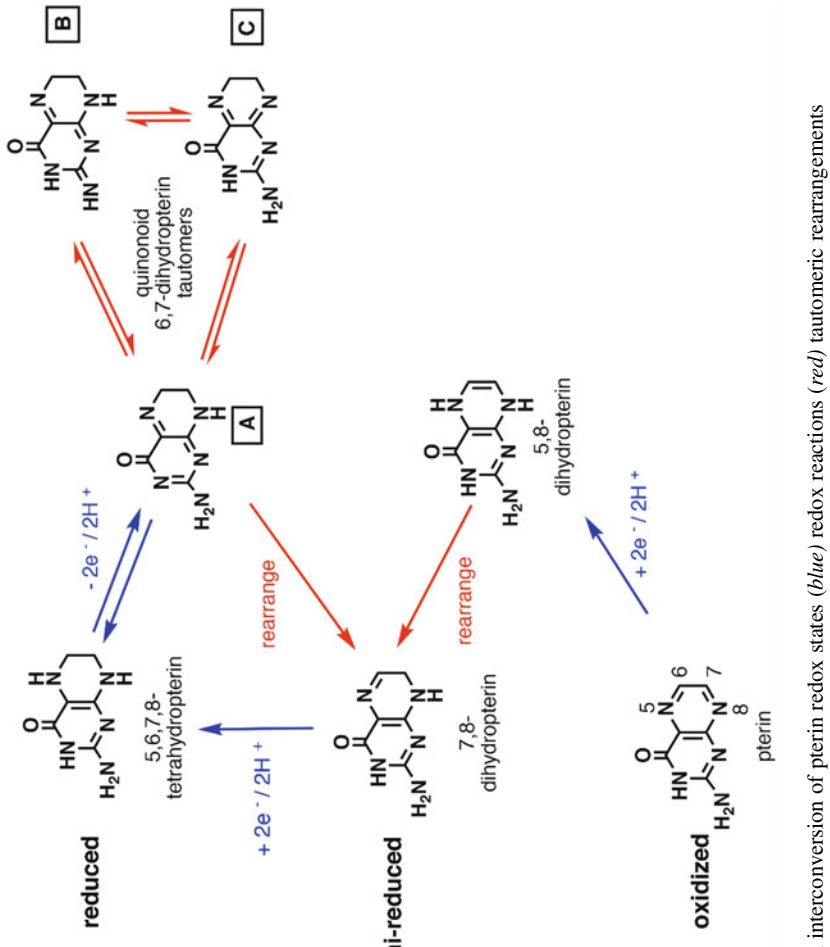

Fig. 13 The electrochemical interconversion of pterin redox states (*blue*) redox reactions (*red*) tautomeric rearrangements

oxidation of tetrahydropterin leads to a quinonoid dihydropterin of several possible tautomeric structures, but this dihydro-level pterin rearranges to a 7,8-dihydropterin, a structure known as the most thermodynamically stable. Similarly, reduction of pterin leads directly to a 5,8-dihydropterin that rearranges to 7,8-dihydropterin if only 2e−, 2H+ are provided.

Chemical reduction of oxidized pterins generally leading to the thermodynamic products, 7,8-dihydro and 5,6,7,8-tetrahydropterin most often uses catalytic hydrogenation or borohydride reagents, while oxidation of reduced pterins by O_2 may produce the fully oxidized pterin. Otherwise oxidants such as hydrogen peroxide, permanganate, or iodine are used to produce the oxidized form of a pterin [55, 126–129].

Redox reactions employed by other pterin cofactors involved in catalysis, e.g., biopterin and folic acid, employ the two reduced states. The biopterin cofactor of the aromatic amino acid hydroxylases cycles between tetrahydropterin and dihydropterin. Folate chemistry is initiated by tetrahydrofolic acid which undergoes addition and transformation of a C1 unit concomitant with oxidation of tetrahydrofolic acid to the dihydropterin level. Specific reductases return the semi-oxidized dihydropterin cofactors to their fully reduced states for continued catalysis [130–134].

3.3 The Pyran

The remaining structural piece of MPT, the pyran ring, was invisible to chemical methods applied to Moco, either as embedded in the protein or as isolated, and was only revealed through protein X-ray crystallography. Subsequently, the nearly universal presence of the pyran as part of the MPT structure, as gleaned from crystallography, has often resulted in the assertion that the static structure depicted in Fig. 2 is *the* structure of Moco. In fact, early on it was recognized that the pyran ring could be considered a result of an intramolecular cyclization reaction where the side-chain hydroxyl group has added across an oxidized 7,8-C=N bond of the pterin core [53]. This cyclization would rationalize the initially proposed structure of MPT with that observed by protein crystallography, as shown in Fig. 14. Later model

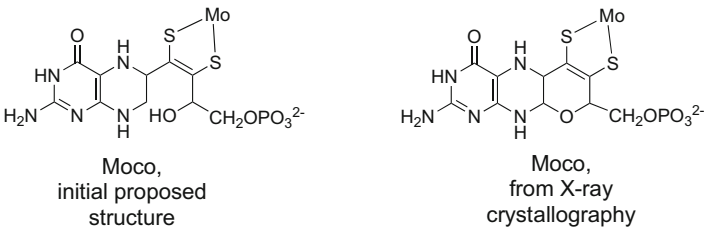

Fig. 14 (*Left*) Structure of Moco proposed by Rajagopalan in 1982. (*Right*) Moco determined by crystallography in 1995

work would confirm this hypothesis that pyran formation may indeed be a dynamic reaction of MPT in Mo and W enzymes (see Sect. 5.4).

A pyran ring fused to pterin or any pteridine was unknown until 1990 when the first evidence for a synthetic pyranopterin was reported by Viscontini et al. and further studied by Pfleiderer et al. [135, 136], just a few years prior to its surprising appearance in the first structural determination of the MPT ligand in 1995. The synthesis of a pyranopterin was an unanticipated intermediate in a new procedure aimed at synthesizing 6-substituted pterins such as neopterin. Of note is that the pyranoneopterin was isolated as a mixture with furanoneopterin, two cyclized forms of an unstable 5,6-dihydroneopterin reaction intermediate in equilibrium (Fig. 15), and foreshadowed the dynamic nature of the pyranopterin structure.

Incorporating the pyranopterin structure and its dynamic cyclization process into the already complicated pterin redox scheme in Fig. 13 adds yet more complexity. For example, as a pyranopterin, the pyrazine ring appears to be in a tetrahydro-redox state, but when the pyran ring is cleaved, the pterin is a dihydropterin. To gain some understanding of how to best view the redox reactivity of the pyranopterin system, the Burgmayer lab studied redox reactions and titrations of Pfleiderer's synthetic pyranopterin to gain some understanding regarding what reaction pathways were followed (Fig. 16) [54]. Through this work, it was clearly demonstrated that a

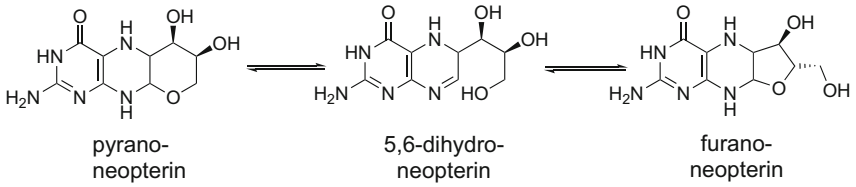

Fig. 15 First report of a pyranopterin detected as equilibrium mixture with an unstable 5,6-dihydropterin and a furanopterin

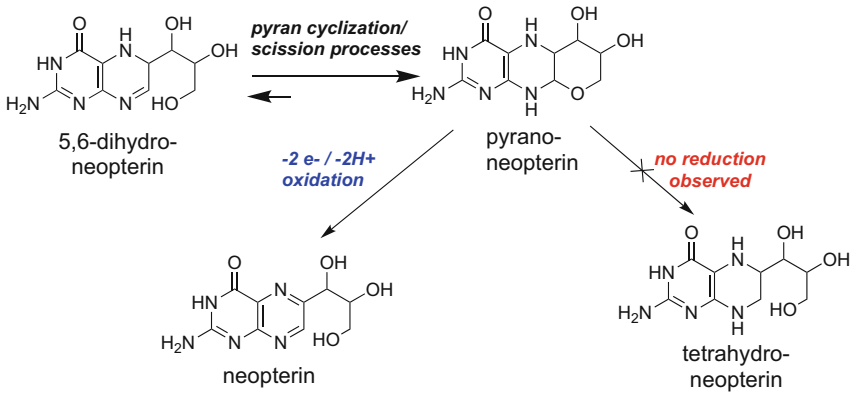

Fig. 16 Redox reactivity of a synthetic pyranopterin

pyranopterin behaves in oxidations as a dihydropterin, despite its structure possessing the saturated pyrazine structure characteristic of a tetrahydropterin. However, the pyranopterin was not able to be further reduced, reactivity consistent with the saturated pyrazine ring. Therefore, the addition of a pyran moiety to a pterin system significantly alters its redox behavior from that of a simple 6-substituted pterin, effectively limiting the 4 e−/4H+ redox chemistry typical of pterin to a single 2 e−/2H+ process.

At this point it is useful to introduce the concept of structural vs. functional tetrahydropterin, a distinction illustrated in Fig. 17. The two pterin molecules in blue both possess a fully reduced and saturated pyrazine ring and structurally are appropriately referred to as "tetrahydro" species. However, in redox reactions, these two pterins exhibit different behaviors because of the ability of the pyranopterin to ring open, exposing its camouflaged dihydropterin structure. Hence functionally, the reduced pyranopterin behaves as a dihydropterin (Fig. 17).

In this section, the characteristics of the three components of MPT – the dithiolene chelate, the pterin, and the pyran ring – have been described. What happens when these three pieces are combined in Moco will be addressed through consideration of recent model compounds in the next section.

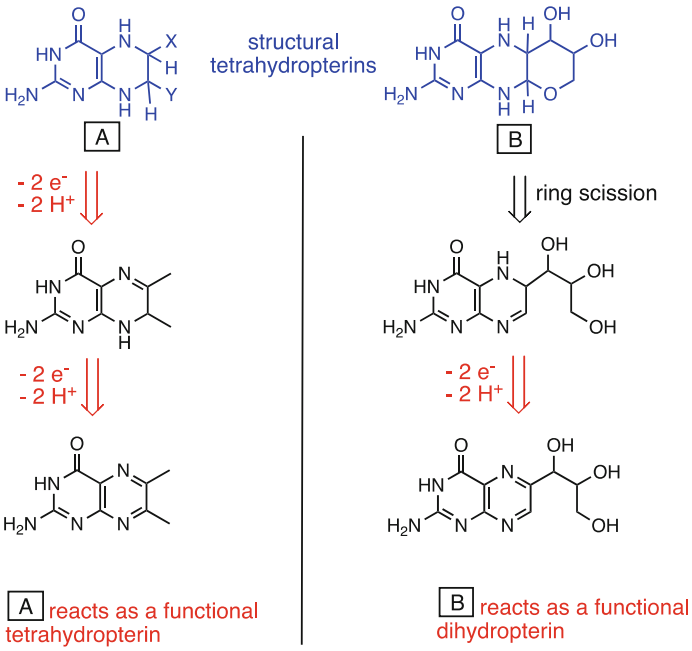

Fig. 17 Illustration of structural vs functional tetrahydropterins

4 What Do We Know About MPTs from Protein Crystallography?

Even though X-ray crystallography has confirmed the basic structure of MPT in members of the SO, XOR, and DMSOR enzyme families, the resolution of these structures is not yet high enough to determine the oxidation or protonation state of MPT directly through the observation of covalently bound hydrogens or bond length correlations. In the previous sections, we have detailed the extreme redox flexibility of MPT. Thus, a greater understanding of MPT electronic and geometric structure will provide much needed insight into how MPT functions in enzymatic catalysis. Obtaining this information from protein structural and spectroscopic studies, and from model systems is extremely important in order to determine the roles of this electronically labile ligand in the electron and atom transfer half reactions of pyranopterin molybdenum enzymes.

The conformations of 319 MPT ligands in 102 different protein structures [26] of pyranopterin molybdenum and tungsten enzymes have been analyzed in order to gain insight into the nature of protein-bound MPT ligands. Two different structure parameters (dihedral angles, red bonds in Fig. 18) have been used to correlate non-planer MPT distortions with enzyme function in members of the XOR, SO, and DMSO reductase enzyme families (Figs. 18 and 19). Interestingly, a linear correlation was observed when the β-dihedral angle is plotted as a function of the α-dihedral angle for these 391 MPTs. The MPTs were further shown to span a continuum of geometries

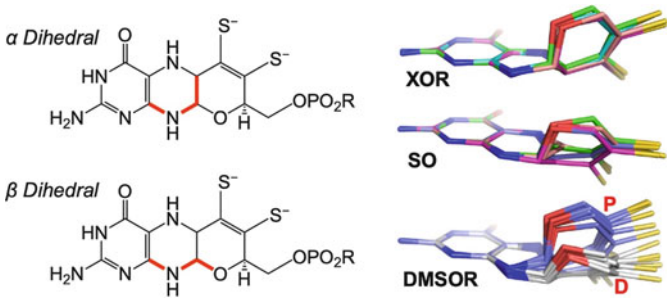

Fig. 18 (*Left*) Structure of the reduced tetrahydro form of MPT showing the two different dihedral angles (red bonds) that have been used to correlate non-planer MPT distortions with enzyme function. (*Right*) Pyranopterin conformations observed in XOR, SO, and DMSOR enzyme families. In this figure, the pyrimidine ring atoms were aligned in order to display the critical out-of-plane distortions associated with the piperazine and pyran rings. Examples of each family are shown. PDB codes for representative structures are provided in parentheses. XOR family enzymes: CO dehydrogenase (1FFV and 1N62); 4hydroxybenzoyl-CoA reductase (1RM6); quinoline-2-oxidoreductase (1T3Q). SO family enzymes: nitrate reductase (2BII); sulfite oxidase (1SOX); MsrQ (1XDQ); and sulfite dehydrogenase (2BLF). DMSOR family enzymes: DMSO reductase (2DMR); arsenite oxidase (1G8K); periplasmic nitrate reductase (2V3V); periplasmic nitrate reductase (3NYA); respiratory nitrate reductase (1R27); and polysulfide reductase (2VPZ). The carbon atoms of proximal (P) and distal (D) MPTs in the DMSO reductase family enzymes are depicted in blue (P) and gray (D)

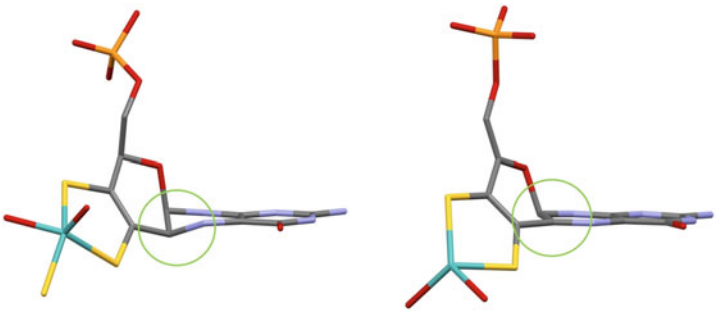

Fig. 19 Different MPT non-planer distortions: (*left*) Moco in xanthine dehydrogenase (PDB: 3UNC) and (*right*) Moco in nitrate reductase (PDB: 2BIH)

that correlate well with computed structures for tetrahydro, dihydro, and quinonoid dihydro MPT oxidation states. Computations show that the out-of-plane MPT distortions decrease as MPT is oxidized from tetrahydro → dihydro → oxidized. Furthermore, the observed MPT conformations appear to correlate with protein folds that define the XOR, SO, and DMSO reductase enzyme families. Although the data do not prove that the MPT ligands in these enzymes possess different oxidation states, the data allows one to hypothesize whether the MPT binding sites in the enzymes act to fine-tune and control metal-dithiolene covalency, redox potential, or MPT oxidation state. XOR family enzymes possess the largest non-planer distortions that correlate well with the fully reduced tetrahydro form of MPT. The MPTs found in SO family enzymes display markedly smaller out-of-plane distortions that correlate with more oxidized MPTs. Remarkably, this study revealed that the bacterial DMSO reductase family enzymes, which are coordinated by two MPTs, possess one XOR-type MPT and one SO-type MPT. This allows for maximal flexibility and implies that one MPT ligand may be used for vectorial electron transfer with endogenous and exogenous redox partners, while the second could function to fine-tune the redox potential of the site.

The nature of these non-planer MPT distortions provides nascent insight into how MPT conformations and perhaps even the oxidation state of MPT function to affect substrate transformation, the active site redox potential, and enzyme function. The MPT structural analysis [26] reveals a correlation between the conformation of the MPT ligand and the potential role of this ligand as an electron transfer conduit in the electron-transfer half reactions of the enzymes. In XOR family enzymes, a structural pathway is evident that consists of an electron transfer chain made up of two 2Fe2S clusters and FAD, which is the locus of the second substrate binding site, typically NAD^+ or dioxygen, that represents the ultimate electron acceptor. These enzymes appear to use more distorted tetrahydro MPT ligands, and when these results are combined with resonance Raman spectroscopic studies [137], this

provides compelling evidence that XOR family enzymes are involved in electron transfer reactivity and possess tetrahydro MPTs. In contrast, SO family enzymes possess less distorted MPTs. In these enzymes, electron transfer occurs between the Mo ion and a heme, where the direct vector connecting these two redox centers does not follow the MPT as in XOR family enzymes. As such, the MPT ligand in SO family enzymes is not likely to play a direct role in electron-transfer regeneration [138] but may still function to control the enzyme reduction potential. Finally, in enzymes that belong to the DMSOR enzyme family, electron transfer is potentially possible between the metal ion and the proximal (P) MPT, but it is not likely to occur via the distal (D) MPT. Thus, this study suggests that more distorted tetrahydro MPT ligands function as electron transfer conduits, while MPTs with more planer geometries play other roles in catalysis and likely control redox potentials to fine-tune the active site for specific substrate transformations [26].

5 Synthetic Model Contributions to Understanding the Role of MPT in the Molybdenum Cofactor

5.1 Highlights from the Evolution of Moco Models

The unique ligand for molybdenum and tungsten enzymes, MPT, was introduced earlier in this chapter, and the chemistry of each of its three main structural components was described. Our fascination with this ligand derives from its rich redox chemistry as well as from the unsolved mystery of what role MPT plays in the function of molybdenum and tungsten enzymes. We, and others, have approached the goal of identifying the role of MPT through the strategy of model chemistry [27, 56, 57, 76, 139, 140], and an overview of recent developments in synthetic models is presented in this section. Before delving into these developments, it is useful to put the contemporary model work into the larger context of several decades of model studies devoted to elucidating the details of how Moco performs catalysis within the enzyme.

For many years, Moco model design was limited to the atoms directly bound Mo, that is, the first coordination sphere. An early example of this focus on the first coordination sphere can be found in the determination that one or more sulfur atoms, likely as a thiolate, were bound to Mo. The incorporation of sulfur atoms was required in model complexes to reproduce the EPR spin-Hamiltonian parameters observed for the enzymes in various states [141–143]. This hypothesis was confirmed later by EXAFS experiments correlating data from models to data from the Mo site in holoenzymes and isolated Moco samples [144]. At this point it was recognized that all molybdoenzymes required at least one oxo ligand and two or three thiolate S donor ligands, though the origin of the thiolate was still unknown. The nature of oxo

coordination appeared to depend on Mo oxidation state, where reduced Mo(IV) forms bore only a single Mo≡O group whereas oxidized Mo(VI) forms possessed a dioxo, $Mo(=O)_2$ core in nitrate reductases and sulfite oxidases, while a Mo(≡O)(=S) motif [145] was typical in oxidized, Mo(VI) forms of xanthine oxidase and aldehyde oxidase. This information was elaborated by model work developed to mimic certain substrate reactivity, notably the simple transfer of oxygen atoms between Mo model complexes and O atom donors like DMSO and TMAO, and, subsequently, the oxygen atom transfer (OAT) mechanism became embedded in the field of molybdenum enzymes [146, 147]. Analyses of the thermodynamics of OAT model reactions began to correlate electronic variation at the Mo ion created by different coordination environments with reactivity. With the discovery of the pterin and the dithiolene moieties between 1982 and 1984, synthetic models that included the dithiolene chelate were synthesized, and their reaction chemistries explored. The dithiolene-containing models allowed detailed electronic structure studies which contributed to the next significant improvement in our understanding of how Moco functions [57, 70, 73, 76, 86, 87, 89, 90, 103]. Several key points emerged from Mo-dithiolene models (Fig. 20). The first finding is that a dithiolene chelate is in fact not electronically equivalent to two thiolate ligands due to the additional molecular orbitals involving the –C=C– portion of the dithiolene ligand (Fig. 20a) [90]. Another feature of dithiolene chelates is their ability to "buffer" or modulate the changes in the charge developed at the metal [69]. A third concept that resulted was the "oxo gate" notion, where the *cis*-position of the Mo=O group to the dithiolene was crucial in energetically isolating the redox orbital on Mo, which is the orbital involved in the oxidation or reduction during catalysis (Fig. 20b) [90, 148]. In

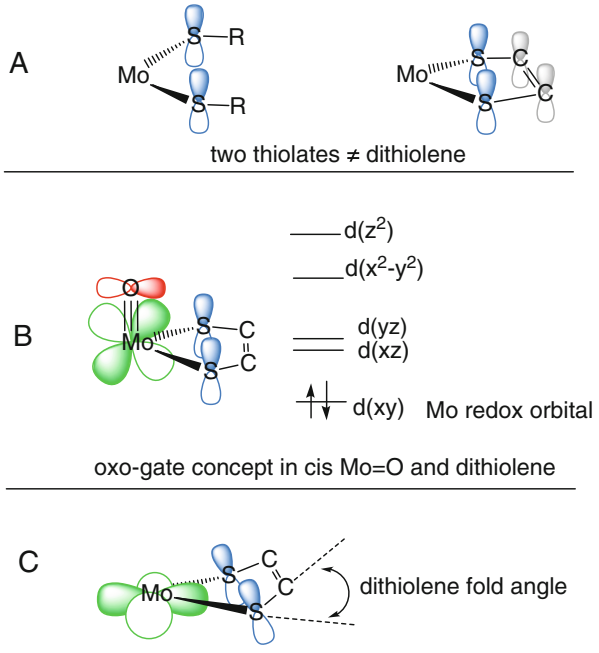

Fig. 20 Key aspects of dithiolene ligands in Moco illustrating: (**a**) difference in orbitals of a *bis*-thiolate and a dithiolene chelate; (**b**) the oxo-gate concept; (**c**) the dithiolene fold angle

addition to identifying these unique features of dithiolene ligands, the recognition of how the orientation of an additional thiolate ligand could tune the reactivity at Mo also emerged from these model studies [149, 150]. Lastly, the dithiolene fold angle, already introduced in Sect. 3, was identified as providing additional orbital interactions between Mo and dithiolene sulfur atoms (Fig. 20c).

This earlier body of work married studies of model compounds with data from enzymes and thereby accomplished a great deal and seemed to provide a nearly complete picture of what occurs at the Mo center during catalysis. However, nowhere in the fundamental concepts extracted from these many studies, based primarily on tweaking the first coordination sphere of molybdenum, was the presence of the obligatory pterin portion of Moco involved or required. This provided the impetus for this review chapter whose focus is on the second coordination sphere of Moco and beyond. The questions of "what does the pterin do?" and "how does the appended pterin alter the dithiolene?" are the motivations for the recent research that is presented next.

The organization of the remainder of this section considers three categories of Moco model complexes: models where the dithiolene ligand is in different oxidation states; models incorporating simpler N-heterocycles related to pterin, such as quinoxaline or pyrazine; and, lastly, models that incorporate a pterin-substituted dithiolene. Figure 21 illustrates some of the model structures for Moco and for the MPT ligand that will be discussed.

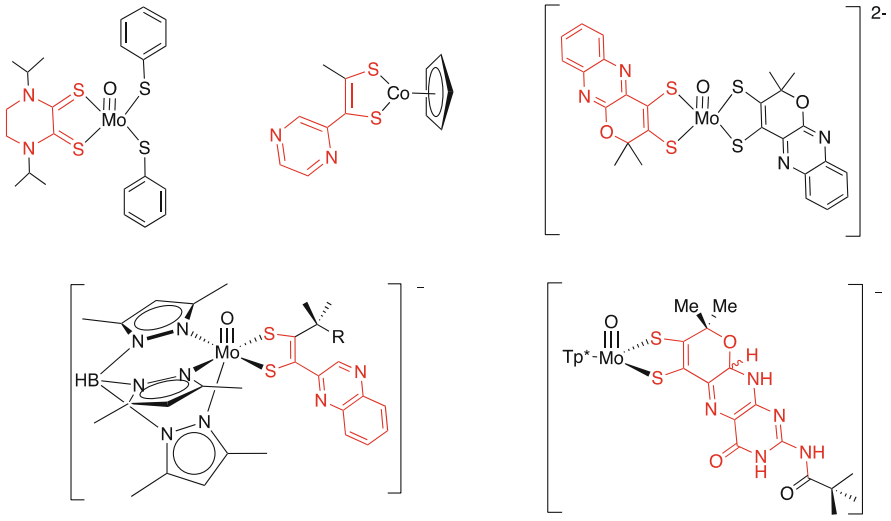

Fig. 21 Examples of recent Moco and MPT models highlighting in red the structures relevant to MPT

5.2 *Models with Different Dithiolene Oxidation States*

The redox capability, or "non-innocent" nature, of the dithiolene component of MPT has already been introduced. Here recent model complexes that were developed to explore the characteristics of dithiolate, dithione, and mixed thione/thiolate forms will be discussed.

The piperazine dithione ligand in Fig. 22 has a resonance tautomer where the thioamide moiety can be redrawn in an eneolate type of structure. The behavior of this fascinating chelate for metal ions has been explored.

The earliest report (2006) of a piperazine dithione ligand on molybdenum described $(Me_2Pipdt)Mo(CO)_4$. Here, the electronic structure of the chelating ligand was interpreted as being mainly in the dithione resonance form where it is a strong π-acid ligand and favors formation of Mo(0) complex [151]. DFT calculations were employed to help decipher the nature of the ligand redox state since bond distances alone can be ambiguous.

Subsequently in 2011, the isopropyl analog of the ligand in Fig. 22 was used to prepare an oxo-Mo complex possessing two piperazinyl dithione chelates $[MoO(i\text{-}Prpdt)_2Cl](PF_6)$ [76]. A detailed analysis of the electronic structure using absorption spectroscopy and time-dependent DFT calculations concluded that the ligands were best described by a 2:1 mixture of neutral dithione and zwitterionic dithiolate resonance forms in this d^2, Mo(IV) complex.

This interpretation is consistent with two observations: (1) two low-energy absorptions that are uncharacteristic of Mo(IV) dithiolene complexes and (2) the planar geometry at the N atoms. The absorptions were assigned as MLCT transitions arising from one-electron promotions from the Mo (HOMO) to unoccupied ligand π-orbitals involving combinations of both dithiolene ligands (LUMO and LUMO+1), where Mo electron density is shifted specifically to the $N_2C_2S_2$ portion of the chelate ligands. This model complex is a nice example of the concept of non-innocent dithiolene-type ligands, and it illustrates how the dithiolene in MPT might similarly adopt other resonance forms to effectively electronically buffer the Mo center against changes in charge that accompany redox processes. In this way, the dithiolene in MPT may play a fundamental role facilitating catalysis in molybdenum enzymes.

The i-Prpdt dithione ligand was used in a second Mo model complex reported in 2016, this time combined with two thiolate ligands in $[MoO(i\text{-}Prpdt)(SPh)_2]$ [86]. This mixed ligand complex was synthesized from $[MoO(i\text{-}Prpdt)_2Cl](PF_6)$ discussed above through ligand exchange of chloride and one dithiolene ligand by

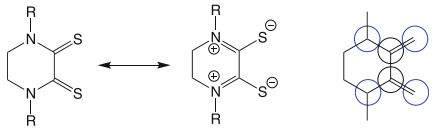

Fig. 22 (*Right*) A dithione chelate fused to a piperazine accesses a tautomeric dithiolene resonance form. (*Left*) The two resonance forms may contribute through $N_2C_2S_2$ π-delocalization in the ground state electronic structure

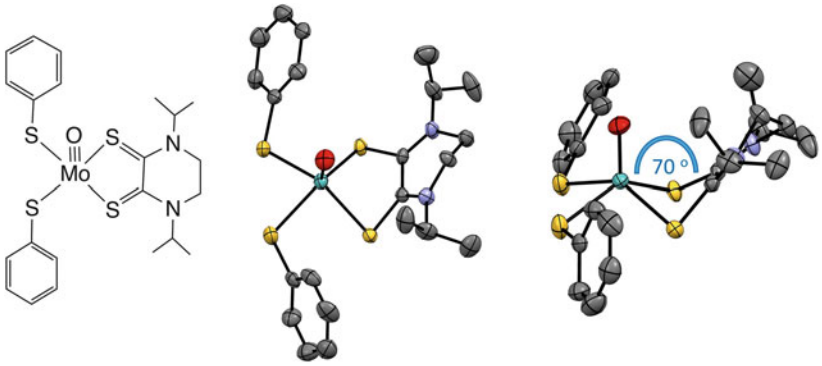

Fig. 23 Two views of the crystal structure of a mixed dithione-*bis*-thiolato complex [MoO(i-Prpdt)$(SPh)_2$]. (*Left*) The ChemDraw line drawing at left corresponds to the orientation of the left structure. (*Right*) The view emphasizes the extreme 70° dithiolene fold angle

two phenylthiolates. The most intriguing aspect of this complex is the remarkably large dithiolene fold angle of 70° adopted by the atoms of the chelate ring, Mo-S_2C_2. The fold directs the piperazine ring toward the oxo ligand on Mo (Fig. 23).

The unprecedented large fold angle has a major impact on the electronic structure, and this is most immediately detected in an intense charge transfer absorption which is uncommon for d^2 Mo(IV) complexes, as mentioned earlier. Aided by DFT time-dependent calculations and experimental data from resonance Raman, the strong absorption in the visible region of the electronic absorption spectrum was determined to result from several LL'CT transitions, involving significant mixing of occupied and virtual orbitals composed of dithione and -SPh thiolate ligand orbitals and the Mo(dx^2-y^2) redox orbital. The large fold angle serves to optimize orbital overlap between the filled Mo(dx^2-y^2) orbital and unoccupied out-of-plane π-orbital on the dithione. The authors note that the fold angle observed in [MoO(i-Prpdt)$(SPh)_2$] is a geometric distortion that results from charge flow in a direction opposite to that typically observed for dithiolene complexes of Mo in higher oxidation states. So, for a dithione chelate on d^2 Mo(IV), the fold angle favors electron donation from Mo → dithione, whereas in dithiolene complexes of d^0 Mo(VI), the large fold angle accomplishes a delocalization of electron density from the filled π-orbitals of the dithiolene to an empty dπ orbital of Mo.

5.3 Models Where the Dithiolene Bears Various N-Heterocyclic Substituents

Quinoxaline is a bicyclic N-heterocycle that is structurally related to pterin and was one of the first nitrogen heterocycles combined with a dithiolene chelate in model studies. Figure 24 illustrates the structural relationship of quinoxaline to pterin,

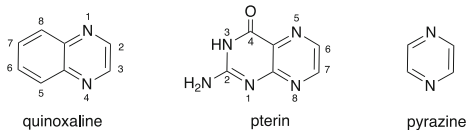

Fig. 24 The structural relationship between quinoxaline, pyrazine, and pterin systems

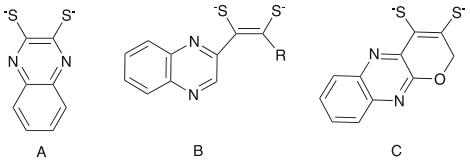

Fig. 25 Three types of quinoxaline-dithiolene ligands

including the conventional numbering scheme for each system. The pyrazine ring, shown at right in Fig. 24, is the shared structural feature between quinoxaline and pterin and is the ring directly attached to the dithiolene chelate. For this reason, some model studies have employed a simple pyrazine to approximate the electronic effect of pterin.

Quinoxaline has appeared in Moco models as a dithiolene substituent in several forms, as depicted in Fig. 25. These three quinoxalyl-dithiolene ligands will be highlighted in the examples that follow.

The 2,3-quinoxalyldithiolene ligand (qdt) (Fig. 25a) was the first example of a N-heterocycle incorporated into a molybdenum(IV) *tris*-(dithiolene) complex $[Mo(qdt)_3]^{2-}$, to explore the effect of protonation by trifluoroacetic acid (TFA) at the quinoxaline N atoms on the redox behavior of the complex [152]. Using cyclic voltammetry to monitor the reaction, a dramatic nearly 1 V positive shift in the reversible reduction couple of the parent complex was observed and interpreted as a net 3 e−reduction. This 3 e−reduction process was proposed to be the addition of one proton and one electron at each of the three quinoxaline ligands forming a *tris*-(quinoxalinium radical-dithiolene) Mo(IV) complex (Eq. 1).

$$\left[Mo(qdt)_3\right]^{2-} + 3H^+ + 3\,e- \rightarrow \left[Mo(Hqdt\cdot)_3\right]^{2-} \quad (1)$$

The presence of three quinoxaline-dithiolene ligands in $[Mo(qdt)_3]^{2-}$ thwarted attempts to identify individual protonated forms of the complex because of the complexity of equilibria involved. Hence, subsequent work to better understand the electronic changes due to protonation sought to isolate one quinoxalyldithiolene for study, and Garner and co-workers prepared a $CpCo(S_2C_2(H)(2\text{-quinoxaline}))$ complex [153]. This work led to a more recent investigation of the CpCo(dithiolene) system, $CpCo(S_2C_2(H)(R))$, where [R = phenyl, pyridin-3-yl or pyrazin-2-yl] (Fig. 26) [154]. The quinoxaline or other N-heterocycles in the recent work are connected to the dithiolene as illustrated by the middle structure in Fig. 25b. All of these CpCo(dithiolene) studies used electrochemistry and absorption spectroscopy, in addition to analysis by EPR spectroscopy and DFT molecular orbital calculations,

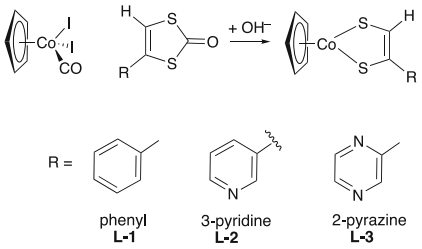

Fig. 26 A recently studied cobalt dithiolene system

to probe the electronic effects of N-heterocycle protonation. It should also be noted here that the effect of N-heterocycle protonation on the electronic structure of dithiolene had been investigated for Cp_2Mo-dithiolenes substituted with quinoxaline, as well as pyrazine and pyridine [155–157]. In that work, it was observed that the pKa values for protonated N-heterocycles on dithiolene-chelating Mo(IV) increase by 1–3 units as compared to the free heterocycles due to the resonance stabilization by the metallo-1,2-enedithiolate.

The recent CpCo(dithiolene) study also explored the effects of N-heterocyclic protonation on the electronic structure of CpCo-dithiolenes and the impact at the metal ion. As in the earlier electrochemical study of $CpCo(S_2C_2(H)(quin))$ (Cp, cyclopentadienide; quin, 2-quinoxaline), the presence of multiple tautomers of protonated quinoxaline N atoms was indicated for the CpCo complex of L-3 [153, 154]. The key findings from all studies of quinoxaline-, pyrazine-, and pyridine-substituted dithiolene chelates on either molybdenum or cobalt featured similar conclusions. Protonation at heterocycle N atoms shifted metal reduction potentials (Mo(V/IV), Co(III/II)) more positive, thereby favoring the reduced metal oxidation state. This is because N-protonation induces a reorganization of electron density throughout the entire dithiolene ligand since the N-heterocycle is in conjugation with the dithiolene. Figure 27 illustrates how this electronic reorganization can be illustrated by consideration of various resonance structures. Consistent with this interpretation, the CpCo(dithiolene) complexes where the appended N-heterocycle is oriented more co-planar to the dithiolene had larger shifts in the reduction potentials as more effective delocalization from dithiolene to ring was possible. In both the studies of $CpCo(S_2C_2H(quin))$ and $CpCo(S_2C_2H(pyz))$, two redox processes were observed that were assigned to the two tautomers of the protonated species A and D (Fig. 27).

Figure 27 foreshadows a significant outcome of placing a N-heterocycle substituent on a Mo-dithiolene. Protonating a ring N atom induces a shift of electron density from Mo or the dithiolene resulting in a partially oxidized thione-thiolate chelate. This electronic reorganization hints at the rich chemistry possible when a N-heterocycle is appended to a dithiolene on a redox active metal. N-heterocycle protonation also has a strong effect on electronic transitions in these complexes where the relative energies of d-based and ligand-based unoccupied orbitals can be switched, accessing luminescent emissive intraligand charge transfer (ILCT) excited states.

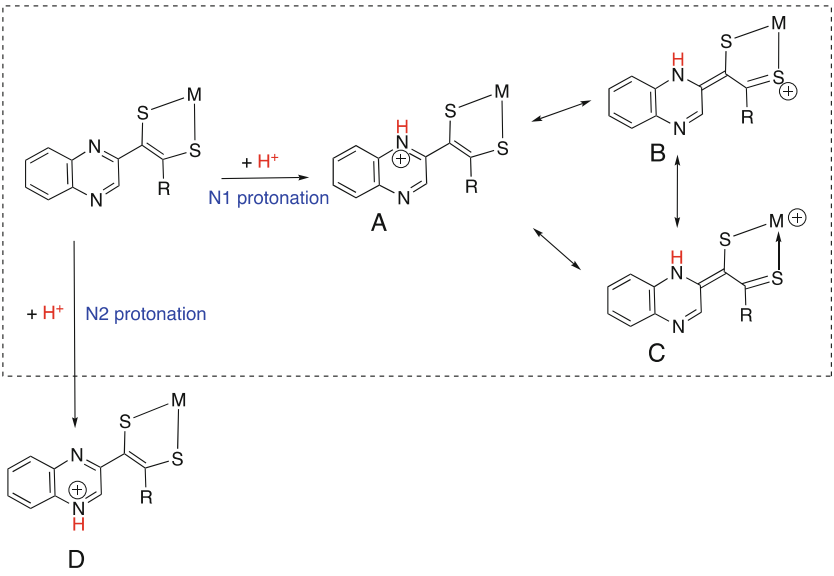

Fig. 27 Quinoxaline protonation can access other resonance forms including thiolate-thione chelates as observed for Co and Mo complexes. M = Cp_2Mo- and CpCo-

For paramagnetic CpCo(II)(dithiolene) complexes, the most significant results from EPR analyses are that the metal hyperfine values indicate a small contribution of metal orbitals to the SOMO (singly occupied molecular orbital). For example, DFT calculations indicate that the SOMO composition includes only ~15% Co orbitals. Small Mo hyperfine values were similarly reported for $[Cp_2Mo(V)(\text{dithiolene})]^+$ [158, 159].

DFT molecular orbital calculations on the three members of the $CpCo(S_2C_2(H)(R))$ system [154] show that the HOMO and LUMO composition is very similar across the complexes of L-1, L-2, and L-3 and is characterized by extensive mixing among orbitals from Co with π-orbitals of the dithiolene and N-heterocycle. However, significant differences were observed in the LUMO+1 and LUMO+2 orbitals. Specifically, for the pyrazine dithiolene complex of L-3, the LUMO+1 has a tenfold larger percentage of pyrazine character compared to the LUMO+1 orbitals of L-1 and L-2. In the protonated forms of the compounds, the HOMO and LUMO compositions are similar to those in the unprotonated parent complexes, while the LUMO+1 is largely localized (75–90%) on the N-heterocycles. Time-dependent DFT calculations for $CpCo(S_2C_2(H)(R))$ complexes revealed features of the absorption spectra due to intraligand charge transfer (ILCT) transitions from orbitals predominantly localized on the dithiolene to orbitals localized on the N-heterocycle. This observation will be repeated in other model studies later in this chapter. On the basis of their results, these researchers speculated that, should a form of MPT in which the pyran ring is open be integral to the catalytic cycle of the Mo- and W-enzymes, protonation of this ring-opened form of MPT could provide a

mechanism for linking the proton and electron transfer that is essential for the catalytic action of the Mo and W-oxotransferase enzymes. But in fact, later studies on a pyranopterin dithiolene Mo model will show that delocalization from dithiolene to pterin is favored *especially* when the pyran is maintained. Effects of pterin protonation similar to those presented here for dithiolenes substituted by quinoxaline and other N-heterocycles can be expected for complexes of pterin-dithiolenes, and these studies are currently underway in the Burgmayer labs.

The quinoxaline-dithiolene ligand has been elaborated to include a fused pyran ring in a series of model oxo-Mo-bis-dithiolene complexes (Fig. 28). Here, the pyrazine ring in the quinoxaline has been modified to access the most oxidized, the semi-reduced, and fully reduced redox states.

These Mo complexes were designed as "bioinspired" catalysts for electro- and photoreduction of protons to H_2 and of CO_2 to formate, mimicking the *bis*-MPT-Mo (=O) structure of Moco in formate dehydrogenase, an enzyme known to catalyze CO_2 reduction in nature [160, 161]. The synthetic strategy targets a di-protected dithiolene (R in Fig. 28) built onto a pyranoquinoxaline system. Deprotection of the thiolate groups generates a free dithiolate anion that is reacted immediately with $K_3Na[MoO_2(CN)_4]$ producing air-sensitive $[MoO[dithiolene)_2]^{2-}$ isolated as the Bu_4N^+ salt.

An X-ray crystal structure of the *bis*-qpdt Mo complex shows the typical distorted square pyramidal geometry around Mo which sits ~0.8 Å above the square plane formed by sulfur atoms from the two dithiolenes, each equidistant from the Mo atom [161]. The $[MoO[qpdt)_2]^{2-}$ complex is a very good photoactive catalyst for the reduction of protons to hydrogen when used in a photoredox system including $[Ru(II)bpy_3]^{2+}$ as photosensitizer and ascorbic acid as sacrificial electron donor. It was also observed that addition of protons generates a protonated complex that is more easily reduced than the dianionic parent complex and can electrocatalytically reduce H+ to H_2. Therefore, a 2e− prereduction of the Mo complex is speculated to be required for catalytic activity in the photoredox system. DFT calculations used to explore possible catalytic mechanistic pathways indicated that the first protonation occurs at a quinoxaline N atom and this step activates a 1e− reduction, but a second protonation occurs at the oxygen atom of Mo≡O, followed by a second 1 e− reduction and protonation to yield a molecule of H_2 via a Mo-hydride intermediate (Fig. 29).

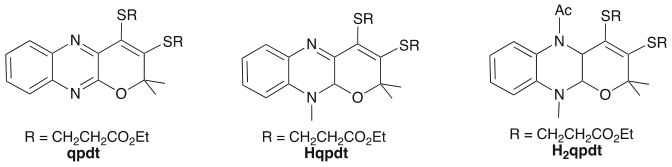

Fig. 28 (*Left*) Pyranoquinoxaline dithiolene ligands in three oxidation states: qpdt, oxidized; Hqpdt, semi-reduced; H_2pdt, fully reduced

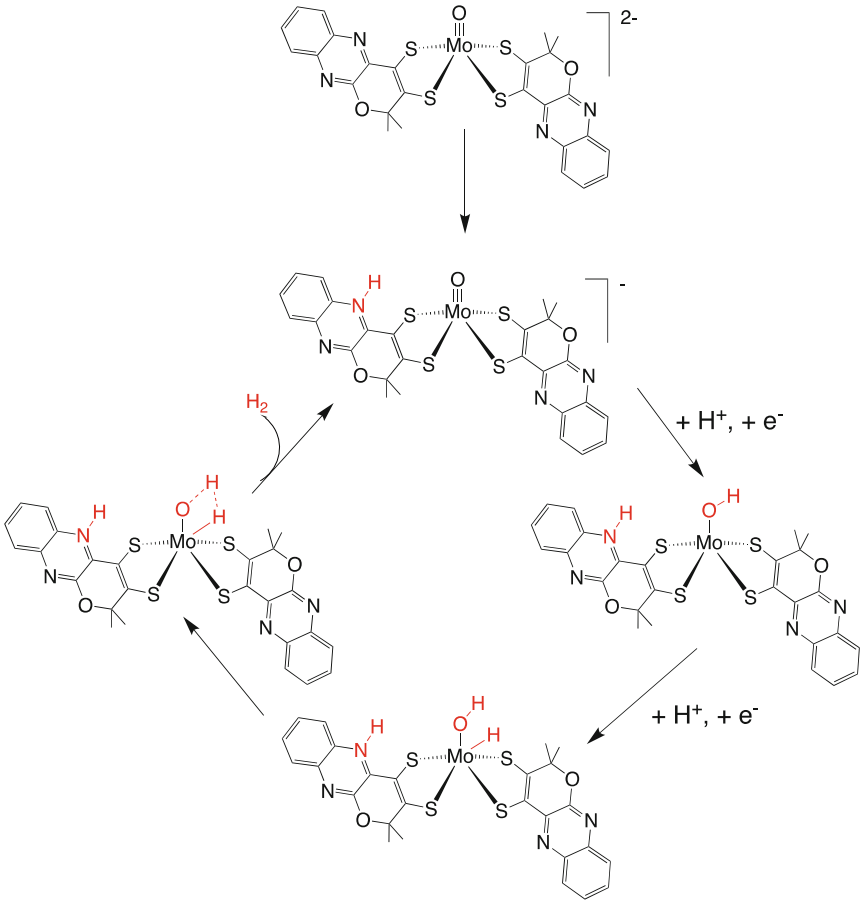

Fig. 29 Proposed catalytic production of hydrogen

The prereduction step inferred from the details of the catalytic reaction suggested a reduced form of the pyranoquinoxaline might be the active catalyst. This experimental information combined with the reduced pterin structure of MPT in *bis*-MPT-containing enzymes prompted the modification of qpdt to explore the catalytic behavior of analogous complexes with reduced quinoxaline units. Hqpdt and H_2qpdt and their oxo-Mo(IV)-bis-dithiolene complexes were synthesized using the same general strategy as for qpdt [160]. It is notable that for the fully reduced pyranoquinoxaline ligand H_2pdt, the configuration at the bridgehead C atoms is *cis* (i.e., R,R), duplicating the stereochemistry known for MPT in Moco in many enzymes. The oxo-Mo complex derived from the reduced ligand H_2qpdt is isolated in the Mo(V) oxidation state, in contrast to the Mo(IV) complexes isolated for qpdt and Hqpdt. Only the $K_2[Mo(IV)(O)(Hqpd)_2]$ complex was crystallized and the X-ray structure determined.

Comparison of the Mo(V/IV) reduction potentials shows that H_2qpdt shifts the potential 60 mV more negative, and the authors attribute this significant difference to the more electron rich reduced quinoxaline in H_2qpdt. Noting that these complexes, especially that of H_2qpdt, now more closely resemble the Moco structure in formate dehydrogenase (FDH), the ability of $[MoO(H_2qpdt)_2]^{2-}$ to effect reduction of CO_2 was explored using a photocatalytic system of $[Ru(II)bpy_3]^{2+}$, dimethyl-2-phenyl-2,3-dihydro-1H-benzoimidazole) and ACN/triethanolamine. The CO_2 reduction products detected were formic acid in addition to CO and H_2, where the ratios of these three molecules depended on the specific pyranoquinoxaline dithiolene on the Mo complex. The complex with the most oxidized form of quinoxaline qpdt exhibited the highest turnover number, but it produced predominantly (~80%) hydrogen gas with lesser amounts of formic acid and CO. In contrast, use of the Mo complex where the quinoxaline is most reduced, H_2qpdt, catalyzed the greatest percentage of reduced CO_2 products formate and CO (60%), a fitting outcome since it has a Mo environment most similar to Moco in FDH.

For this series of $[MoO(dithiolene)_2]^{2-}$ complexes having a pyranoquinoxaline in different oxidation states, the observation that the redox level of the quinoxaline can affect the selectivity for substrates is an intriguing example of how the pterin in MPT might exist in different oxidation states in enzymes in order to achieve the required reactivity.

The third model system involving quinoxaline-dithiolene ligands to be discussed is shown in Fig. 30 [57]. The quinoxalyldithiolene ligand is the middle type shown in Fig. 25, where the quinoxaline group is linked to a dithiolene ethene C atom at the 2-position. An alkyl substituent is positioned at the second ethene C atom, which is either a 2-hydroxyisopropyl group or a tert-butyl group. The Mo complex includes a tridentate *tris*-pyrazolyl hydroborate ligand, Tp*, and an oxo ligand.

This model system is synthesized by an entirely different route than the above examples, via a coupling reaction of a $Mo(S_4)$ group and the appropriate quinoxalylalkyne precursor (Fig. 30). The model has an octahedral Mo environment with an apical oxo ligand, in contrast to the square pyramidal Mo inner coordination sphere of the *bis*-dithiolene complexes discussed above. The variation in the side-chain substituent (R) was used to explore the chemistry of the dithiolene ligand and allowed access to different electronic environments, as discussed below. The hydroxyl was built into the structure with the anticipation of forming a pyrano-quinoxaline structure, while the t-Bu group brings steric bulk that adjusts the conformation of the quinoxaline with respect to the dithiolene chelate. This pair of model complexes are the quinoxaline analogs to pterin dithiolenes that will be discussed in the last portion of this section [162].

Figure 31 shows the X-ray crystal structures of Mo-BMOQO and Mo-BDMQO. The Tp*Mo(≡O) portion is nearly identical in the two molecules, as are the metrical parameters of the dithiolene chelate on Mo, but the conformation of the quinoxaline and alkyl substituents is considerably different. For Mo-BMOQO, the crystal grown from chloroform and diethyl ether has rotated the quinoxaline from the orientation shown in Fig. 30 to benefit from formation of an intramolecular hydrogen bond between the side-chain hydroxyl and a quinoxaline N atom [163].

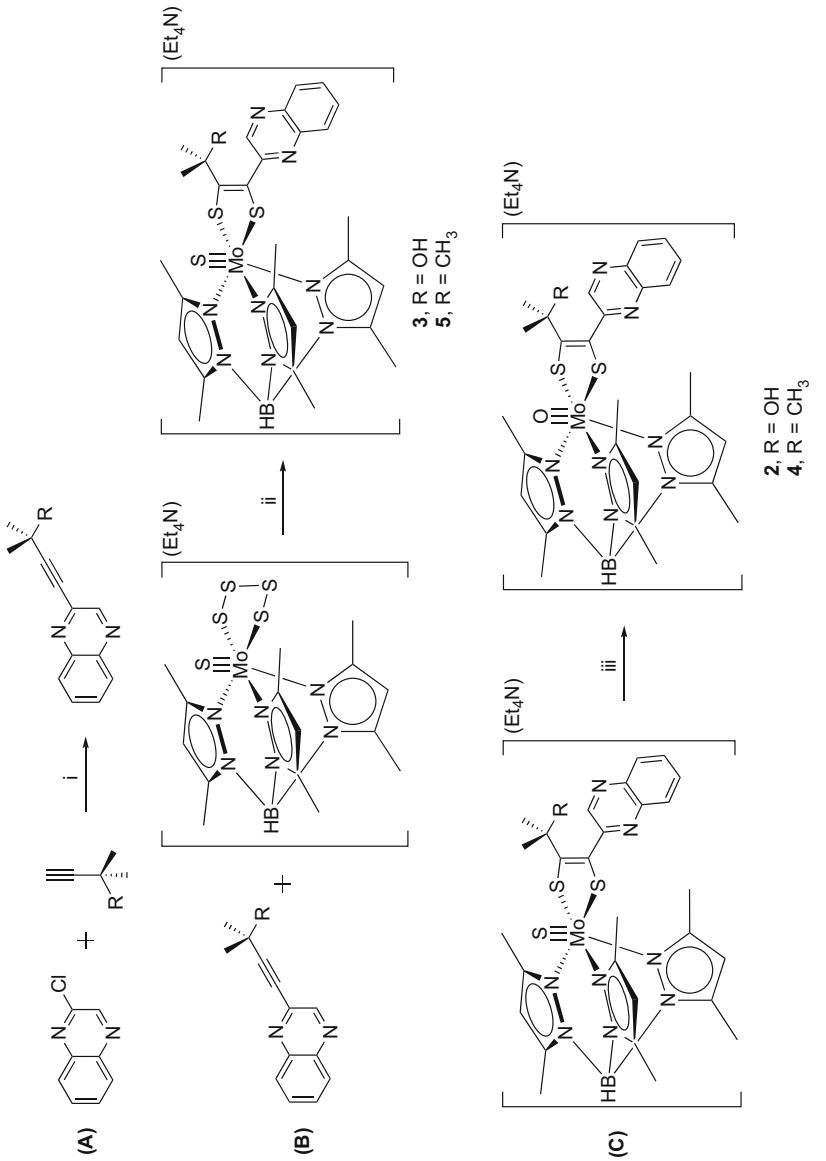

Fig. 30 Synthetic route to an octahedral oxo-Mo-(quinoxalyldithiolene) complex

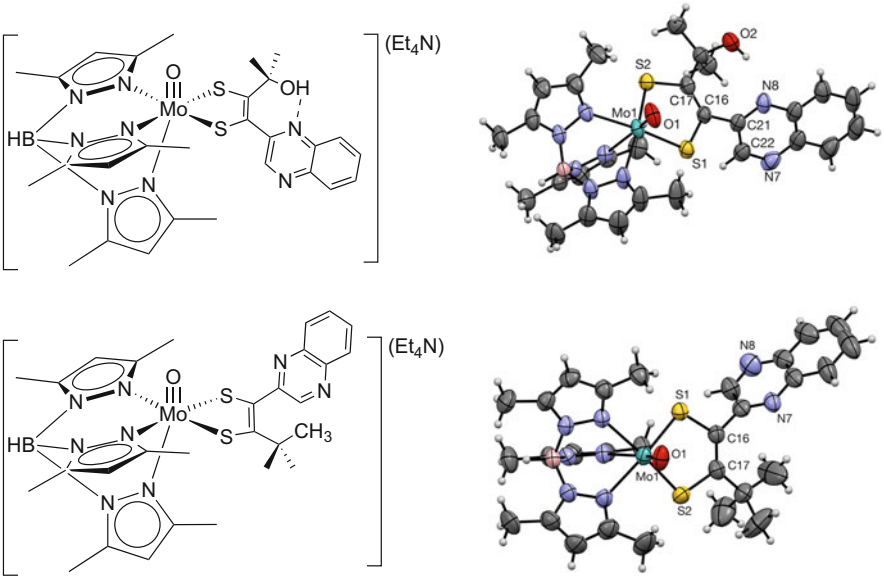

Fig. 31 Two quinoxaline-dithiolene oxo-Mo models (*top*) [Tp*MoO(S_2BMOQO)](TEA) (*bottom*) [Tp*MoO(S_2BDMQO)](TEA) (TEA = tetraethylammonium)

An important consequence of this H-bond formation is that it requires the quinoxaline plane to sit more nearly coplanar to the dithiolene plane of the five atoms Mo-S1-C=C-S2. In contrast, the structure of [Tp*MoO(S_2BDMQO)](TEA) has the quinoxaline rotated away from the dithiolene plane in order to minimize steric repulsion from the large t-Bu group.

This pair of models allowed an investigation of the subtle electronic differences resulting from different quinoxaline conformations. The choice of solvent was determined to affect the quinoxaline conformation in the solution structure of [Tp*MoO(S_2BMOQO)](TEA) when monitored by ^{1}H NMR and absorption spectroscopy. In $CDCl_3$, a broad singlet downfield near 8 ppm is assigned to the -OH proton, consistent with a deshielded proton participating in an H-bond. When dissolved in ACN-d^3, however, the hydroxyl proton resonance sharpens markedly and shifts 2 ppm upfield to 5.6 ppm, a change interpreted resulting from the ACN solvent disrupting the H-bond. The other quinoxaline protons exhibit smaller shifts between $CDCl_3$ and ACN, signaling their minimal change in environment.

In the absorption spectra of [Tp*MoO(S_2BMOQO)](TEA) dissolved in chloroform and acetonitrile, significant changes occur that are attributed to the differing quinoxaline environments. A strong absorption at 506 nm (4,960 M^{-1} cm^{-1}) in chloroform broadens and decreases in intensity in CH_3CN (490 nm, 3,484 M^{-1} cm^{-1}). In comparison, [Tp*MoO(S_2BDMQO)](TEA) is nearly featureless in the lower-energy region in both $CHCl_3$ and CH_3CN, except for an extremely broad and low-intensity shoulder centered at 468 nm (2,139 M^{-1} cm^{-1}) in $CHCl_3$ that is largely unchanged in CH_3CN (486 nm, 1,691 M^{-1} cm^{-1}). Finally, a significant positive shift

(115 mV) in the Mo(V/IV) redox potential is observed for [Tp*MoO(S_2BMOQO)](TEA) vs [Tp*MoO(S_2BDMQO)](TEA) in chloroform, whereas the E(MoV/IV) difference is reduced to just 50 mV in acetonitrile.

The explanation of the different physical data obtained for [Tp*MoO(S_2BMOQO)](TEA) and [Tp*MoO(S_2BDMQO)](TEA) follows from similar trends that had been observed in pterin dithiolene models, discussed in detail below, that depend on the orientation of the N-heterocycle relative to the M-dithiolene plane. As the quinoxaline plane approaches coplanarity with the dithiolene plane, π conjugation throughout the dithiolene-quinoxaline structure is turned on. Due to the relative orbital composition and energy of the frontier orbitals, π-electron density on the dithiolene S atoms is delocalized away to reside in the electron-deficient quinoxaline ring. This accounts for the sensitivity of the Mo reduction potential to the quinoxaline conformation that can be influenced by solvent interactions. Facile electronic communication between dithiolene and quinoxaline also favors an ILCT transition that disappears as the quinoxaline rotates out of plane with the dithiolene.

The presence of the hydroxy-isopropyl side chain in [Tp*MoO(S_2BMOQO)](TEA) introduces additional quinoxaline-based reactions within the second coordination sphere of the Mo center. The hydroxyl group was positioned on the side chain to facilitate pyran ring formation; however, no such cyclization in [Tp*MoO(S_2BMOQO)](TEA) is observed in the solid-state structure nor in solution. However, on addition of TFAA acid to [Tp*MoO(S_2BMOQO)](TEA), a distinct color change from magenta to red signals the formation of a new species. This red species persists for hours and then slowly degrades to produce a blue species. Following this reaction sequence by ^{1}H NMR suggests these proton-induced reactions follow the reaction sequence depicted in Fig. 32.

Protonation of the quinoxaline N4 atom increases the electrophilicity of the adjacent C3 atom which is subsequently attacked by the hydroxyl O atom to cyclize and form the pyran. The red-colored product contains a pyranoquinoxaline structure whose NMR features are assigned based on characteristic resonance for the H atom on the bridgehead C near 6 ppm. An intense absorption at 490 nm is assigned as an ILCT transition. The blue product is a pyrroloquinoxaline generated by dehydration from the [Tp*MoO(S_2BMOQO)](TEA) molecule promoted by protonation at the pyran oxygen atom. The blue species produced as the final product of the

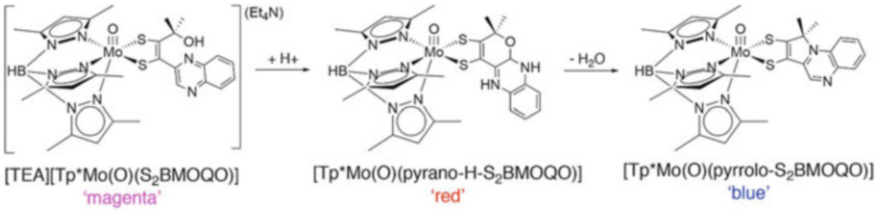

Fig. 32 Two types of cyclizations occur when quinoxaline in [Tp*MoO(S_2BMOQO)](TEA) is protonated

protonation reaction is confirmed by its NMR resonances and absorption spectrum that match data previously reported in an earlier study [56].

The significance of this study is that protonation of the N-heterocycle promotes pyran ring formation, a cyclization reaction that does not occur in the parent quinoxaline-dithiolene complex. It follows that for Moco within the protein, adjacent acidic residues near the pterin of Moco may similarly initiate pyran cyclization by protonation of N atoms.

5.4 *Models Having Pterin-Dithiolene Ligands*

There are now several reports of model complexes that include a pterin-substituted dithiolene. The first such compound was reported in 1991, where the pterinyl-dithiolene ligand was formed through the coupling reaction of a tetrasulfide ligand such as Mo(S_4) and a pterinyl alkyne (Fig. 33) [158, 159].

This synthetic approach was further developed to prepare several recently reported oxo-Mo-pterin-dithiolene complexes, and these systems will be discussed in detail (Fig. 34).

The success of the tetrasulfide ligand and alkyne coupling methodology on the oxo-Mo-*tris*-(pyrazolyl)hydroborate framework was demonstrated in 2007 for two cases where R were aryl substituents and where products were isolated as Mo(V) complexes, the Mo oxidation resulting from a purification step using aerobic chromatography. The recent extension of this work has focused on new derivatives where R is various alkyl substituents [58].

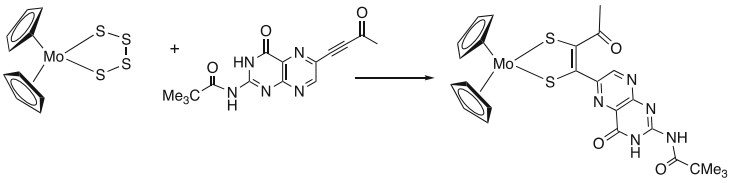

Fig. 33 The first synthesis of a pterin-dithiolene ligand on molybdenum(IV)

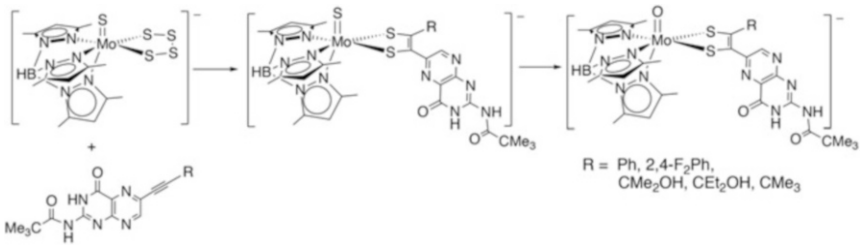

Fig. 34 The first synthesis of a pterin-dithiolene ligand on oxo-molybdenum(IV)

Hydroxyalkyl side-chain groups such as $–C(OH)Me_2$ and $–C(OH)Et_2$ incorporated into the Tp*MoO (pterin-dithiolene) model system make analogs related to the quinoxaline-dithiolene model Mo-BMOQO whose chemistry was described earlier (Figs. 30, 31, and 32). However, the presence of the pterin system instead of quinoxaline leads to significantly different reactivities. For example, a spontaneous cyclization of the side-chain hydroxyl group at the pyrazine ring of pterin generates a pyranopterin dithiolene ligand, and this reaction is depicted for the $–C(OH)Me_2$ derivative in Fig. 35 [164]. This was the first example of a synthetic Moco model complex that possessed all three structural pieces characteristic of Moco, i.e., the Mo center, an oxo ligand, and a pyranopterin dithiolene chelate. Both Mo(IV) and Mo(V) complexes of the pyranopterin dithiolene ligand were structurally characterized by X-ray crystallography and have similar metrical parameters, with the exception of the dithiolene chelate fold angle. As expected for Mo-dithiolene complexes in different oxidation states, the fold angle between planes formed by S-Mo-S atoms and S-C=C-S atoms of the dithiolene is nearly planar (9°) for the d^2 Mo(IV) complex but expands to 25° for the d^1 Mo(V) analog [164].

The pyran cyclization on a pterin dithiolene model complex was studied in detail to extract information regarding how a chemical transformation occurring in the second coordination sphere of the molybdenum could affect the characteristics of the metal center [165]. Pyran cyclization in this system depends on the solvent environment where polar solvents favor the pyrano form, and nonpolar solvents favor the ring-opened form. For example, in dimethyl sulfoxide, the pyrano form predominates 93% over the open form, while in the low-polarity solvent chloroform, the open form predominates ~70% over the cyclized, pyranopterin form. Equilibrium constants and thermodynamic parameters ΔG, ΔH, and ΔS were determined for the cyclization reaction in solvents over a range of dielectric constants, and these showed that pyran formation is a low-energy process (1–7 kJ mol^{-1}), less than that of a hydrogen bond [165].

This facile reversible pyran cyclization was the first example of such a reaction on pterin, though it had been speculated to occur for MPT in Moco in the absence of any experimental data. Protein X-ray structures of several *bis*-MPT enzymes had been reported where one of the MPT ligands on Mo was in an open, uncyclized form

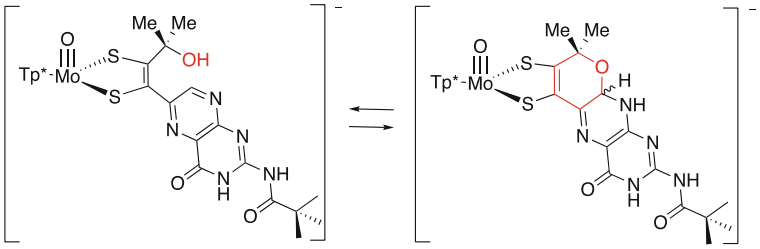

Fig. 35 Reversible pyran cyclization demonstrated in a Moco model for the first time

analogous to the open form of the model in Fig. 35 (left) [62, 63, 116]. The model system in Fig. 35 made it possible to ask further questions about how changes in the second coordination sphere might adjust the reactivity of Mo.

The most recent work on the BMOPP pyranopterin model system examined the changes in electronic environment within the Mo-pterin-dithiolene unit in response to pyran ring formation [139]. The study focused on the two complexes in Fig. 36, where the complex on the right was designed to preclude any cyclization and thus provide a comparison to the pyranopterin dithiolene complex on the left studied under conditions where the pyranopterin form predominates >90%. The two complexes were compared by absorption, FTIR, resonance Raman and X-ray absorption spectroscopies, and by cyclic voltammetry electrochemistry experiments, and the experimental results were correlated with DFT molecular orbital calculations to interpret what the consequence of pyran ring formation are for the Mo environment.

The collection of physical measurements on the pyranopterin model complex (Fig. 36, left) and the uncyclized pterin model complex (Fig. 36, right) showed the following. The pyranopterin model has a more positive Mo(V/IV) reduction potential (ΔE_{red} = +54 mV) and a slightly higher frequency Mo=O stretching vibration ($\Delta\nu$(MoO)) = 8 cm^{-1}) compared to the uncyclized pterin model complex. The pyranopterin model has two intense intraligand charge transfer (ILCT) transitions (22,500 and 26,000 cm^{-1}) that are absent in the uncyclized pterin model. Mo K-edge XAS data indicates the Mo ion in the pyranopterin model has a higher effective nuclear charge and, hence, is more electron deficient than the Mo in the same formal oxidation state in the uncyclized pterin complex.

All of these data are consistent with an electronic structure for the pyranopterin dithiolene model complex that includes electronic communication between the dithiolene and the pterin units, where electron density in π-type sulfur orbitals is delocalized into the π system of the pterin, as depicted by resonance structures drawn in Fig. 37. A consequence of pyranopterin dithiolene formation, the Mo ion gains less electron density from sulfur π-donor orbitals on the dithiolene and is electron deficient, relative to the Mo ion in the uncyclized pterin complex. This electronic communication between dithiolene and pterin uniquely occurs in the pyranopterin ligand due to the pyran pinning the pterin orientation nearly co-planar with the

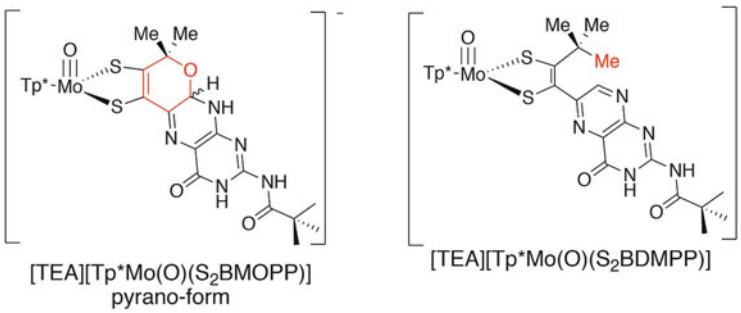

Fig. 36 A pair of pterin dithiolene models used to study electronic structure

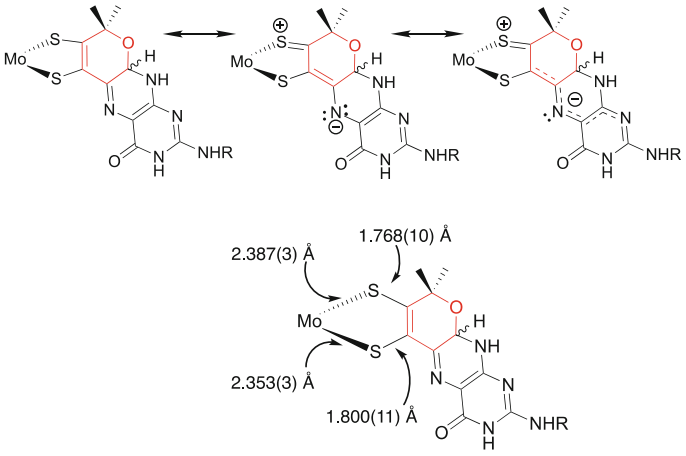

Fig. 37 Resonance structures for the pyranopterin dithiolene complex that contribute to observed bond distances

dithiolene plane, facilitating electronic coupling. In contrast, for the uncyclized pterin model complex, the steric pressure of the t-Bu side chain causes the pterin to rotate ~40° out of the dithiolene plane, effectively decoupling electronic interactions between dithiolene and pterin.

In addition to modulating the Mo charge density, the electronic delocalization from the dithiolene to the pterin causes an asymmetry in the Mo-dithiolene structure that may be considered a result of the ILCT excited state mixing into the ground state. This asymmetry is clearly detected in the X-ray crystal structure where different Mo-S and C-S bond lengths are observed (Fig. 37, bottom) [164]. The configurational mixing effectively introduces oxidized thione-thiolate valence bond character into the ground state wave function.

Studies of the Mo-BMOPP model system that successfully incorporate a pyranopterin into a dithiolene ligand have provided a wealth of information that otherwise would not be possible by studying the cofactor as part of the holoprotein. Key information gleaned from these studies is that pyran ring scission and formation has very low-energy barriers, and pyran cyclization forming a semi-reduced dihydropterin structure switches on a subtle electronic flow from dithiolene to pterin, making the Mo center electron poor and the dithiolene partially oxidized. In the pyran ring-opened model complex, electronic communication between the pterin and dithiolene components of the cofactor will be a function of the pterin-dithiolene interplane dihedral angle, with electronic communication being minimized when these planes are mutually orthogonal. It should be noted that the protein environment may have a role in determining this dihedral angle that controls S → pterin charge donation and the reduction potential. For the fully reduced tetrahydropterin form of the cofactor, it is predicted that the absence of a pterin π-system will result in dramatically less electronic communication with the dithiolene. Thus, the oxidation state of the pterin ring, coupled with the ring-opened/ring-closed nature of the pyran,

conspires to fine-tune the reduction potential of the Mo ion by modifying the electron donor ability of the dithiolene sulfurs.

The various Moco model studies presented above have all contributed to enlarging our understanding of the special chemistry available to a pterin or pyranopterin appended to a dithiolene chelate. The heterocycles quinoxaline and pyrazine, among others, have often been useful in developing synthetic methods to the pterin dithiolene analogs. However, it is also clear that the pterin structure brings unique features to MPT and that simpler N-heterocycles do not adequately duplicate a pterin-dithiolene ligand. For example, dithiolenes substituted by oxidized pterin as well as quinoxaline or pyrazine all exhibit characteristics of electronic communication from dithiolene to heterocycle of electronic delocalization from heterocycle to pterin, resulting in asymmetric Mo-dithiolene bond metrics and ILCT transitions as measurable evidence. Only the pterin dithiolene exhibits a spontaneous and reversible pyran formation, while quinoxaline can be induced to pyran cyclization under acidic conditions. This difference in reactivity points to subtle differences between pterin and quinoxaline and serves to underscore the merits of developing pterin-dithiolene models further.

6 Perspective

The role of the pyranopterin dithiolene in the molybdenum enzymes is the focus of this review, where its special reactivity and ability to modulate electronic structure have been highlighted. The range of MPT conformations observed in protein X-ray structures is consistent with a range of pterin oxidation states, and a redox role would be consistent with nature's use of pterin cofactors elsewhere in biology. Pterin and related heterocycles, positioned on dithiolene chelates in model complexes, are key to accessing other redox states of dithiolene resulting in partial oxidization to a thione/thiolate. The impact at Mo in these models is measurable, if often subtle, and such subtle effects are a hallmark of how Nature builds selectivity and control into enzyme through a multitude of small adjustments.

The model studies have demonstrated many significant aspects of the MPT ligand that may contribute to molybdenum and tungsten enzyme catalysis and behavior. The dithiolene can adopt other resonance forms for electronically buffering the Mo center against changes in charge that accompany redox processes. There are results to support the hypothesis that variation in redox level of the pterin might be used to adjust reactivity and substrate selectivity. It has been demonstrated that pyran ring scission and formation has a very low-energy barrier. Additionally, pyran cyclization forming a semi-reduced dihydropterin structure switches on a subtle electronic flow from dithiolene to pterin, modifying the electron donor ability of the dithiolene sulfurs and making the Mo center electron poor and the dithiolene partially oxidized. Generally, it is clear that the metal reduction potential is sensitive to the pterin conformation and that it will be influenced by solvent and local amino acid interactions, such as protonation.

Several recent studies on Mo enzymes have reported interpretations that involve the pterin and/or dithiolene components of MPT. An electrochemical investigation of the *E. coli* protein YedY (now MsrP) produced evidence of pterin reduction that preceded substrate reaction (DMSO reduction) [60] Curiously, in this work no change in the catalytically active Mo 4+ redox state was observed during catalysis, leading the authors to suggest that perhaps the tetrahydropyranopterin form of MPT was crucial to initiate catalysis as well as the moiety donating two electrons for substrate reduction via oxygen atom transfer to Mo (Fig. 38). This unprecedented catalytic mechanism that proceeds via pterin redox rather than Mo redox might be understood as the limiting extreme of a highly covalent Mo-pyranopterin-dithiolene system where the redox event has shifted from the metal completely to the pterin component of the MPT ligand.

A second example from the current molybdenum enzyme literature also ascribes a role for pterin reduction in accessing active enzyme. It is well-documented that isolated samples of proteins in the DMSOR family, such as dissimilatory nitrate reductases, often are heterogeneous samples that require a prereduction step in order to generate catalytically active enzyme [117, 118, 166–168]. One such enzyme, dissimilatory *E. coli* nitrate reductase, was studied using protein film voltammetry to gain information about the kinetics of the reductive

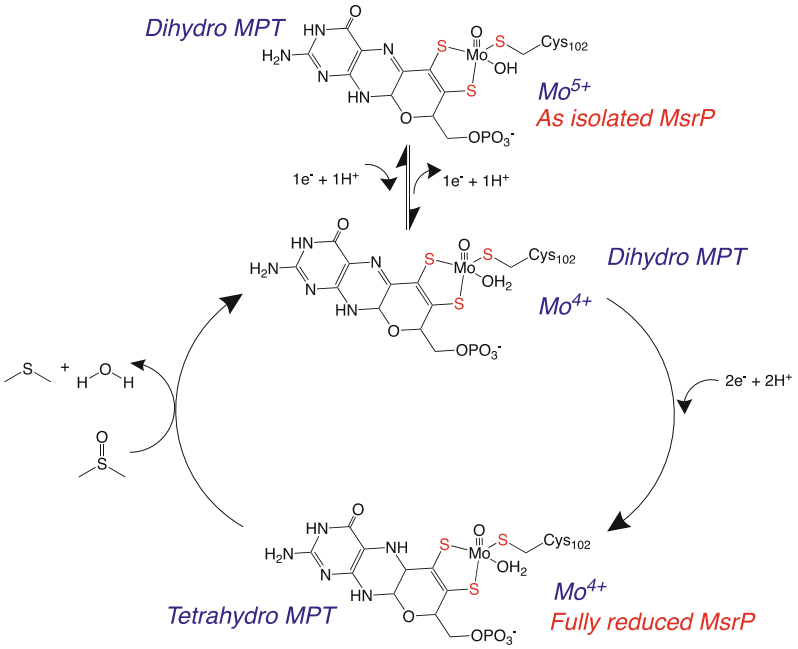

Fig. 38 Proposed mechanism for MsrP based on electrochemical studies. During catalysis, the Mo ion remains in the Mo(IV) state, and the two-electron redox chemistry associated with oxygen atom transfer reactivity involves MPT and not molybdenum (adapted from [60])

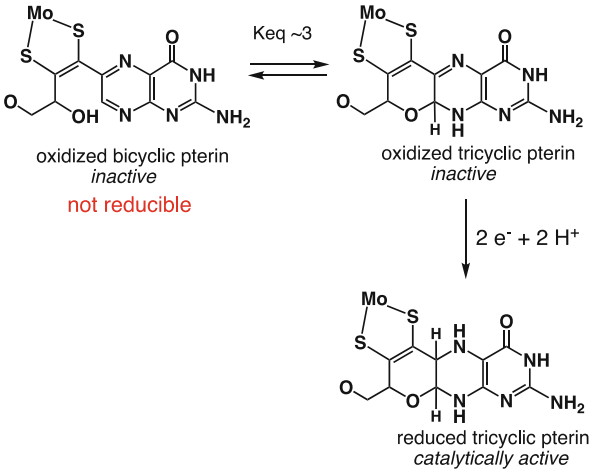

Fig. 39 Proposed mechanism of reductive activation of dissimilatory *E. coli* nitrate reductase. Only one of the two MPT ligands on Mo is shown

activation process [118]. These experiments led to the proposal that the inactive Nar enzyme involves two species in equilibrium where only one of these species is reducible (Fig. 39). The equilibrium process was speculated to be the cyclization of the open pterin form of MPT to the pyranopterin form of MPT, where only the pyranopterin form of MPT is reducible to produce the active Nar enzyme. In fact, thermodynamic studies of the pterin-dithiolene model system described above (Fig. 35) provide experimental data that confirms this proposed prereduction mechanism [165]. The open and pyranopterin forms of the model system shown in Fig. 35 exist in equilibrium with a K_{eq} value similar to that determined for the Nar enzymes [118]. Furthermore, the electronic structure basis for understanding the differences in reduction potential between ring-closed MPTs and their ring-opened forms provides a rationale for why the pyranopterin form of MPT is selectively reduced over the open MPT form [139].

Regarding the role of MPT as a structural component and a mediator of electron transfer reactivity, X-ray crystal structures show that MPT is bound to the proteins by an extensive hydrogen-bonding network. The presence of this hydrogen bonding between the protein and MPT strongly supports an argument that MPT assists in anchoring Moco to the protein and properly orienting Moco for catalysis. Additionally, the extensive hydrogen bonding may also function to modulate Moco for electron- and atom-transfer reactivity in the catalytic cycles of the enzymes. Although direct spectroscopic studies probing MPT in enzymes are sparse, recent resonance Raman spectroscopic studies detailed the nature of Moco-protein interactions in bovine xanthine oxidase (XOR) [73] and wild-type xanthine dehydrogenase (XDH), including XDH Q102G and Q197A variants [108]. Small vibrational frequency shifts were observed in the low-frequency region of XDH variants relative to wt-XDH indicating that these residues were involved in a combination of weak

hydrogen-bonding and electrostatic interactions between Q102 and the MPT $-NH_2$ and between Q197 and the terminal oxo of XOR/XDH in the reduced Mo(IV) form of the enzyme. These Raman data were collected on resonance with a Mo(IV) → product charge-transfer transition, which mimics the loss of electron density on Mo during electron transfer to generate Mo(V). Since Raman frequency shifts were observed between wt-XDH and the Q102G variant, this observation supports an argument that electron density changes at Mo are felt as far away as the MPT amino terminus. Such distortions at the distant MPT amino terminus imply a primary role for MPT as an electron transfer conduit that is directly involved in enzymatic electron-transfer reactivity in xanthine oxidase family enzymes.

In this chapter we have presented an overview of the pyranopterin dithiolene (MPT) component of the molybdenum cofactor (Moco) and how MPT may contribute to enzymatic catalysis. The extraordinary redox complexity of MPT was described and then followed by examples of biomimetic small molecule studies. These combined studies have contributed to the current understanding of the roles that this remarkable ligand plays in the catalytic cycles of the enzymes.

7 Acknowledgments

The authors would like to acknowledge all of the undergraduate, graduate, and postdoctoral researchers who have contributed to the authors' work cited in this manuscript. A special thank you goes to Dr. Doug Gisewhite for valuable discussions. The authors acknowledge the National Institutes of Health (GM-057378 to M. L. K. and GM-081848 to S. J. N. B.) for continued financial support of our work on molybdoenzymes. S. J. N. B. also acknowledges the National Science Foundation (CHE-0958996).

References

1. Pritsos CA (2000) Cellular distribution, metabolism and regulation of the xanthine oxidoreductase enzyme system. Chem Biol Interact 129(1–2):195
2. Rooseboom M, Commandeur JNM, Vermeulen NPE (2004) Enzyme-catalyzed activation of anticancer prodrugs. Pharmacol Rev 56(1):53
3. Kotthaus J et al (2011) New prodrugs of the antiprotozoal drug pentamidine. ChemMedChem 6:2233–2242
4. Havemeyer A et al (2010) Reduction of N-hydroxy-sulfonamides, Including N-hydroxy-valdecoxib, by the molybdenum-containing enzyme mARC. Drug Metab Dispos 38:1917–1921
5. Mendel RR, Kruse T (2012) Cell biology of molybdenum in plants and humans. BBA-Mol Cell Res 1823(9):1568–1579
6. Mendel RR, Schwarz G (2011) Molybdenum cofactor biosynthesis in plants and humans. Coord Chem Rev 255(9-10):1145–1158

7. Kotthaus J et al (2011) Reduction of N(ω)-hydroxy-L-arginine by the mitochondrial amidoxime reducing component (mARC). Biochem J 433:383–391
8. Sparacino-Watkins CE et al (2014) Nitrite reductase and nitric-oxide synthase activity of the mitochondrial molybdopterin enzymes mARC1 and mARC2. J Biol Chem 289 (15):10345–10358
9. Hille R, Hall J, Basu P (2014) The mononuclear molybdenum enzymes. Chem Rev 114 (7):3963–4038
10. Hille R (2002) Molybdenum enzymes containing the pyranopterin cofactor: an overview. Marcel Dekker, Inc, New York, pp 187–226
11. Berry CE, Hare JM (2004) Xanthine oxidoreductase and cardiovascular disease: molecular mechanisms and pathophysiological implications. J Physiol 555(3):589–606
12. Reiss J (2000) Genetics of molybdenum cofactor deficiency. Hum Genet 106(2):157
13. Stein BW, Kirk ML (2015) Electronic structure contributions to reactivity in xanthine oxidase family enzymes. J Biol Inorg Chem 20(2):183–194
14. Kirk ML, Stein B (2013) The molybdenum enzymes. In: Jan R, Kenneth P (eds) Comprehensive inorganic chemistry II, 2nd edn. Elsevier, Amsterdam, pp 263–293
15. Jones RM, Inscore FE, Hille R, Kirk ML (1999) Freeze-quench magnetic circular dichroism spectroscopic study of the "very rapid" intermediate in xanthine oxidase. Inorg Chem 38 (22):4963–4970
16. Hille R, Nishino T, Bittner F (2011) Molybdenum enzymes in higher organisms. Coord Chem Rev 255(9-10):1179–1205
17. Hille R (2005) Molybdenum-containing hydroxylases. Arch Biochem Biophys 433 (1):107–116
18. Hille R (1997) Mechanistic aspects of the mononuclear molybdenum enzymes. J Biol Inorg Chem 2(6):804–809
19. Mtei RP et al (2011) Spectroscopic and electronic structure studies of a dimethyl sulfoxide reductase catalytic intermediate: implications for electron- and atom-transfer reactivity. J Am Chem Soc 133(25):9762–9774
20. Hemann C et al (2005) Spectroscopic and kinetic studies of Arabidopsis thaliana sulfite oxidase: nature of the redox-active orbital and electronic structure contributions to catalysis. J Am Chem Soc 127(47):16567
21. Yang J et al (2015) Oxyl and hydroxyl radical transfer in mitochondrial amidoxime reducing component-catalyzed nitrite reduction. J Am Chem Soc 137(16):5276–5279
22. Maia L, Moura JG (2015) Nitrite reduction by molybdoenzymes: a new class of nitric oxide-forming nitrite reductases. J Biol Inorg Chem 20(2):403–433
23. Hille R, Retey J, Bartlewski Hof U, Reichenbecher W, Schink B (1998) Mechanistic aspects of molybdenum containing enzymes. FEMS Microbiol Rev 22(5):489–501
24. Hille R (1996) Structure and function of mononuclear molybdenum enzymes. J Biol Inorg Chem 1(5):397–404
25. Hille R (1996) The mononuclear molybdenum enzymes. Chem Rev 96(7):2757–2816
26. Rothery RA, Stein B, Solomonson M, Kirk ML, Weiner JH (2012) Pyranopterin conformation defines the function of molybdenum and tungsten enzymes. Proc Natl Acad Sci U S A 109 (37):14773–14778
27. Kirk ML (2016) Spectroscopic and electronic structure studies of Mo model compounds and enzymes. In: Russ Hille CS, Kirk ML (eds) Molybdenum and tungsten enzymes: spectroscopic and theoretical investigations, RSC metallobiology series no. 7, The Royal Society of Chemistry, Cambridge, pp 13–67
28. Pushie MJ, George GN (2011) Spectroscopic studies of molybdenum and tungsten enzymes. Coord Chem Rev 255(9–10):1055–1084
29. Schwarz G (2016) Molybdenum cofactor and human disease. Curr Opin Chem Biol 31:179–187
30. Mendel RR, Leimkuhler S (2015) The biosynthesis of the molybdenum cofactors. J Biol Inorg Chem 20(2):337–347

31. Maia LB, Moura JJG, Moura I (2015) Molybdenum and tungsten-dependent formate dehydrogenases. J Biol Inorg Chem 20(2):287–309
32. Metz S, Thiel W (2011) Theoretical studies on the reactivity of molybdenum enzymes. Coord Chem Rev 255(9–10):1085–1103
33. Sugimoto H, Tsukube H (2008) Chemical analogues relevant to molybdenum and tungsten enzyme reaction centres toward structural dynamics and reaction diversity. Chem Soc Rev 37 (12):2609–2619
34. Niks D, Hille R (2018) Molybdenum- and tungsten-containing formate dehydrogenases and formylmethanofuran dehydrogenases: structure, mechanism and cofactor insertion. Protein Sci 28(1):111–122
35. Kaufholdt D, Baillie C-K, Meinen R, Mendel RR, Hänsch R (2017) The molybdenum cofactor biosynthesis network: in vivo protein-protein interactions of an actin associated multi-protein complex. Front Plant Sci 8:1946
36. Johnson JL, Rajagopalan KV (1982) Structural and metabolic relationship between the molybdenum cofactor and urothione. Proc Natl Acad Sci U S A 79:6856–6860
37. Groves JT (2006) High-valent iron in chemical and biological oxidations. J Inorg Biochem 100(4):434–447
38. Rittle J, Green MT (2010) Cytochrome P450 compound I: capture, characterization, and C-H bond activation kinetics. Science 330(6006):933–937
39. Holt BTO et al (2009) Reaction coordinate of a functional model of tyrosinase: spectroscopic and computational characterization. J Am Chem Soc 131(18):6421–6438
40. Mirica LM et al (2005) Tyrosinase reactivity in a model complex: an alternative hydroxylation mechanism. Science 308(5730):1890–1892
41. Schwarz G, Mendel RR, Ribbe MW (2009) Molybdenum cofactors, enzymes and pathways. Nature 460(7257):839–847
42. Weiss MC et al (2016) The physiology and habitat of the last universal common ancestor. Nat Microbiol 1(9):16116
43. Leimkuhler S & Mendel R (2016) Molybdenum cofactor biosynthesis. In: Hille R, Schulzke C, Kirk ML (eds) Molybdenum and tungsten enzymes, RSC metallobiochemistry, vol 1, RSC, Cambridge, pp 100–111
44. Schwarz G, Mendel RR (2006) Molybdenum cofactor biosynthesis and molybdoenzymes. Annu Rev Plant Biol 57(1):623–647
45. Llamas A, Otte T, Multhaup G, Mendel RR, Schwarz G (2006) The mechanism of nucleotide-assisted molybdenum insertion into molybdopterin – a novel route toward metal cofactor assembly. J Biol Chem 281(27):18343–18350
46. Krausze J et al (2018) The functional principle of eukaryotic molybdenum insertases. Biochem J 475:1739–1753
47. Krausze J et al (2017) Dimerization of the plant molybdenum insertase Cnx1E is required for synthesis of the molybdenum cofactor. Biochem J 474(1):163
48. Sempombe J, Stein B, Kirk ML (2011) Spectroscopic and electronic structure studies probing covalency contributions to C-H bond activation and transition-state stabilization in xanthine oxidase. Inorg Chem 50(21):10919–10928
49. Ilich P, Hille R (1999) Mechanism of formamide hydroxylation catalyzed by a molybdenum-dithiolene complex: a model for xanthine oxidase reactivity. J Phys Chem B 103 (25):5406–5412
50. Fischer B, Enemark JH, Basu P (1998) A chemical approach to systematically designate the pyranopterin centers of molybdenum and tungsten enzymes and synthetic models. J Inorg Biochem 72:13–21
51. Schwarz, G, Mendel RR (2006) Molybdenum cofactor biosynthesis and molybdoenzymes. Annu Rev Plant Biol 57(1):623–647
52. Greatbanks SP, Hillier IH, Garner CD, Joule JA (1997) The relative stabilities of dihydropterins; a comment on the structure of Moco; the cofactor of the oxomolybdoenzymes. J Chem Soc Perkin Trans 2(8):1529–1534

53. Enemark JH, Garner CD (1997) The coordination chemistry and function of the molybdenum centres of the oxomolybdoenzymes. J Biol Inorg Chem 2(6):817–822
54. Burgmayer SJN, Pearsall DL, Blaney SM, Moore EM, Sauk-Schubert C (2004) Redox reactions of the pyranopterin system of the molybdenum cofactor. J Biol Inorg Chem 9 (1):59–66
55. Basu P, Burgmayer SJN (2011) Pterin chemistry and its relationship to the molybdenum cofactor. Coord Chem Rev 255(9,10):1016–1038
56. Matz KG, Mtei RP, Rothstein R, Kirk ML, Burgmayer SJN (2011) Study of molybdenum(4+) quinoxalyldithiolenes as models for the noninnocent pyranopterin in the molybdenum cofactor. Inorg Chem 50(20):9804–9815
57. Matz KG, Mtei RP, Leung B, Burgmayer SJN, Kirk ML (2010) Noninnocent dithiolene ligands: a new oxomolybdenum complex possessing a donor acceptor dithiolene ligand. J Am Chem Soc 132(23):7830–7831
58. Burgmayer SJN et al (2007) Synthesis, characterization, and spectroscopy of model molybdopterin complexes. J Inorg Biochem 101(11-12):1601–1616
59. Kirk ML (2016) Spectroscopic and electronic structure studies of Mo model compounds and enzymes. In: Molybdenum and tungsten enzymes: spectroscopic and theoretical investigations, vol 3, Molybdenum and tungsten enzymes, The Royal Society of Chemistry, London, pp 13–67
60. Adamson H et al (2015) Electrochemical evidence that pyranopterin redox chemistry controls the catalysis of YedY, a mononuclear Mo enzyme. Proc Natl Acad Sci U S A 112 (47):14506–14511
61. Hille R, Anderson RF (1991) Electron transfer in milk xanthine oxidase as studied by pulse radiolysis. J Biol Chem 266(9):5608–5615
62. Bertero MG et al (2003) Insights into the respiratory electron transfer pathway from the structure of nitrate reductase A. Nat Struct Biol 10(9):681–687
63. Kloer DP, Hagel C, Heider J, Schulz GE (2006) Crystal structure of ethylbenzene dehydrogenase from Aromatoleum aromaticum. Structure 14(9):1377–1388
64. Jormakka M, Richardson D, Byrne B, Iwata S (2004) Architecture of NarGH reveals a structural classification of Mo-bisMGD enzymes. Structure 12(1):95–104
65. Dietzel U et al (2009) Mechanism of substrate and inhibitor binding of rhodobacter capsulatus xanthine dehydrogenase. J Biol Chem 284(13):8759–8767
66. Enroth C et al (2000) Crystal structures of bovine milk xanthine dehydrogenase and xanthine oxidase: structure-based mechanism of conversion. Proc Natl Acad Sci U S A 97 (20):10723–10728
67. Leimkuhler S, Hodson R, George GN, Rajagopalan KV (2003) Recombinant Rhodobacter capsulatus xanthine dehydrogenase, a useful model system for the characterization of protein variants leading to xanthinuria I in humans. J Biol Chem 278(23):20802–20811
68. Truglio J et al (2002) Crystal structures of the active and alloxanthine-inhibited forms of xanthine dehydrogenase from Rhodobacter capsulatus. Structure 10(1):115–125
69. Westcott BL, Gruhn NE, Enemark JH (1998) Evaluation of molybdenum-sulfur interactions in molybdoenzyme model complexes by gas-phase photoelectron spectroscopy. The “electronic buffer” effect. J Am Chem Soc 120(14):3382–3386
70. Inscore FE et al (2006) Understanding the origin of metal-sulfur vibrations in an oxo-molybdenum dithiolene complex: relevance to sulfite oxidase. Inorg Chem 45(3):967
71. Hille R (1991) Electron transfer within xanthine oxidase: a solvent kinetic isotope effect study. Biochemistry 30(35):8522–8529
72. Hille R, Massey V (1981) Studies on the oxidative half-reaction of xanthine oxidase. J Biol Chem 256(17):9090–9095
73. Dong C, Yang J, Leimkühler S, Kirk ML (2014) Pyranopterin dithiolene distortions relevant to electron transfer in xanthine oxidase/dehydrogenase. Inorg Chem 53(14):7077–7079
74. Gray HB, Winkler JR (2005) Long-range electron transfer. Proc Natl Acad Sci U S A 102 (10):3534

75. Kirk ML et al (2013) Superexchange contributions to distance dependence of electron transfer/transport: exchange and electronic coupling in oligo(para-phenylene)- and oligo(2,5-thiophene)-bridged-donor-bridge acceptor biradical complexes. J Am Chem Soc 135(45):17144–17154
76. Mtei RP et al (2011) A valence bond description of dizwitterionic dithiolene character in an oxomolybdenum–bis(dithione) complex. Eur J Inorg Chem 2011(36):5467–5470
77. Stiefel EI, Eisenberg R, Rosenberg R, Gray H (1966) Characterization and electronic structures of six-coordinate trigonal-prismatic complexes. J Am Chem Soc 88(13):2956–2966
78. Fourmigué M, Domercq B (1998) A non-innocent ligand in coordination chemistry: the dithiolene complexes. Actualite Chim 11–12:9–13
79. Wang K, McConnachie JM, Stiefel EI (1999) Syntheses of metal dithiolene complexes from thiometalates by induced internal redox reactions. Inorg Chem 38(19):4334–4341
80. Helton ME, Gruhn NE, McNaughton R, Kirk ML (2000) Control of oxo-molybdenum reduction and ionization potentials by dithiolate donors. Inorg Chem 39(11):2273–2278
81. Harmer MA et al (1986) Ligand and induced internal redox processes in Mo-S and W-S systems. Polyhedron 5(1–2):341–347
82. Stiefel EI (1998) Transition metal sulfur chemistry and its relevance to molybdenum and tungsten enzymes. Pure Appl Chem 70(4):889–896
83. Helton ME, Gebhart NL, Davies S, Garner CD, Kirk ML (2000) Thermally driven intramolecular charge transfer in an oxo-molybdenum dithiolate complex. J Am Chem Soc. Manuscript in Preparation
84. Ray K, George SD, Solomon EI, Wieghardt K, Neese F (2007) Description of the ground-state covalencies of the bis(dithiolato) transition-metal complexes from X-ray absorption spectroscopy and time-dependent density-functional calculations. Chemistry 13(10):2783–2797
85. Kirk ML, Helton ME, RL MN (eds) (2004) The electronic structure and spectroscopy of metallo-dithiolene complexes, vol 52. John Wiley and Sons, Inc, Hoboken, pp 111–212
86. Yang J, Mogesa B, Basu P, Kirk ML (2016) Large ligand folding distortion in an oxomolybdenum donor acceptor complex. Inorg Chem 55(2):785–793
87. Sugimoto H et al (2010) Monooxomolybdenum(VI) complexes possessing olefinic dithiolene ligands: probing Mo-S covalency contributions to electron transfer in dimethyl sulfoxide reductase family molybdoenzymes. Inorg Chem 49(12):5368–5370
88. McNaughton RL, Lim BS, Knottenbelt SZ, Holm RH, Kirk ML (2008) Spectroscopic and electronic structure studies of symmetrized models for reduced members of the dimethylsulfoxide reductase enzyme family. J Am Chem Soc 130(14):4628–4636
89. Kirk ML, McNaughton RL, Helton ME (2004) The electronic structure and spectroscopy of metallo-dithiolene complexes. In: Stiefel EI, Karlin KD (eds) Progress in inorganic chemistry: synthesis, properties, and applications, Progress in inorganic chemistry, vol 52, Wiley, Hoboken, pp 111–212
90. Inscore FE et al (1999) Spectroscopic evidence for a unique bonding interaction in oxo-molybdenum dithiolate complexes: implications for sigma electron transfer pathways in the pyranopterin dithiolate centers of enzymes. Inorg Chem 38(7):1401–1410
91. Yang J et al (2018) Ground state nuclear magnetic resonance chemical shifts predict charge-separated excited state lifetimes. Inorg Chem 57(21):13470–13476
92. Yang J et al (2014) Ligand control of donor-acceptor excited-state lifetimes. Inorg Chem 53 (10):4791–4793
93. Chang C-SJ, Rai-Chaudhuri A, Lichtenberger DL, Enemark JH (1990) He I valence photoelectron spectra of oxomolybdenum (V) complexes containing diolato or alkoxide ligands. Polyhedron 9(15–16):1965–1973
94. Lalitha S, Manoharan PT (1989) X-ray photoelectron spectroscopic studies on some dithiolate complexes. J Electron Spectros Relat Phenom 49(1):61–75
95. Gleiter R, Spanget-Larsen J (1979). Top Curr Chem Spectrosc 86:139–195
96. Donahue JP, Holm RH (1998) 3,4-bis(l-adamantyl)-1,2-dithiete: the first structurally characterized dithiete unsupported by a ring or benzenoid frame. Acta Crystallogr C 54:1175–1178

97. Davison A, Holm RH (1967) Metal complexes derived from *cis*-1,2-cyano-1,2-ethylenedithiolate and bis(trifluoromethyl)-1,2-dithiete. Inorg Synth 10:8–26
98. Frei F et al (2014) Ultrafast electronic and vibrational relaxations in mixed-ligand dithione-dithiolato Ni, Pd, and Pt complexes. Dalton Trans 43(47):17666–17676
99. Espa D et al (2014) Role of the acceptor in tuning the properties of metal [M (II)= Ni, Pd, Pt] dithiolato/dithione (donor/acceptor) second-order nonlinear chromophores: combined experimental and theoretical studies. Inorg Chem 53(2):1170–1183
100. Deplano P, Pilia L, Espa D, Mercuri ML, Serpe A (2010) Square-planar d(8) metal mixed-ligand dithiolene complexes as second order nonlinear optical chromophores: structure/property relationship. Coord Chem Rev 254(13–14):1434–1447
101. Perera E, Basu P (2009) Synthesis, characterization and structure of a low coordinate desoxomolybdenum cluster stabilized by a dithione ligand. Dalton Trans (25):5023–5028
102. Sproules S et al (2009) Characterization and electronic structures of five members of the electron transfer series [Re(benzene-1,2-dithiolato)(3)](z) (z=1+,0,1-,2-,3-): a spectroscopic and density functional theoretical study. Inorg Chem 48(23):10926–10941
103. Stein BW et al (2018) Vibrational control of covalency effects related to the active sites of molybdenum enzymes. J Am Chem Soc. Accepted for Publication
104. Pauff JM, Cao H, Hille R (2009) Substrate orientation and catalysis at the molybdenum site in xanthine oxidase crystal structures in complex with xanthine and lumazine. J Biol Chem 284 (13):8751–8758
105. Hemann C, Ilich P, Stockert AL, Choi EY, Hille R (2005) Resonance Raman studies of xanthine oxidase: the reduced enzyme – product complex with violapterin. J Phys Chem B 109 (7):3023–3031
106. Hemann C, Ilich P, Hille R (2003) Vibrational spectra of lumazine in water at pH 2-13: Ab initio calculation and FTIR/Raman spectra. J Phys Chem B 107(9):2139–2155
107. Davis M, Olson J, Palmer G (1984) The reaction of xanthine oxidase with lumazine: characterization of the reductive half-reaction. J Biol Chem 259(6):3526–3533
108. Dong C, Yang J, Reschke S, Leimkühler S, Kirk ML (2017) Vibrational probes of molybdenum cofactor–protein interactions in xanthine dehydrogenase. Inorg Chem 56(12):6830–6837
109. Qiu D, Kilpatrick LT, Kitajima N, Spiro TG (1994) Modeling blue copper protein resonance Raman spectra with thiolate-Cu(II) complexes of a sterically hindered tris(pyrazolyl)borate. J Am Chem Soc 116(6):2585–2590
110. Garton SD et al (2000) Resonance Raman characterization of biotin sulfoxide reductase: comparing oxomolybdenum enzymes in the Me_2SO reductase family. J Biol Chem 275 (10):6798–6805
111. Johnson MK, Garton SD, Oku H (1997) Resonance Raman as a direct probe for the catalytic mechanism of molybdenum oxotransferases. J Biol Inorg Chem 2(6):797–803
112. Garton SD et al (1997) Active site structures and catalytic mechanism of *Rhodobacter sphaeroides* dimethyl sulfoxide reductase as revealed by resonance Raman spectroscopy. J Am Chem Soc 119(52):12906–12916
113. Johnson MK (ed) (2004) Vibrational spectra of dithiolene complexes, vol 52, John Wiley and Sons, Inc., Hoboken, pp 213–266
114. Rajagopalan K (1991) Novel aspects of the biochemistry of the molybdenum cofactor. Adv Enzymol Relat Areas Mol Biol 64:215–290
115. Hille R, Massey V (1982) The presence of a reducible disulfide bond in milk xanthine oxidase. J Biol Chem 257(15):8898–8901
116. Youngblut MD et al (2016) Perchlorate reductase is distinguished by active site aromatic gate residues. J Biol Chem 291(17):9190–9202
117. Jacques JGJ et al (2014) Reductive activation in periplasmic nitrate reductase involves chemical modifications of the Mo-cofactor beyond the first coordination sphere of the metal ion. BBA-Bioenergetics 1837(2):277–286
118. Ceccaldi P et al (2015) Reductive activation of E. coli respiratory nitrate reductase. BBA-Bioenergetics 1847(10):1055–1063

119. Gardlik S, Rajagopalan K (1991) Oxidation of molybdopterin in sulfite oxidase by ferricyanide-effect on electron transfer activities. J Biol Chem 266(8):4889–4895
120. Gardlik S, Rajagopalan KV (1990) The state of reduction of molybdopterin in xanthine-oxidase and sulfite oxidase. J Biol Chem 265(22):13047–13054
121. Karber LG, Dryhurst G (1984) Electrochemical oxidation of 5-methyl-5,6,7,8-tetrahydropterin. J Electroanal Chem 160(1–2):141–157
122. Karber LG, Dryhurst G (1982) Electrochemistry of 6-methyl-5,6,7,8-tetrahydropterin. J Electroanal Chem 136(2):271–289
123. Egeserpkenci D, Raghavan R, Dryhurst G (1983) Oxidation of methylated tetrahydropterins – structure of the initial quinonoid-dihydropterin intermediate. Bioelectrochem Bioenerg 10 (4):357–376
124. Dryhurst G, Raghavan R, Egeserpkenci D, Karber LG (1982) Electrochemistry of reduced pterin cofactors. Adv Chem Ser (201):457–487
125. Raghavan R, Dryhurst G (1981) Redox chemistry of reduced pterin species. J Electroanal Chem 129(1–2):189–212
126. Bailey SW, Ayling JE (1983) 6,6-Dimethylpterins – stable quinoid dihydropterin substrate for dihydropteridine reductase and tetrahydropterin cofactor for phenylalanine hydroxylase. Biochemistry 22(8):1790–1798
127. Brown DJ (1988) Fused pyrimidines. Wiley, New York
128. Pfleiderer W, Zondler H (1966) Pteridine, 31. Synthese und Eigenschaften blockierter 7.8-Dihydro-pterine. Chemische Berichte-Recueil 99(9):3008
129. Randles D, Armarego WLF (1985) Reduced 6,6,8-trimethyllpterins – preparation, properties and enzymic reactivities with dihydropteridine reductase, phenylalanine hydroxylase, and tyrosine hydroxylase. Eur J Biochem 146(2):467–474
130. Kappock TJ, Caradonna JP (1996) Pterin-dependent amino acid hydroxylases. Chem Rev 96 (7):2659–2756
131. Kemsley JN et al (2003) Spectroscopic and kinetic studies of PKU-inducing mutants of phenylalanine hydroxylase: Arg158Gln and Glu280Lys. J Am Chem Soc 125(19):5677–5686
132. Stoll S et al (2010) Nitric oxide synthase stabilizes the tetrahydrobiopterin cofactor radical by controlling its protonation state. J Am Chem Soc 132(33):11812–11823
133. Hurshman AR, Krebs C, Edmondson DE, Marletta MA (2003) Ability of tetrahydrobiopterin analogues to support catalysis by inducible nitric oxide synthase: formation of a pterin radical is required for enzyme activity. Biochemistry 42(45):13287–13303
134. Marletta MA (1993) Nitric oxide synthase structure and mechanism. J Biol Chem 268 (17):12231–12234
135. Soyka R, Pfleiderer W, Prewo R (1990) Pteridines, 94. Synthesis and characteristics of 5,6-dihydro-6-(1,2,3-trihydroxypropyl)pteridines – covalent intramolecular adducts. Helv Chim Acta 73(4):808–826
136. Schircks B, Bieri JH, Viscontini M (1985) Pterinechemistry, 84. A new, regiospecific synthesis of L-biopterin. Helv Chim Acta 68(6):1639–1643
137. Dong C, Yang J, Leimkuhler S, Kirk ML (2014) Pyranopterin dithiolene distortions relevant to electron transfer in xanthine oxidase/dehydrogenase. Inorg Chem 53(14):7077–7079
138. Kappler U, Bailey S (2005) Molecular basis of intramolecular electron transfer in sulfite-oxidizing enzymes is revealed by high resolution structure of a heterodimeric complex of the catalytic molybdopterin subunit and a c-type cytochrome subunit. J Biol Chem 280 (26):24999–25007
139. Gisewhite DR et al (2018) Implications of pyran cyclization and pterin conformation on oxidized forms of the molybdenum cofactor. J Am Chem Soc 140(40):12808–12818
140. Sugimoto H et al (2016) A model for the active-site formation process in DMSO reductase family molybdenum enzymes involving oxido alcoholato and oxido thiolato molybdenum (VI) core structures. Inorg Chem 55(4):1542–1550
141. Spence J (1983) Modeling the molybdenum centers of the molybdenum hydroxylases. Coord Chem Rev 48(1):59–82

142. Pilato R, Stiefel E (1993) Bioinorganic catalysis. Marcel Dekker, New York, pp 131–188
143. Maia LB, Moura I, Moura JJG (2017) Molybdenum and tungsten-containing enzymes: an overview. The Royal Society of Chemistry, Cambridge, pp 1–80
144. Enemark JH, Young CG (1993) Bioinorganic chemistry of pterin-containing molybdenum and tungsten enzymes. Adv Inorg Chem 40:1–88
145. Doonan CJ et al (2008) Electronic structure description of the cis-MoOS unit in models for molybdenum hydroxylases. J Am Chem Soc 130(1):55–65
146. Enemark JH, Cooney JJA (2004) Synthetic analogues and reaction systems relevant to the molybdenum and tungsten oxotransferases. Chem Rev 104(2):1175–1200
147. Holm RH (1987) Metal-centered oxygen atom transfer-reactions. Chem Rev 87(6):1401–1449
148. McNaughton RL, Helton ME, Rubie ND, Kirk ML (2000) The oxo-gate hypothesis and DMSO reductase: implications for a psuedo-sigma bonding interaction involved in enzymatic electron transfer. Inorg Chem 39(20):4386
149. McNaughton RL, Tipton AA, Rubie ND, Conry RR, Kirk ML (2000) Electronic structure studies of oxomolybdenum tetrathiolate complexes: origin of reduction potential differences and relationship to cysteine-molybdenum bonding in sulfite oxidase. Inorg Chem 39 (25):5697–5706
150. Peariso K, Helton ME, Duesler EN, Shadle SE, Kirk ML (2007) Sulfur K-edge spectroscopic investigation of second coordination sphere effects in oxomolybdenum-thiolates: relationship to molybdenum-cysteine covalency and electron transfer in sulfite oxidase. Inorg Chem 46 (4):1259–1267
151. Nemykin VN, Olsen JG, Perera E, Basu P (2006) Synthesis, molecular and electronic structure, and TDDFT and TDDFT-PCM study of the solvatochromic properties of (Me(2) Pipdt)Mo(CO)(4) complex (Me(2)Pipdt = N,N′-dimethylpiperazine-2,3-dithione). Inorg Chem 45(9):3557–3568
152. Boyde S, Garner CD (1991) Electrochemistry of tris(quinoxaline-2,3-dithiolato)molybdate (IV) in acidic solution: multi-electron ligand-based redox activity. J Chem Soc Dalton Trans 713–716
153. Armstrong EM et al (1993) Synthesis of cyclopentadienyl-ene-1,2-dithiolatocobalt complexes and coupled proton-electron transfer in a substituted quinoxalinyl derivative. Heterocycles 35 (2):563–568
154. Dicks JP et al (2015) Synthesis, structure and redox properties of asymmetric (cyclopentadienyl)(ene-1,2-dithiolate)cobalt(III) complexes containing phenyl, pyridyl and pyrazinyl units. Eur J Inorg Chem 21:3550–3561
155. Hsu JK et al (1996) Direct conversion of alpha-substituted ketones to metallo-1,2-enedithiolates. Inorg Chem 35(16):4743–4751
156. Kaiwar SP, Vodacek A, Blough NV, Pilato RS (1997) Protonation-state-dependent luminescence and excited-state electron-transfer reactions of 2- and 4-pyridine (-ium)-substituted metallo-1,2-enedithiolates. J Am Chem Soc 119:9211–9214
157. VanHouten KA, Boggs CV, Pilato RS (1998) Synthesis and characterization of alpha-phosphorylated ketones: models for the molybdopterin precursor. Tetrahedron 54 (37):10973–10986
158. Pilato RS et al (1993) Pterins, quinoxalines, and metallo-ene-dithiolates – synthetic approach to the molybdenum cofactor. ACS Symp Ser 535:83–97
159. Pilato RS et al (1991) Model complexes for molybdopterin-containing enzymes: preparation and crystallographic characterization of a molybdenum-ene-1-perthiolate-2-thiolate (trithiolate) complex. J Am Chem Soc 9372–9374
160. Fogeron T, Retailleau P, Chamoreau LM, Li Y, Fontecave M (2018) Pyranopterin related dithiolene molybdenum complexes as homogeneous catalysts for CO2 photoreduction. Angew Chem Int Ed 57(52):17033–17037
161. Porcher JP et al (2015) A bioinspired molybdenum complex as a catalyst for the photo- and electroreduction of protons. Angew Chem Int Ed 54(47):14090–14093

162. Gisewhite DR, Nagelski AL, Cummins DC, Yap GPA, Burgmayer SJN (2019). Modeling pyran formation in the molybdenum cofactor: protonation of quinoxalyl-dithiolene promoting pyran cyclization. Inorg Chem 58(8):5134–5144. https://doi.org/10.1021/acs.inorgchem.9b00194
163. Gisewhite D (2018) The molybdenum cofactor: modeling the Swiss army knife of metabolic diversity. PhD, Bryn Mawr College
164. Williams BR, Fu YC, Yap GPA, Burgmayer SJN (2012) Structure and reversible pyran formation in molybdenum pyranopterin dithiolene models of the molybdenum cofactor. J Am Chem Soc 134(48):19584–19587
165. Williams BR, Gisewhite D, Kalinsky A, Esmail A, Burgmayer SJN (2015) Solvent-dependent pyranopterin cyclization in molybdenum cofactor model complexes. Inorg Chem 54 (17):8214–8222
166. Bray R, Adams B, Smith A, Bennett B, Bailey S (2000) Reversible dissociation of thiolate ligands from molybdenum in an enzyme of the dimethyl sulfoxide reductase family. Biochemistry 39(37):11258–11269
167. Bell AF et al (2001) Active site heterogeneity in dimethyl sulfoxide reductase from Rhodobacter capsulatus revealed by Raman spectroscopy. Biochemistry 40(2):440–448
168. George GN, Hilton J, Temple C, Prince RC, Rajagopalan KV (1999) Structure of the molybdenum site of dimethyl sulfoxide reductase. J Am Chem Soc 121:1256–1266

Struct Bond (2019) 179: 153–166
DOI: 10.1007/430_2018_27

Published online: 7 September 2018

Mechanism of Ni,Fe-Containing Carbon Monoxide Dehydrogenases

Holger Dobbek

Contents

Abstract Carbon monoxide dehydrogenases catalyze the reversible oxidation of CO with water to CO_2, two protons and two electrons. Phylogenetically diverse bacteria and archaea living under anaerobic conditions employ different classes of Ni,Fe-containing carbon monoxide dehydrogenases to use CO as an energy source or to contribute in converting CO_2 to acetyl-CoA.

The active site of carbon monoxide dehydrogenases contains a unique $[NiFe_4S_4]$-cluster, the only known example in nature where Ni is integrated into a heterocubane structure. The Ni ion serves as the catalytic nucleophilic center for activating CO and CO_2, in which it is supported by an electrophilic Fe ion placed in *exo* to the heterocubane cluster.

This review gives an overview on current ideas how Ni,Fe-containing carbon monoxide dehydrogenases reversibly oxidize CO to CO_2, with a focus on recent structural studies of the enzymes.

Keywords Carbon dioxide · Carbon monoxide · Iron-sulfur cluster · Nickel · Small molecule activation

H. Dobbek (✉)
Department of Life Sciences, Institute of Biology, Structural Biology/Biochemistry, Humboldt-Universität zu Berlin, Berlin, Germany
e-mail: holger.dobbek@hu-berlin.de

1 Introduction

Enzymes catalyzing the oxidation of carbon monoxide (CO) with water to carbon dioxide (CO_2), two protons and two electrons, acting as CO/acceptor oxidoreductases, are called carbon monoxide dehydrogenases, or short CODHs [1]. Two different types of CODHs have been isolated from aerobically and from anaerobically living microorganisms. We can easily distinguish the two types as they share no sequence similarity, use different cofactors, contain different metals in the active site, and contrast in their ability to reduce CO_2 and in their reactivity with oxygen and thus their stability in air [2].

Cu,Mo-containing CODHs are encountered in aerobic carboxydotrophic bacteria. These air-stabile CODHs are molybdo-iron/sulfur flavoenzymes whose active site comprises a binuclear Cu,Mo-site linked by a sulfido-ligand [3]. Their physiological task is entirely in oxidizing CO and they don't support CO_2 reduction. The enzymes are unreactive to air in the oxidized state (Cu(I)-Mo(+VI)) but become air-sensitive under turnover conditions.

Ni,Fe-containing CODHs, occurring as mono-, bi-, and multifunctional enzyme complexes, are found in anaerobically living bacteria and archaea and are iron-sulfur cluster-containing enzymes [1, 2, 4, 5]. Their active sites comprise a Ni,Fe/S cluster, whose structure will be reviewed. While the physiological role of monofunctional CODHs is to oxidize CO, in most bi- and multifunctional CODH complexes, CO_2 reduction is the goal [4, 6]. Independent of their physiological task, Ni,Fe–CODHs catalyze CO_2 reduction at high rates [7]. Recent reviews focused on physiological functions and pathways [4–6], the electrochemistry of CODHs [8], their maturation [9, 10], as well as the direct comparison of Ni,Fe– and Cu,Mo–CODHs and their parallels and differences [1, 2]. This review will focus on the insight gained during the last 5 years on Ni,Fe–CODHs in different states.

2 Chemistry of CO and CO_2

To better understand the task of CODHs, we first look at their substrates.

CO is a colorless, odorless, and flammable gas. Famous for its great toxicity to oxygen-respiring organisms, it is an ubiquitous pollutant in the present atmosphere [11, 12]. We can find anthropogenic enrichments of CO in any place where incomplete combustion processes starting from reduced carbon compounds occur, such as dense urban traffic zones, but also near fires and in charcoal production [11, 12]. Anthropogenic and natural emissions account for 2,500–2,600 Tg of CO per year [11, 12]. While in the early earth volcanic emission raised CO concentrations in the atmosphere to approximately 100 ppm, volcanic environments can foster CO-dependent life today.

CO is isoelectronic with CN^- and N_2. The formal CO polarization with a negative charge at C and a positive charge at O is essentially canceled out by the counteracting

polarization due to the higher electronegativity of oxygen, giving CO a special character with an unusually electron-rich carbon atom [13].

The highest occupied molecular orbital (HOMO) of CO is centered at C, favoring metal CO interactions by M–C bonds. Its typical interaction with metals is governed by backbonding, where CO donates σ-electrons to the metal and accepts the metals d-π electrons into its π*-orbital (Fig. 1) [13]. Compared to free CO, the carbon atom in the metal-bound carbonyl becomes more positively charged and its oxygen atom more negatively charged. Thus, when bound to a metal, CO gets polarized and activated, becoming susceptible to a nucleophilic attack, which gets more pronounced when CO binds to a metal of low π-basicity [13]. Nucleophilic attack at the metal carbonyl can cause carbene-like intermediates with a strong metal-carbon interaction. When the attacking nucleophile is activated water/hydroxide, we reach the water-gas shift reaction (WGSR) which is used to alter the CO/H_2 ratio in synthesis gas [14]. In the first step of WGSR, CO binds to a metal and goes through a nucleophilic attack of a hydroxyl group, arising from activated water. The resulting metal carboxylic acid is decarboxylated by a β-hydride shift, and protonation of the formed metal hydride liberates H_2, which closes the cycle after CO_2 release [13]. The WGSR reaction is analogous to the reaction catalyzed by CODHs, with the difference that the enzyme keeps the protons and electrons separated [1].

The product of CO oxidation is CO_2, a colorless, non-flammable gas that does not support respiration. CO_2 is a linear molecule with formal C=O double bonds. The different electronegativities of C and O result in a positively polarized C atom and negatively polarized O atoms [1].

To catalyze CO_2 reduction, the molecule needs to be activated [1]. The lowest unoccupied molecular orbital (LUMO) of CO_2 is localized at the carbon atom, allowing the attack of nucleophiles and reduction at this position. Activation in biological systems typically occurs by a cooperation of nucleophilic and electrophilic centers, decreasing the C–O bond order and the O–C–O bond angle (Fig. 1). The resulting bent state stabilizes the LUMO such that CO_2 rather experiences a two-electron reduction than reduction by a single electron, which is thermodynamically unfavorable [1].

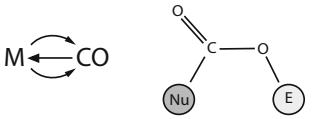

Fig. 1 Activation of CO and CO_2 by binding to metals. Left side: CO binding to a metal is stabilized by backbonding. CO is a good π-acceptor able to form strong M–L bonds. Its empty π*-orbitals interact with the filled d-π-orbitals of the metal as π-acceptor (indicated by the two bended arrows). The HOMO at carbon acts as a σ-donor (indicated by the from right to left arrow). To form stable CO complexes, metals need to be in a reduced state and have a high electron density, also described as being electron-rich. Right side: The LUMO of CO_2 at the carbon atom makes it susceptible to attack of nucleophiles (Nu) and reduction at this position. The activation is typically assisted by an electrophile (E) interacting with the HOMO of CO_2 at the oxygen(s). The activated state of CO_2 is bent

CO_2 reduction by two electrons may yield two different products, CO or formate. A study of a $[Ni(cyclam)]^+$ complex shows that the initial complex formed with CO_2 determines the fate of the reaction. While a η^1-OCO complex gives formate, a reaction catalyzed by Mo- and W-containing formate dehydrogenases, a η^1-CO_2 complex gives CO, the product of CODHs [15].

3 Physiology of Ni,Fe–CODHs

Depending on the physiological conditions and source organism, CODHs are isolated from their bacterial hosts either as individual enzymes or in complex with one or more enzymes [1]. Monofunctional CODHs typically oxidize CO to CO_2 and occur in the genome of many anaerobic bacteria and archaea [16, 17]. Although they are isolated from the organism as individual enzymes, at least some of them form complexes with a ferredoxin termed CooF and a membrane-bound Ni,Fe-containing hydrogenase [18–20]. Creating a complex between CODH and a CO-insensitive hydrogenase allows coupling CO oxidation to proton reduction ($CO + H_2O \rightarrow CO_2 + H_2$), a reaction corresponding to the WGSR. But unlike the WGSR, the bacteria store the energy difference of CO oxidation and proton reduction by producing a proton-motive force across the cytoplasmic membrane needed for ATP synthesis [19, 21–23].

In contrast to the monofunctional CODHs, which form relatively unstable complexes, the bifunctional complex between CODH and acetyl-CoA synthase (ACS; condensing CO, CH_3^+, and CoA to acetyl-CoA) is stable enough to allow diffusion of the CO generated from CO_2 reduction in the CODH subunit to the ACS active site through a molecular tunnel without leaking CO into the solution [24, 25]. The complex appears so strong that CODH variants found in complex with ACS are not observed as individual enzymes without their partner.

The multifunctional CODHs are encountered in methane-producing (methanogenic) archaea [1]. They are composed of five different subunits (α, β, γ, δ, and ε) comprising a CODH subunit, an ACS subunit, and a corrinoid-iron/sulfur protein [26]. The latter abstracts and transfers the methyl group of a methylated pterin (sarcinapterin or methanopterin) to the active site of ACS. The three enzymes must therefore act in a concert for which we lack yet the instruments to listen.

4 Overall Structure of Ni,Fe–CODHs

Crystal structures have been determined for all three known types of CODHs: mono-, bi-, and multifunctional CODHs (Fig. 2).

Crystal structures of three different monofunctional CODHs have been resolved: the CODH of *Rhodospirillum rubrum* ($CODH_{Rr}$) and two different CODHs from

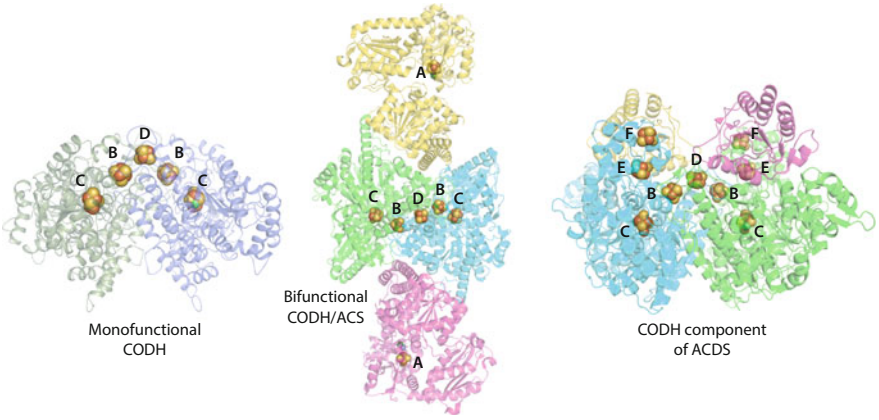

Fig. 2 Overall structure of CODHs. The three classes of Ni,Fe-containing CODHs, mono-, bi-, and multifunctional CODHs, are displayed from left to right. Of the latter, only the structure of the CODH component has been determined. The secondary structure is depicted as semitransparent cartoons and the iron-sulfur clusters as space-filling van der Waals models with Ni atoms in green, iron in orange, and sulfur in yellow. Clusters are labeled A–F. Cluster A is the active site cluster of ACS. Structures shown in Figs. 2, 3, and 4 have been prepared using PyMol [62]

Carboxydothermus hydrogenoformans ($CODHII_{Ch}$ and $CODHIV_{Ch}$) [27–29]. The crystal structure of the CODH component of the bifunctional CODH/ACS complex of *Moorella thermoacetica* is remarkably similar to that of the monofunctional CODHs, with all presenting a mushroom-shaped homodimeric structure with five metal clusters, holding three cubane-type [4Fe4S]-clusters (two cluster B and one cluster D) and the active site Ni,Fe-cluster (cluster C) [30, 31].

The CODH component of the multifunctional acetyl-CoA decarbonylase/synthase (ACDS) complex from *Methanosarcina barkeri* is larger than the two other types of CODHs, accommodating two additional [4Fe4S]-clusters (clusters E and F), and forms a tight structure with an additional subunit (epsilon subunit) of unidentified function [32].

Monofunctional Ni,Fe–CODH consists of three domains: the predominantly alpha-helical N-terminal domain (residues 3–237; numbering $CODHII_{Ch}$) harboring the binding regions for clusters B and D and the middle (238–406) and C-terminal (407–636) domains with Rossmann-fold topology between which cluster C is resting [27]. The three domains provide the architecture needed for substrate entry and product egress, including different gas channels. One of the gas channels is conserved among mono- and bifunctional CODHs and corresponds to the tunnel connecting cluster C of Ni,Fe–CODH and the active site cluster A of ACS in bifunctional Ni,Fe–CODH [2, 31, 33, 34]. A second channel appears to be exclusive to monofunctional Ni,Fe–CODHs. A dynamically formed gas channel through which CO_2 may diffuse from the solvent to cluster C has been observed in bifunctional CODH/ACS complex by a combination of molecular dynamics and density functional theory computations [35].

5 Structure and Electronic States of Cluster C

The active site of Ni,Fe-containing CODHs contains a [$NiFe_4S_4$]-cluster (cluster C), in which a distorted $NiFe_3S_4$ heterocubane cluster is attached to a ferrous Fe(II) in *exo* (Fig. 3). The Fe(II) ion (Fe1 in the structure) is also known as ferrous component II (FCII) and is coordinated by a hydroxyl ligand in the state ready to react with CO [36–38].

Cluster C can take up at least four different oxidation states [39]. Above −200 mV the oxidized state, called C_{ox}, is adopted, a diamagnetic and catalytically inactive state. CO oxidation takes place only after a one-electron reduction of C_{ox} to the C_{red1} state. C_{red1} is paramagnetic ($S = 1/2$ spins) and has likely the oxidation state {[Ni^{2+} Fe^{2+}]: [Fe_3 S_4]$^-$}. After an additional two-electron reduction, C_{red1} converts to C_{red2} with a midpoint potential of $E^{\circ\prime} = -530$ mV, which coincides with the midpoint potential of the CO_2/CO couple ($E^{\circ\prime} = -558$ mV) [36, 40, 41]. C_{red2} displays only a minor shift in the paramagnetic resonance spectrum compared to C_{red1} despite the two added electrons supposed to be contained in this state [42, 43]. Where these two electrons are located is unknown, and a zero-valent nickel – Ni^0, a hydride-bound to Ni^{2+}, and a Ni–Fe bond (dative metal–metal bond) have been suggested [44, 45]. One-electron oxidation of C_{red2} results in the transient C_{int} state, which is bare of a paramagnetic signal [43]. Midpoint potentials and spectroscopic signatures change when adducts are bound to the cluster [37, 46].

6 Reversible Oxidation of CO to CO_2 at Cluster C

The oxidation state to commence with the reaction of CO is C_{red1} (Fig. 4). Cluster C has up to two open coordination sites at the Ni ion to bind CO, and the hydroxyl ligand is bound to Fe1 [38]. CO is rapidly oxidized by CODHs with $CODHII_{Ch}$ having a

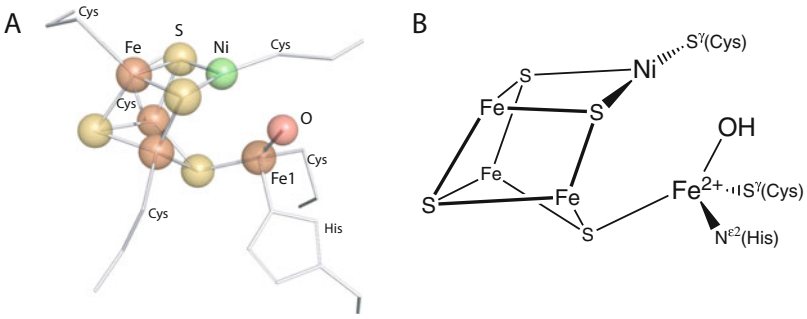

Fig. 3 Structure of the active site cluster C. (**a**) Ball-and-stick presentation of cluster C, with the metals (Ni and Fe) and their nonamino acid ligands (S and O) shown as semitransparent spheres with Ni in green, iron in orange, sulfur in yellow, and oxygen in red. (**b**) Schematic drawing of the inorganic core of cluster C

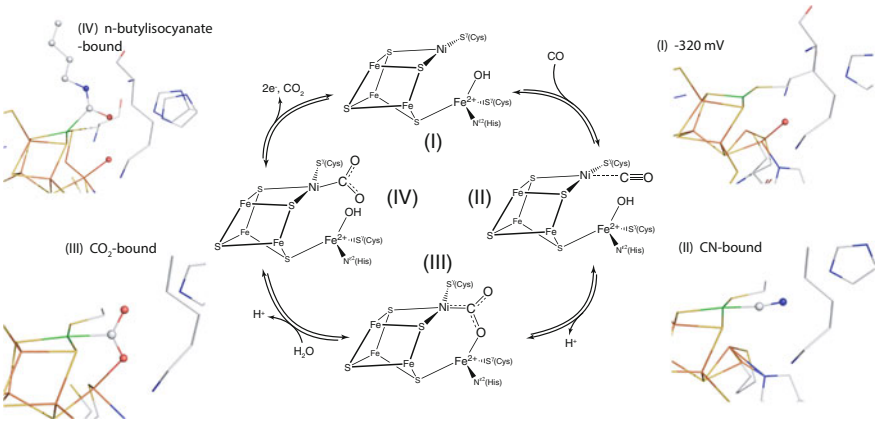

Fig. 4 Structure-based mechanism of CO oxidation. CO oxidation involves at least the four states (states I–IV) shown in the center of the figure. The four states are surrounded by crystal structures, which serve as models for how CO oxidation/CO_2 reduction may occur at cluster C with Ni in green, iron in orange, sulfur in yellow, carbon in white, nitrogen in blue, and oxygen in red (PDB-IDs: I, 3B53; II, 5FLE; III, 4UDX; IV, 2YIV)

turnover number (k_{cat}) of 31,000 s^{-1} and a Michaelis constant (K_M) for CO of 18 μM at 70°C [21]. Some monofunctional CODHs belong to the few, perfect enzymes known: $CODHIV_{Ch}$ has an efficiency constant k_{cat}/K_M of 3×10^8–10^9 M^{-1} s^{-1} over the entire temperature range for which it was tested and is therefore only limited by the diffusion of CO [29]. Arrhenius-type activation energies are typically in the range of 40–60 kJ mol^{-1} except for $CODHIV_{Ch}$ where the activation energy of CO oxidation is 100 kJ mol^{-1} [29, 41, 47].

CO_2 reduction starts from the C_{red2} state, which is two electrons more reduced than C_{red1}. CO_2 reduction is slower than CO oxidation and the kinetics strongly dependent on the source of electrons. $CODH_{Rr}$ catalyzes CO_2 reduction with a k_{cat} of 45 s^{-1} and a K_M for CO_2 of 0.18 mM when methyl viologen is used as a mediator for electron transfer between reducing agent and enzyme [7].

We have only indirect insights into the CO-bound cluster C [48]. Producing a stable state with CO for structural or spectroscopic investigation has proofed difficult so far, likely because of the high turnover numbers. Additional electron density at Ni has sometimes been modeled as CO. While CO was modeled in the expected linear Ni–C–O arrangement, also a tilted CO-bound ligand was suggested [31, 32]. However, the tilted CO ligand was observed in preparations where CO has not been added, and it is unclear how it could remain stably bound during purification and crystallization, when turnover occurs in less than a millisecond with an equilibrium, in the absence of strong reducing agents, strictly on the side of CO oxidation. Thus, if these states are truly reflecting a bound CO molecule, it is likely not a substrate, but either a potential placeholder for substrate binding or a spectator ligand. Indeed, a Ni catalyst for CO_2 reduction indicates that a bound CO could help to reduce the Ni to become able to bind and reduce CO_2 [49]. The hypothesis of a "spectator" CO was

advanced in investigations of *R. rubrum* CODH [50]. But elongated electron densities are also frequently encountered for two alternative positions of one water molecule which are difficult to differentiate from a diatomic ligand at medium resolution, and CODHs notoriously consist of a mixture of states only clearly resolved once the resolution of the crystal structures is high enough to allow the detection of multiple positions [51]. Not surprisingly, the crystallographic assignment of the tilted CO has not been supported by an independent evaluation of the electron density [44].

A more stable state, amenable to spectroscopic and structural investigation than that of CO, may be reached with cyanide. Cyanide is isoelectronic to CO and has early been used to reversibly inhibit CO oxidation in bacterial extracts by adding low concentrations of cyanide [52]. Cyanide is a slow-binding, competitive inhibitor (competitive in respect to CO) with a K_i of 8.5 μM in $CODH_{Rr}$ and of 21.7 μM for $CODHII_{Ch}$ [48, 53, 54]. Both are within the typical range of K_M values for CO, and their similar properties made cyanide a plausible model for the binding of CO. Binding of cyanide has been followed by IR spectroscopy revealing a band at 2,110 cm^{-1}, while EPR spectroscopy revealed a change in the C_{red1} signal [37, 55]. In the structure of the bifunctional CODH/ACS complex from *Moorella thermoacetica*, a bent conformation for cyanide with a distorted tetrahedral coordination of Ni was found after adding cyanide to crystals [56]. However, a reevaluation of the structure casted doubt on the evidence for the ligand in the electron density [44]. Crystals of $CODHII_{Ch}$ treated with cyanide resolved cyanide at the open equatorial coordination site of Ni, with a nearly linear Ni–C–O axis and is stabilized by hydrogen bonds with Lys563 and His93 (Fig. 4) [57]. The OH ligand on Fe1 is lost, and Fe1 shifts to an alternative position ($Fe1_B$), which is more close to Ni. A combined structural, IR-spectroscopic, and computational study showed little influence of an exchange of the nearby Lys563 to Ala [55]. Surprisingly, Lys563 remained stably deprotonated likely from protonating the OH ligand at Fe1 upon its dissociation as water.

From the structural studies, it is clear that there are two available positions for CO binding to Ni: the apical position, where some weak electron density was reported for it, and the equatorial position, in which the cyanide molecule was modeled. From the course of the reaction, bringing the carbon atom of CO close enough to react with the hydroxyl ligand, it is clear that it needs to react in the equatorial position, reaching it either by flipping from an apical coordination or by binding in the equatorial position from the beginning on. The reaction of CO with the hydroxyl ligand at Fe1 would then result in an arrangement observed in a crystal structure in the presence of CO_2 [38, 51].

Insights into CO/CO_2 activation were derived from a CO_2-bound structure (Fig. 4) [38, 51]. $CODHII_{Ch}$ crystals were incubated in a solution of Ti(III)-citrate adjusted to a reduction potential of −600 mV together with 45 mM $NaHCO_3$, corresponding to 0.45 mM solvated CO_2 at pH 8.0. The crystals were allowed to react for several minutes and were then flash cooled in liquid nitrogen. The resulting $[NiFe_4S_4(CO_2)]$-cluster clearly resolves a carboxylate ligand bridging Ni and Fe1 acting as a μ_2-η^2 ligand. CO_2 completes the square-planar coordination of Ni (η^1-CO_2 mode) and binds

in the mode favoring CO instead of $HCOO^-$ production. CO_2 binding displaces the water ligand at Fe1 where it binds with an oxygen atom (η^1-OCO mode). The resolution of 1.03 Å allowed to resolve the oxidation state of CO_2, which is clearly in an activated state with an O–C–O-bending angle of 117° [51]. The O–C–O angle and C–O bond length (1.30 and 1.32 Å) indicate that CO_2 is reduced by two electrons. Finally the short Ni–C bond of 1.8 Å reveals substantial π-backbonding, resembling a Ni-carbene stabilized by hydrogen bonds to a lysine and a histidine residue.

The same kind of activation and interaction is also found for cyanate [51]. Cyanate is a C_{red2}-specific inhibitor, inhibiting CO_2 reduction in the C_{red2} state and stabilizing it by its binding [58, 59]. Addition of cyanate to crystals previously incubated in a strong reducing agent able to produce C_{red2} resulted in a bent structure for the three atoms at cluster C, strongly resembling the binding of CO_2. Likewise cyanate is reduced by two electrons giving a bound carbamoyl group stabilized by strong π-backbonding interactions with Ni. In solution cyanate is reduced to cyanide, which is detected by IR spectroscopy by following the characteristic 2,110 cm^{-1} band of CN bound to cluster C [60].

The first step in converting the metal-bound carboxylate to free CO_2 is initiated by splitting the Fe1–O bond, possibly assisted by an incoming water molecule substituting the oxygen of CO_2 at Fe1. To be released through the gas channel, CO_2 might rearrange, moving closer to the gas channel when the Ni coordination changes from square-planar to tetrahedral. A similar state was observed in crystals treated with *n*-butyl isocyanide (*n*-BIC) [34].

N-BIC is one of several alternative substrates, including carbonyl sulfide, cyanate, nitrous oxide, and hydroxylamine, which are slowly reduced and thus rather analogous to CO_2. In contrast, *n*-BIC is a substrate related to CO, acting as a rapid binding competitive inhibitor of CO and slow-turnover substrate of Ni,Fe–CODHs [61]. Crystals of $CODHII_{Ch}$ treated with *n*-BIC seem to undergo at least one round of turnover as *n*-butyl isocyanate, the product of oxidizing *n*-BIC by two electrons, is produced and trapped in the active site (Fig. 4) [34]. The *n*-butyl isocyanate bound in the active site is stabilized by H bonds with the OH ligand of Fe1 and neighboring side chains. Interestingly, treatment of crystals of Cu,Mo-CODH produces an analogous product molecule stuck in the active site, revealing another parallel between these nonhomologous, differently structured enzymes.

The remaining steps would see a release of CO_2 from the cluster, at which moment cluster C would take up the two electrons gained from CO oxidation, converting to C_{red2}. The two electrons in the next step would be transferred one-by-one from cluster C to cluster B and possibly to cluster D from where they would be transported to external electron acceptors, which in case of monofunctional CODHs is mostly the ferredoxin CooF, finally closing the catalytic cycle.

7 Outlook

There is a common trend in metalloenzymology: the explosion of genomic data and the advance of computational tools to analyze enzyme evolution in large sequence data sets open new ways to look on old enzymes.

We discover today increasingly different variants of our pet enzymes, which are not just copies of each other separated by divergent evolution but which are distinct owing to different physiological functions and adaptations to diverse environments. These variations are also interesting for mechanistic enzymologists and chemists.

Ni,Fe-containing CODHs are widespread among anaerobic bacteria and archaea and appear to have existed as far back in time as we can see in enzyme evolution. They had a long time to evolve in various directions and adapt to divergent physiological functions and different substrates. An example of this diversification is CODHIV$_{Ch}$, with its atypical high affinity for CO and adaptation to support the oxidative stress response of *C. hydrogenoformans*.

Our ability to explore this diversity increased within the last years as it became possible to produce CODHs by recombinant methods, allowing us to study enzymes that had never been isolated from the native organisms, either because they are expressed in low amounts or because the organism has not been cultivated, maybe not even isolated from its environment. The recombinant production also allows us to exchange key amino acids by site-directed mutagenesis, permitting us to explore the roles of first and second coordination spheres of the metals on the reaction mechanism. Care has to be taken not to overlook the nonlocal effects and conformational changes so frequently found when exchanging amino acids, necessitating structural studies of the CODH variants to interpret the causes of changed reactivities. Recombinant production is additionally fostered by novel insights into the maturation of CODHs and may allow a more widespread use of the enzymes in biotechnology [9, 10].

To explore, understand, and employ this diversity will require efforts in all fields including microbiology, enzymology, spectroscopy, electrochemistry, structural biology, and theoretical modeling – a task for the entire community.

Acknowledgments I would like to acknowledge all past and present co-workers and collaborators working on CODHs. Research has been funded by the DFG through DO 785/6 and the excellence initiative through the cluster “Unifying Concepts in Catalysis – UniCat” (EXC 314).

References

1. Appel AM, Bercaw JE, Bocarsly AB, Dobbek H, DuBois DL, Dupuis M, Ferry JG, Fujita E, Hille R, Kenis PJA, Kerfeld CA, Morris RH, Peden CHF, Portis AR, Ragsdale SW, Rauchfuss TB, Reek JNH, Seefeldt LC, Thauer RK, Waldrop GL (2013) Frontiers, opportunities, and challenges in biochemical and chemical catalysis of CO_2 fixation. Chem Rev 113 (8):6621–6658. https://doi.org/10.1021/Cr300463y

2. Jeoung JH, Fesseler J, Goetzl S, Dobbek H (2014) Carbon monoxide. Toxic gas and fuel for anaerobes and aerobes: carbon monoxide dehydrogenases. Met Ions Life Sci 14:37–69. https://doi.org/10.1007/978-94-017-9269-1_3
3. Hille R, Dingwall S, Wilcoxen J (2015) The aerobic CO dehydrogenase from *Oligotropha carboxidovorans*. J Biol Inorg Chem 20(2):243–251. https://doi.org/10.1007/s00775-014-1188-4
4. Ragsdale SW (2008) Enzymology of the Wood-Ljungdahl pathway of acetogenesis. Ann N Y Acad Sci 1125:129–136. https://doi.org/10.1196/Annals.1419.015
5. Ragsdale SW, Pierce E (2008) Acetogenesis and the Wood-Ljungdahl pathway of CO(2) fixation. Biochim Biophys Acta 1784(12):1873–1898. https://doi.org/10.1016/j.bbapap.2008.08.012
6. Ragsdale SW (2004) Life with carbon monoxide. Crit Rev Biochem Mol Biol 39(3):165–195
7. Ensign SA (1995) Reactivity of carbon-monoxide dehydrogenase from *Rhodospirillum rubrum* with carbon-dioxide, carbonyl sulfide, and carbon-disulfide. Biochemistry 34(16):5372–5381
8. Wang VC, Ragsdale SW, Armstrong FA (2014) Investigations of the efficient electrocatalytic interconversions of carbon dioxide and carbon monoxide by nickel-containing carbon monoxide dehydrogenases. Met Ions Life Sci 14:71–97. https://doi.org/10.1007/978-94-017-9269-1_4
9. Dobbek H (2017) CO dehydrogenase and acetyl-CoA synthase assembly. Encyclopedia of inorganic and bioinorganic chemistry. Wiley, Hoboken. https://doi.org/10.1002/9781119951438.eibc2473
10. Merrouch M, Benvenuti M, Lorenzi M, Leger C, Fourmond V, Dementin S (2018) Maturation of the [Ni-4Fe-4S] active site of carbon monoxide dehydrogenases. J Biol Inorg Chem 23 (4):613–620. https://doi.org/10.1007/s00775-018-1541-0
11. Khalil MAK, Rasmussen RA (1990) The global cycle of carbon-monoxide – trends and mass balance. Chemosphere 20(1–2):227–242. https://doi.org/10.1016/0045-6535(90)90098-E
12. Khalil MAK, Pinto JP, Shearer MJ (1999) Atmospheric carbon monoxide. Chemosphere Global Change Sci 1:xi–xiii
13. Crabtree RH (2009) The organometallic chemistry of the transition metals5th edn. Wiley, Hoboken
14. Newsome DS (1980) The water-gas shift reaction. Catal Rev Sci Eng 21(2):275–318. https://doi.org/10.1080/03602458008067535
15. Song J, Klein EL, Neese F, Ye S (2014) The mechanism of homogeneous CO_2 reduction by Ni (cyclam): product selectivity, concerted proton-electron transfer and C-O bond cleavage. Inorg Chem 53(14):7500–7507. https://doi.org/10.1021/ic500829p
16. Lindahl PA, Chang B (2001) The evolution of acetyl-CoA synthase. Orig Life Evol Biosph 31 (4–5):403–434
17. Adam PS, Borrel G, Gribaldo S (2018) Evolutionary history of carbon monoxide dehydrogenase/acetyl-CoA synthase, one of the oldest enzymatic complexes. Proc Natl Acad Sci U S A 115(6):E1166–E1173. https://doi.org/10.1073/pnas.1716667115
18. Fox JD, He YP, Shelver D, Roberts GP, Ludden PW (1996) Characterization of the region encoding the CO-induced hydrogenase of *Rhodospirillum rubrum*. J Bacteriol 178 (21):6200–6208
19. Soboh B, Linder D, Hedderich R (2002) Purification and catalytic properties of a CO-oxidizing: H_2-evolving enzyme complex from *Carboxydothermus hydrogenoformans*. Eur J Biochem 269 (22):5712–5721
20. Wu M, Ren Q, Durkin AS, Daugherty SC, Brinkac LM, Dodson RJ, Madupu R, Sullivan SA, Kolonay JF, Haft DH, Nelson WC, Tallon LJ, Jones KM, Ulrich LE, Gonzalez JM, Zhulin IB, Robb FT, Eisen JA (2005) Life in hot carbon monoxide: the complete genome sequence of *Carboxydothermus hydrogenoformans* Z-2901. PLoS Genet 1(5):e65. https://doi.org/10.1371/journal.pgen.0010065
21. Svetlitchnyi V, Peschel C, Acker G, Meyer O (2001) Two membrane-associated NiFeS-carbon monoxide dehydrogenases from the anaerobic carbon-monoxide-utilizing eubacterium *Carboxydothermus hydrogenoformans*. J Bacteriol 183(17):5134–5144

22. Svetlichny VA, Sokolova TG, Gerhardt M, Ringpfeil M, Kostrikina NA, Zavarzin GA (1991) *Carboxydothermus hydrogenoformans* gen-nov, sp-nov, a CO-utilizing thermophilic anaerobic bacterium from hydrothermal environments of Kunashir-Island. Syst Appl Microbiol 14 (3):254–260
23. Henstra AM, Stams AJ (2011) Deep conversion of carbon monoxide to hydrogen and formation of acetate by the anaerobic thermophile *Carboxydothermus hydrogenoformans*. Int J Microbiol 2011:641582. https://doi.org/10.1155/2011/641582
24. Maynard EL, Lindahl PA (1999) Evidence of a molecular tunnel connecting the active sites for CO_2 reduction and acetyl-CoA synthesis in acetyl-CoA synthase from *Clostridium thermoaceticum*. J Am Chem Soc 121(39):9221–9222. https://doi.org/10.1021/Ja992120g
25. Seravalli J, Ragsdale SW (2000) Channeling of carbon monoxide during anaerobic carbon dioxide fixation. Biochemistry 39(6):1274–1277. https://doi.org/10.1021/Bi991812e
26. Grahame DA, DeMoll E (1996) Partial reactions catalyzed by protein components of the acetyl-CoA decarbonylase synthase enzyme complex from *Methanosarcina barkeri*. J Biol Chem 271 (14):8352–8358
27. Dobbek H, Svetlitchnyi V, Gremer L, Huber R, Meyer O (2001) Crystal structure of a carbon monoxide dehydrogenase reveals a [Ni-4Fe-5S] cluster. Science 293(5533):1281–1285. https://doi.org/10.1126/science.1061500
28. Drennan CL, Heo J, Sintchak MD, Schreiter E, Ludden PW (2001) Life on carbon monoxide: X-ray structure of *Rhodospirillum rubrum* Ni-Fe-S carbon monoxide dehydrogenase. Proc Natl Acad Sci U S A 98(21):11973–11978. https://doi.org/10.1073/pnas.211429998
29. Domnik L, Merrouch M, Goetzl S, Jeoung JH, Leger C, Dementin S, Fourmond V, Dobbek H (2017) CODH-IV: a high-efficiency CO-scavenging CO dehydrogenase with resistance to O2. Angew Chem Int Ed Engl 56(48):15466–15469. https://doi.org/10.1002/anie.201709261
30. Doukov TI, Iverson TM, Seravalli J, Ragsdale SW, Drennan CL (2002) A Ni-Fe-Cu center in a bifunctional carbon monoxide dehydrogenase/acetyl-CoA synthase. Science 298(5593):567–572. https://doi.org/10.1126/Science.1075843
31. Darnault C, Volbeda A, Kim EJ, Legrand P, Vernede X, Lindahl PA, Fontecilla-Camps JC (2003) Ni-Zn-[Fe-4-S-4] and Ni-Ni-[Fe-4-S-4] clusters in closed and open subunits of acetyl-CoA synthase/carbon monoxide dehydrogenase. Nat Struct Biol 10(4):271–279. https://doi.org/10.1038/Nsb912
32. Gong W, Hao B, Wei Z, Ferguson DJ Jr, Tallant T, Krzycki JA, Chan MK (2008) Structure of the $alpha_2epsilon_2$ Ni-dependent CO dehydrogenase component of the *Methanosarcina barkeri* acetyl-CoA decarbonylase/synthase complex. Proc Natl Acad Sci U S A 105(28):9558–9563. https://doi.org/10.1073/pnas.0800415105
33. Doukov TI, Blasiak LC, Seravalli J, Ragsdale SW, Drennan CL (2008) Xenon in and at the end of the tunnel of bifunctional carbon monoxide dehydrogenase/acetyl-CoA synthase. Biochemistry 47(11):3474–3483. https://doi.org/10.1021/Bi702386t
34. Jeoung JH, Dobbek H (2012) n-Butyl isocyanide oxidation at the [NiFe4S4OH(x)] cluster of CO dehydrogenase. J Biol Inorg Chem 17(2):167–173. https://doi.org/10.1007/s00775-011-0839-y
35. Wang PH, Bruschi M, De Gioia L, Blumberger J (2013) Uncovering a dynamically formed substrate access tunnel in carbon monoxide dehydrogenase/acetyl-CoA synthase. J Am Chem Soc 135(25):9493–9502. https://doi.org/10.1021/ja403110s
36. Lindahl PA, Ragsdale SW, Munck E (1990) Mossbauer study of CO dehydrogenase from *Clostridium thermoaceticum*. J Biol Chem 265(7):3880–3888
37. DeRose VJ, Telser J, Anderson ME, Lindahl PA, Hoffman BM (1998) A multinuclear ENDOR study of the C-cluster in CO dehydrogenase from *Clostridium thermoaceticum*: evidence for HxO and histidine coordination to the [Fe4S4] center. J Am Chem Soc 120(34):8767–8776
38. Jeoung JH, Dobbek H (2007) Carbon dioxide activation at the Ni,Fe-cluster of anaerobic carbon monoxide dehydrogenase. Science 318(5855):1461–1464. https://doi.org/10.1126/science.1148481

39. Lindahl PA (2002) The Ni-containing carbon monoxide dehydrogenase family: light at the end of the tunnel? Biochemistry 41(7):2097–2105
40. Lindahl PA, Munck E, Ragsdale SW (1990) CO dehydrogenase from *Clostridium thermoaceticum* – EPR and electrochemical studies in CO_2 and argon atmospheres. J Biol Chem 265(7):3873–3879
41. Kumar M, Lu WP, Liu L, Ragsdale SW (1993) Kinetic evidence that carbon monoxide dehydrogenase catalyzes the oxidation of carbon monoxide and the synthesis of acetyl-CoA at separate metal centers. J Am Chem Soc 115(24):11646–11647. https://doi.org/10.1021/ja00077a093
42. Hu ZG, Spangler NJ, Anderson ME, Xia JQ, Ludden PW, Lindahl PA, Munch E (1996) Nature of the C-cluster in Ni-containing carbon monoxide dehydrogenases. J Am Chem Soc 118 (4):830–845. https://doi.org/10.1021/Ja9528386
43. Anderson ME, Lindahl PA (1996) Spectroscopic states of the CO oxidation/CO_2 reduction active site of carbon monoxide dehydrogenase and mechanistic implications. Biochemistry 35 (25):8371–8380. https://doi.org/10.1021/bi952902w
44. Amara P, Mouesca JM, Volbeda A, Fontecilla-Camps JC (2011) Carbon monoxide dehydrogenase reaction mechanism: a likely case of abnormal CO_2 insertion to a Ni-H(−) bond. Inorg Chem 50(5):1868–1878. https://doi.org/10.1021/ic102304m
45. Lindahl PA (2012) Metal-metal bonds in biology. J Inorg Biochem 106(1):172–178. https://doi.org/10.1016/j.jinorgbio.2011.08.012
46. Seravalli J, Kumar M, Lu WP, Ragsdale SW (1995) Mechanism of CO oxidation by carbon monoxide dehydrogenase from *Clostridium thermoaceticum* and its inhibition by anions. Biochemistry 34(24):7879–7888
47. Möller-Zinkhan D, Thauer RK (1990) Anaerobic lactate oxidation to 3 CO2 by *Archaeoglobus fulgidus* via the carbon monoxide dehydrogenase pathway: demonstration of the acetyl-CoA carbon-carbon cleavage reaction in cell extracts. Arch Microbiol 153(3):215–218. https://doi.org/10.1007/BF00249070
48. Seravalli J, Ragsdale SW (2008) 13C NMR characterization of an exchange reaction between CO and CO_2 catalyzed by carbon monoxide dehydrogenase. Biochemistry 47(26):6770–6781
49. Sahoo D, Yoo C, Lee Y (2018) Direct CO_2 addition to a Ni(0)-CO species allows the selective generation of a nickel(II) carboxylate with expulsion of CO. J Am Chem Soc. https://doi.org/10.1021/jacs.7b11074
50. Heo J, Staples CR, Halbleib CM, Ludden PW (2000) Evidence for a ligand CO that is required for catalytic activity of CO dehydrogenase from *Rhodospirillum rubrum*. Biochemistry 39 (27):7956–7963
51. Fesseler J, Jeoung JH, Dobbek H (2015) How the [NiFe4S4] cluster of CO dehydrogenase activates CO_2 and NCO(−). Angew Chem Int Ed Engl 54(29):8560–8564. https://doi.org/10.1002/anie.201501778
52. Daniels L, Fuchs G, Thauer RK, Zeikus JG (1977) Carbon monoxide oxidation by methanogenic bacteria. J Bacteriol 132(1):118–126
53. Ensign SA, Hyman MR, Ludden PW (1989) Nickel-specific, slow-binding inhibition of carbon monoxide dehydrogenase from *Rhodospirillum rubrum* by cyanide. Biochemistry 28 (12):4973–4979. https://doi.org/10.1021/bi00438a011
54. Ha SW, Korbas M, Klepsch M, Meyer-Klaucke W, Meyer O, Svetlitchnyi V (2007) Interaction of potassium cyanide with the [Ni-4Fe-5S] active site cluster of CO dehydrogenase from *Carboxydothermus hydrogenoformans*. J Biol Chem 282(14):10639–10646. https://doi.org/10.1074/jbc.M610641200
55. Ciaccafava A, Tombolelli D, Domnik L, Fesseler J, Jeoung JH, Dobbek H, Mroginski MA, Zebger I, Hildebrandt P (2016) When the inhibitor tells more than the substrate: the cyanide-bound state of a carbon monoxide dehydrogenase. Chem Sci 7(5):3162–3171. https://doi.org/10.1039/c5sc04554a

56. Kung Y, Doukov TI, Seravalli J, Ragsdale SW, Drennan CL (2009) Crystallographic snapshots of cyanide- and water-bound C-clusters from bifunctional carbon monoxide dehydrogenase/acetyl-CoA synthase. Biochemistry 48(31):7432–7440. https://doi.org/10.1021/bi900574h
57. Jeoung JH, Dobbek H (2009) Structural basis of cyanide inhibition of Ni, Fe-containing carbon monoxide dehydrogenase. J Am Chem Soc 131(29):9922–9923. https://doi.org/10.1021/ja9046476
58. Wang VC, Can M, Pierce E, Ragsdale SW, Armstrong FA (2013) A unified electrocatalytic description of the action of inhibitors of nickel carbon monoxide dehydrogenase. J Am Chem Soc 135(6):2198–2206. https://doi.org/10.1021/ja308493k
59. Wang VC, Islam ST, Can M, Ragsdale SW, Armstrong FA (2015) Investigations by protein film electrochemistry of alternative reactions of nickel-containing carbon monoxide dehydrogenase. J Phys Chem B 119(43):13690–13697. https://doi.org/10.1021/acs.jpcb.5b03098
60. Ciaccafava A, Tombolelli D, Domnik L, Jeoung JH, Dobbek H, Mroginski MA, Zebger I, Hildebrandt P (2017) Carbon monoxide dehydrogenase reduces cyanate to cyanide. Angew Chem Int Ed Engl 56(26):7398–7401. https://doi.org/10.1002/anie.201703225
61. Kumar M, Ragsdale SW (1995) N-butyl isocyanide – a structural and functional analog of carbon-monoxide for carbon-monoxide dehydrogenase from *Clostridium-thermoaceticum*. J Am Chem Soc 117(46):11604–11605. https://doi.org/10.1021/Ja00151a036
62. Schrodinger LLC (2015) The PyMOL molecular graphics system, version 1.8

Index

,